Editorial Board of International Journal of Mining Science and Technology

Abstracted/Indexed in: Ei Compendex, CA, AJ, CSA, Coal Abstracts, Scopus, etc.

International Journal of Mining Science and Technology 27 (2017) 1

Contents lists available at ScienceDirect

International Journal of Mining Science and Technology

journal homepage: www.elsevier.com/locate/ijmst

Guest editorial–Special issue on ground control in mining in 2016

Gerald L. Finfinger [a,*], Syd S. Peng [b,*]

[a] National Institute for Occupational Safety and Health, Division of Mining Research Operations, Pittsburgh, PA 15236-0070, USA
[b] West Virginia University, Morgantown 26506, USA

In 1981 a Professor at West Virginia University recognized the need to establish a program for bringing together members of the mining community to share and discuss methods, technology and experiences related to ground control in mining operations [1]. From this initial idea the International Conference on Ground Control in Mining (ICGCM) was established. Professor Syd S. Peng was that individual and 35 years later this event is widely recognized as the premier gathering of ground control researchers, consultants, regulators, manufacturers and mine operators [2–6]. From the initial gathering in 1981, the Conference has grown significantly and has been expanded to include a sister event held annually in China [7]. Both events are focused on advancing the knowledge and science of ground control in mining applications with the overall goal of providing solutions for the mining industry. The range of topics covered at the conferences is extensive and the individuals attending and presenting is truly a who's who of the ground control community. Prior to the first Conference in 1981, ground control failures in underground coal mines accounted for more than 50% of all fatalities and all severe injuries. This number has decreased significantly and for 2014 ground control failures only account for about 14%. Virtually all of the advances in technology, knowledge and operational strategies for ground control have been presented and published at the International Conference on Ground Control in Mining over the last 35 years.

The 35th ICGCM was held on July 26–28, 2016 in Morgantown, WV. Each Conference was well-attended by the domestic and international community and more than 40 peer-reviewed papers were presented at each event. While not every paper submitted, approved and peer-review was presented, due to time limitations, all of the papers are published in a hard copy proceedings. More than 1600 papers have been published at the two events since the modest beginning 1981. A special session was held at the Conference in Morgantown WV this year that was dedicated to ground control mining practices in China.

This year's conference in Morgantown, WV covered an extensive range of subjects including numerical modeling, instrumentation design tools, rib stability, support performance, operator case studies, pillar design, subsidence and fundamental studies.

As in past years the papers presented during the Support Performance Assessments session generated a good deal of discussion both, during the formal presentation session, and continuing during the breaks. The engineering analyses and ultimately the value of the assessments for controlling the behavior of ground is an interesting topic and worthy of additional discussion and study.

Each of the papers was noteworthy and the analysis and interpretation of the data was thoughtful and provided information that will be useful for future consideration.

Twenty-five of the papers were selected for publication in this special issue on ground control in mining in International Journal of Mining Science and Technology. All other papers from this year's (and previous years) conference can be found on the International Conference on Ground Control in Mining's website (http://icgcm.conferenceacademy.com/papers/allpapers.aspx). More than 80 abstracts were received for this year's Conference and after peer-review by the Organizing Committee. Each paper selected for final publication was peer-reviewed by several researchers with expertise in the specific area.

We hope this special issue will provide useful references for engineers worldwide and for researchers and scholars in the field of ground control.

References

[1] ICGCM website that stores all 33 conference proceedings since 1981 for free distribution is: www.icgcm.conferenceacademy.com.
[2] Peng SS. Topical areas of research needs in ground control: a state of the art review on coal mine ground control. Int J Min Sci Technol 2015;25(1):1–6.
[3] Peng SS. Coal mine ground control. 3rd ed. Morgantown: Syd Peng Publisher; 2008.
[4] Peng SS. Ground control failures. Morgantown: Syd Peng Publisher; 2007.
[5] Heasley KA, Su DWH. 25 years of progressive in numerical modeling for ground control-What have we accomplished and where do we go next? In: Proceedings of the 25th international conference on ground control in mining. Morgantown; 2006. p. 11–7.
[6] Hasenfus GJ, Su DWH. Horizontal stress and coal mines: twenty five years of experience and perspective. In: Proceedings of the 25th international conference on ground control in mining. Morgantown; 2006. p. 256–67.
[7] Murphy MM, Finfinger GL, Peng SS. Guest editorial–special issue on ground control in mining. Int J Min Sci Technol 2016;1(26):1–2.

Received 18 August 2016; Revised 10 October, Accepted 15 November 2016; Available online 20 December 2016

* Corresponding authors. Tel.: +1 412 386 4172.
E-mail addresses: gbf8@cdc.gov (G.L. Finfinger), Syd.Peng@mail.wvu.edu (S.S. Peng).

http://dx.doi.org/10.1016/j.ijmst.2016.11.018
2095-2686/

International Journal of Mining Science and Technology 27 (2017) 3–7

Contents lists available at ScienceDirect

International Journal of Mining Science and Technology

journal homepage: www.elsevier.com/locate/ijmst

A review of the geomechanics aspects of a double fatality coal burst at Austar Colliery in NSW, Australia in April 2014

Hebblewhite Bruce *, Galvin Jim

School of Mining Engineering, UNSW, Sydney 2052, Australia

ARTICLE INFO

Article history:
Received 18 June 2016
Received in revised form 25 August 2016
Accepted 9 October 2016
Available online 29 December 2016

Keywords:
Underground coal mining
Roadway development
Strata control
Coal burst
Coal geology
Mine safety

ABSTRACT

A coal burst occurred on 15 April, 2014 at the Austar Coal Mine, located west of Newcastle, NSW, Australia. The burst resulted in fatal injuries to two men working as part of the mining crew at the development face. At the time, a continuous miner was being used to mine a longwall development gate road through heavily structured coal, at a depth of approximately 550 m. A number of pre-cursor bumps had occurred on previous shifts, emanating from the coal ribs of the roadway, in proximity to the coal face. This paper reviews the geological, geotechnical and mining conditions and circumstances leading up to the coal burst event; and presents and discusses the available evidence and possible interpretations relating to the geomechanical behaviour mechanisms that may have been critical factors in this incident. The paper also discusses some key technical and operational considerations of ground support systems and mining practices and strategies needed for operating in such conditions in the future.

1. Introduction

Austar Coal Mine is an underground longwall coal mine located near Cessnock in the Hunter Valley of New South Wales (NSW), Australia and is the only underground mine still extracting the Greta Seam in this region. The mine was the first in Australia to adopt the Chinese-developed longwall top coal caving (LTCC) method for thick seam extraction. Typically seam thickness ranges from 4 to 7 m and depth of mining from 480 to 560 m, with future mining planned down to depths of up to 700 m, making it one of the deepest operating coal mines in Australia.

On 15 April 2014, a pressure burst occurred in the left hand rib at the active mining face of B Heading, 2–3 cut-through, maingate A9 panel, during development of the gateroads for the ninth longwall top coal caving panel. Strata in the general vicinity was affected by disturbed geology and multiple geological structures. Fig. 1 shows a section of the mine plan as in October 2014 (six months after the accident), indicating the current longwall extraction panel (A8) and the development panel A9 where the accident occurred (note: neither development nor longwall face positions changed significantly between the time of the accident and the date of this plan). At the time of the accident the current longwall face was in excess of 1000 m away from the Maingate A9 development panel face position.

When the accident occurred, the development face was being advanced by a crew of seven mine workers. Messrs Jamie Mitchell and Phillip Grant were located on a working platform on the left hand side of the ABM25 continuous miner (bolter-miner), immediately adjacent to a ribline that had already been supported with bolts and mesh (rib bolting consisted of 1.5 m mechanically anchored bolts in the lower and upper sections of the seam, supplemented by 2.1 m chemically anchored bolts in the mid-seam section). The two men were engulfed by material ejected from the ribline during the pressure burst and died at the scene.

The accident was reported by the NSW Mine Safety Investigation Unit (MSIU) following an extensive investigation, which included a detailed technical report prepared by Galvin and Hebblewhite [1,2].

1.1. Terminology

In any situation, four conditions have to be satisfied simultaneously in order for a dynamic (violent) rock failure to occur. The first is self-evident and implicit in the other three conditions reported by Salamon and Wagner [3]. These four conditions are:

(1) The stress environment must be sufficiently high to result in rock failure.

* Corresponding author. Tel.: +61 2 9385 5160.
E-mail address: hebble@bigpond.com (B. Hebblewhite).

http://dx.doi.org/10.1016/j.ijmst.2016.10.002
2095-2686/

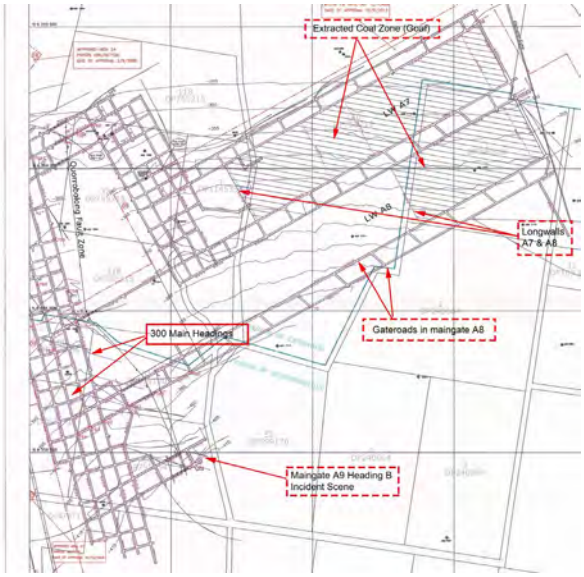

Fig. 1. Extract from Austar Mine Plan (31 October 2014) (after NSW MSIU (2015).

(2) A situation must exist which can result in a state of unstable equilibrium. This could be a low friction bedding plane, for example, where the potential exists for the coefficient of friction to drop rapidly from its static to dynamic value once movement is initiated along this plane.
(3) A change in the loading system. Potential triggers include, for example, a reduction in system strength due to a local change in rock mass material or structural properties; an increase in system stress associated with a local geological structure; or a decrease in confinement due to the formation of one or more excavations.
(4) A large amount of energy has to be stored in the system. This energy can be generated, for example, by depth of mining, bridging strata or geological structures.

Whilst these conditions were applied by Salamon and Wagner to rock burst behavior in hard rock mines, they are also potentially applicable to similar dynamic, stress-driven events in underground coal mining.

There are a number of terms used across the international underground mining industry (including both hard and soft rock mining) that are of relevance to any discussion of dynamic ground failure events in underground mines, including the type of event that occurred at Austar Coal Mine on 15 April 2014. It is important to clarify and adopt a consistent set of terms used in the context of such dynamic rock failures. It must be recognised that there is no universally accepted and unique set of definitions for all of these terms, however the following descriptions are widely regarded as appropriate–at least within the Australian mining context.

The terms to be discussed are as follows: (1) rock burst, (2) strain burst, (3) pressure bump, (4) pressure burst, (5) shake-down, (6) outburst, (7) coal bump, (8) coal burst, (9) pillar bump, and (10) pillar burst.

All of the above describe events associated with some form of dynamic energy release, usually associated with intact rock failure. This release of energy can vary greatly in magnitude and may or may not generate a measurable seismic signal.

Rock bursts and strain bursts are terms used to describe such dynamic energy releases and rock failure associated with hard rock mining. The source of the energy is directly related to stress levels within the rock, albeit that the manifestation of the stresses and the triggers for the release of the energy can be quite complex, involving many factors. The difference between a rock burst and a strain burst is simply one of consequence scale, due to different energy magnitudes–with strain bursts being of much lower energy magnitude, such that the resulting rock damage is far less than for a typical rock burst. These terms are not generally used in underground coal mining, although the geotechnical mechanisms involved may be very similar to the coal mining equivalent events summarized below.

The next two terms are those most commonly used to describe dynamic energy releases in underground coal mining–pressure bumps and pressure bursts. Both terms refer again to dynamic energy events associated with stress levels in the rock mass, which includes but is not limited to the coal seams. However, the commonly accepted difference between a pressure bump and a pressure burst relates to the magnitude and, hence, consequence. A pressure bump is a dynamic release of energy within the rock (or coal) mass in a coal mine, often due to intact rock failure or failure/displacement along a geological structure, that generates-an audible signal; ground vibration; and potential for displacement of existing loose or fractured material into mine openings. A pressure bump is also sometimes referred to as a bounce. On the other hand, a pressure burst is a pressure bump that actually causes consequent dynamic rock/coal failure in the vicinity of a mine opening, resulting in high velocity expulsion of this broken/failed material into the mine opening. The energy levels and, hence, velocities involved here can cause significant damage to, or destruction of conventional installed ground support elements such as bolts and mesh. A shake-down is another term taken from the hard rock mining sector, referring to damage caused by a bump event, where existing broken rock material is destabilized and collapses into the mine excavation.

An outburst in Australian mining terminology is also a dynamic energy release that can lead to some form of rock failure, however the source of energy is primarily associated with in situ gas pressure, sometimes also supplemented by stress-related energy. Therefore, outbursts are normally only associated with coal mining (where there is more prevalence of in situ gas), and usually only occur within the coal seam. Caution is emphasized with the use of the term ‘outburst’, when reviewing international literature. Whilst most European deep coal mining industries adopt the terminology as described above, the US coal industry often uses the term ‘outburst’ more broadly, to describe dynamic events that are purely stress driven as the energy source–events that in Australia would be referred to as a pressure burst or a coal burst.

The terms coal bump and coal burst, together with pillar bump and pillar burst are generally synonymous with pressure bump and pressure burst-and are all terms used to describe such dynamic events in underground coal mining. These terms are in some ways an alternative name for a sub-set of the more general events covered by pressure bump and pressure burst. Coal bumps and bursts are specific to events emanating from within the coal seam (as opposed to roof or floor origin); while pillar bumps and bursts relate to events within pillars as opposed to either in solid development drivage or on a longwall face, for example.

1.2. Mining background

The following background information is provided regarding the mining operations at Austar Coal Mine (Austar). Austar is a deep underground coal mine located approximately 10 km southwest of Cessnock in the Newcastle Coalfields of New South Wales, Australia. It is owned by Yancoal Australia Ltd., an Australian-Chinese partnership. Yancoal purchased the mine (formerly known as Southland Colliery) in December 2004. Austar commenced mining operations in April 2005 and in September 2006 became the first mine in Australia to adopt the mining method called longwall

top coal caving (LTCC), with the technology based on Chinese experience. The LTCC operations at Austar, and associated geotechnical challenges, were described by Moodie and Anderson [4]. Fig. 2 is a simplified schematic of the LTCC face and surrounding caving behaviour. Longwall development for LTCC is conducted in the same way as for conventional retreat longwall faces, using a two-heading gate road development configuration, mined using a single-pass bolter-miner and shuttle cars.

Austar mines the Greta Seam at depths approaching 600 m, with plans to proceed to greater depths (towards 700 m) within the medium-term future. At the time of the incident, the depth being mined was 555 m. The Greta Seam has had a chequered history associated with difficult mining conditions due to high stresses, gas and other high risk factors. There is a long history of pressure bumps associated with mining in the Greta Seam at Austar and other operations. Much of this is anecdotal, particularly within mine management circles. Large and frequent bumps have been experienced in previous neighbouring mines, in first workings at a depth of around 300 m, especially when mining through geological structures. Previous mine managers from the region consistently reported that rib spall was associated with bumps. There was some uncertainty as to whether some bumps may have constituted coal bursts under the definitions above. It was considered by the majority of experienced senior mine personnel in the region that bumping was 'normal' in the Greta Seam and could be quite severe.

Austar has experienced regular bump activity during the past five to ten years. In fact, the general consensus amongst the mining workforce was that bumping was "normal" and to be expected, and served to relieve high stress concentrations in and around the face–in this sense, regular bumping was regarded as a good thing, a "pressure relief" mechanism. In 2011 Austar experienced a major bump and shake-down event in the 300 Mains development panel. This incident involved the loss of the sidewall of the roadway for about 50–60 m, resulting in the sidewall needing to be resupported.

In spite of this experience, the consensus of the technical staff at Austar at the time, and prior to the accident, was that the coal seam characteristics were not prone to pressure bursts, as the structured nature of the coal would prevent sufficient stress to be stored in the coal to cause a burst. This view is in contrast to extensive international experience suggesting that virtually all coals can burst under certain circumstances, and that the physical and mechanical properties of coal are not necessarily key factors in determining propensity to bursting [5–7].

2. Geotechnical environment

It is well known that the immediate roof at Austar (and some floor strata) can include a number of massive sandstone strata units which are then overlain by the massive sandstone Branxton Formation in the upper roof.

In terms of structural geological features, Fig. 1 indicates the presence of a major zone of faulting known as the Quorrobolong Fault Zone, which ran to the east, and roughly parallel to the 300 mains development panel (see Fig. 1). This zone of faults intersected each of the longwall development panels, including maingate A9 Panel, which is shown in close-up detail in Fig. 3. The significant amount and throw of faulting between cut-throughs 1 and 2 resulted in very slow development progress through this region (over six months), and included an amount of stone drivage using a roadheader. Prior to the accident, an additional, unexpected inbye fault was intersected in A heading resulting in a roof fall. As a result of this fault being encountered in A heading, a decision was taken to mine an angled stub-heading off 2 cut-through below B heading in an attempt to prove the fault location prior to advancing B heading. As this angled stub was extended, a significant sheared zone was encountered and another roof fall occurred, although it is not clear if there was also a fault present just beyond this fall.

The mine was well aware of the presence of the initial zone of regional faulting between 1 and 2 cut-throughs. In addition to the larger scale structural geological features, visual inspection of the rib conditions (evident in photographs taken of the site MSIU) revealed some quite variable rib characteristics, which suggested localised potential variation in cleat distribution impacting on rib behavior [1].

3. Accident circumstances

Pressure bumps were quite commonplace during the development of the previous gateroads in maingate A8 panel – both during the intersection of the Quorrobolong Fault Zone, and also beyond it. This experience was repeated during the initial maingate A9 development. The following is an abbreviated description of events prior to the accident, summarised from the Accident Investigation Unit Report (NSW MSIU) [2].

During the course of the shifts immediately preceding the accident, a number of pressure bumps were reported by the deputies in the panel, with these bumps occurring especially during the process of cutting coal.

The shift 24 h before the incident was an afternoon shift with the same crew that was present when the accident occurred. On this shift the deputy reported a very large pressure bump emanating from the right hand rib in B heading while cutting was taking place. The bump was of such intensity that a decision was taken

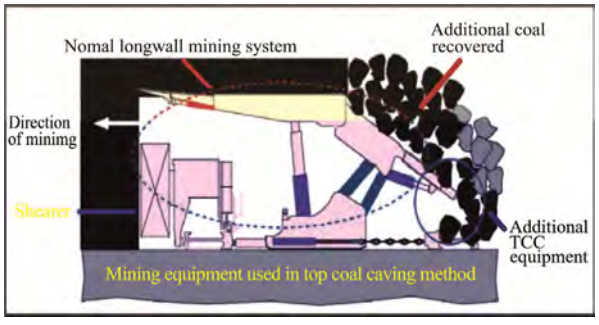

Fig. 2. Schematic view of LTCC face and caving behavior (after Moodie & Anderson (2011).

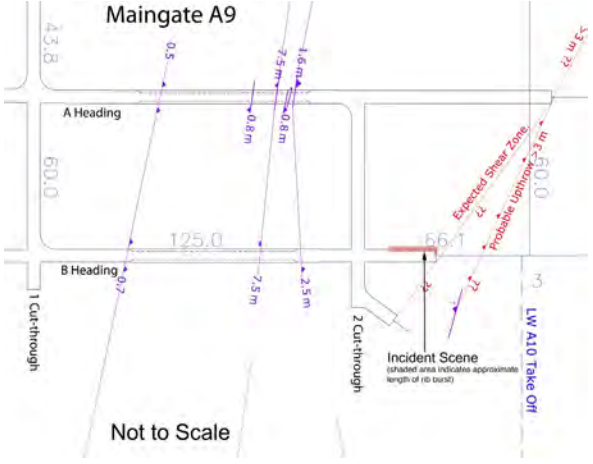

Fig. 3. Structural geology crossing maingate A9 Panel (after NSW MSIU, 2015).

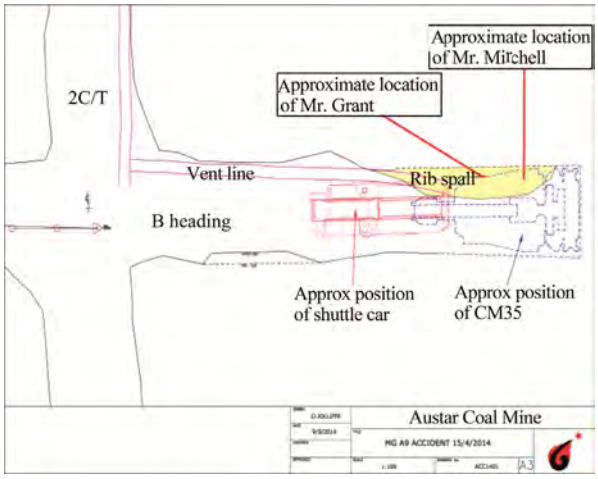

Fig. 4. Plan of accident site in B heading, MG A9 panel (after NSW MSIU (2015).

by the deputy and the miner driver to stop bolting while cutting, so that all bolting (roof and rib) would be completed prior to commencing the next cutting sequence. The shift directly preceding the incident was the day shift of 15 April 2014. There was no production on this shift as it was a planned maintenance shift. There is no record of any pressure bumping during day shift.

The afternoon shift of 15 April 2014 began at 3 pm. The incident occurred at 9.05 pm in B heading inbye of 2 cut through. Mr. Mitchell and Mr. Grant were both on the left-hand side of CM 35. The operator of CM 35 had just completed loading the shuttle car and had raised the cutting-head to the roof to park the cutting head. As soon as he turned off the conveyor, the incident occurred. Approximately 38 m^3 of coal was ejected from the left-hand side wall. The exact force and speed of the ejection is not known, but it is clear from the eye witness accounts that the coal was ejected from the side wall with significant force. The deputy in charge of MG A9 B crew (the deputy) was driving the shuttle car at the time of the incident and describes the event as follows:

> "It was like there was an explosion. It was, there was massive, I was sitting in the shuttle car, it blew me into the mesh guarding on the shuttle car. I lost my helmet. When I sort of, after it, it was like a split second, it was just that quick and that intense and it just, I sort of gathered myself."

Mr. Mitchell and Mr. Grant were both on the left hand side of the work platform on board the continuous miner, directly adjacent to where the rib burst occurred and were buried as a result of the burst. Fig. 4 is a plan of the accident site, indicating the burst location on the left hand rib, extending from a position just over a metre back from the face, to over 12 m back from the face. The rib in this location had been bolted and meshed. The depth of the burst into the rib is not known accurately, but it certainly extended well beyond the depth of the installed rib bolts (1.5 and 2.1 m bolts) which were fully ejected amongst the broken coal.

Fig. 5a and b shows the roadway conditions in the heading at the time of the burst. Fig. 5a is a view taken from the rear of the shuttle car that is parked directly behind the continuous miner at the face. The burst coal can be seen on the left of the miner,

(a) Heading showing the continuous miner and shuttle car at the burst site (left hand side of CM) (after NSW MSIU, 2015)

(b) Rib conditions on either side of B heading just outbye the burst site (after NSW MSIU, 2015)

Fig. 5. Roadway conditions at the coal burst site.

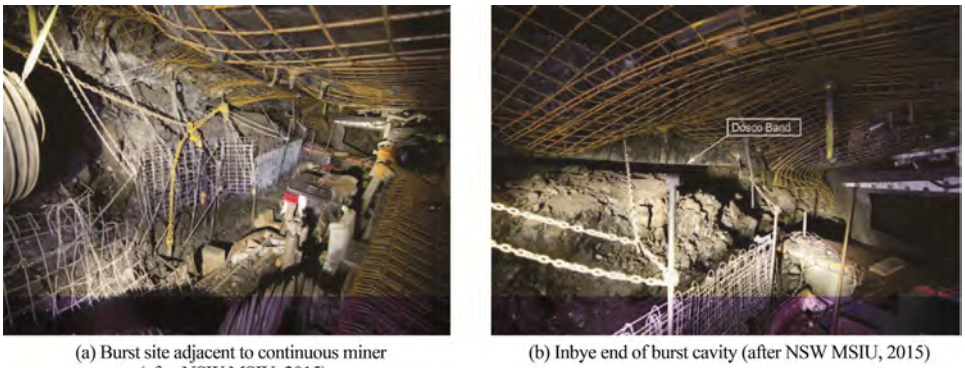

(a) Burst site adjacent to continuous miner (after NSW MSIU, 2015)

(b) Inbye end of burst cavity (after NSW MSIU, 2015)

Fig. 6. The fatal coal burst.

where the installed mesh is displaced outward, beneath the ventilation ducting. Fig. 5b is a similar photograph taken from further back in B heading towards the shuttle car position. In this photograph, the different rib conditions leading up to the burst location are evident, with the left had rib standing much more vertically than the right hand rib which had experienced a considerable amount of ongoing spalling. Fig. 6a and b are close-up photographs of the actual burst site in the left hand rib, with Fig. 6a showing the burst coal adjacent to the continuous miner (after body recovery) and Fig. 6b being closer to the face towards the right hand end of the burst.

A number of significant features are evident in these images. Firstly, the collars of some of the previously installed rib bolts can be seen displaced amongst the loose coal material (in Fig. 6a); secondly, the sizing of the coal that has been expelled from the burst is quite variable, ranging from well fragmented small particles, together with a number of larger blocks; thirdly, the upper bound of the burst cavity is clearly visible (Fig. 6b) as a very smooth, flat bedding plane within the seam known as the "Dosco Band". Rib coal above the Dosco band has not displaced at all, whereas all the coal beneath it is part of the burst. The exposed surface of the Dosco band showed signs of horizontal shearing activity, with a quite distinctive reddish-brown dust coating on much of the surface. Newman and others have reported similar evidence of reddish-brown pulverised coal particles at burst sites [8].

4. Possible failure mechanisms–contributing factors

There is no doubt that the mechanics of what causes a pressure burst, and what are the contributing factors, is extremely complex. There remains a considerable amount of research effort to be applied in the future to this complex and dynamic rock failure behaviour–in all its different manifestations. However, there is extensive international experience already available. International experience with bumps and bursts suggests that most such events are the result of multiple different mechanisms and factors coming together.

In the case of the Austar event, the following factors were present–all of which could potentially have contributed to the accident:

(1) High stress, associated with the depth of mining, and possibly supplemented by some additional stress concentrations resulting from any or all of regional faulting zones immediately adjacent to the event location, and of lensing and variations in stiff overburden sandstone units (and possibly also floor units).
(2) The presence of quite intense regional geological structure in the area, combined with severely distorted and complex local geology.
(3) The presence of massive sandstone units within the immediate 20 m+ of overburden roof, and the possibility of massive units also in the floor.
(4) A very dominant, smooth horizontal shear plane represented by the Dosco band, providing a dynamic shear failure surface below which the crushed and sheared coal could move.
(5) The effect of development mining providing a trigger either to destabilising the rock material above the burst zone in proximity to the fault surfaces ahead of mining, and/or providing a loss of confinement to the highly stressed coal in the rib that was undoubtedly subject to high levels of vertical stress.

Research in the US and elsewhere has identified similar elements in coal burst events [9,10].

5. Conclusions

It is not possible on the evidence available to categorically state the precise cause(s) of the pressure burst that occurred at Austar on 15 April 2014, nor to state the relative magnitude of the contributory factors, with a high degree of certainty. However, it is clear that a range of geological and geotechnical parameters all contributed to this event, together with a change in mining-induced stresses associated with removal of confinement simply by the incremental process of development mining.

In terms of future prevention and/or control measures, the ultimate measure is to move towards fully automated mining to ensure personnel are not located in the vicinity of the development roadway faces. However, this remains an elusive goal, at least for the short to medium term. Therefore, what is needed is a combination of: (1) ongoing investigative research into potential burst mechanisms and prediction and control measures; and (2) a comprehensive strategy of measures by mine operators to identify zones of potential burst-prone conditions, such as those characterised by disturbed structural geology (both large and small scale features); zones where stress concentrations may occur due to either geological variations or mining activity; zones where bumping and related seismic activity is present, to potentially provide a greater understanding of bump/burst behaviour and also to serve as a locator of high risk zones. On the basis of such burst-potential zone identification, there is then a need to develop modified remote-mining practices and ground support regimes for such zones, in order to minimise the risk of injury or disruption.

References

[1] NSW Mine Safety Investigation Unit (MSIU). Investigation report: report into the deaths of James Mitchell and Phillip Grant at the Austar Coal Mine, Paxton, NSW on 15 April 2014. NSW Dept of Industry (Resources & Energy); 2015.
[2] Galvin J, Hebblewhite B. Pressure burst incident at Austar coal mine on 15 April 2014. Report to NSW MSIU (unpublished); 2015.
[3] Salamon MDG, Wagner H. The role of stabilising pillars in the alleviation of rockburst hazard in deep mines Research Report No. 27/79. Johannesburg: Chamber of Mines of South Africa Research Organisation. COMRO; 1979.
[4] Moodie A, Anderson J. Geotechnical considerations for longwall top coal caving at Austar Coal Mine. In: Proceedings of 30th Int. Conf. on Ground Control in Mining. Morgantown, WV, USA. p. 238–47.
[5] Bräuner G. Rockbursts in coal mines and their prevention. Rotterdam: A.A. Balkema; 1994.
[6] Iannacchione AT, Zelanko JC. Occurrence and remediation of coal mine bumps: a historical review. Seminar on the mechanics and mitigation of violent failure in coal and hard-rock mines. US Bureau of Mines; 1995.
[7] Mark C. Coal bursts in the deep longwall mines of the United States. In: AusRock 2014: Third Australasian Ground Control in Mining Conference Sydney. AusIMM 2014. p. 33–39.
[8] Newman D. A case history investigation of two coal bumps in the Southern Appalachian Coalfield. In: Proceedings of 21st Int. Conf. on Ground Control in Mining. Morgantown, WV, USA. p. 90–7.
[9] Mark C, Gauna M. Evaluating the risk of coal bursts in underground coal mines. Int J Min Sci Technol 2016;26(1):47–52.
[10] Iannacchione A, Tadolini S. Occurrence, prediction and control of coal bursts in the US. Int J Min Sci Technol 2016;26(1):39–46.

International Journal of Mining Science and Technology 27 (2017) 9–15

Contents lists available at ScienceDirect

International Journal of Mining Science and Technology

journal homepage: www.elsevier.com/locate/ijmst

An assessment of coal pillar system stability criteria based on a mechanistic evaluation of the interaction between coal pillars and the overburden

Reed Guy *, Mctyer Kent, Frith Russell

Mine Advice Pty Ltd, Newcastle, NSW 2322, Australia

ARTICLE INFO

Article history:
Received 9 June 2016
Received in revised form 18 August 2016
Accepted 19 September 2016
Available online 18 December 2016

Keywords:
Coal pillars
Stability
Overburden
Post-failure behaviour
Stability criteria

ABSTRACT

Coal pillar design has historically assigned a factor of safety (FoS) or stability factor (SF) according to their estimated strength and the assumed overburden load acting on them. Acceptable FoS values have been assigned based on past mining experience or a statistical link between FoS and probability of failure (PoF). Pillar width-to-height (w/h) ratio has long been established as having a material influence on both pillar strength and its potential failure mode. However, there has been significant disagreement on using both factor of safety (FoS) and w/h as part of pillar system stability criterion, as compared to using FoS in isolation. This paper will argue that there are valid technical reasons to bring w/h ratio into system stability criteria (other than its influence on pillar strength), as it is related to the post-failure stiffness of the pillar, as measured in situ, and its interaction with overburden stiffness. When overburden stiffness is also brought into pillar system stability considerations, two issues emerge. The first is the width-to-depth (W/D) ratio of the panel and whether it is sub-critical or super-critical from a surface subsidence perspective. The second relates to a re-evaluation of pillar FoS based on whether the pillar is in an elastic or non-elastic (i.e., post-yield) state in its as-designed condition, as this is relevant to maintaining overburden stiffness at the highest possible level. The significance of the model is the potential to maximise both reserve recovery and mining efficiencies without any discernible increase in geotechnical risk, particularly in thick seams and higher depth of cover mining situations. At a time when mining economics are, at best, marginal, removing potentially unnecessary design conservatism is of interest to all mine operators and is an important topic for discussion amongst the geotechnical community.

1. Introduction

The majority, if not all, of the established coal pillar design methodologies are statistically derived and typically utilise a "classical" pillar strength formulae divided by full tributary area loading (i.e., full cover depth loading) to provide a FoS against core pillar failure. Pillar w/h ratio is typically included as a variable within the pillar strength formulae but, otherwise, is not formally used to help validate likely pillar stability outcomes as part of a combined system stability criterion. Similarly, potential design parameters, such as W/H ratio or the presence of thick, massive strata units within the overburden (both of which could significantly influence the overburden load acting on individual pillars within a panel) are seldom directly considered.

Stability outcomes could be potentially very conservative if these additional parameters are not used when designing mining layouts that incorporate load-bearing pillar systems. This could result in reduced mining efficiencies and the unnecessary sterilisation of mining reserves.

This paper will demonstrate that there are a number of valid technical reasons to incorporate these factors into the pillar design process using a series of logical mechanistic arguments, resulting in a more holistic pillar design approach.

2. Coal pillar failure mechanics

In order to understand the technical justification for the mechanistic pillar system design being proposed, it is necessary to briefly consider coal pillar failure mechanics and the key parameters that are involved.

Fig. 1 illustrates the well-established concept for stable and unstable behaviour of a structure (e.g., a coal pillar system) once

* Corresponding author. Tel.: +61 2 4088 0600.
E-mail address: russellfrith@mineadvice.com.au (G. Reed).

http://dx.doi.org/10.1016/j.ijmst.2016.09.031
2095-2686/

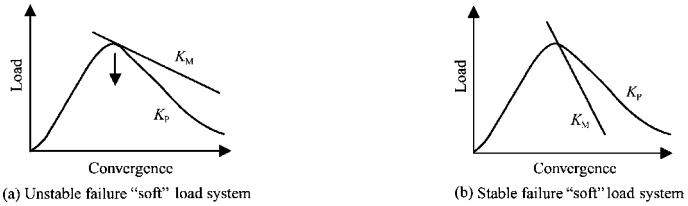

Fig. 1. Illustration of stable and unstable post-failure behaviour.

it reaches its maximum loading-bearing condition. This includes the two critical elements of the post-failure stiffness of the structure (K_p) and the stiffness of the system that is directly loading the structure (K_M). It is not necessary to explain this in significant detail other than to make the following points:

(1) It is necessary for the applied load to exceed the maximum load-bearing ability of the structure in order to drive the system as a whole into a post-failure condition. Without this condition, the structure remains in a pre-failure state and is naturally stable irrespective of the characteristics of the loading system.
(2) In the post-failure state, if the stiffness of the loading system (K_M) is less than the post-failure stiffness of the structure (K_p), the system as a whole becomes naturally unstable because the structure will lose its load-bearing ability at a faster rate than the loading system. While this condition remains, the structure will inevitably progress to a fully collapsed state.
(3) Conversely, if the stiffness of the loading system (K_M) is greater than the post-failure stiffness of the structure (K_p), the system will tend to remain naturally stable despite the maximum load-bearing ability of the structure having been exceeded. This is because the structure will lose its load-bearing ability at a slower rate than the loading system; hence, the system as a whole can attain post-failure equilibrium.

In coal pillar mechanics, the structure is the pillar itself, and the loading system is the overburden above it. Therefore, it is necessary to consider the post-failure stiffness of coal pillars and the overburden stiffness in order to develop a more comprehensive pillar design approach.

Other researchers have used both lab-based testing of coal samples and in situ testing of coal pillars to evaluate post-failure stiffness of coal pillars (see Figs. 2 and 3). More confidence is placed in the in situ test data shown in Fig. 3 because it more accurately represents real-life field conditions present in an underground coal mine, as compared to the lab-tested samples shown in Fig. 2 and the non-in situ data points shown in Fig. 3. Figs. 2 and 3 demonstrate the following points [1,2]:

(1) Post-failure stiffness decreases as a function of increasing w/h ratio. Both data sets clearly demonstrate this principle.
(2) The in situ test data in Fig. 3 shows post-failure stiffness becomes "asymptotic" when increasing w/h ratio above approximately 2. This is in contrast to the post-failure stiffness of cases that have w/h ratio values of <2, whereby, post-failure stiffness increases rapidly with ever-decreasing w/h ratio (NB increasing post-failure stiffness is detrimental to coal pillar system stability).
(3) Post-failure stiffness transitions from negative to positive (which is highly beneficial to system stability) at a w/h ratio as low as 5, based on an extrapolation of the in situ test data in Fig. 3.

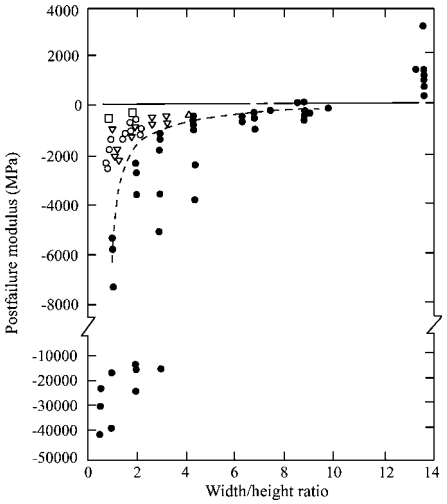

Fig. 3. Post-failure stiffness of coal pillars as a function of width to height (w/h) ratio – NB open symbols represent in situ tests [2].

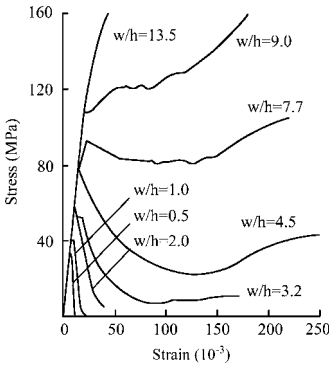

Fig. 2. Stress-strain behaviour of coal for varying width to height (w/h) ratio [3].

The data in Figs. 2 and 3 allow two other very important statements to be made in relation to the stability and hence design of stable coal pillar systems:

(1) For w/h ratios of >7, coal pillars are almost certain to work-harden as a post-failure behaviour and can, therefore, be classified as "indestructible" (i.e. they retain a confined core at all times and thus cannot collapse in the traditional sense), under normal overburden loading conditions, even though they will still compress significantly if loaded to a high level.
(2) For w/h ratios above 2, coal pillar system collapse requires the overburden to have little or no inherent stiffness in order to overcome the potentially re-stabilising influence of the asymptotically low post-failure stiffness of the pillars.

The integrity of these two statements will now be tested against known failed pillar cases.

3. An evaluation of coal pillar failed cases

The previous section of the paper has listed a number of coal pillar system design "rules" in reference to the stress-strain behaviour of coal according to varying *w*/*h* ratio. This section will examine those rules in reference to published cases of pillar system failures.

The listed "rules" are evident in the coal pillar failure representation first put forward by Hill (Fig. 4) whereby [3]

(1) Over 50% of the failed pillar cases included in that database have a design FoS of <1.5 and a pillar *w*/*h* ratio <2;
(2) The density of failed cases starts to reduce for *w*/*h* ratios >2 and is effectively almost 0 for values >5;
(3) The only documented failed case at a *w*/*h* ratio of >5 (approximately 8) had an FoS < 1 and was likely to be a floor-bearing failure rather than a core pillar failure (This has been the subject of some industry discussion in recent times). This is based on the geotechnical setting, which comprised thick soft floor with a history of allowing remnant coal pillars to punch through [4].

The data on the failed cases in Fig. 4 are also mirrored in the US failed cases described by Mark, Chase, and Zipf, shown in Table 1 and summarised in Fig. 5. In this regard, it is noted that 10 out of the 16 failed cases have a *w*/*h* ratio of ⩽2 (with none being >3) while all safety factor (SF) values are <1.5. Again, the substantial

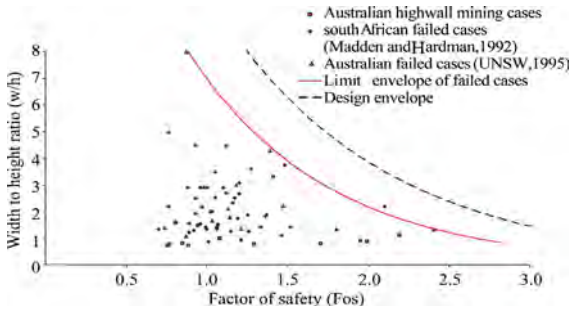

Fig. 4. Database of pillar collapses – width to height ratio vs. FoS [3].

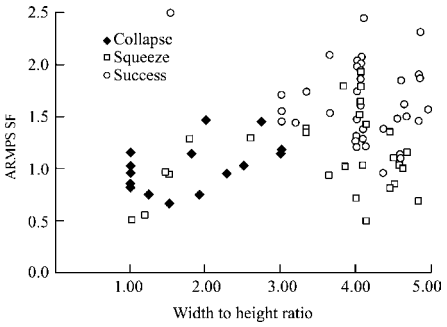

Fig. 5. ARMPS SF vs. pillar *w*/*h* ratio for pillar collapses and other case histories [8].

stabilising effect of combining a design FoS of at least 1.5 with a pillar *w*/*h* ratio of no less than 3–5 is clearly evident [2].

This leads to a potential resolution to the disagreements that have arisen due to Hill's original publication of the data seen in Fig. 4. Galvin pointed out that pillar *w*/*h* ratio was included in both axes because it was already part of the FoS calculation through its inclusion in the pillar strength formulae [5]. This is correct and, at face value, appears to justify that this type of graphical representation of failed cases has no merit and could, in fact, be misleading. However, if it is accepted that pillar *w*/*h* ratio also has a significant influence on post-failure pillar stiffness, and this has a controlling influence on whether a coal pillar collapse will occur or not, then Hill's representation has significant merit. The argument that *w*/*h* ratio is included in both axes of the graph is not a valid reason to dispense with the representation [5].

The other coal pillar system design "rule" suggested by Fig. 4 relates to pillars with *w*/*h* ratios <2 and their seeming ability to be prone to failure/collapse at FoS values that should, otherwise, not occur. The commonly stated reason for this is that, at such low *w*/*h* values, coal pillar strength can be significantly compromised by the presence of localised geological structures, such as joint swarms, faults, and dykes. This is in contrast to higher *w*/*h* ratios whereby a confined pillar core is likely to be developed irrespective of the weakening defects within the pillar. This issue simply dictates that other pillar system stability controls need to be put in place when developing a panel or mine layout that incorporate large numbers of coal pillars with *w*/*h* ratios of <2 as will now be described in relation to using the stiffness of the overburden as a pillar stability control.

Table 1
Listing and description of failed pillars cases in the US.

Case history	State	Depth (m)	Pillar size (m)	ARMPS SF	*w*/*h* ratio	Collapsed area, ha	Collapsed size (m)	Damage from airblast
A	WV	84	3 by 12	0.86	1.05	2.3	150 by 150	26 stoppings, 1 injury
B_1	WV	73	3 by 12	0.96	1.00			32 stoppings, fan wall out
			3 by 18	1.10	1.00			
B_2	WV	75	3 by 12	0.94	1.00	1.7	100 by 150	40 stoppings
B_3	WV	85	9 by 9	1.46	3.00	2.8	180 by 180	70 stoppings
			6 by 12	1.47	2.00			
C_1	WV	60	3 by 12	1.19	1.00	2.1	140 by 150	103 stoppings
C_2	WV	99	9 by 9	1.15	3.00	1.9	100 by 180	Minimal
D	WV	69	6 by 6	1.15	1.82	1.7	100 by 160	37 stoppings
			9 by 9	1.42	2.73			
E_1	WV	91	3 by 12	0.79	1.42	7.4	240 by 290	Major damage
E_2	WV	91	3 by 12	0.71	1.11	6.7	220 by 275	Major damage
F	OH	76	2 by 12	0.66	2.12	2.0	90 by 215	Minimal
G	UT	168	12 by 12	0.95	2.29	7.9	150 by 490	Major damage, 1 injury
O	WV			1.03	2.50	1.8	120 by 150	
R	CO	120 (400)	4 by 24	0.57	1.71	2.8	180 by 150	Minor damage

Note: dash indicates no data available.

4. Role of overburden stiffness

Having detailed the influence of both pillar FoS and w/h ratio as independent parameters that influence the role of the coal pillar in pillar system failures, it is now necessary to address the role of the overburden. Based on Fig. 1, it is evident that the post-failure stiffness of the overburden needs to be suitably low for coal pillars to be driven to a state of full collapse once they have been overloaded.

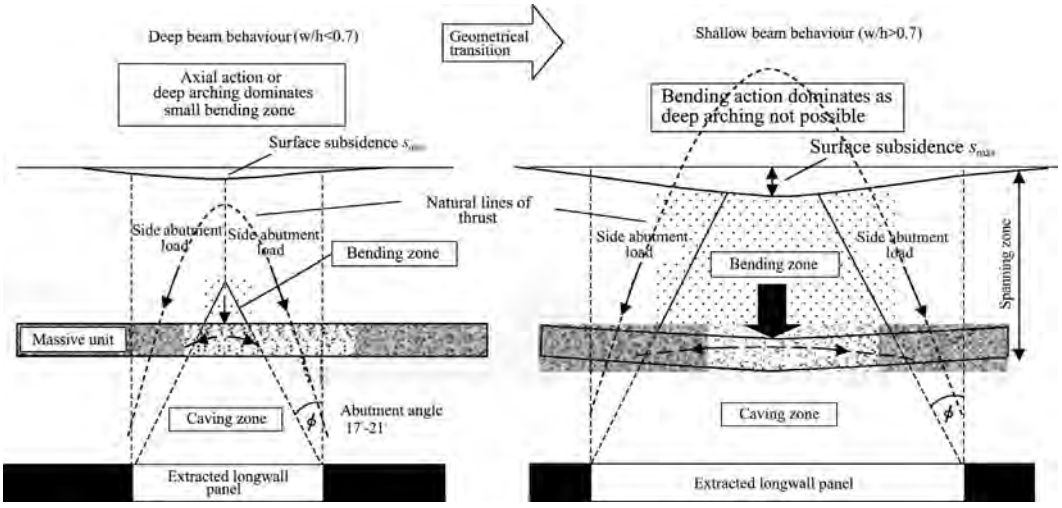

Fig. 6. Schematic representation of the mechanics of sub-critical (“deep” beam) and super-critical (“shallow” beam) subsidence behaviour [6].

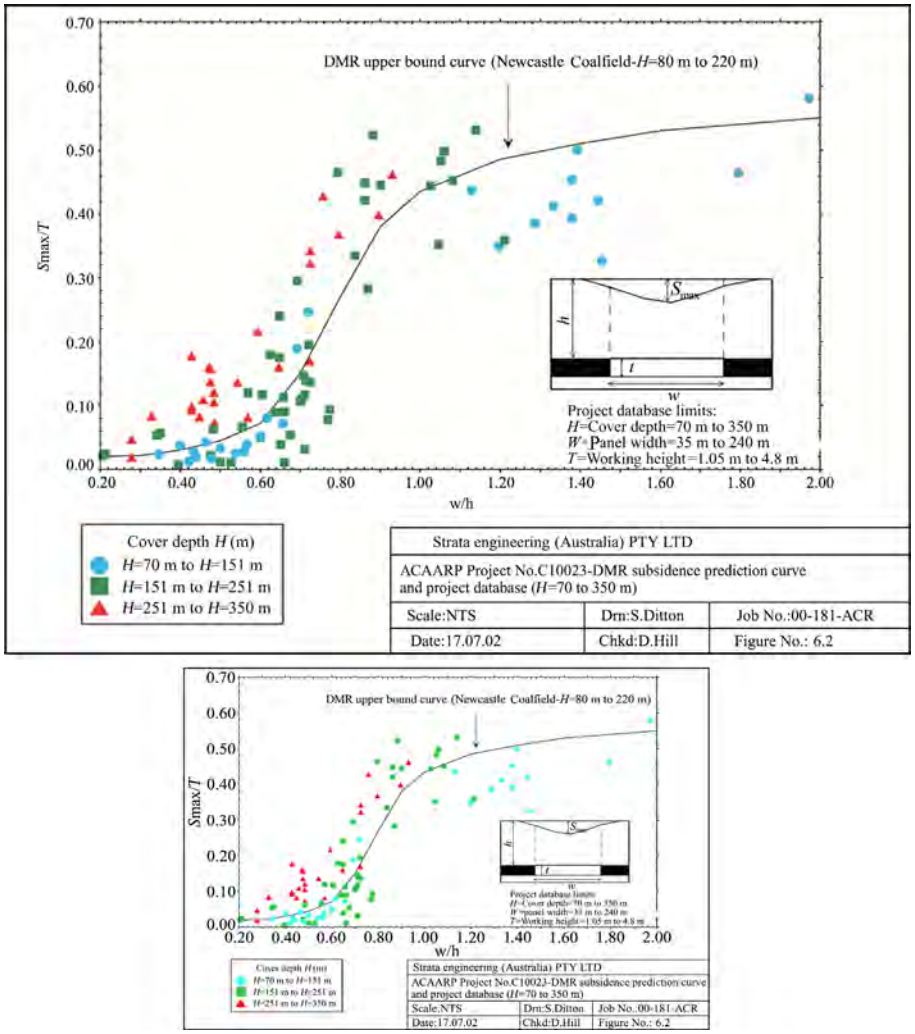

Fig. 7. Measured S_{max} values analysed according to extraction height (T), panel width (W) and cover depth (H) [6].

An instructive way to address overburden stiffness is to use the established concepts of "sub-critical," "critical transition," and "super-critical" surface subsidence as illustrated in Fig. 6 with actual subsidence data being provided in Fig. 7. This representation is known colloquially in Australia as a "Holla" curve after the late lax Holla.

The point of this is to demonstrate that it is only in the super-critical range that the entire overburden to surface loses most, if not all, of its inherent stiffness, effectively behaving as a "detached" loading block (with no inherent stiffness) that can drive overloaded coal pillars to a full state of collapse. Conversely, in the sub-critical range, at least a portion of the upper overburden is demonstrably being controlled by either the excavation geometry or the spanning capabilities of massive strata units (or both), which by definition must therefore retain some level of stiffness within part of the overburden, as its natural settlement at the surface under gravity is being restricted.

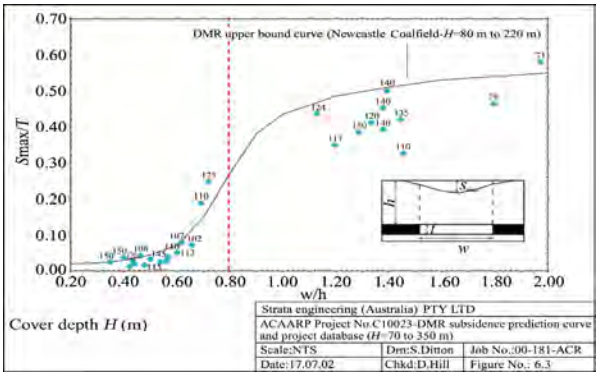

Fig. 8. Measured S_{max} values analysed according to extraction height (T), panel width (W) and cover depth (H) for depths ranging from 70 to 150 m [6].

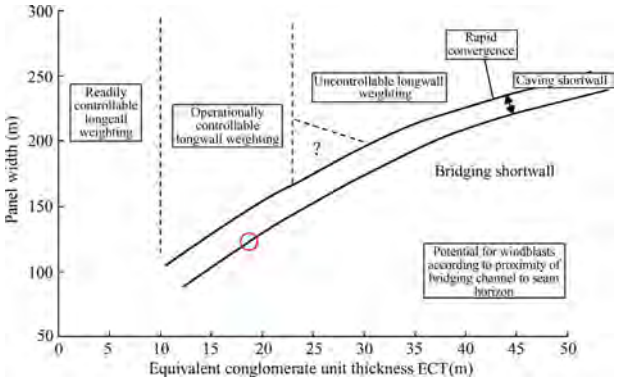

Fig. 9. Periodic weighting classification [5].

Evidence for the controlling influence of W/H ratio on coal pillar system failures can be found in Table 1 and also in the unpublished results of a study into pillar failures in highwall mining where large numbers of coal pillars with very low w/h ratios are commonly used. The US data presented in Table 1 contains minimum W/H ratio values of >0.9 but typically >1.5 for all collapsed cases with the unpublished highwall mining collapsed cases again being exclusively associated with W/H ratio values >0.9.

The significance of a W/H value in the order of $\geqslant$0.9 is obvious in Fig. 8, which contains measured surface subsidence data (S_{max}) for cover depths in the range of 70–150 m. The red dotted line represents the "mid-point" of the critical transition, whereby values of W/H > 0.8 tend towards being super-critical but values <0.8 tend towards being sub-critical. The minimum W/H value of 0.9 has been found in two separate studies on two different continents as being the lower defining value for failed pillar cases. This strongly confirms the important role of super-critical overburden behaviour and hence low overburden stiffness to surface in pillar collapses. It also confirms the potential additional stabilising influence of W/H values <0.8 when coal pillars have been designed for full tributary area loading.

Following on from the description of the influence of W/H ratio on overburden stiffness to surface according to different surface subsidence conditions, the influence of lithology on overburden stiffness for a given panel width will now be considered.

Two fundamental studies will be discussed: one relating to the influence of thick near-seam massive strata units on overburden periodic weighting and caveability as it affects longwall face stability and the other relating to the ability of massive strata units to influence surface subsidence magnitudes [6,7].

The periodic weighting classification developed by Frith and McKavanagh (Fig. 9) provides a useful first approximation as to how a massive strata unit may behave based on its thickness, the extraction panel width, and its material type (specifically conglomerate or sandstone) [5]. The defined "bridging shortwall" outcome is likely to result in overburden spanning and, therefore, inevitably a reduction in surface subsidence due to overburden sag, which implies the retention of significant overburden stiffness.

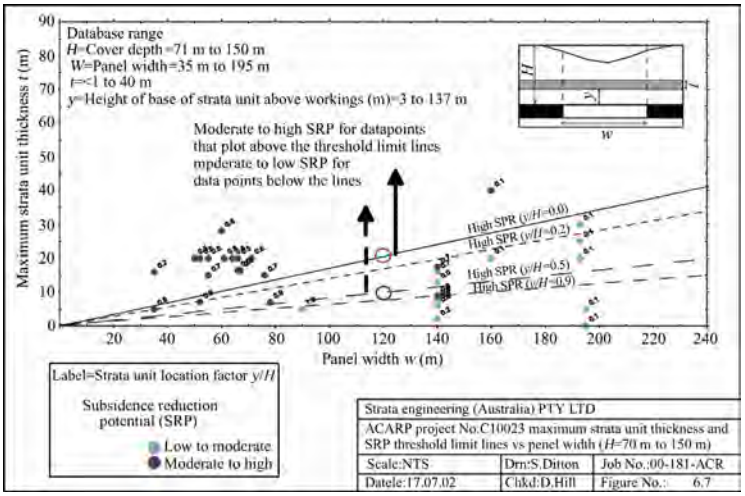

Fig. 10. Subsidence reduction potential (SRP) according to strata unit thickness, location of strata unit above the seam and panel width [4].

Ditton and Frith also defined the potential spanning phenomenon associated with thick and massive strata units in the overburden in relation to the ability of certain strata units to reduce levels of surface subsidence over and above what W/H ratio alone would suggest [6]. Fig. 10 shows what is termed as subsidence reduction potential (SRP).

As an example, for a panel width of 120 m, the strata unit thickness above which spanning of that unit can be reliably inferred is just <20 m (marked as red circles in Figs. 9 and 10). In other words, two different classification schemes that were developed to address different mining outcomes show a very close correlation in terms of the onset of strata unit spanning across an extraction panel of a given width.

Fig. 10 allows the analysis to be taken a step further because it brings in the varying location of a thick, massive unit within the overburden: the higher the unit above the extraction horizon (as given by y/h in Fig. 10), the lower the unit thickness required to develop high SRP. This makes sense when natural arching and consequent narrowing of the span above an extraction panel due to caving is considered (Fig. 6). At a distance of half the cover depth above the extraction horizon (i.e. H $y/h = 0.5$), the unit thickness required to modify surface subsidence across a 120 m wide panel is only 50% of what is required when the unit is present in the immediate roof (i.e., $y/h = 0$).

Combining the W/H ratio of a proposed panel of pillars with the thickness and location of significant lithological units within the overburden makes credible predictions possible. This data set can predict whether coal pillars will be loaded under full tributary area loading to surface by a "soft" loading system or whether the overburden has the ability redistribute overburden load to adjacent barrier pillars or solid coal due to its inherent stiffness. This is a useful layout aspect to bring into the pillar design process and further develops the design criterion contained within ARMPS-HWM whereby the number of HWM plunges between barriers is limited to 20.

5. Overburden load distributions within a pillar system

If one uses the concept of a sub-critical panel width between barrier pillars (or solid abutments) in coal pillar design, the concept of coal pillar FoS is modified to coal pillar system FoS. What this means is that the stability of any smaller coal pillars between the larger barrier pillars needs to be evaluated with the barrier pillars also included within the overall pillar system. This changes the definition of a barrier pillar from one that has the ability to truncate a coal pillar run to one that has the ability to prevent the pillar run.

Fig. 11 contains an illustration of a coal pillar system containing small pillars located between larger barrier pillars, and shows the basic scenario of individual pillar loading based solely on individual pillar width. This allows individual pillar FoS values under full

Fig. 11. Bord and pillar type assessment of pillar stability (pillar load distribution based solely on individual pillar width).

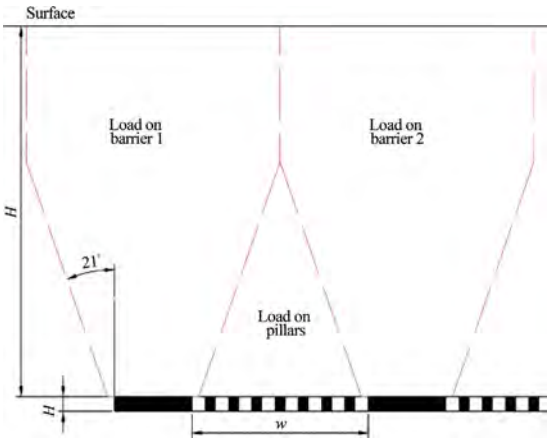

Fig. 12. "Double goaf loading" of pillars within a sub-critical panel bound by suitably sized barrier pillars of solid abutments (worst case unequal pillar load distribution).

tributary area loading to be determined, along with an overall system FoS for the combined influence of both the small pillars and the barriers.

To demonstrate how one may evaluate the potential influence of overburden load redistribution due to the sub-critical nature of the spans between barriers, Fig. 12 presents the same sub-critical panel layout of small pillars with the initial load exceeding their strength. Due to the sub-critical nature of the panel, overburden load is redistributed to the adjacent larger barrier pillars. The worst-case example of this assumes that an extraction goaf or gob has effectively formed between the adjacent panel barriers (or solid abutments) so that the overburden load acting on the barrier pillars increases, but the overburden load acting on the smaller in-panel pillars consequently decreases.

This does not suggest that such a situation, including the necessary significant overburden fracturing via the development of a caving angle, can realistically develop within such a layout. It is simply one method of demonstrating that, for sub-critical panel geometries, it is seemingly mechanistically improbable for the overburden to drive low FoS pillars between larger barriers to failure, and the panel geometries of known failed cases supports this assertion.

6. Comments on design factor of safety

Our current use of pillar FoS or SF is based largely on a statistical assessment of failed cases. The idea is to ensure that the design value used is sufficiently conservative so that the various unknowns of the design do not, in practice, combine to cause a pillar system failure where the analysis indicated otherwise. As a basis for further discussion, this paper suggests another possible interpretation of FoS based on the concepts presented herein, which are all based around the interplay between coal pillar stiffness and overburden stiffness rather than simply pillar strength/load.

With the exception of the failed HWM cases in Fig. 4, all of the collapsed cases in both Figs. 4 and 5 are associated with FoS or SF values <1.5. There are no collapsed cases above this value, yet the UNSW Pillar Design Procedure (PDP) extrapolates beyond this to determine Probability of Failure (PoF) values for FoS values that are well above 1.5.

The question being raised in this paper is whether there is a mechanistic reason as to why the collapsed cases truncate at a maximum FoS of around 1.5. If so, there is then perhaps a reason to argue that, for values >1.5, the potential for pillar collapse is

effectively eliminated for mechanistic reasons. If this were shown to be the case, it would necessitate a complete reconsideration of the statistical evaluation of failed cases for design FoS guidance above 1.5. The practical significance of such a change in approach would be quite considerable.

If one accepts that a specific role of coal pillars is to limit overburden movements to maximise the level of retained overburden stiffness (thus assisting overall system stability), a different interpretation of FoS in the failed cases is forthcoming. If one assumes that the strength formula provides reasonable approximation of the maximum load-bearing capacity of the pillar, a design FoS of 1.5 would represent the pillar being loaded at or close to its elastic limit. For FoS values above 1.5, the pillar would be in an elastic state, whereas below 1.5 it would enter a non-elastic state with an ever-decreasing stiffness towards its maximum strength. In terms of overburden stiffness being maximised by minimising overburden settlements, the difference between an FoS of 1.4 as compared to 1.6 would be highly significant when considered in this manner. The work has not yet been done to prove this hypothesis. However, it is interesting to consider that there may be a mechanistic explanation for collapsed cases usually having pillar FoS values <1.5, rather than simply assuming that it is all based on design uncertainty and, therefore, applying statistical methods to address the problem of determining acceptable design FoS values to prevent future collapses.

7. Summary

This paper outlines various technical arguments for the use of a mechanistic and more holistic approach to coal pillar system design, in which the independent influences of pillar w/h ratio, overburden W/H ratio and the presence of thick, massive strata units within the overburden are considered in conjunction with pillar FoS. The objective of combining these parameters is to provide far more robust design outcomes whereby more than just the strength of the coal pillar is acting to promote system stability. The potential mining advantage is more efficient mining layouts that recover more of the available coal reserves.

Combining the stabilising influences of occasional high w/h pillars within a mining layout and sub-critical working panels according to both geometry (W/H) or spanning strata units within the overburden could produce stable mining layouts that would have previously been discarded due to smaller production pillars having insufficient FoS or SF under full tributary area loading. This is of particular relevance to thick seam room and pillar workings in deeper cover whereby mine design using only FoS under full tributary area loading is highly restrictive.

Shifting the focus of coal pillar design from a simple load balance to one of maximising the stiffness of the pillar system (and thus minimising of overburden movements) as an aid to global stability is analogous to the change from roof suspension to roof reinforcement that transformed the way that mine roadway roofs are stabilised with rock bolts. This is an intriguing possibility to consider and one that will be the subject of future research.

At a time when mining economics are, at best, marginal, removing unnecessary design conservatism without negatively affecting safety is of interest to all mine operators and is an important topic for discussion amongst the geotechnical community.

References

[1] Das M. Influence of width/height ratio on post-failure behaviour of coal. Int J Min Geol Eng 1986;1(4):79–87.
[2] Chase FE, Zipf RK, Mark C. The massive collapse of coal pillars – case histories from the United States. In: Proceedings of the 13th international conference on ground control in mining. Morgantown: West Virginia University; 1994. p. 69–80.
[3] Hill D. Coal pillar design criteria for surface protection. In: Proceedings of the 2005 coal operators' conference. Wollongong, NSW: University of Wollongong; 2005. p. 31–8.
[4] Colwell M. Pillar design procedures and research methodologies – can there or should there be a unified approach? In: Proceedings of the second Australasian ground control in mining conference. Sydney: University of New South Wales; 2010. p. 67–77.
[5] Galvin JM. Considerations associated with the application of the UNSW and other pillar design formulae. In: Proceedings of the 41st U.S. symposium on rock mechanics. Golden, CO: American Rock Mechanics Association; 2006.
[6] Ditton S, Frith R. Review of industry subsidence data in relation to the influence of overburden lithology on subsidence and an initial assessment of a subsurface fracturing model for groundwater analysis. ACARP: final project report C10023 2003.
[7] Frith RC, McKavanagh B. Optimisation of longwall mining layouts under massive strata conditions and management of the associated safety and ground control problems. ACARP: end of grant report C7019 2000.
[8] Mark C, Chase F, Zipf K. Preventing massive pillar collapses in coal mines. In: Faculty research & creative works. Paper 12564. Pittsburgh, PA; 1997. p. 35–48.

International Journal of Mining Science and Technology 27 (2017) 17–27

Contents lists available at ScienceDirect

International Journal of Mining Science and Technology

journal homepage: www.elsevier.com/locate/ijmst

Green coal mining technique integrating mining-dressing-gas draining-backfilling-mining

Zhang Jixiong [a], Zhang Qiang [a,*], Spearing A.J.S. (Sam) [b], Miao Xiexing [a,c], Guo Shuai [c], Sun Qiang [a]

[a] Ministry of Education's Key Laboratory of Deep Coal Resource Mining, School of Mines, China University of Mining and Technology, Xuzhou 221116, China
[b] Western Australian School of Mines, Curtin University, Kalgoorlie 6433, Australia
[c] State Key Laboratory for GeoMechanics and Deep Underground Engineering, China University of Mining and Technology, Xuzhou 221116, China

ARTICLE INFO

Article history:
Received 2 May 2016
Received in revised form 12 August 2016
Accepted 15 September 2016
Available online 18 December 2016

Keywords:
Integrated green mining technique
Protective and protected coal seams
Mixed workface
Solid backfill with gangue
Gas drainage

ABSTRACT

Aiming to address the following major engineering issues faced by the Pingdingshan No. 12 mine: (1) difficulty in implementing auxiliary lifting because of its depth (i.e., beyond 1000 m); (2) highly gassy main coal seam with low permeability; (3) unstable overlying coal seam without suitable conditions for implementing conventional mining techniques for protective coal seam; and (4) predominant reliance on "under three" coal resources to ensure production output. This study proposes an integrated, closed-cycle mining-dressing-gas draining-backfilling-mining (MDGBM) technique. The proposed approach involves the mining of protective coal seam, underground dressing of coal and gangue (UDCG), pressure relief and gas drainage before extraction, and backfilling and mining of the protected coal seam. A system for draining gas and mining the protective seam in the rock stratum is designed and implemented based on the geological conditions. This system helps in realizing pressure relief and gas drainage from the protective seam before extraction. Accordingly, another system, which is connected to the existing production system, is established for the UDCG based on the dense medium-shallow trough process. The mixed mining workface is designed to accommodate both solid backfill and conventional fully mechanized coal mining, thereby facilitating coal mining, USCG, and backfilling. The results show that: The mixed mining workface length for the Ji_{15}-31010 protected seam was 220 m with coal production capacity 1.2 million tons per year, while the backfill capacity of gangue was 0.5 million tons per year. The gas pressure decreased from 1.78 to 0.35 MPa, and the total amount of safely mined coal was 1.34 million tons. The process of simultaneously exploiting coal and draining gas was found to be safe, efficient, and green. This process also yielded significant economic benefits.

1. Introduction

Highly gassy mines and collieries are found all over China. These mines and collieries are mainly concentrated in Guizhou, Sichuan, Heilongjiang, Shanxi, Henan, and Anhui provinces. The Chinese statistics for 2010 has indicated that 2197 highly gassy mines account for approximately 17% of all collieries in the country. Consequently, mining levels have been extended with the increase in coal production. This development has resulted in a gradual increase in the proportion of highly gassy coal seams with low permeability. More than 95% of the coal seams in China's highly gassy mines actually have low permeability. Their permeability coefficients are less than 0.1 $m^2/(MPa^2 \cdot d)$, which makes coal exploitation and gas draining a very challenging process.

The most common mining method presently employed for highly gassy coal seams with low permeability is used in mining the protective seam, to achieve pressure relief and gas drainage before extracting protected seam [1–3]. However, this method has limitations, and requires the existence of coal or parting thin seam that can act as the protective seam. The positions of the protective and protected seams must also be aligned relative to each other. Finding suitable methods of relieving gas pressure and increasing drainage rate before seam extraction is a major challenge in mining highly gassy coal seams without the requisite protective seams. This approach can facilitate simultaneous coal exploitation and gas draining, which would lead to safe and efficient coal production.

The Pingdingshan No. 12 mine, named as No. 12 mine for short, is owned by the Pingdingshan Tianan Coal Mining Co., Ltd. The Ji_{15} coal seam of the mine is highly gassy, has low permeability, and does not have a protective seam, which is the requisite condition

* Corresponding author. Tel.: +86 13775981147.
E-mail address: leafkky@163.com (Q. Zhang).

http://dx.doi.org/10.1016/j.ijmst.2016.11.014
2095-2686/

for conventional mining. This study proposes a coal mining technique that integrates the processes of mining-dressing-gas draining-backfilling-mining (MDGBM) to address the previously mentioned challenges. This framework includes various processes, including the mining of protective seam in the rock stratum, underground dressing of coal and gangue (UDCG), development of a system for exploiting coal and draining gas, and using a mixed mining technique that combines solid backfill and conventional, fully mechanized coal mining. The MDGBM technique was successfully implemented in the Ji_{14}-31010 and Ji_{15}-31010 workface, which are located in the third level of the No. 12 Mine. This result proves that the approach is safe, efficient, and green for simultaneously exploiting coal and draining gas.

2. Project overview

2.1. Background

The No. 12 mine, which is buried at a depth of 1100 m and has a production capacity of 1.3 Mt/a, is located in the Henan province. Its mining depth extends from −150 to −800 m. The remaining recoverable reserves of the mine currently amount to 23.849 Mt, 12.343 million tons (51.75%) of which is classified as "under three" coal resources. "Under three" refers to pressure-relieved coal buried under railways, waterbodies, or buildings. The first and second levels of the No. 12 mine have been fully mined. The third level has total reserves amounting to 32.323 million tons, 21.253 million tons (65.75%) of which is recoverable. The third level is also a single mining area with two wings. It is presently used as the main mining area with main coal seams belonging to the Ji group. The Ji_{15} coal seam, which has a permeability coefficient of 0.0776 $m^2/MPa^2 \cdot d$, specifically contains 15.256 m^3/t of raw gas at a pressure of 1.78 MPa. This seam is overlaid by the 0.5 m-thick Ji_{14} seam, which is a non-outburst seam with inherent instability and a gas pressure of 0.26 MPa.

Mining of the Ji_{15} seam is faced with the following challenges:

(1) The implementation of auxiliary lifting and other deep mining processes is difficult because the mining depth exceeds 1100 m.
(2) The Ji_{15} seam is highly gassy, but has low permeability and poor drainage efficiency. These characteristics pose serious potential risks and make safe mining very difficult to achieve.
(3) The overlying Ji_{14} coal seam is inherently unstable, too thin for mining, and does not have the requisite technical conditions for conventional mining of protective seams. On the one hand, abandoning the seam will result in serious resource wastage. On the other hand, designating it as the protective seam will involve mining it in the rock stratum, which will inevitably cause the coal flow to contain a high proportion of gangue (i.e., as much as 73.7%). The protective seam workface will create approximately 8.1 million m^3 of gangue, the surface discharge of which will significantly increase underground transportation and lifting costs. Secondary issues include choosing either lifting the gangue for surface discharge or treating them underground.
(4) The mine is predominantly reliant on "under three" coal resources, especially those under buildings. Therefore, its production output cannot be guaranteed. Accordingly, the engineering issue to be resolved is how to mine the J_{15} seam safely and efficiently.

2.2. Concept behind the integrated MDGBM technique

The Backfilling Mining Task Force from the China University of Mining and Technology has proposed the integrated MDGBM technique to address the engineering issues in the No. 12 mine. The basic concept behind this integrated technique is a green and cyclical mining system targeting the highly gassy Ji_{15} seam with low permeability. The MDGBM technique is entirely implemented underground and comprises the following processes: coal (rock) seam mining, UDCG, pressure relief, and gas drainage before extraction, and development of a mixed mining technique that combines solid backfill and fully mechanized conventional coal mining.

The conditions for protective seam mining are specifically created based on the basic requirements for protected seam mining. These requirements indicate that mining of the Ji_{14} protective coal (rock) seam should free the underlying highly gassy Ji_{15} seam with low permeability. The previous process produces raw coal with high gangue contents. This raw coal goes through the UDCG system. The resultant gangue is simultaneously transported to the underlying Ji_{15} seam workface, where mixed mining (i.e., solid backfill and conventional fully mechanized coal mining) is conducted. The backfill mining technique is subsequently used for goaf backfilling [4–15]. Protective seam mining increases the protected

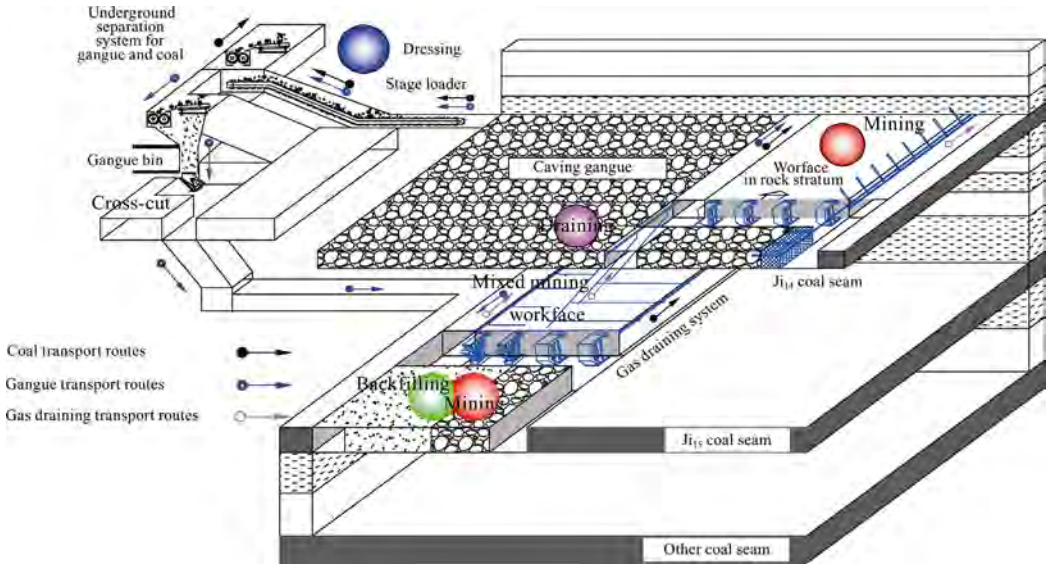

Fig. 1. Overall concept behind the integrated MDGBM technique.

permeability of the seam. Therefore, the gas in the latter can be extracted using a gas drainage system installed between the protective and protected seams. Consequently, simultaneous coal exploitation and gas drainage from the highly gassy Ji_{15} seam can be safely and efficiently realized. Fig. 1 shows the overall concept behind the integrated MDGBM technique for coal mines.

2.3. Geological mine conditions

The third level, which has a strike length of 2250 m, sloping width of 1800 m, and a mining depth ranging between 800 and1240 m, is located in the northern region of the No. 12 mine. The elevations of its upper bound and ground level range from −620 to −840 and +180 to +400 m, respectively. The Ji group, which is mined at the third level, comprises the Ji_{14}, Ji_{15}, Ji_{16}, and Ji_{17} seams arranged downward from the top. The Ji_{14} seam cannot be mined, while the Ji_{15} seam is isolated. The Ji_{16} and Ji_{17} seams are combined to form the $Ji_{16\text{-}17}$ seam.

The Ji_{15} seam, which produces high-quality coking coal, is the main seam being currently mined. This seam has an average thickness of 3.2 m, a dip of 6–10°, and consists of an 8.5–16.5 m-thick grayish black sandy mudstone roof. It has a Protodyakonov's hardness coefficient (f) of 2–5 and a vertical compressive strength of 29.4–45 MPa. The main roof is 25–30 m thick, and grayish white coarse-grained sandstone with a Protodyakonov's hardness coefficient of 6–10 while a vertical compressive strength of 53.9–186.2 MPa. The direct floor of the Ji_{15} seam is the immediate roof of the $Ji_{16\text{-}17}$ seam. This roof is 0.6–1.8 m thick, and consists of dark gray mudstone with a Protodyakonov's hardness coefficient of 0.8–3 and a compressive strength of 8.6 MPa.

Fig. 2 presents the synthetical stratum histogram of the Ji_{15} seam. The first mining face of the protective seam is the Ji_{14}-31010 workface, which has a strike length of 571.9, 150 m sloping width of 150 m, average dip of 5.5°, and average seam thickness of 0.5 m. The Ji_{14}-31050 protective seam workface is located in the north and is adjacent to the Ji_{14}-31010 workface. It has a strike length of 1040 m and a sloping width of 150 m. The first mining face of the protected seam is the Ji_{15}-31010 workface, which has a face length of 220 m, strike length of 929 m, depth of 1005–1166 m, and an average dip of 5°. Fig. 3 shows the plane layout of the test mining area.

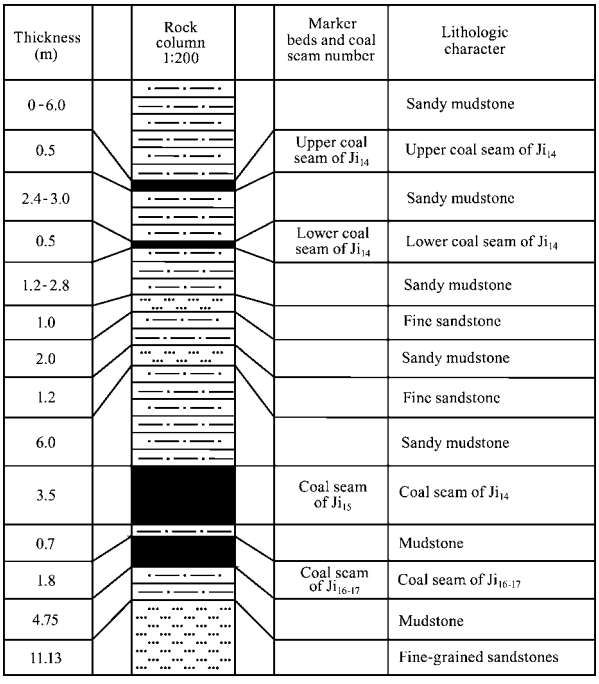

Fig. 2. Synthetical stratum histogram of the Ji_{15} seam.

3. Mining method for protective seams in rock strata

3.1. Method contents

The workface generally involve mining a rock stratum with a particular thickness before the protective seam can attain the ideal pressure relief effect. Therefore, the desired effect cannot be achieved if the mining of the thin coal seam is designed solely on the pressure relief principle. The technique of mining the protective seam in a rock stratum is intended for highly gassy coal seams with low permeability, which necessitates implementing pressure relief mining of the protective seam. However, a suitable protective seam is not available. The technique requires mining the thinner coal seam located near the outburst seam and portions or even the entirety of the nearby rock stratum to create the requisite protective seam. This step ensures the realization of the pressure relief effect during protective seam mining, thereby eliminating the risk of coal seam outbursts.

The workface may involve part of or even the entire rock stratum when its coal line is relatively thin and the rock stratum being mined is thick. Under these circumstances, the conventional, fully mechanized coal shearer cannot achieve the ideal rock-cutting effect. In other words, specialized mining processes, such as upgrading the coal shearer and related equipment, water-infused softening of the stratum, and pre-splitting blasting, are needed for workface mining in a rock stratum. We developed a coal-rock cutting method for the workfaces in rock strata after considering a comprehensive study of the methods used for mining parting thin seams proposed by researchers from China and overseas [16–19]. The method is applicable to the workfaces of protective seams in rock strata with different characteristics with regard to coal-rock thickness. Table 1 presents the specific features of the various cutting methods.

3.2. Production system for protective seams in rock strata

The first protective seams to be mined in the rock strata are the Ji_{14}-31010 and Ji_{14}-31050 workfaces (Fig. 3). The average coal seam thickness at these workfaces is only 0.5 m, while the designed mining height is 1.9 m. The workface stratum, which has a Protodyakonov's hardness coefficient of 7–9, is thicker than 0.8 m for more than 80% of the entire protective seam. Considering the varying workface stratum thickness, the shearer model is changed from MG320/710-WD (original) to MG500/1130-WD and then combined with pre-splitting blasting. The shearer is specifically used for direct cutting of coal rock when the rock stratum is thinner than 0.6 m. Meanwhile, pre-splitting blasting is executed prior to shearer cutting when the rock stratum is 0.6 m or thicker.

The boreholes for blasting are designed for real-time adjustment according to variations in the thickness of the rock stratum. A single row of boreholes at an elevation of 10° is laid out when the rock stratum is 0.6–0.8 m thick. On the contrary, a tri-petal layout is used for boreholes at elevations of 15° and dips of 15°-20° when thickness exceeds 0.8 m. The interval of boreholes for both layouts is the same at 0.5–0.7 m, while the depth of each borehole is 1.2–1.5 m. Figs. 4 and 5 show the cutting methods for the protective seam in a rock stratum of varying thickness and the blasting borehole layouts, respectively.

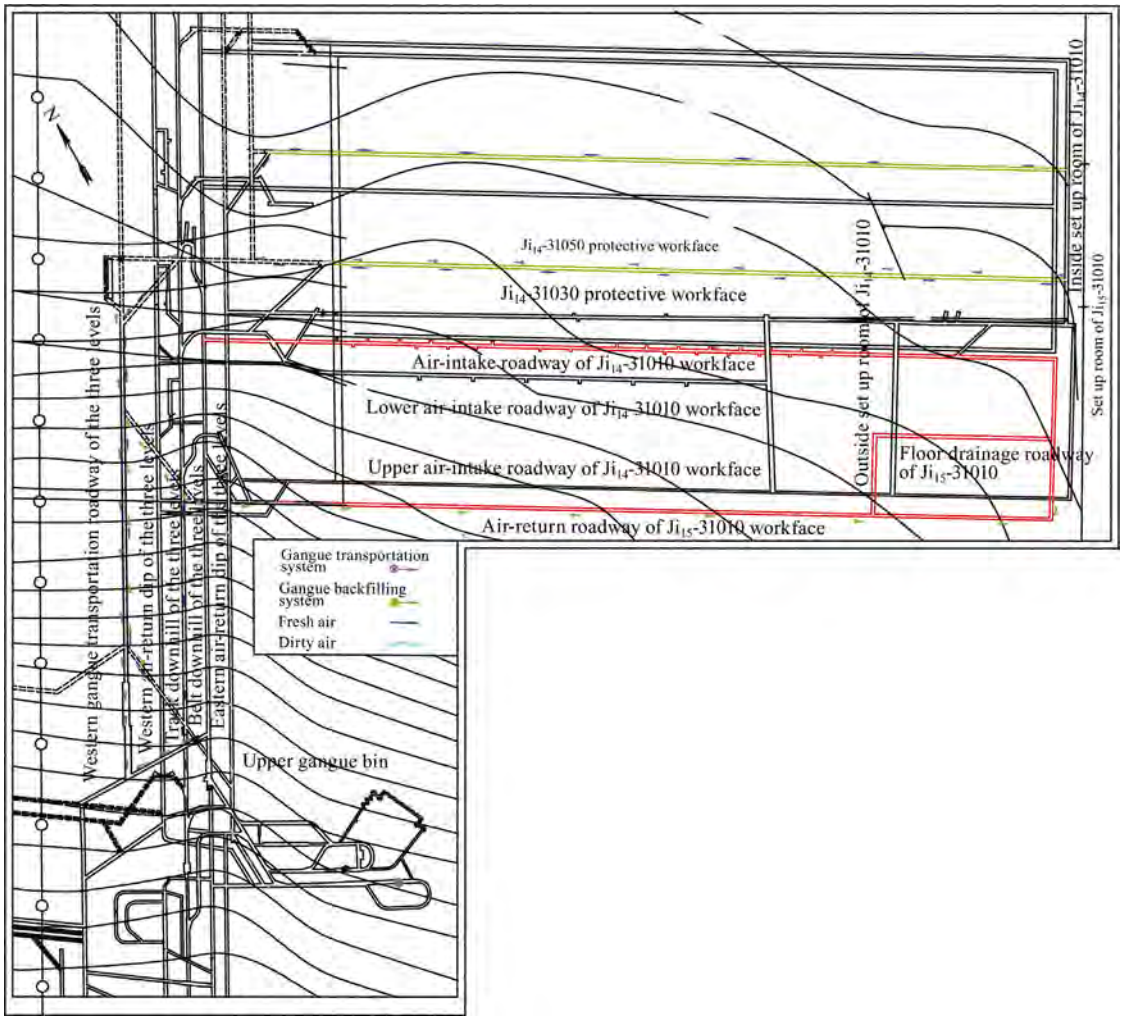

Fig. 3. Plane layout of the test mining area.

Table 1
Coal-rock cutting methods for protective seams in rock strata.

Cutting methods	Condition of use	Process flow	Main disadvantage
Conventional, fully mechanized mining	Rock stratum that lacks hardness and thickness	Mining that combines high-powered coal shearers and high-strength picks	Pick damage rate is high; maintenance cycle is short
Blasting mining	Rock stratum with good hardness or recovery of resources in irregular blocks or segments	Coal blasting, mechanized coal transportation, and roof propped up with support units	Labor-intensive, potential safety hazards, and low efficiency
Fully mechanized mining combined with water-infusion softening	Rock stratum with moderate hardness	Hole drilling to facilitate water-infusion softening of the rock stratum, followed by fully mechanized mining	Softening effect is very gradual and causes serious water accumulation
Fully mechanized mining combined with pre-splitting blasting	Rock stratum with moderate hardness and large-scale operations	Localized pre-splitting blasting of hard rocks, followed by cutting using a coal shearer	Equipment is easily damaged during rock blasting

4. UDCG

4.1. Main UDCG method

Present UDCG methods are mainly based on the existing processes and techniques used by aboveground coal preparation plants. The equipment used above ground for the dressing the coal and gangue are basically redesigned and reconstructed before being transported underground, where a dressing chamber is set up for the UDCG. The most commonly used UDCG methods are selective crushing, movable sieve jig, and dense medium-shallow trough (DM-ST) [20–24]. Table 2 summarizes the advantages and disadvantages of these methods.

The gangue contents in the coal flow from the Ji_{14} protective seam in the rock stratum can be as high as 73.7%. Accordingly, 35.4% of these sieved substances consists 0–13 mm particles, while the remaining 61.5% consists of ash contents. The dressing density is 1.7 kg/L. This composition requires a very high degree of discrimination during the coal and gangue dressing process. Considering the aforementioned features and the actual conditions in the

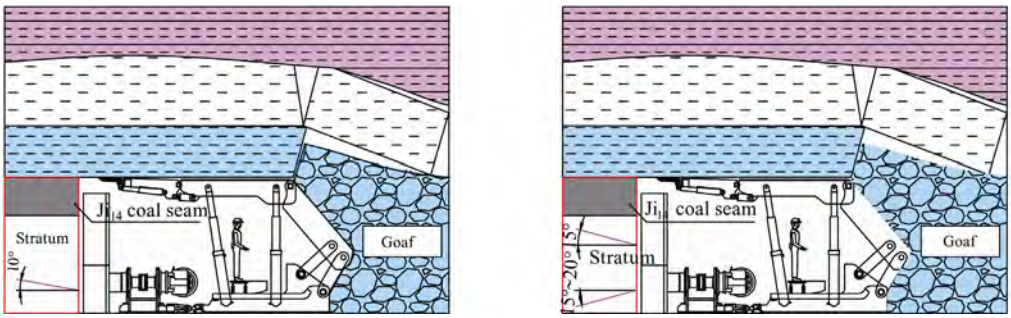

Fig. 4. Cutting methods for the protective seam in a rock stratum with varying thickness.

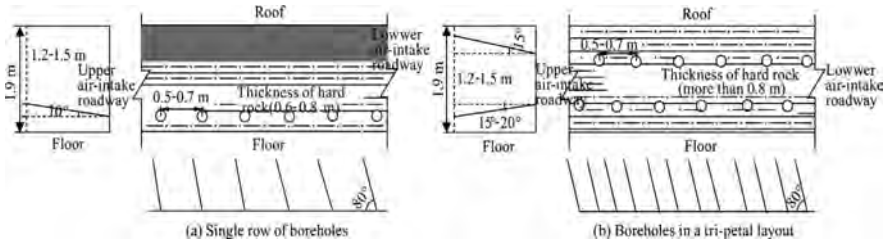

Fig. 5. Blasting borehole layouts.

Table 2
Comparative analysis of the UDCG methods.

Dressing methods	Key dressing equipment	Advantage	Disadvantage
Selective crushing	Selective crusher	Simple system and processing layout and small equipment investment	Low gangue recovery efficiency and limited applicability
Movable sieve jig	Jig, separator, crusher	Amount of gangue transported out of the mine is reduced, thereby saving aboveground space; simple processing system; and gangue recovery efficiency up to 85%	Difficulty of setting up tall and bulky equipment, and the particle size range that can be separated is limited
DM-ST	DM-ST separator, crusher, sculpting sieve	Amount of gangue transported out of the mine is reduced; raw coal quality is improved; savings on various costs; and dressing efficiency up to 98%, among others	Huge equipment investment, large space needed for bulky equipment, and high production costs

No. 12 mine, a 13, 250 mm three-product toothed roller sieve is used to initially separate gangue in the coal flow based on the particle diameter. A DM-ST separator is then utilized to execute the final dressing process based on the substance density.

4.2. DM-ST dressing system

The UDCG method is mainly composed of the following two components: the DM-ST discharging system and the slurry treatment system. These two components are utilized in the coal and gangue dressing process. The overall process flow of the dressing system is described below. First, a roller sieve with an appropriate mesh size is used to sieve the run-of-mine coal from the Ji_{14} protective seam in the rock stratum. This step aims to reduce the amount of ash contents, with small particle sizes, to a certain level. Second, the DM-ST separator is employed for the recovery treatment of substances remaining in the sieve before the slime recovery system conducts another round of slime washing. Fig. 6 shows the process flowchart of the DM-ST dressing system.

After evaluating the actual mine conditions, a dressing chamber is then set up in the connecting area between the third level's west wing gangue transportation and the inclined gangue transportation lanes. The UDCG chamber is 49.7 long, 8.8 tall, and 4 m wide along the horizontal direction. Immediately adjacent to the UDCG chamber is another chamber holding the conveyor head of the third level's west wing refuse transportation lane. This chamber is 60 m long, 6 m tall, and 8.4 m wide along the horizontal direction. The dressing chamber contains the key equipment, a three-product toothed roller sieve (Type of XCG-16/28), a roller crusher, and a DM-ST separator (Type of XZQ1525). The separator is suitable for segregating 13–250 mm coal and gangue particles with a dressing capacity of 2.2 million tons per yeart/a. Fig. 7 shows the UDCG chamber and the key equipment.

5. Gas drainage methods

Gas drainage is carried out underground. Accordingly, a 3D drainage pattern is set up to execute pressure relief mining and gas draining. Previous studies and experiments have successfully implemented various gas drainage methods for the working and adjacent seams and goaf combined with the use of an upper (lower) roadway or stay lane. These techniques have been used until now, and include the following aspects: (1) roadway on the protected seam floor along with upward-facing crossing boreholes, (2) pressure relief during multiple mining of a coal group, (3) roadway on the roof of the first mining (protective) seam, (4) removal of outbursts from the workface through coal seam bedding drilling, (5) drilling along the roof strike of the protective seam, (6) buried pipes in the goaf of the protective seam workface, (7) pressure relief of goaf, and (8) gas drainage through the upper workface corner [25–29].

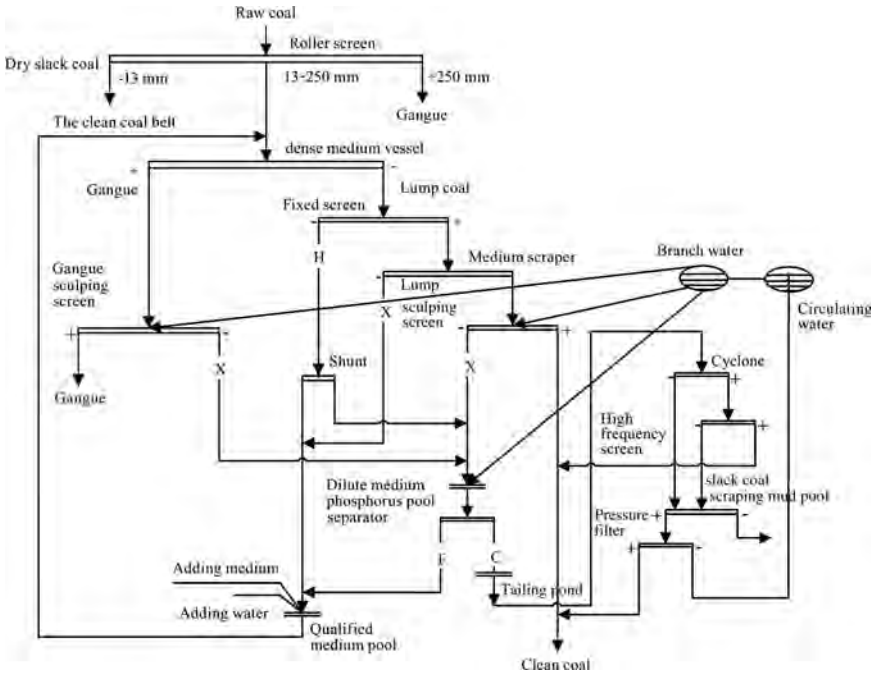

Fig. 6. Overall processing flow of the DM-ST dressing system.

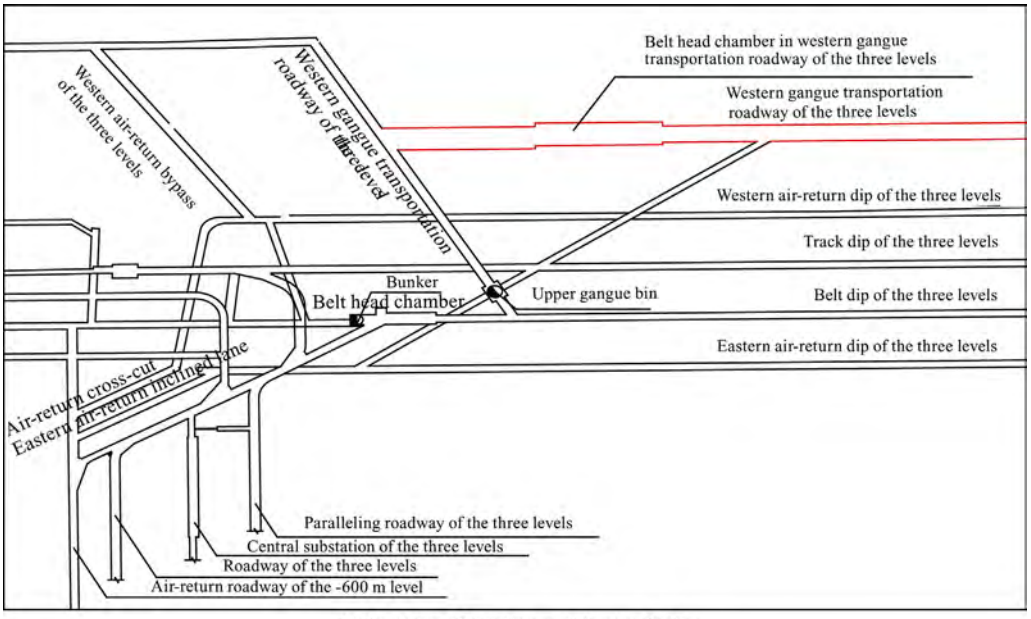

(a) Plane layout of the underground dressing chamber

(b) Underground dressing chamber

(c) DM-ST separator (plan view)

Fig. 7. UDCG chamber layout and key equipment photographs.

Table 3
Technical parameters of the boreholes for the Ji_{14}-31010 workface.

Borehole	Diameter (mm)	Depth (m)	Inter-borehole distance (m)	Dip angle (°)	Type	Location
1	89	30	15	−22	Crossing boreholes for gas drainage	Through cut of the Ji_{14}-31010 workface
2	89	60	30	−11	Crossing boreholes for hydraulic fracturing	
3	89	90	15	−8	Crossing boreholes for gas drainage	
4	89	30	50		Crossing boreholes for gas drainage along the roof strike	Lower head entry for the Ji_{14}-31010 workface
5	89	40	10		Crossing boreholes along the floor	

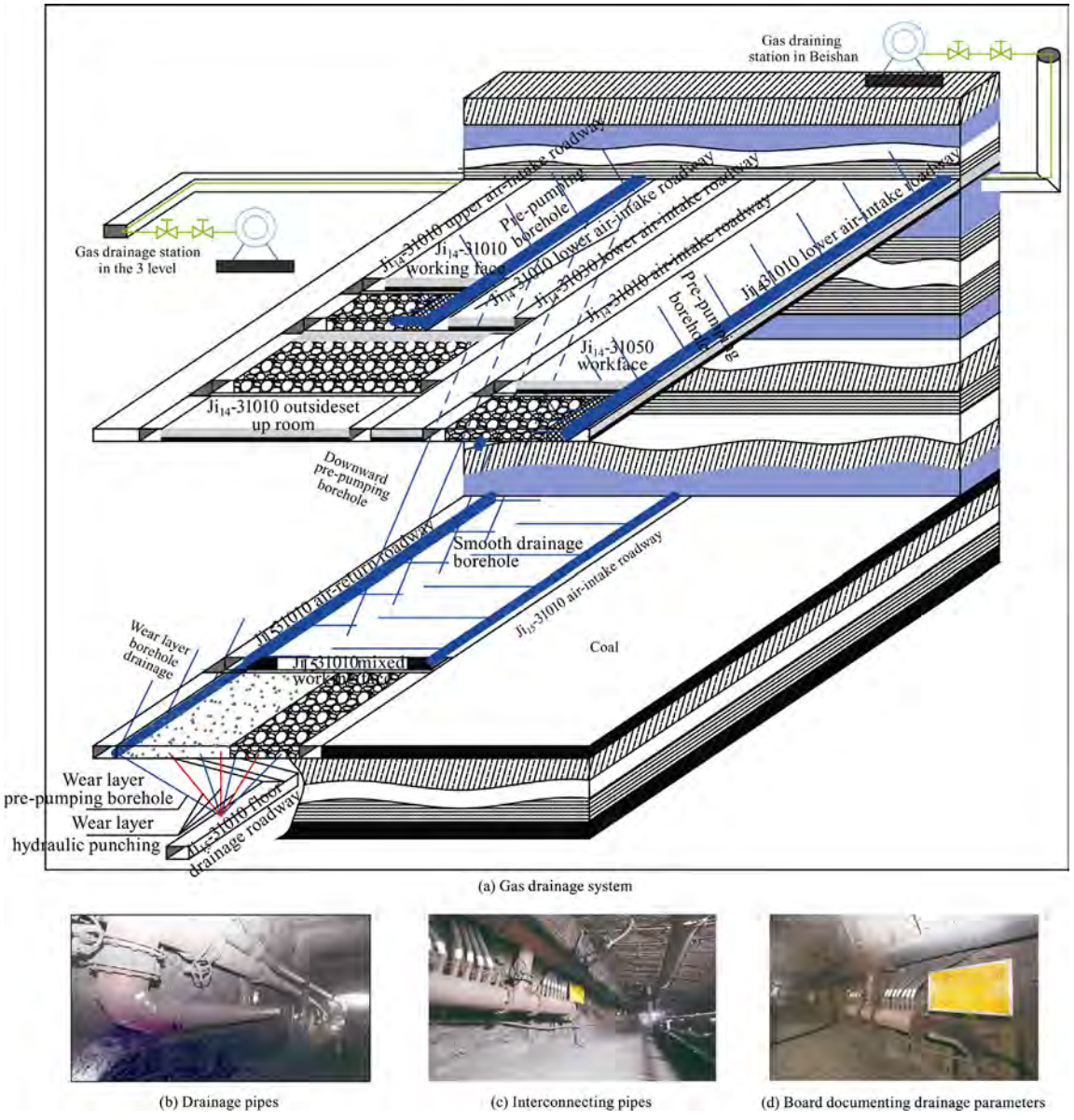

Fig. 8. Gas drainage system layout and drainage pipe photographs.

The aforementioned gas drainage methods have been referenced for designing a system for the Ji_{14} and Ji_{15} seams. The crossing boreholes for gas drainage and hydraulic fracturing are specifically set up at the through cut of the Ji_{14}-31010 workface for pressure relief and gas drainage of the Ji_{15} seam. The crossing boreholes are drilled along the roof strike at the lower head entry for the Ji_{14}-31010 workface. Concurrent drilling of crossing predrainage boreholes is also conducted on the floor for relieved gas drainage from the Ji_{15} seam. Table 3 presents the technical parameters of the boreholes. Subsequently, 300-mm-diameter drainage pipes are buried along the lower head entry and the gob-side entry wall at 10 m intervals. Doing this drains the gas accumulated at the upper goaf portion.

Boreholes are also drilled in the bedding order on the vertical coal walls of the head and tail entries of the Ji_{15}-31010 workface for gas drainage from the working seam. The boreholes have a diameter of 89 mm, depths of 70 and 140 m, and are located at 2 m intervals. At the same time, upward-facing crossing boreholes are drilled in the Ji_{15}-31010 tail entry to drain gas that had dissipated upward from the Ji_{15} seam to the fracture belt on the protec-

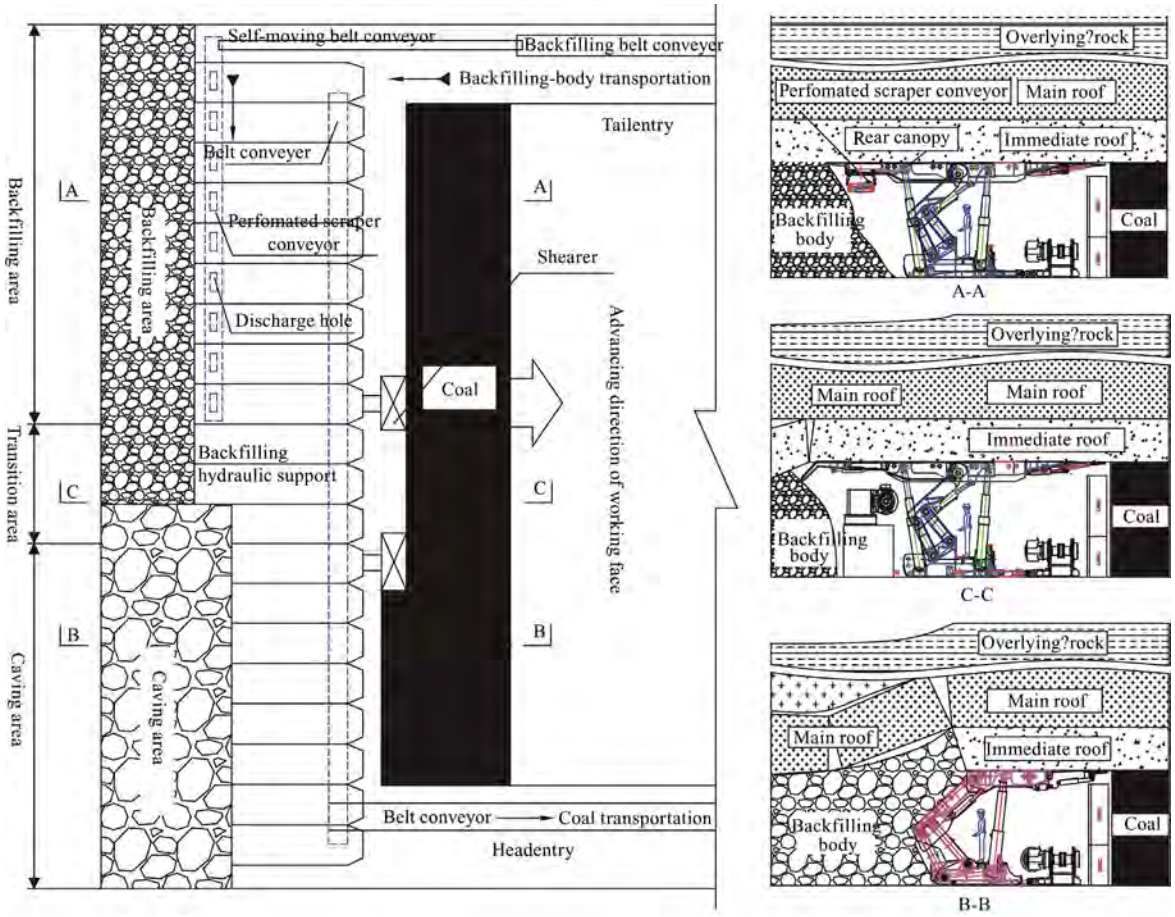

Fig. 9. Mixed mining workface and equipment layout with solid backfill and conventional fully mechanized coal mining.

Table 4
Selected equipment models for the mixed mining workface.

Index No.	Equipment name	Model No.	Quantity
1	Coal shearer	MG400/940 WD	1
2	Front scraper conveyor	SGZ-800/800WS	1
3	Stage loader for coal transportation	SZZ764/200	1
4	Dual-column fully mechanized mining support	ZY6800/20/40	76
5	Backfilling support	ZC5200/20/40	66
6	Backfilling transition support A	ZCGa5200/20/40	2
7	Backfilling transition support B	ZCGb5200/20/40	1
8	Backfilling transition support C	ZCGc5200/20/40	1
9	Rear scraper conveyor	SGZ764/2 × 200	1
10	Belt conveyor	DTL80/50/30	1

tive seam roof. The boreholes have a diameter of 75 mm and are located at 10 m intervals.

A set of crossing pre-drainage boreholes is drilled on the Ji_{15} seam on the floor drainage gateway of the Ji_{15}-31010 workface at 5 m intervals. Each set comprises 11 boreholes at 5 m intervals. These boreholes facilitate gas pre-drainage from the Ji_{15} seam. Fig. 8 shows the overall layout of the gas drainage system for the Ji_{14}-31010 protective seam, Ji_{14}-31050, and Ji_{15}-31010 workfaces.

6. Mixed method of combining solid backfill and conventional fully mechanized mining

6.1. Method contents

The most commonly used mixed mining methods are as follows: (1) high-grade, conventionally mechanized mining mixed with blasting mining, (2) fully mechanized mining mixed with blasting mining, (3) fully mechanized mining mixed with longwall top coal caving, and (4) solid backfill mixed with conventional fully mechanized mining [30–33]. The fourth method refers to the concurrent equipment setup for both fully mechanized solid backfill and conventional fully mechanized mining at the same workface. The different equipments have coordinated operations, which jointly completes the coal and solid backfill mining processes. The mixed mining workface comprises three areas, namely, backfilling, transition, and caving. At the backfilling area, the solid backfill method is used for coal mining. A backfilling hydraulic support and a perforated scraper conveyor are used to backfill the goaf with gangue. At the caving area, the conventional, fully mechanized coal mining method is employed. This area is equipped with a conventional, fully mechanized hydraulic support. Furthermore, the mine roof is allowed to naturally collapse. The transition area is located

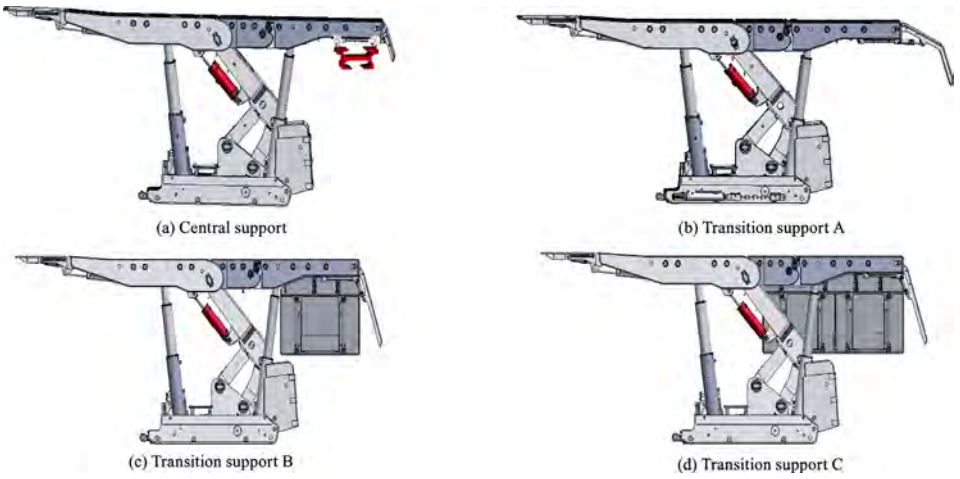

Fig. 10. Basic structure of the backfilling hydraulic support.

between the two previously mentioned areas. It also consists of a backfilling transition support and a perforated scraper conveyor head.

A coal shearer and a scraper conveyor for coal transportation are subsequently installed at the front of the mixed mining workface. The crusher, stage loader, belt conveyor, and other equipment are located within the coal transportation lane. The gangue transportation lane holds a separate gangue belt conveyor and a gangue stage loader. The total length of the mixed mining workface exceeds 200 m. It is capable of processing gangue for workface solid backfilling. It also has the ability to overcome the disadvantages of a plain backfilling workface, including low production capacity and poor efficiency. Therefore, the requirements of production capacity of the mine can be satisfied with a single workface. Fig. 9 shows the production system of the mixed mining workface and the equipment layout.

6.2. Key technical parameters and equipment selection for the Ji_{15}-31010 mixed mining workface

The first mining face of the Ji_{15} seam in the third level is the Ji_{15}-31010 mixed mining workface (Fig. 9). The Ji_{15}-31030 will be its replacement face. The Ji_{15}-31010 mixed mining workface is designed based on the requirements of production capacity of the mine, processing gangue from the Ji_{14} protective seam in the rock stratum, and the stress distribution characteristics of the transition area. The workface has a total length of 220 m, of which the lengths of the backfilling, caving, and transition areas correspond to 120, 94, and 6 m, respectively.

The following matching principles must be considered in selecting the equipment for the mixed mining workface: (1) compatibility between backfilling and coal mining capabilities, (2) parallel backfilling and coal mining operations, and (3) safety management of the transition zone. The finalized list of selected key equipment includes MG400/940 WD coal shearer, SGZ-800/800WS scraper conveyor, ZC5200/20/40 backfilling hydraulic support, SZZ764/200 self-moving belt conveyor, and SGZ764/2 × 200 perforated scraper conveyor.

The coal shearer and the scraper conveyor are standard equipment used for conventional, fully mechanized coal mining. The basic support chosen for the transition area, which has been selected after considering ventilation management, conveyor head layout, and requirements for refuse blocking, is similar to that for the backfilling area. The transition support rear is fixed with a holder that connects to the lifting platform of the conveyor head, as well as the equipment at the rear and side for refuse blocking. Table 4 presents the equipment models for the mixed mining workface. Fig. 10 shows the basic structure of the backfilling hydraulic support used in the backfilling and transition areas.

7. Implementation results

7.1. Integrated MDGBM technique

The concept of an integrated MDGBM technique successfully brings together several systems. These systems include underground mining of the protective seam in the rock stratum, underground low coal and high gangue contents dressing, gas drainage from seams with low permeability, and combination of extended solid backfill with conventional, fully mechanized mining. These various production systems are mutually coordinated with a temporally sequential and spatial matching of the rock mining, dressing, drainage, backfill, and coal mining processes. This coordination ensures a safe and efficient operation of the integrated MDGBM system. Fig. 11 shows the overall process flowchart of the system.

7.2. Pressure-relief effect of the Ji_{15} protected seam

Fig. 12 shows change in gas pressure for the mixed mining workface of the Ji_{15}-31010 protected seam during protective seam mining. After mining the Ji_{14}-31010 protective seam in the rock

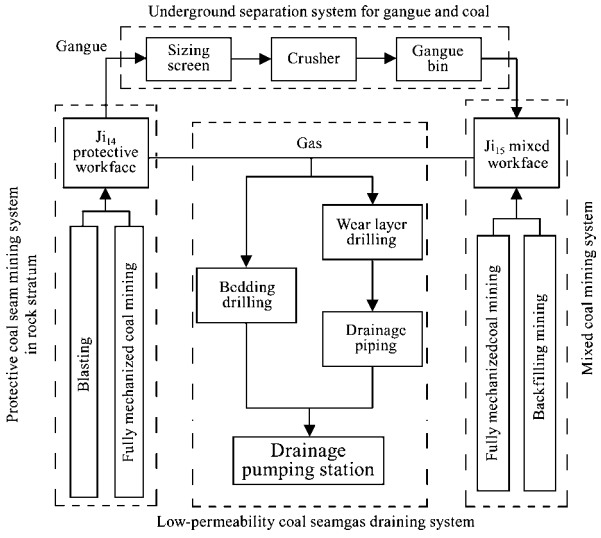

Fig. 11. Overall process flow of the integrated MDGBM system.

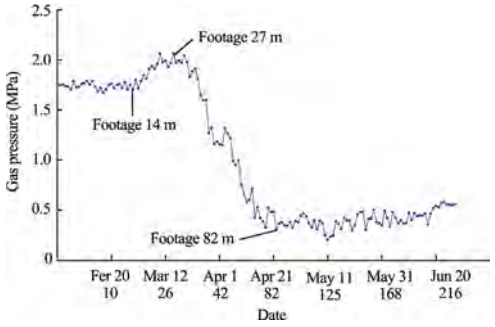

Fig. 12. Changes in the gas pressure of the Ji_{15}-31010 workface.

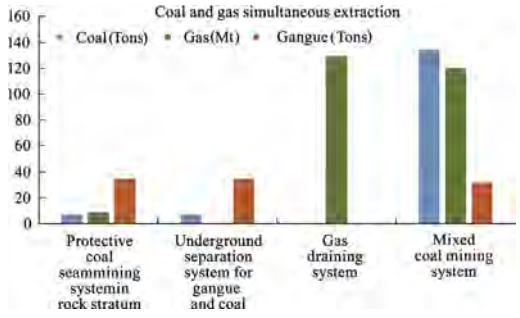

Fig. 13. Simultaneous coal exploitation and gas draining situation.

stratum, desorbed gas from the protected seam dissipates to the goaf of the protective seam through roof fractures. This dissipation leads to a sustained decrease in the gas pressure of the protected seam. The gas pressure of the Ji_{15}-31010 workface decreases by 80% from 1.78 to 0.35 MPa. This finding shows that protective seam mining is effective at pressure relief.

7.3. Effect of simultaneous coal exploitation and gas draining in the protective and protected seams

The Ji_{14}-31050 protective seam in the rock stratum was mined on October 23, 2014. The excavation reached 600 m by December 2015. The maximum footage capacity of the workface was 120 m/month. The amount of raw coal obtained was separated using the DM-ST system, which resulted in approximately 72,000 and 347,000 tons of coal and gangue, respectively. Accordingly, 9.6 million m^3 of gas was drained during the protective seam mining period. The length of the mixed mining workface of the Ji_{15}-31010 protected layer was 220 m, coal production capacity of 1.2 million ton per year, maximum unit production rate of 150,000 ton per month, and gangue processing capacity of 500,000.

This workface was mined on July 14, 2014, and was safely completed in November 2015. The cumulative amount of mined coal was 1.34 million tons, while that of gangue used for backfilling was 320,000 tons. The gas drained during that mining period amounted to 120 million m^3. Fig. 13 illustrates the simultaneous coal exploitation and gas draining.

7.4. Analysis of economic benefits

The integrated MDGBM system has the following major investments: (1) system for mining the protective seam in the rock stratum, (2) system for separating coal and gangue, (3) gas management system, (4) mixed system combining extended solid backfill and conventional fully mechanized mining, and (5) other expenses. Total investments amount to 337.474 million RMB, or the unit cost of coal mining at 240 RMB/t.

Table 5
Analysis of benefits.

Category	First mining face only	All mining faces
Total investments (hundred million RMB)	3.375	
Coal capacity (10,000 t)	134.0	1,171.5
Total revenue (hundred million RMB)	6.700	58.575
Unit cost of coal mining (RMB/t)	240.0	
Profits (hundred million RMB)	3.325	30.381
Economic benefits (10,000 RMB/a)		
Improved coal quality	4040.8	
Savings from eliminating coal washing costs	1176.0	
Savings from eliminating transportation costs	586.2	
Comprehensive use of discharged gas	44.7	

The main benefits obtained are as follows: (1) improved quality of produced coal owing to the use of the coal and gangue dressing system (2) cost savings obtained by eliminating the need for auxiliary lifting of coal for aboveground dressing (3) energy savings from using discharged gas for aboveground power generation and (4) use of discharged gas for preheating. The actual selling price of coal produced by the Ji_{15}-31010 workface is 500 RMB/t. The economic benefits from the first mining face would amount to 332.5 million RMB when the actual selling price was used as the basis. The total amount of coal obtained from all the workfaces in the third level was worth 11.715 million tons. Accordingly, the expected profit was 3.0381 billion RMB.

Table 5 lists the specific economic benefits. The aforementioned analysis indicated that the integrated MDGBM system was successfully implemented in the No. 12 mine. This system application resulted in significant technical and economic benefits.

8. Conclusions

The following conclusions are drawn from this study.

(1) Using the integrated MDGBM technique has successfully overcome the mining difficulties due to lack of a conventional protective seam for the Ji_{15} seam at the No. 12 mine. It also solved the challenges posed by the low permeability and highly gassy coal seam. The technique integrates mining of the protective seam in the rock stratum, UDCG method, gas drainage system, and mixed mining method combining solid backfilling and conventional, fully mechanized mining together.

(2) The proposed technique results in the following significant technical benefits: the gas pressure of the protected seam decreases from 1.78 to 0.35 MPa after mining the protective seam; a maximum footage capacity of 120 meter per month is attained for the workface for the Ji_{14}-31050 protective seam in the rock stratum; the mixed workface of the Ji_{15}-31010 protected seam is 220 m long, and a coal production capacity of 1.2 million t/a, gangue processing capacity of 0.5 million tons per year, cumulative coal production of 1.34 million tons, and processed gangue amounting to 0.32 million tons are achieved. Overall, the economic benefits are significant. Accordingly, the first mining workface amounts to 332.5 million RMB, while the total coal mined from all the workfaces in the third level is approximately 11.715 million tons, which could generate profits of 3.0381 billion RMB.

(3) Implementing the proposed technique has the following benefits: realizing the safe and efficient mining of the highly gassy coal seam with low permeability, improving the

mining rate for coal resources, establishing a method for outburst removal through pressure relief and permeability increase while mining a rock stratum, helping expand the technology for mining protective seams, building a completely new mixed mining method combining solid backfilling and conventional, fully mechanized mining, decreasing the environmental pollution associated with the above-ground discharge of gangue found within the coal flow, and fulfilling the important need for an integrated and green mining method to be used in deep resources.

Acknowledgments

This work was supported by the Qing Lan Project Foundation of Jiangsu Province in 2014, Foundation for Distinguished professor of Jiangsu Province in 2015, Science Fund for Creative Research Groups of the National Natural Science Foundation of China (No. 51421003), Project funded by China Postdoctoral Science Foundation (2016M601915), and National Key Basic Research Program of China (No. 2013CB227905).

References

[1] Liu HY, Cheng YP, Zhao CC, Zhou HX, Zhang ZP. Classification and judgment method of the protective layers. J Min Saf Eng 2010;27(4):468–74.
[2] Wang HF. Pressure relief functional principle of stope underlying coal-rock mass and application in gas extraction of protected coal seam. Xuzhou: China University of Mining and Technology; 2008.
[3] Hui GL, Song JH. Parameter calculation analysis of the coal rock dynamical evolution of the deep protective seam mining. Saf Coal Mines 2013;44 (6):168–71.
[4] Zhang JX, Zhou N, Huang YL, Zhang Q. Impact law of the bulk ratio of backfilling body to overlying strata movement in fully mechanized backfilling mining. J Min Sci 2011;47(1):73–84.
[5] Huang YL, Zhang JX, Zhang Q, Nie SJ. Backfilling technology of substituting waste and fly ash for coal underground in china coal mining area. Environ Eng Manage J 2011;10(6). 769-755.
[6] Huang YL, Zhang JX, An BF, Zhang Q. Overlying strata movement law in fully mechanized coal mining and backfilling longwall face by similar physical simulation. J Min Sci 2011;47(5):618–27.
[7] Zhang JX, Jiang HQ, Deng XJ, Ju F. Prediction of the height of water-conducting zone above the mined panel in solid backfill mining. Mine Water Environ 2014;33(4):317–26.
[8] Zhang Q, Zhang JX, Zhao X, Liu Z, Huang YL. Industrial tests of waste rock direct backfilling underground in fully mechanized coal mining face. Environ Eng Manage J 2014;13(5):1291–7.
[9] Zhang JX, Zhang Q, Sun Q, Gao R, Germain D, Abro S. Surface subsidence control theory and application to backfill coal mining technology. Environ Earth Sci 2015;74(2):1439–48.
[10] Zhang Q, Zhang JX, Kang T, Sun Q, Li WK. Mining pressure monitoring and analysis in fully mechanized backfilling coal mining face – a case study in Zhai Zhen Coal Mine. J Central South Univ 2015;22(5):1965–72.
[11] Zhang Q, Zhang JX, Tai Y, Fang K, Yin W. Horizontal roof gap of backfill hydraulic support. J Central South Univ 2015;22(9):3544–55.
[12] Zhang JX, Miao XX, Guo GL. Consolidated solid Method backfill mining method and its applications. Beijing: Science Press; 2015.
[13] Zhang JX. Study on strata movement controlling by raw waste backfilling with fully-mechanized coal winning technology and its engineering applications. Xuzhou: China University of Mining and Technology; 2008.
[14] Sun Q, Zhang JX, Ju F, Li LY, Zhao X. Research and application of schemes for constructing concrete pillars in large section finishing cut in backfill coal mining. Int J Min Sci Technol 2015;25(6):915–20.
[15] Zhang JX, Zhang Q, Huang YL, Liu JW, Zhou N, Zan DF. Strata movement controlling effect of waste and fly ash backfillings in fully mechanized coal mining with backfilling face. Min Sci Technol 2011;21(5):721–6.
[16] Yang XJ. Hard compound safe and efficient mining of coal seam thickness dirt band the key technology research. Sci Technol Inform 2013;25:402–3.
[17] Song GJ. Thick coal seam mining gangue transport backfilling mining research area space. China Coal 2014;40(S1):61–65+68 [in Chinese].
[18] Wang L, Liu AQ. Analysis on economic benefit comparison between fully mechanized mining in slice of thick seam with thick partings and fully mechanized top coal caving mining in seams combined. Coal Eng 2012;12:135–7.
[19] Cheng WW, Kong XB, Huang ZY. Many layered with thick coal gangue put technology research and practice. Coal Mine Modernization 2012;01:10–3.
[20] Li JP, Du CL, Xu LJ. Impactive crushing and separation experiment of coal and gangue. J China Coal Soc 2011;36(4):687–90.
[21] Zhao CX, Ye GS. Study of heavy-medium coal preparation process control model and control algorithm. J China Coal Soc 2000;25(S1):196–200.
[22] Liang HP. Integrated technology of backfill mining and raw coal separation in underground mine. Coal Sci Technol 2013;41(8):35–7. 41.
[23] Aaron N, Luttrell GH. A review of state-of-the-art processing operations in coal preparation. Int J Min Sci Technol 2015;25(4):511–21.
[24] Ma FQ, Ding EJ. Intelligent control for jigging process. J China Univ Min Technol 2002;31(3):80–4.
[25] Wang L. Fracture evolution and seepage characteristics of distant pressure relief coal-rock masses and application in gas extraction under an extremely thick igneous rock. Xuzhou: China University of Mining and Technology; 2009.
[26] Zhang YJ, Yu GM, Lu SB, Li L, Yang DF. Numerical analysis of gas flow law with short distance upper protective layer gas extraction. Rock Soil Mech 2010;31 (S1):398–404.
[27] Sun Q, Zhang JX, Zhang Q, Yin W, Germain D. A protective seam with nearly whole rock mining technology for controlling coal and gas outburst hazards: a case study. Nat Hazards 2016:1–14.
[28] Yang TH, Tang CA, Feng QY. Coupling analysis of seepage and stresses in rock failure process. Chinese J Geotech Eng 2001;23(4):489–93.
[29] Xu XL, Zhang N, Tian SC. Mining-induced movement properties and fissure time-space evolution law in overlying strata. Int J Min Sci Technol 2012;22 (6):817–20.
[30] Xu QB, Yao SY. Production practice of combined mining in fully mechanized coal face and blasting mining face. Coal Technol 2006;25(6):64–5.
[31] Wu YF, Gao ZF. The production process and the roof management method of the workface of the machine and blasting mining. Coal Mine Supports 2007;3:37–8.
[32] Li HC. Approach on roof control technology for combined mining and blasting mixed mining. Mech Manage Develop 2006;3:45–6.
[33] Liu K, Xu JH. Study and practice of selection and matching of equipment on workfaces combining fully-mechanized mining with caving. Min Process Equip 2010;38(21):17–20.

International Journal of Mining Science and Technology 27 (2017) 29–35

Contents lists available at ScienceDirect

International Journal of Mining Science and Technology

journal homepage: www.elsevier.com/locate/ijmst

Design concerns of room and pillar retreat panels

Klemetti Ted M. *, Sears Morgan M., Tulu Ihsan B.

Mining Engineer Ground Control Branch NIOSH, Office of Mine Safety and Health Research, Pittsburgh, PA, USA

ARTICLE INFO

Article history:
Received 18 June 2016
Received in revised form 4 September 2016
Accepted 15 October 2016
Available online 7 December 2016

Keywords:
Room and pillar
Retreat mining
Deep cover
Safety
Multiple seam

ABSTRACT

Why do some room and pillar retreat panels encounter abnormal conditions? What factors deserve the most consideration during the planning and execution phases of mining and what can be done to mitigate those abnormal conditions when they are encountered? To help answer these questions, and to determine some of the relevant factors influencing the conditions of room and pillar (R & P) retreat mining entries, four consecutive R & P retreat panels were evaluated. This evaluation was intended to reinforce the influence of topographic changes, depth of cover, multiple-seam interactions, geological conditions, and mining geometry. This paper details observations were made in four consecutive R & P retreat panels and the data were collected from an instrumentation site during retreat mining. The primary focus was on the differences observed among the four panels and within the panels themselves. The instrumentation study was initially planned to evaluate the interactions between primary and secondary support, but produced rather interesting results relating to the loading encountered under the current mining conditions. In addition to the observation and instrumentation, numerical modeling was performed to evaluate the stress conditions. Both the LaModel 3.0 and Rocscience Phase 2 programs were used to evaluate these four panels. The results of both models indicated a drastic reduction in the vertical stresses experienced in these panels due to the full extraction mining in overlying seams when compared to the full overburden load. Both models showed a higher level of stress associated with the outside entries of the panels. These results agree quite well with the observations and instrumentation studies performed at the mine. These efforts provided two overarching conclusions concerning R & P retreat mine planning and execution. The first was that there are four areas that should not be overlooked during R & P retreat mining: topographic relief, multiple-seam stress relief, stress concentrations near the gob edge, and geologic changes in the immediate roof. The second is that in order to successfully retreat an R & P panel, a three-phased approach to the design and analysis of the panel should be conducted: the planning phase, evaluation phase, and monitoring phase.

1. Introduction

During an evaluation of unexpected conditions experienced at an eastern Kentucky room and pillar retreat mine that was conducted as part of a NIOSH research effort, it became evident that several factors associated with stress redistribution were involved. The initial efforts and results were published in the past two International Conference on Ground Control in Mining (ICGCM) proceedings by Tulu et al. [1,2]. These two publications concluded that topographical changes and multiple-seam interactions were the cause of the unexpected conditions leading to the difficulties experienced in panels L6 and L4.

While visiting the mine and evaluating the unexpected conditions to determine the most likely causes, it became apparent to NIOSH researchers that this study would provide insight into a new research effort being developed to investigate the stress redistribution resulting from full extraction mining. This eastern Kentucky R & P mine provided an opportunity to evaluate the interactions between depth of cover, topographic changes, and multiple-seam interactions at a full extraction mine. This paper describes the field observations, instrumentation, and numerical modeling of four consecutive room and pillar panels retreated at the mine. The results of this study should provide additional factors to include in future designs and assessments both in the planning stage and prior to retreat mining.

2. Mining and geotechnical parameters

The Darby Fork No. 1 mine is operated by Lone Mountain Processing, Inc., and is located in Harlan County, KY. The mine produces bituminous coal from the Darby and Kellioka coal beds by

* Corresponding author. Tel.: +1 412 386 5240.
E-mail address: TKlemetti@cdc.gov (T.M. Klemetti).

http://dx.doi.org/10.1016/j.ijmst.2016.11.006
2095-2686/

the retreat room and pillar mining method. The operator has been mining the Owl, Darby, and Kellioka coal beds for at least the last 20 years. This paper focuses on mining in the Kellioka Seam, located below workings in the Owl and Darby coal beds. The majority of the mining layout and geotechnical parameters for the study areas were published in previous papers [1,2]. Two particular parameters to be expanded upon in this paper are the multiple-seam mining geometry and the variable geology encountered in these four panels.

2.1. Multiple-seam mining geometry

The Kellioka, Darby, and previously mined Owl panels have been stacked vertically so that the panel edges and barrier pillars between panels are superimposed. In all of the seams, the panel widths were subcritical, included 5 entries, utilized slab cuts during retreat, and included barrier pillars between the subsequent panels. The overmining conducted in these four consecutive R & P retreat panels varied as mining progressed to the west. For the L6, L5, and L4 panels, both the Darby and Owl seams were fully extracted above the Kellioka Seam prior to mining. Above the L3 panel, the Owl seam was developed, but not retreat mined, while the Darby seam was fully extracted. The interburden between the Kellioka and Darby seams ranges from 9 to 15 m within this area, while the interburden between the Darby and Owl seams ranges from 15 to 18 m. In general the interburden between the Kellioka and Darby seams decreases as the mining progressed from the L6 to the L3 panel. Over the same area the depth of cover increases from a minimum of 244 m to a maximum of 518 m. The previously discussed multiple-seam mining geometry is graphically represented in Fig. 1.

2.2. Geological conditions

The typical geology in the area of interest consists mainly of interbedded shales, siltstones, and sandstones (Fig. 1). In general, the interburden between the Kellioka and Darby seams consists of a medium strength dark shale that is relatively massive. A sandstone may be present in the interval, but the thickness is variable and ranges from 3 to 6 m over the L7 panel to less than 0.6 m over the L1 and L0 panels. The sandstone is not thought to be within the reach of installed roof support. However, thicker sandstone is reported to result in improved rood stability in the Kellioka Seam.

The immediate roof of the Kellioka Seam is described as a dark grey shale that is somewhat massive but can delaminate into thin slabs during buckling and cutter formation. Laboratory and field tests were conducted to determine the relative strength variations that could be expected during mining. The typical roof shale has a uniaxial compressive strength (UCS) varying between 51.7 and 103.4 MPa and an average Brazilian tensile strength of 7.6 MPa. From field analysis, the coal mine roof rating (CMRR) can vary between 35 and 55 while the majority of the roof encountered in this area is about 45 and dents when struck by a ball peen hammer. Visual observations of the immediate roof in areas of extended height included highly fossilized shales, sandstones, massive shales (both grey and black), and occasionally coal streaks or rider seams, as seen in Fig. 2. However, there are considerable differences in the description of the roof strata that do not always indicate a difference in strength.

3. Field observations and instrumentation

The primary techniques utilized to evaluate the conditions and potential elevated stresses observed in the four R & P retreat panels were visual observation and instrumentation. During the progression of mining from the L6 to the L3 panel, the visual observations included condition mapping and photographs to document the observed conditions. The results of the visual observations of the L6, L5, and L4 panels from the initial study were discussed in publications presented at the 33rd and 34th ICGCM by Tulu et al. [1,2]. In general these panels experienced poor conditions in the #5 entry were whenever the entry was not shifted further towards the center of the overlying gob. Although there were localized poor conditions encountered in all entries, entries #1-#4 experienced much better conditions than #5 in all three panels. The most interesting observations from the L6-L4 panels in relation to this new study included the following:

(1) Anytime the #5 entry was not shifted, conditions quickly worsened and required the mine to shift the entry back;
(2) The multiple-seam interactions were readily observable and were where expected;
(3) The poor conditions observed included ragged, high, and slickensided roof areas, roof cutting along riblines, roof sag in entries and crosscuts, open fractures in the roof, floor heave, joint sets, and rolls;
(4) The conditions in the #5 entry appeared to worsen as the rider seam came closer in proximity to the immediate roof;
(5) The gob generally formed quite rapidly and the roof did not hang for extended distances.

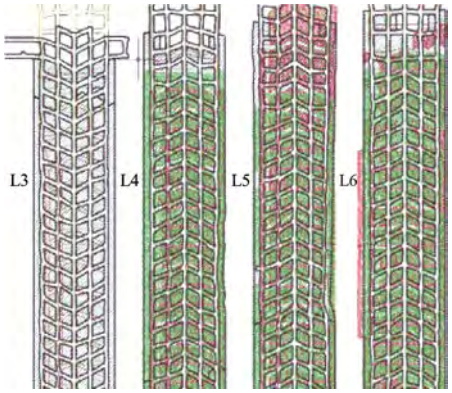

Fig. 1. General layout of the panels in the area of interest (showing previous mining above the current seam).

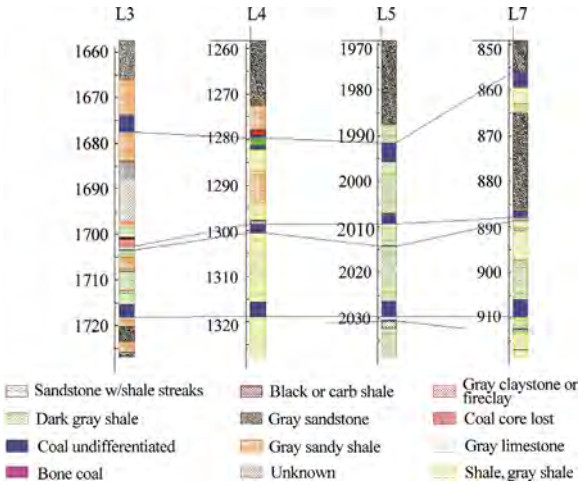

Fig. 2. Geological core logs from the L7 to L3 panel area, showing significant changes in the immediate roof, floor, and interburden strata at the mine.

3.1. Visual observation

In this paper, the focus is on the observations during development and retreat of the L3 panel. The observations of the L3 panel produced similar results for the #2, #3, #4, and #5 entries (see Figs 3 and 4). In general, the #2, #3, and #4 entries experienced relatively good conditions and only experienced difficulties while passing an overlying gob solid boundary or remnant pillar. On occasion, these entries did encounter very weak immediate roof that caused less than ideal conditions. The #5 entry experienced poor conditions relative to the other entries similar to those of the previous 3 panels. The #1 entry appeared to have an increased occurrence of poor conditions in comparison to the previous three panels observed (see Fig. 5). Although they were not as extreme or continuous, the conditions were less desirable than those experienced in entries #2, #3, and #4. This entry did not experience the frequency nor the severity of the conditions observed in the #5 entry.

In addition to the surface evaluations, several test holes were evaluated for cracking and shifting in all 5 entries near the instrumentation site when the pillar line was approximately ten, two, and one row(s) inby the instrumentation site. The test holes in entry #1 and #5 had the highest prevalence of both cracking and shifting and tended to increase as the pillar line approached the holes. Shifting was prevalent in the #1 entry test holes while cracking was most common in the #5 entry.

It was also observed that poor conditions generally coincided with rolls, roof sag, open fractures in the roof, and roof strata changes. There was no apparent elevated loading or condition deterioration attributable to the pillar extraction. It appears that aside from time-dependent deterioration, the conditions tend to remain the same during retreat as they were during development. The time-dependent deterioration was most frequently encountered well in advance of the pillar line resulting in some pillars or partial pillars being left due to poor conditions, increased cribbing, and previous roof falls.

3.2. Instrumentation

While mining was underway in the L4 panel, an instrumentation plan was developed to investigate the interaction between primary and secondary supports for the L3 panel. The instrumentation actually produced rather interesting results in relation to the loading experienced due to the topography, multiple-seam interactions, and geological setting. The instrumentation plan included one 4-point roof extensometer, two 8-point roof extensometers, and four load cells installed on the 3.66 m two-piece superbolts (75 grade 19 mm). The 4-point extensometer had anchors located 4.9, 3.7, 2.7, and 1.2 m above the roof line while the 8-point extensometers had anchors located 2.7, 2.4, 2.1, 1.8, 1.5, 1.2, 0.9, and 0.6 m above the roof line. The instruments were located in the #2 entry at crosscut 13 and mid-pillar between crosscuts 12 and 13, as shown in Fig. 6. The instrumentation was installed during development of the panel in an attempt to capture as much movement and loading as possible. Data acquisition from the instruments in the intersection was terminated during the course of mining after extraction inby crosscut 13 and prior to extraction outby. However, the instrumentation located mid-pillar captured all retreat mining surrounding the instrumentation location and is detailed below.

Fig. 3. Entry #4 panel L3 exhibiting good conditions, common to all panels observed.

Fig. 4. Entry #5 panel L3 showing heavily cribbed area due to roof deterioration, pillar spalling, and floor heave, common to all panels observed.

Fig. 5. Entry #1 panel L3 exhibiting poor conditions: floor heave, minor pillar spalling, and cutter roof.

Both locations showed little to no roof movement or superbolt loading prior to the extraction of pillars inby the instrumentation locations as can be seen in Figs. 7–10. The mid-pillar location began experiencing roof movement and superbolt loading upon extraction of the pillars inby crosscut 12. Prior to the removal of the data logging system for the mid-pillar site, the roof in the #2 entry still had not collapsed for at least one break inby the pillar line. The superbolt loading was greater on the gob side cells and began earlier on the inby cells. The inby cells showed an abrupt load increase followed by a period of minor load increase and then another abrupt load increase. The outby cells did not show the "stepping" in the readings, possibly due to the timing of instrumentation removal. The cells closer to the gob showed a greater

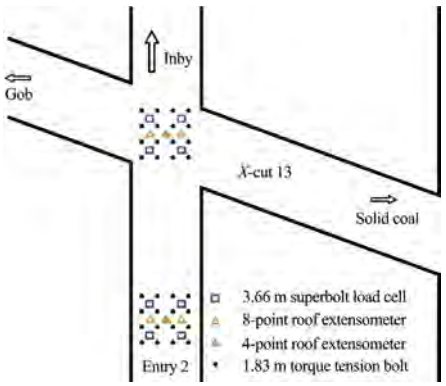

Fig. 6. Instrumentation site showing location of roof extensometers and load cells.

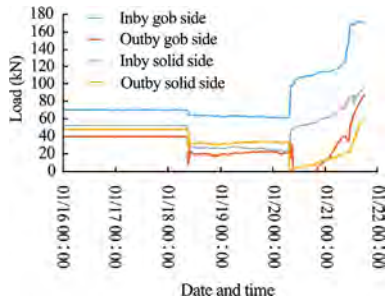

Fig. 7. Superbolt loading response to R & P retreat.

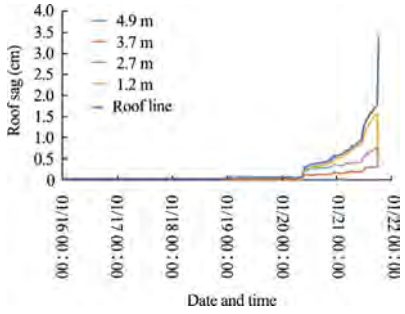

Fig. 8. 4.9 m extensometer data in response to R & P retreat mining.

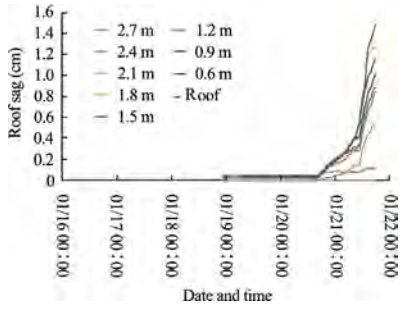

Fig. 9. 2.7 m gob side roof extensometer reading in response to R & P retreat mining.

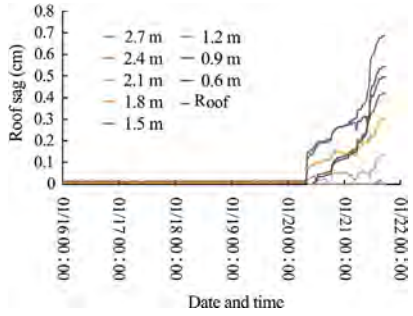

Fig. 10. 2.7 m solid side roof extensometer reading in response to R & P retreat mining.

increase in load than those closer to the solid coal side. The average of the inby load increase was approximately 75.62 kN and the outby load increase was approximately 26.6 kN. The 4.9 m roof extensometer showed a maximum roof sag of 3.48 cm with the majority of the sag occurring in the first 1.2 m of the roof. The 2.7 m roof extensometers showed an average maximum roof sag of 1.09 cm with very little movement above the 1.8 m horizon.

The timing, rates, and maximum values of roof sag and loading were fairly consistent among most instruments. All of the instruments that were installed slightly closer to the previous panels' gob showed greater load increases or roof sag, indicating a preferential loading of the entry on the gob side. The instruments showed that the roof was most active during mining of the same entry that the instruments were in. During mining of the furthest entries from the instrumentation site, there was little additional change in the roof sag or superbolt load.

4. Numerical modeling

After the initial visual observations were conducted it became apparent that the addition of numerical model simulations would provide more insight into the mechanisms at work in this multiple-seam mining scenario. Two different numerical modeling programs were used to study the responses to the mining conducted in the four R & P retreat panels: LaModel 3.0 and Rocscience Phase 2. The primary focus of the numerical modeling efforts was to assess the stress redistribution due to the topographical relief, multiple-seam interactions, and full extraction mining. The LaModel simulations will be described first to discuss the purely vertical loading evaluation of the four panels. Unlike the LaModel simulations, Phase 2 incorporates horizontal stress and strain while limiting the model to two-dimensional space.

4.1. LaModel analysis

The widely used boundary element program, LaModel was used to simulate the vertical stresses and displacements experienced during both development and retreat mining of the L6-L3 panels [3]. To incorporate as much of the mining district as possible, the three seams were discretized using 1.5 m elements and the overburden was discretized using 15.2 m elements. This resulted in seam grids of 1380×1600 elements and an overburden grid extending 305 m beyond the mine grid.

4.1.1. Input parameters

The critical input parameters for calculating accurate stresses and pillar loads are the overburden stiffness, gob stiffness, and coal strength [4]. To accentuate the multiple-seam stresses in this particular model, the rock mass modulus and lamination thickness were kept at the default 20.7 GPa and 15.2 m values, respectively [5]. The gob stiffness for each panel was calibrated independently such that the average gob stress matches that of the empirically suggested 21° abutment angle as used in the ALPS and ARMPS programs [6,7]. Finally, the default 6.2 MPa insitu coal strength was used along with the Mark-Bieniawski pillar strength formula to create the coal seam material properties. Elastic-plastic coal materials were chosen because pillar failure was not explicitly being simulated [8].

4.1.2. Development mining stresses

Prior to mining, the panels of interest are located in a state of decreased in situ stress which is defined by the overlying gob characteristics (stiffness) and the overburden load applied to them. The average overburden stress and in situ (pre-development) stress across the AA cross section for each panel can be seen in Fig. 11. Panel L6 was initially driven on 25.9 m centers when problems were encountered. The #4 and #5 entries of panels L5-L3 were mined on 19.8 m centers reducing the panel width by 9.1 m, and consequently the vertical stress on the right half of the panel [1,2]. The L3 panel is not only deeper, but is also only overmined in one seam, resulting in higher vertical in situ stress on the active seam when compared to panels L4 and L5.

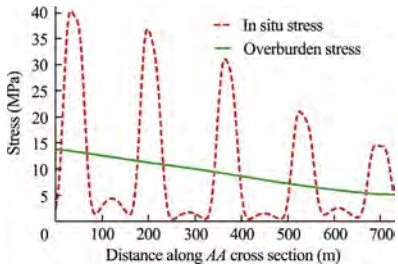

Fig. 11. Insitu and overburden stress simulated for the Kellioka Seam.

The development loading experienced by the pillars as each successive panel is mined, as is depicted in Fig. 12. One can observe that the total vertical stress on the developed workings is elevated in areas under the overlying barrier pillars, which is widely published and accepted. However, the focus of this paper is the conditions encountered under the overlying stress shadow. Total vertical stresses simulated on the pillars in this region range from less than 3.45 MPa (the white areas) to stresses of as much as 6.9 MPa in the L3 Panel and 10.34 MPa in the widened portion of the L6 panel.

Retreat mining of the L3 panel was also simulated in the area of the instrumentation site at the mid-pillar location between crosscuts 12 and 13. A comparison with the single-seam case, calibrated using the LaModel deep cover pillar retreat calibration technique, is seen in Fig. 13 [9].

The total vertical stress distributions across the pillar line at crosscut 13 for the multiple-seam case show a steep increase in stress along the front abutment that dissipates rapidly as the instrumentation location is neared. This is equivalent to an abutment extent of about 15.2 m and closely relates to the timing of increased load on the roof bolts and associated roof sag. In contrast, the single-seam case simulates a much smoother transfer of the abutment stresses and results in an abutment extent of about 61 m (two pillar rows) near the center of the panel. As expected, both the magnitude of the stresses and the abutment extent for the single-seam model are drastically larger than those observed in the L3 panel both on development and during retreat.

4.2. Phase2 stress analysis

In order to determine the total stress distribution induced by overburden and multiple-seam stress conditions, the Phase 2 numerical model that was previously used by Tulu et al. [10]. It was updated to improve the estimate of the horizontal stress due to tectonic loading and the depth across the four R & P retreat panels [11]. The analysis was conducted by modeling different cross sections across the panels, capturing the topographic effect of the mountains and a stream valley. The model simulated vertical stress

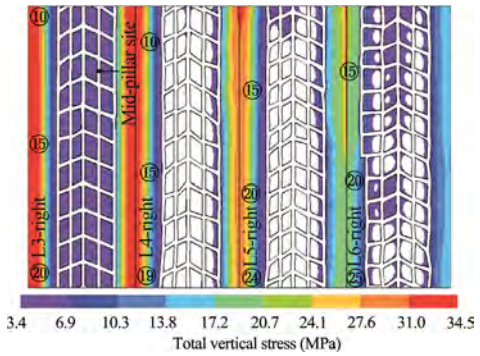

Fig. 12. Total vertical stress for panels L6-L3 under development loads.

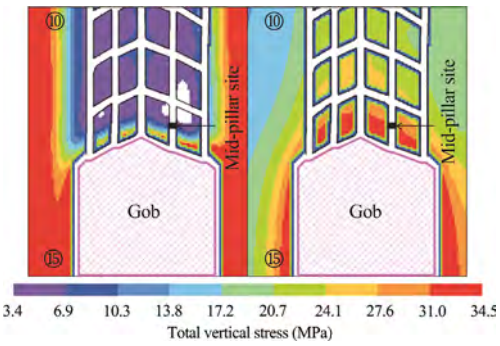

Fig. 13. Total vertical stress during retreat near the instrument location for the multi-seam (left) and single-seam (right) cases.

Table 1
Horizontal stress, vertical stress, and strength factor for entries 1, 3, and 5 for panels L6 through L3.

Panel	Entry	Sigma *XX* (MPa)	Sigma *ZZ* (MPa)	Strength factor
6	1	11.05	4.84	2.64
	3	8.86	3.52	3.55
	5	12.29	6.23	2.22
5	1	10.85	5.07	2.34
	3	7.83	3.04	3.77
	5	10.70	4.13	2.39
4	1	10.56	4.41	2.14
	3	6.18	2.80	5.04
	5	9.80	3.33	2.41
3	1	10.10	5.16	1.83
	3	3.80	2.61	12.68
	5	7.72	3.05	2.80

due to gravity, and the tectonic stress was modeled with the locked-in stress option in the Phase 2 model. The updated model results in in situ horizontal stresses and K-ratios that are consistent with expectations based on stress measurements in the Appalachian coal region [1,10]. The multi-seam effect caused by the full extraction of the panels in the overlying Darby and Owl coal beds as modeled prior to entry development in the Kellioka seam. The gob in the Owl and Darby panels was modeled as a soft material that attracted loads similar to what would be predicted by an abutment angle of 21°. The elastic modulus of each gob is calibrated separately to give the expected 21° abutment angle loading. Heights of the gobs in the Owl and Darby panels were selected as 4.6 and 6.1 m based on the experience at the mine.

4.2.1. Horizontal and vertical stresses

The average horizontal stress, vertical stress, and strength factors for the as-mined location of each of the entries in the Kellioka Seam were queried from the Phase 2 model and are presented in Table 1. Model results indicate that for all panels, stress concentration around the entries between #5 and #1 were destressed (Fig. 14). Since the #5 entries of panels 3, 4, and 5 were shifted 9.1 m to the east of the planned position, the strength factors for these entries are higher than the corresponding #1 entries. The #5 entry of the L6 panel has a lower strength factor than the #1 entry of the same panel.

5. Discussion

Visual observations throughout these studies have provided the most insight into the actual conditions, causes, and potential mitigation techniques. The instrumentation and numerical modeling

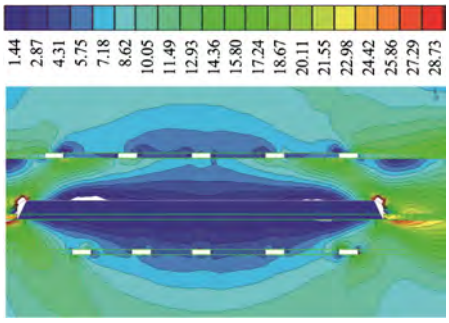

Fig. 14. Phase 2 model results showing stress redistribution around the overlying gobs and panels developed in the Kellioka seam.

efforts provided significant support to the results of these visual observations. The LaModel results showed that there was a significant reduction in development load, front abutment load, and front abutment extent in comparison to a panel without the overlying gob. This was apparent in the lack of stress-related rib deformation across all of the observed panels and was confirmed with the instrumentation measurements in the L3 panel.

Similar results were produced using Phase 2, where emphasis was placed on modeling the horizontal stress impact on the outside entries of the L3 panel. This horizontal stress orientation was apparent in the roof and floor deformation observed in these entries as well as the prevalence for cutter formation along the inside rib. This horizontal stress field is the primary cause of the poor conditions experienced in the #5 entry throughout this mining district as previously ascertained [1,2]. The effect of the topographical relief on the stresses across the panels continues to be evident; however it is less pronounced that it was in panel L6. This is most likely due to the applied mitigation technique of shifting the #4 and #5 entries as well as a general smoothing of the topographic stress as the panels get deeper.

The conditions observed along each entry showed considerable variability even though the predicted stresses were very consistent along the length of the panel. This implies that the geology encountered plays a significant role in the stability of the mine openings. This mechanism is best described as a stress-driven, geologically constrained failure. That is, the observed roof deterioration is caused by the encountered stress field, but failure of the roof beam is limited to areas of substandard geology. Roof deterioration in this area of the mine was mostly constrained by the proximity of the rider seam and the prevalence of a joint set running roughly perpendicular to the mined headings. Generally speaking, as mining progressed from the L6 panel to the L3 panel, the depth of cover increased, the interburden thickness decreased, the distance to the rider seam decreased, and the strength of the immediate roof decreased.

The instrumentation study was initially designed to provide some insight into the interaction of primary and secondary support. Due to the fact that the initiation of the loading on the superbolts and the associated roof sag occurred just prior to the removal of the data loggers, there is limited data available to assess these interactions. In addition, the relative strength of the roof strata in the vicinity of the instrumentation in combination with reduced abutment extent and stress did not provide an adequate test of the roof support in this entry prior to gob formation.

6. Conclusions

Based on the results of this study, the following four factors appear to be significant and should be considered during R & P retreat mine planning and execution:

(1) Topographic relief across panels can lead to very different conditions than those associated with relatively flat overburden.
(2) An overlying gob can relieve a large portion of the overburden pressure, as evidenced from the four panels observed.
(3) As the entries get closer to the overlying gob solid boundary, the entries appear to encounter higher stresses leading to more roof and rib deterioration.
(4) Geological changes in the immediate roof can significantly affect the condition of the entries resulting in stress-driven, geologically constrained failure.

Furthermore, based on the study outcomes and discussions with mine operators, successful retreat mining in increasingly difficult ground conditions requires a three-phased approach. Planning, evaluation, and monitoring should be conducted throughout the mining cycle. The approach to each phase is a mine-specific and evolving process subject to change based on prevailing conditions, changes in mining techniques, or changes in the geology from one area of the mine to another. To date, the majority of research and design recommendations fall into the planning phase where pillar design is a factor of importance. However, relatively little exists in the form of guidelines for the evaluation and monitoring phases (MSHA "Roof Control Plan Approval and Review Procedures").

The planning phase should rely heavily on sound engineering design procedures. These procedures should evaluate the expected loading, displacement, and timing of the planned mining. Factors of importance include: pillar design, panel layout, depth of cover, topographic relief, roof support design, the potential for multiple-seam influence, and geologic setting. Numerous techniques for pillar design, roof support design, and rock mass classification have been developed to assist in this type of mine planning. Pillar design programs such as ARMPS, AMSS, and LaModel based on the Mark-Bieniawski pillar strength formula have gained nearly industry-wide acceptance. Other techniques such as those used by Salamon and Munro, Obert and Duvall, Wilson, Baron and others have seen usage in the US and abroad [11]. Roof support design techniques such as ARBS, STOP, reinforcement density index (RDI), tensioned bolt design charts, suspension calculations, and numerical models such as FLAC when combined with past experiences have been used with varying degrees of success. The coal mine roof rating (CMRR) was developed from several rock mass classification systems (RQD, RMR, URCS, Q, etc.) and provides a quantitative method to identify geologic factors affecting the quality of the mine roof [12]. The CMRR is the most widely used rock mass classification system in US coal mines and can be incorporated in all three design analyses.

The evaluation phase should be conducted prior to retreat mining and rely more heavily on assessment of the prevailing conditions of the area(s) to be mined. This pre-retreat mining evaluation phase should assess the amount of loading, deterioration, and deformation on the roof, rib, floor, and installed supports that have occurred due to development, multiple-seam, and abutment loadings. A re-evaluation of the pillar design should be completed if the as-mined input parameters differ from those used in the planning phase. The prevailing geologic setting, transition zones, and geologic anomalies that are encountered can be assessed at any time during development. Common geologic considerations include: joints and fractures, faults, seam rolls due to differential compaction from sand channels, rider seams, slickensides, location of strong and/or weak beds in the roof, ground water inflow, etc. Logically, focus should be applied to those conditions, which have caused problems in the past as well as those which are rarely encountered. At this point, a judgement must be made on the appropriate course of action such as increased monitoring,

installation of additional support, or leaving a partial pillar or pillars or the entire pillar or pillars.

The monitoring phase should be conducted during retreat mining and should rely on observation and evaluation of the change in conditions as retreat mining progresses. Increased monitoring of ground conditions on the working section should be considered with emphasis on increased roof, rib, and floor deformations and excessive support loading. Additional consideration should be placed on conditions that are unexpected or differ significantly from those encountered in prior experience, particularly in areas identified with potential hazards prior to retreat mining. Again, as conditions dictate, the final decision to continue monitoring, install additional support, or leave a partial or entire pillar or pillars can be made.

Research efforts moving forward can probably have a more significant effect on the safety of miners if they focus on the monitoring phase of the hazard assessment using methods similar to those implemented in Australia. What type, frequency, and detail of evaluations would provide the most valuable assessment of potential failures that may lead to injuries and fatalities in underground coal mines? What skills are necessary and who would be responsible for performing those hazard assessments? These are two fundamental questions whose answers would improve the safety of underground coal miners.

Disclaimer

The findings and conclusions in this report are those of the author(s) and do not necessarily represent the views of the National Institute for Occupational Safety and Health.

References

[1] Tulu IB, Esterhuizen GS, Klemetti T, Murphy MM, Sumner J, Sloan M. A case study of multi-seam coal mine entry stability analysis with strength reduction method. Int J Mining Sci Technol 2016;26(2):193–8.
[2] Tulu IB, Klemetti T, Esterhuizen GS, Sumner, J. A Case Study of Topography-Related Stress Rotation Effects on Multi-seam Stability. In: Proceedings of the 33rd international conference on ground control in mining. Morgantown, West Virginia; 2014. p. 1–7.
[3] Heasley KA. Numerical Modeling of Coal Mines with a Laminated Displacement-Discontinuity Code. PhD diss., Advisor: Miklos D.G. Salamon, Dept. of Mining Engineering. Colorado School of Mines; 1998.
[4] Heasley, KA. Some Thoughts on Calibrating LaModel. In: Proceedings of the 27th International Conference on Ground Control in Mining. Morgantown, West Virginia; 2008. p. 7–13.
[5] Sears MM, Heasley KA. Calibrating the LaModel Program for Shallow Cover Multiple-Seam Mines. In: Proceedings of the 32nd International Conference on Ground Control in Mining. Morgantown, West Virginia; 2013. p. 99–106.
[6] Mark C. Analysis of Longwall Pillar Stability (ALPS): an Update. In: Proceedings of the Workshop on Coal Pillar Mechanics and Design. U.S. Department of the Interior, Bureau of Mines, IC 9315, Pittsburgh, PA; 1992. p. 238–49.
[7] Mark C, Chase FE. Analysis of Retreat Mining Pillar Stability (ARMPS). In: Proceedings of New Technology for Ground Control in Retreat Mining. National Institute for Occupational Safety and Health, IC 9446, Pittsburgh, PA; 1997. p. 17–34.
[8] Mark C. Empirical Methods for Coal Pillar Design. In: Proceedings of the 2nd International Workshop on Coal Pillar Mechanics and Design. National Institute for Occupational Safety and Health, IC 9448, Pittsburgh, PA; 1999. p. 145–54.
[9] Heasley KA, Sears MM, Tulu IB, Calderon-Arteaga C, Jimison L. Calibrating the LaModel Program for Deep Cover Pillar Retreat Coal Mining. In: Proceedings of the 3rd International Workshop on Coal Pillar Mechanics and Design. Morgantown, WV; 2010. p. 47–57.
[10] Dolinar D. Variation of Horizontal Stresses and Strains in Mines in Bedded Deposits in the Eastern and Midwestern United States. In: Proceedings of the 22nd International Conference on Ground Control in Mining. Morgantown, West Virginia; 2003. p. 178–85.
[11] Peng SS. Coal Mine Ground Control. 3rd ed. Morgantown, WV: Syd S; 2008.
[12] Molinda GM, Mark C. Coal Mine Roof Rating (CMRR): A pratical rock mass classification for coal mines; 1994. p. 9387.

International Journal of Mining Science and Technology 27 (2017) 37–41

Contents lists available at ScienceDirect

International Journal of Mining Science and Technology

journal homepage: www.elsevier.com/locate/ijmst

Development of a six drillhead roof bolting machine

Kyslinger Bill A. *

J.H. Fletcher & Co., Huntington, WV 25722, USA

ARTICLE INFO

Article history:
Received 9 June 2016
Received in revised form 21 September 2016
Accepted 18 October 2016
Available online 8 December 2016

Keywords:
Roof bolter
Mining
Six-head
Fletcher
Latched
Material handling

ABSTRACT

In underground mining, machine design is predominantly dictated by mine conditions and individual customer desires. In partnership with Foresight Energy, J. H. Fletcher & Company was tasked to design and manufacture a new roof bolting machine with six independent drilling apparatus on board capable of drilling and bolting the roof and ribs with material handling. The objective was to produce a machine capable of drilling and installing six bolts simultaneously with a limited number of operators. The goal of the mine is to decrease the time to bolt a cut to improve the safety level of the current roof bolting method, improve efficiency and to improve the bottom line cost of entry development. The customer wanted four drills at the front of the machine dedicated to installing roof bolts and then another two drills behind them dedicated to rib bolts. This dictated the requirement of latched controls, which would allow the operator to start drilling one hole and then latch the controls to be able to move on to the next. The result of the design is a machine with a single platform and six independent masts with drillheads: four masts strictly for drilling and installing roof bolts on the front of the platform and two masts on the back of the platform for rib bolts. The controls at each operator's station include a latch control for drilling. The six-head roof bolter allows fewer operators to drill and install roof and rib bolts, which in turn lowers the miners' roof exposure per cut. This design reduces the operator's exposure from the inherent pinch points and rotary hazards once he has engaged the latch drilling. Therefore, the machine will help to decrease the time to bolt a cut, improving productivity while enhancing the ability to operate the machine safely.

1. Introduction

When mining underground, it is necessary to support the roof quickly to prevent it from collapsing after an area has been mined. Since the 1950s, the primary method for supporting the roof has been the installation of roof bolts. Roof bolting is one of the most basic functions yet one of the most dangerous jobs in the underground mining operation [1]. The Mine Safety and Health Administration's (MSHA) Health and Safety Accident Classification injury database showed an average of 660 roof bolter operator accidents per year over a 5-year period (1999–2003) [2]. The numbers show that roof bolting is the most hazardous machine-related job in underground mining. It represents 39% of all machine-related accidents in underground coal mines. In 1993, the U.S. Bureau of Mines conducted a study that has shown the activity of drilling as the most hazardous job task performed by a roof bolter operator, accounting for 31% of all roof bolting injuries [3]. Almost half (46%) of these drilling injuries were due to falling rocks or coal from the roof. All of these injuries occurred under supported roof. The majority of these injuries (about 99%) are not caused by a major roof collapse but from falls of smaller rock from the immediate roof. This type of roof failure has also been termed "skin fall."

In Spring of 2014, Foresight Energy and J. H. Fletcher & Company started conceptualizing a new six-drillhead roof bolting machine. The objective was to produce a machine to provide the capability of drilling and installing six bolts simultaneously while using a limited number of operators. The machine would have the capability of drilling the mine roof and side walls (rib), as well as having a material handling system and approved dry dust system. J. H. Fletcher & Company agreed to design, develop, and manufacture the six-drillhead roof and rib bolter with the expected delivery to the mine site of summer 2015.

The six-drillhead roof and rib bolting machines (Fig. 1) were specifically designed for Foresight Energy to be used in their mine located in the Illinois Coal Basin. The initial two machines were shipped and are currently being used in production at the Williamson Energy-Mach Mining coal mine. The mining method used at this particular mine is room and pillar with coal being

* Tel.: +1 304 5257811.
E-mail address: bkyslinger@jhfletcher.com

http://dx.doi.org/10.1016/j.ijmst.2016.11.010
2095-2686/

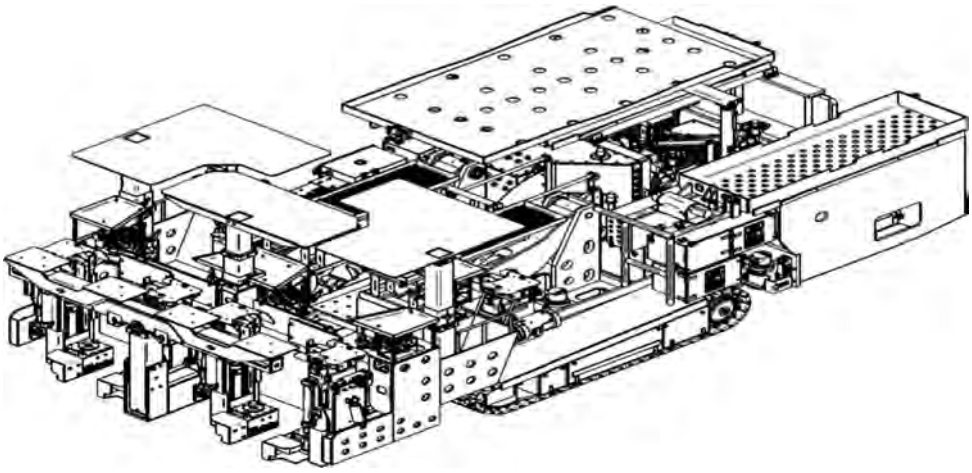

Fig. 1. Six drillhead roof and rib bolting machine.

extracted in 10.67 m cuts by way of a continuous miner, followed by a dual-boom CHDDR-style bolter that installs mesh and rib bolts. The entry width of their operation is 5.49–6.1 m with a mining height of 2.44–4.27 m; the average working height is 3.05 m. The current bolting process uses a 1.22 m × 1.22 m bolt pattern, which involves installing roof mesh panels and corner rib bolts with 90°, 610 mm × 610 mm channel. The mine has good top and bottom conditions. Fig. 2 shows one of the mine's proposed bolting patterns that the six-drillhead roof bolter would achieve.

The exploitation of such deposits requires the continuous upgrading of mining technology in order to minimize the risk of injury, costs of excavation, processing and storage of barren rock. The main focus is on minimizing the operator's risk of injury by means of reducing or eliminating their exposure to dust, noise, machine and geological hazards as well as upgrading the operator's ergonomics.

2. The design

J. H. Fletcher and Company has always operated with the philosophy of designing custom machines detailed to customers' requirements. Furthermore, the company maintains its focus on safety, reliability, ergonomics and efficiency while building on previous designs. Given the customer's desire for a semi-automatic drilling system, we decided to start with our existing four-head roof bolter design and see how it could be expanded to a six-head roof and rib bolter to meet the customer's needs. The main design concerns were how to fit two more drilling apparatus along with material handling onto this machine and how to get this new machine and the concept of a latched feed and rotation drilling system approved by the Mine Safety and Health Administration (MSHA).

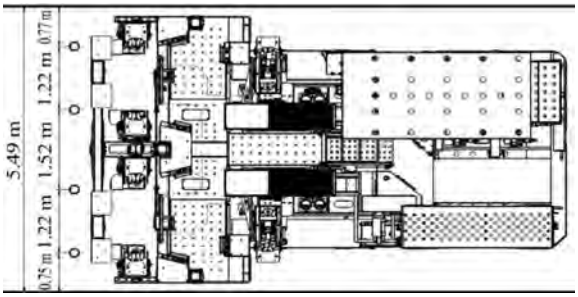

Fig. 2. One of the mine's intended bolting patterns for bolter.

With two more drilling apparatus for rib drilling, the four-head designed machine had to be augmented to handle the additional hydraulic requirements and mass of the additional drilling components. The first major obstacle for this new machine was that a new, higher-capacity crawler drive system had to be designed to handle a machine of this size. A completed six-head machine loaded with drilling components is approximately 10 tons heavier than a twin-boom crawler machine. Therefore, a 508 mm wide crawler pad drum miner type crawler assembly was developed with a bolt-on style gear case. The large crawler pad lowered the machine's ground pressure and the higher-capacity crawler drive system had the increased torque needed for a machine of this size. To accommodate the increased hydraulic demand, the chassis had to be enlarged to be able to handle the much larger hydraulic tank (1306 L) and the addition of another electric motor. The machine now consisted of two 74.6 kW, electric motors used on the four-head design and an additional 56 kW electric motor to power the two new rib drills attached to the machine. In addition to the motor and pump, other necessary elements that accompany two more drilling devices, such as filters, control valves, and dust systems, were added. The two additional blowers for the dust system were added to the 74.6 kW electrical motors, consequently having three blowers for each 74.6 kW electric motor. The 74.6 kW electric motors have a shaft at both ends so that two blowers are belt driven on the front end and one blower is belt driven on the back end, thus giving six blowers, one for each drill mast.

Due to the magnitude, and quick turnover in supplies of the six head bolter, it was essential to have the ability to stock various bolting supplies on the machine. To bolt a 10.67 m cut in an entry width of 5.49 m and a mining height of 3.05 m, it would require installing approximately 36 panels of mesh and 45 roof bolts, roof plates and resin. This situation dictated the need for a storage system, called a material handling system, which provides the operator immediate access to large varieties of roof bolts, roof bolt plates, steel straps and steel screen or mesh that can be installed on the roof to prevent small rock or debris from falling. On the rear of the machine, the material handling system had to be added containing two material pods: a large pod over the two 74.6 kW electric motors and a smaller pod located over the cable reel and 56 kW electric motor. The mine staff would have to lift these pods onto the machine; however, machine mounted hydraulic winches would pull the pods into position once they were on the machine. The operator could then lock them into place. A mesh tray that

could hold mesh sheets measuring 3.0 m × 1.5 m was also included and controls were added to lift, tilt, and sump the mesh tray to a comfortable position for the operators when positioning mesh for installation. The mesh sheets would also have to be lifted to the machine, but then they could be pulled up into the mesh tray using the hydraulic mounted winch. To maximize material handling, it was necessary to design the machine with radio remote control so a tram compartment would not be necessary, which would take up valuable material storage space on the machine. The remote control includes the following functions: platform lift, rear stab jacks, front left stab jack, front right stab jack, left tram, right tram, tram speed, cable reel, left hand winch, right hand winch, front mesh lift, rear mesh lift and mesh sump.

The material handling system also addresses risks associated with manually loading materials. Roof bolts, bolt plates, steel straps, mesh and other implements used in bolting are often heavy and awkward to carry, which increases an operator's risk of back, shoulder, knee and other physical injuries. The material handling system's design enables tacks or bundles of mesh to be loaded onto the machine at one time without the operator needing to lift them individually. Materials can also be loaded onto pods by the vendor outside of the mine and then be taken underground by supply cars, lifted to the proper location and then pulled onto the rear of the machine by the material handling system. This design promotes a reduction in occurrences of injuries associated with repetitive tasks, such as lifting roof bolting materials onto the machine.

One of the main focuses of the design was the location of the rib drills. The mine wanted the capability of installing one rib bolt a 305 mm below the roof, without requiring that the rib bolt be in line with the roof bolts. The first idea to accomplish this was to put the rib drills on their own booms, which would provide them with their own independent lift, sump and roll. This design concept required a considerable amount of space and presented the challenge of positioning the operator's controls. After several design iterations, the decision was to mount the rib drills at the rear of the lifting platform. By mounting them there, the functions required to manipulate them were reduced and fewer hoses were required on the platform boom. Thus, all six drilling devices are located on the front lifting and extending platform. The platform is designed to lift 1524 mm and each side platform has the capability of extending 965 mm (Figs. 3–5).

The four roof drills are located at the front of the platform. All of the roof drills have the ability to tilt 2.5° forward as well as 2.5° backward for a total of 5° (Fig. 6). The roof drills also have the ability of tilting side-to-side 10°, 5° in and 5° out, with the exception of the inner roof drill rigs, which only tilt side to side 7.5°, 2.5° in and 5° out (Fig. 7).

The two rib drills are mounted on rotary actuators on the rear of the lifting platform. The rotary actuator allows the rib drills to rotate toward the mine's side wall (rib) 150° before it would contact the side of the machine (Fig. 8). Since they are mounted on the platform's center assembly, they do not move when the side platforms are extended. However, the drill controls are mounted on the extending platform to keep the operator under the drill canopy. The platform is equipped with three driller canopies, one center driller canopy to cover the two inner roof-drill controls and one driller canopy on each outer extending platform to cover the outer roof-drill controls and the rib-drill controls. Beside each of the rib-drill controls there is a rib access pocket for the operator (Fig. 9). The platform is also equipped with an automated temporary roof support (ATRS) and two drill trays for storage.

The other main focus was to provide a machine that is MSHA approved. We contacted MSHA early in the development process and we had several meetings to discuss the project at length. It was determined that without their acceptance of a latched feed and rotation drilling system there was no reason to pursue this project. The latched drilling system allows for hands-off drilling to be performed. It does not replace the normal drilling controls but rather is an enhancement to the existing system. One of the key points that had to be conveyed was that latched drilling was not the same as detented controls. Detented controls are a mechanically engaged valve spool that does not reset automatically but must be done manually. In a 1985 MSHA memorandum, detended controls were banned and controls that did not return to neutral when the operator released them were deemed an unacceptable safety hazard. Again in 1994 MSHA notified the industry of this concern in the Roof Bolter Committee Report, however, at that time latched controls were not being evaluated. Latched drilling has been used on several machines in the past with no history of accidents.

The latched feed and rotation drilling system is accomplished by using a hydraulic latch. Before a latched drilling system is installed on a machine there are several requirements. The drill mast must be fitted with a deep-socket chuck drillhead and drill guide to contain the drill steel. Also the feed pressure must be set below the failure limit of the drill steel and the drillhead rotation must be set to less than 700 r/min. The other important step is that the hole must be collared (the drill bit is into the roof or rib

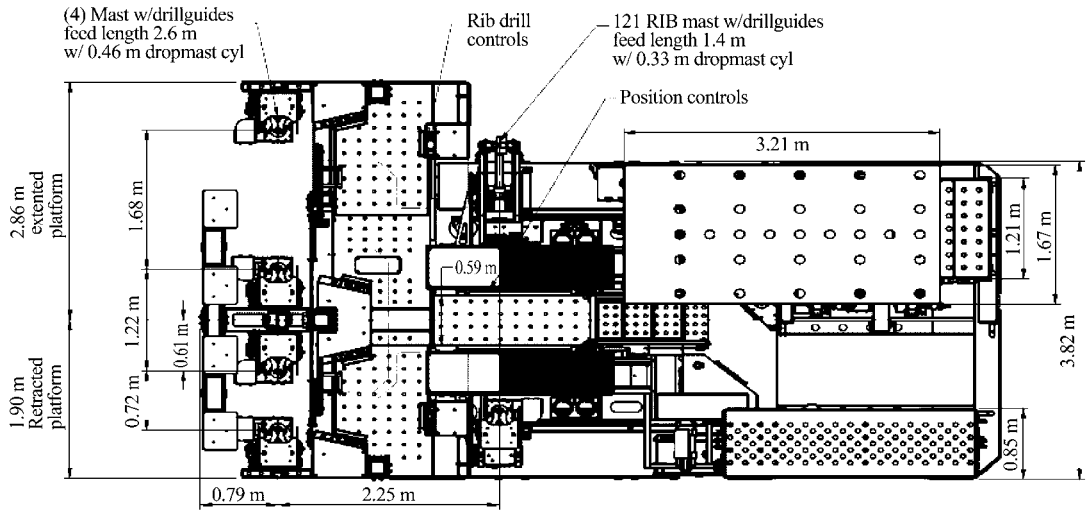

Fig. 3. Six drillhead roof and rib bolter, top view with one side platform collapsed and one extended.

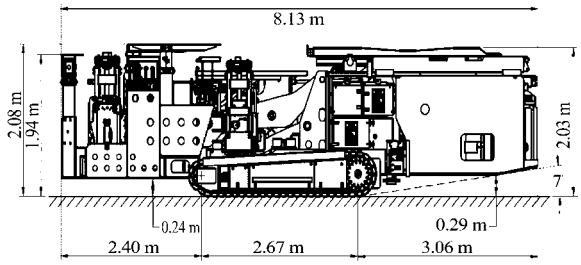

Fig. 4. Six drillhead roof and rib bolter, side view with the front platform collapsed.

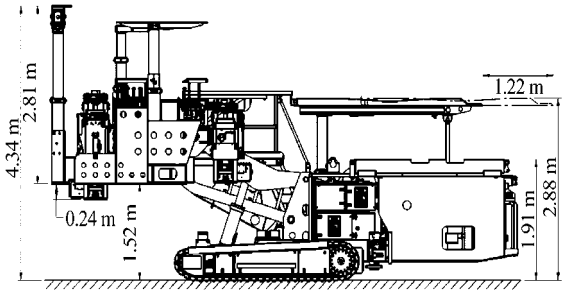

Fig. 5. Six drillhead roof and rib bolter, side view with the front platform extended.

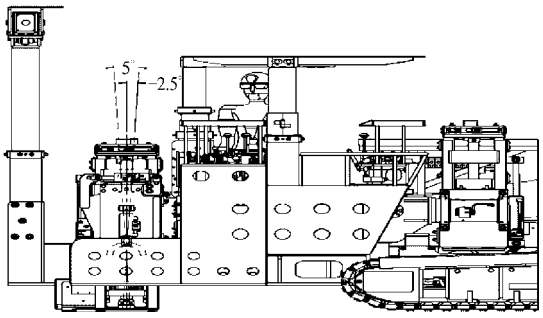

Fig. 6. Roof drills forward to back capability.

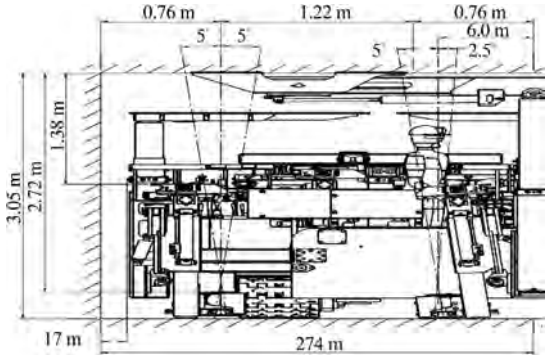

Fig. 7. Roof drills side to side capability.

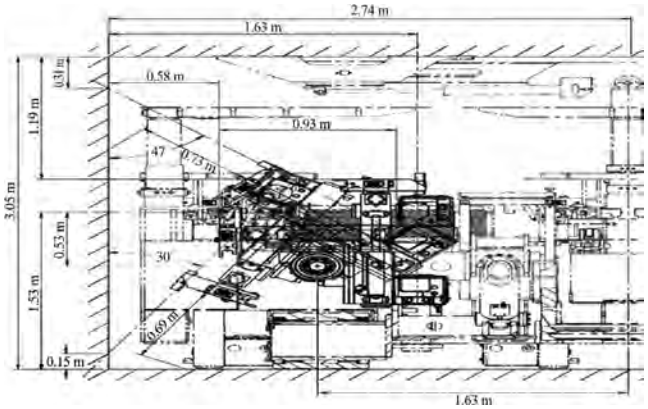

Fig. 8. Rib drills capability.

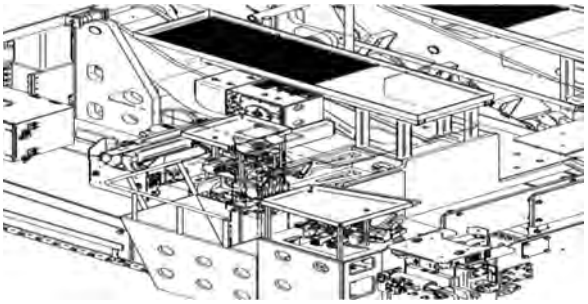

Fig. 9. Rib access and controls (support post and canopy phantom for clarity).

25–76 mm) before the latch system is engaged. With a drill steel in the chuck, the drill guide closed and the hole collared, initiation of the latched drilling may occur. With the operator pushing on the feed and rotation joystick (upward feed and forward rotation) with one hand, the latched drilling handle can be actuated by the other hand pushing it forward. At this time a pilot signal is directed to the feed up and rotation forward pilot end cap on the control valve. This maintains flow to the drill feed cylinder and the drillhead drill motor, allowing for hands-off drilling. Without loss of feed or rotation pressure, the drill steel will continue upwards into the roof or rib, drilling the hole until the operator stops it or it reaches the end of the mast feed length. Without feed and rotation pressure the latched drilling circuit cannot be engaged, ensuring that the drill must be in material and not free air to operate. At the end of the required drilled depth or whenever the operator wants to end the latched drilling he/she may do this by one of the following methods: pulling back on either the latched drilling control handle or the feed and rotation joystick, pushing in the on the hydraulic disconnect bar or pushing on the machine stop strip switch. The latched drilling system cannot be engaged when the feed and rotation joystick are operated in the reverse direction.

This machine is also set up for two different modes of operating the drill rigs. The operator has a drill mode for drilling the hole and a resin mode for installing the bolt. In drill mode the feed pressure is set to only what is required to drill the hole. In resin mode the feed pressure is adjusted higher for pushing the bolt through the resin and the rotation flow is lowered for a lower rotation per minute. In resin mode the latched drilling system is disabled and the dust systems pre-cleaner is piloted open to dump the pre-cleaner, which renders the operator unable to use the higher feed force resin mode to drill a hole.

During the development of this machine, it was determined that the machine design must prevent the operators, to the extent possible, from coming into contact with moving components when the operator is not operating the controls for the drill rigs. Therefore, the platform has been equipped with railings and guards between the operator and drill rig except for a small opening to allow the operator access to install and remove drill steels and bolts. The openings are small enough that an operator could not fall through them. Furthermore, adjacent to each opening is a hydraulic disconnect as well as a machine stop strip switch.

3. Conclusions

The final design result (see Figs. 10 and 11) is a machine that incorporates patented technology with a single platform and six independent mast and drillheads. Four masts strictly for drilling and installing roof bolts are mounted on the front of the platform and two masts are mounted on the back of the platform for rib bolts. This roof bolting machine allows three to four roof bolt operators to operate six drillheads, which decreases the time to bolt an open cut. With the latched feed and rotation drilling system, the roof bolter is able to operate more than one drillhead, which allows productive drilling using fewer operators. With fewer operators and more drillheads, we are reducing the time and exposure of the operator in an open cut and from the inherent pinch points and rotary hazards once he has engaged the latch drilling. Therefore, the machine will help to decrease the time to bolt a cut, improving productivity without sacrificing the ability to operate the machine safely.

It is important to remember latched drilling is not a detented control. The major distinction is that upon startup of the machine, the feed and rotation joystick is in the neutral position, thus removing any hydraulic power from the latch drilling control valve. Additionally, the act of initiating the latched drilling system is a two-handed operation requiring forethought. Fletcher found no increased hazard when using the latched drilling enhancement, which also provides some ergonomic advantages. Machine guarding was added to prevent an operator from coming into accidental contact with a latched drill steel. However, this system should only be used on machines specified by J. H. Fletcher and Company.

There are currently two of these machines working underground. Both machines are successfully installing all roof support for one cut in under an hour. While one of our service personnel was underground with the machine, he was able to time the operators on five rows. With three operators, two on the face drills and one on the rib drills, they were consistently able to bolt one row with four roof bolts and one rib bolt in under three minutes (the fastest row took two minutes and 18 s, and the slowest took two minutes and 55 s). The time was from the start of the first drilled hole to the torqueing of the fifth bolt and the time does not include any advancement time between rows. The operators stated that they have bolted a 12 m cut in a little over 40 min. This is an improvement over the 55 min per cut that it took using their CHDDR roof bolter. Through careful observation and operator input, additional efficiency improvements are being realized, which will result in better times. The roof bolter operators stated that the six-head bolters are faster and easier than their previous dual-head roof bolting machines. The mine has also indicated recently that with four operators they were able to bolt a cut in 27 min, a time that is greatly reduced from their previous methods.

Fig. 10. Six drillhead roof bolting machine.

Fig. 11. Six drillhead roof bolting machine platform.

References

[1] Ambrose DH, Cole GP, Gallagher S. Estimating low back loads of underground mine roof bolter operators using digital human simulations. 2004 SAE International number 2004-01-2148. p. 6.
[2] Ambrose DH, Bartels JR, Kwitowski AJ, Helinski RF, Gallagher S, McWilliams LJ, et al. Mining roof bolting machine safety: a study of the drill boom vertical velocity. U.S. Department of Health and Human Services, Information Circular (IC) 9477; 2005. p. 56.
[3] Robertson SB, Molinda GM, Dolinar DR, Pappas DM, Hinshaw GE. Best practices and bolting machine innovations for roof screening. In: Proceedings of 2003 SME annual meeting. Cincinnati, OH; 2003. p. 8.

International Journal of Mining Science and Technology 27 (2017) 43–47

Contents lists available at ScienceDirect

International Journal of Mining Science and Technology

journal homepage: www.elsevier.com/locate/ijmst

Assessment of energy release mechanisms contributing to coal burst

Zhang Chengguo *, Canbulat Ismet, Tahmasebinia Faham, Hebblewhite Bruce

School of Mining Engineering, UNSW, Sydney 2052, Australia

ARTICLE INFO

Article history:
Received 28 May 2016
Received in revised form 15 August 2016
Accepted 23 September 2016
Available online 12 December 2016

Keywords:
Coal burst
Coal burst mechanisms
Energy release
Numerical modelling
Mine geomechanics

ABSTRACT

Coal burst is a dynamic release of energy within the rock (or coal) mass leading to high velocity expulsion of the broken/failed material into mine openings. This phenomenon has been recognised as one of the most catastrophic failures associated with the coal mining industry, which can often lead to injuries and fatalities of miners as well as significant production losses. This paper aims to examine the mechanisms contributing to coal burst occurrence, with an emphasis on the energy release concept. In this study, a numerical modelling study has been conducted to evaluate the roles and contributions of difference energy components. The energy analysis presented in this paper can help to improve the understanding of energy release mechanisms especially under Australian conditions.

1. Introduction

Coal burst is one of the most hazardous problems encountered in underground coal mines, which occurs at different locations in a variety of mining systems and operations. This phenomenon always involves a violent and dynamic energy release with large rock mass/coal deformation and ejection that can cause severe damage to openings, equipments and may result in fatalities and injuries.

The first coal burst occurrence was reported in Britain in 1738 [1]. Since then, international experiences are available in Canada, South Africa, USA, former Soviet Union, China, India, France, Germany, Poland and Czechoslovakia. Rice classified coal bursts as two general types, namely excessive pressure bumps and shock bumps, and further mentioned that pressure bumps are caused when pillar stress exceeds bearing strength [2]. Shock bumps are induced by the breaking of thick, massive strata at a considerable distance above the coal-bed, causing the immediate roof to transmit a shock wave to the coal.

Coal bursts occur under the effects of complex environments of geology, stress and mining conditions. Various researchers attempted to develop empirical relationships between the identified critical parameters and coal burst proneness, and the phenomenon has been studied from varying perspectives [3–5]. There have been many hypothesised mechanisms discussed as potential driving mechanisms causing coal bursts. From these studies, four critical conditions for the coal burst occurrence can be identified, and the stress environment must be sufficiently high to result in rock failure; a situation must exist which can result in a state of unstable equilibrium [6,7]. This could be a low friction bedding plane, for example, where the potential exists for the coefficient of friction to drop rapidly from its static to dynamic value once movement is initiated along this plane; a change in the loading system and a large amount of energy has to be stored in the system.

It has been recognised that the unstable release of potential energy of the rock mass around the excavations, mainly in the form of kinetic energy, contributes to the coal burst occurrence. Part of this energy is consumed by fracture formation, and the remaining energy is transformed into kinetic energy [8,9]. When the source is located a close approximate to the critical surface, this kinetic energy causes the coal fragments to be ejected. When the source is located in a plane of weakness within the rock mass, the released energy induces shear displacements along the plane, which in turn producing vibrations that induce rock ejections when they reach the excavation boundaries [10].

This paper addresses the energy concepts associated with coal burst phenomenon by conducting analyzes on coal pillars using numerical modelling. ABAQUS/explicit models were developed to model the dynamic behavior of a single pillar under applied quasi-static and dynamic loading. The pillar capacity under both quasi-static and dynamic loading has been assessed and the effects of the pillar width to height (w/h) ratio under different loading conditions have been studied.

* Corresponding author. Tel.: +61 2 9385 5524.
E-mail address: chengguo.zhang@unsw.edu.au (C. Zhang).

http://dx.doi.org/10.1016/j.ijmst.2016.09.029
2095-2686/

2. Energy based approaches

Energy based approach method is one of the common methods to determine the critical regions in the rock mass/coal structures. Cook et al. are one of the pioneers to consider the effect of the energy changes throughout the mining activities as well as excavations [11]. Salamon describes in great detail several energy quantities that are needed to assess the energy release rate when acting through the induced displacements (W), the strain energy content of the volume (Vm) of the rock to be mined (U'), the change in strain energy in the volume (V) of the system that remains unmined (U), and the total work done by the contact and body forces on the permanent supports (Ws) [12].

The first coal burst mechanism is concerned with the perception of energy release, since the coal burst is caused by a dynamic and unstable release of energy within the excessive stresses in the rock mass (coal) during the mining process. In view of the energy contemplations, there are a variety of energy modules. Potential energy is the stored energy of a place in which held by coal, and there are two forms of potential energy including gravitational potential energy and elastic potential energy. Gravitational potential energy is the function of the vertical position or height. Strain energy is the energy stored in coal, due to deformation, and the external work done on the coal is causing it to alter from its unstressed state, which is usually transformed into strain energy.

In the 1960s, the concept of energy release rate (ERR) was initially used by South African researchers in evaluating rock burst potential for deep hard rock mines. The ERR was found to have a reasonable correlation with the risk or potential of coal bursts through an extensive analysis of the coal burst database. Since 1980s, the ERR was implemented in a range of numerical models to investigate the potential coal bursts. Maleki et al. utilized energy calculations with elastic-plastic models to analyze mining plans for burst-prone mine [13]. Heasley used a strain-softening model for energy calculations applied to coal bumps [14]. Sears and Heasley incorporated ERR into the boundary element code LaModel to analyze potential coal bursts [15]. Recently, Poeck et al. developed an approach to assess the potential for coal bumps in room and pillar mines through the use of energy concepts, focusing on the interface properties between the coal and overlying rock [16]. Using this approach they back analyzed the Crandall Canyon Mine in the United State collapse. Previous research in South Africa found that the level of ERR has a significant correlation with the occurrence of rock bursts and the extent of rock fracturing increases with increasing ERR values [12,17,18].

The major energy factors that should be taken into account to evaluate the possibility of the rock/coal burst occurrences are strain energy, external work done, kinetic energy and internal energy or stored energy, which is extracted by the strain energy and it is not converted to the kinetic energy. In the simplest approach, strain energy + external work = kinetic energy + internal energy. There are also other forces that may contribute to kinetic energy release, such as gas expansion energy, which is not considered in this study.

The above simple equation can present the relationship between the induced energy due to external events, which is illustrated by strain energy, and converted energy which are presented with kinetic energy and internal energy. The proportion of the strain energy and kinetic energy is a significant factor to determine whether the strain energy can be released as a kinetic energy or it would be totally destructive energy.

Eq. (1) is suggested as a benchmark to determine the possibility of stored energy situation, which can help to prevent the coal burst occurrence. In this case, both α and β (where $\alpha \geqslant 2$ and $\beta \geqslant 2$), are mathematical parameters which are fully dependent on the expected accuracy in the suggested analytical approach.

$$\left(\frac{E_{kinetic}}{E_{strain}}\right)^{\alpha} + \left(\frac{E_{internal\,work}}{E_{strain}}\right)^{\beta} = 1 \tag{1}$$

Eq. (1) can be accumulative, due to the effect of the time increments in the dynamic analysis. Given that the impulsive loading is applied throughout the different time increments with the different loading magnitudes, Eq. (1) can be written as:

$$\left(\sum_{i=1}^{i=t}\left(\frac{E_{kinetic}}{E_{strain}}\right)_i\right)^{\alpha} + \left(\sum_{i=1}^{i=t}\left(\frac{E_{internal\,work}}{E_{strain}}\right)_i\right)^{\beta} = k \tag{2}$$

where k is a constant value; and t the maximum number of the time increments.

Therefore, the proportion of $\left(\frac{E_{kinetic}}{E_{strain}}\right)^{\alpha}$ is one of the key factors for determining critical sections. For different mining structural systems, it can be assumed that if the proportion of $\left(\frac{E_{kinetic}}{E_{strain}}\right)^{\alpha}$ is equal or higher than 1, there is less likelihood of coal burst occurrence. The kinetic energy, which is a combination of induced works in different layers which can cause moving layers as well as releasing kinetic energy to the different part of the mining structure, can be presented as:

$$E_{kinetic} = \left(\sum\left(\int(\delta_{xx}\cdot A_{xx}\cdot\varepsilon_{xx}\cdot l_x)dx + \int(\delta_{yy}\cdot A_{yy}\cdot\varepsilon_{yy}\cdot l_y)dy + \int(\delta_{zz}\cdot A_{zz}\cdot\varepsilon_{zz}\cdot l_z)dz\right)\right)$$

where $\delta_{xx}, \delta_{yy}, \delta_{zz}$ are the stress components in the different directions; A_{xx}, A_{yy}, A_{zz} the effective area in the different directions; $\varepsilon_{xx}\cdot l_x$ the amount of slip in x direction; $\varepsilon_{yy}\cdot l_y$ the amount of slip in y direction; $\varepsilon_{zz}\cdot l_z$ the amount of slip in z direction.

The factor of $\left(\frac{E_{kinetic}}{E_{strain}}\right)^{\alpha}$ can be represented by:

$$\left(\frac{E_{kinetic}}{E_{strain}}\right)^{\alpha} = \left(\sum\left(\frac{\int(\delta_{xx}\cdot A_{xx}\cdot\varepsilon_{xx}\cdot l_x)dx}{E_{Strain}}\right) + \sum\left(\frac{\int(\delta_{yy}\cdot A_{yy}\cdot\varepsilon_{yy}\cdot l_y)dy}{E_{Strain}}\right) + \sum\left(\frac{\int(\delta_{zz}\cdot A_{zz}\cdot\varepsilon_{zz}\cdot l_z)dz}{E_{Strain}}\right)\right)^{\alpha} \tag{3}$$

Eq. (3) indicates how the slip in different directions can play a key role in releasing the stored energy in the different layers. The amount of the slip between the layers is partially either dependent on the joint properties or structural confinement in the free edges (for instance, the presences of geological structures such as faults, dykes, sandstone channels, and joints). Underground excavations can result in stress concentration as well as stress redistributions on to face and adjacent pillars. Due to the complexity of the causes and mechanisms contributing to coal burst occurrence, a comprehensive 2D and 3D finite element (FE) modelling study has been conducted to numerically evaluate the accuracy and the validation of the above analytical assessments of coal burst occurrence.

3. Numerical modelling strategy

Numerical modelling can provide valuable insight into potential failure modes and bearing capacity in a given mine setting. It is particularly useful for undertaking parametric and sensitivity analyzes to better understand the nature and level of uncertainty, or residual risk, associated with design procedures. The current state of knowledge, albeit incomplete, can also be exploited to manage risk by undertaking a comparative risk assessment. In the current study, a quarter of a single pillar was developed (Fig. 1).

Furthermore, Fig. 2 presents the full geometrical details of the developed model. A surface to surface contact was assigned between engaged surfaces to simulate the interaction between the coal and the rock. Thus, both the overburden and the roof were

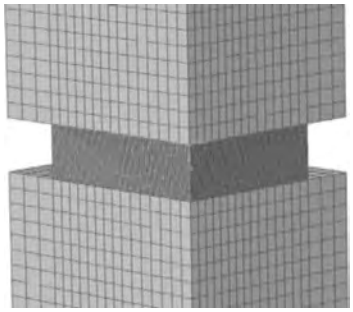

Fig. 1. Illustration of a typical single pillar model.

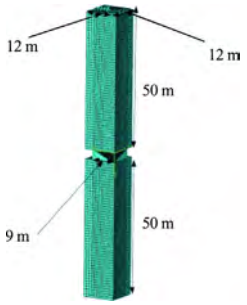

Fig. 2. Dimensions of the simulated model.

considered the master surfaces and coal was assigned as the slave surface. Generally speaking, the allocated mesh density in the master surfaces is significantly coarser in comparison with the slave surfaces to simulate a better energy transition between the engaged surfaces. Consideration was also given to define a joint interface between the coal and overburden rock. Based on the study by Poeck et al., a continuous yielding (CY) joint interface property where it is presented by displacement softening parameters was taken into account to simulate the interface properties between the coal and rock [16].

A dynamic loading is considered in which the top of the model (i.e., overburden) was loaded with a very small, constant velocity to represent a relatively "stiff" loading system to promote a model of pillar failure that progresses slowly. Simulating the right loading condition is significantly important, individually, when it comes to getting a better understating of the structural reaction of a single pillar under dynamic or quasi-static loading conditions.

Symmetrical boundary conditions were applied in the models to create an appropriate boundary condition. Determination of the input material properties is a critical consideration, which is not properly addressed in the past and current simulations. Modelling of mechanical behavior of the coal under both compression and shear stresses is complex, as there are no sound documented reports regarding the uniaxial and tri-axial behavior of coal under both static and dynamic loading conditions. Also, scale effect is another critical consideration which affects the structural responses of the situ pillars. A number of researchers have conducted numerical modelling based on the elastic analysis, means that both stress analysis and energy calculations were arranged according to the linear relationship between the stress and the strain in coal and overburden properties. This type of analysis ignores the peak and post-peak behavior of coal and surrounding rock masses. Thus, in those reported studies, the calculated stress, strain and kinetic energy were significantly overestimated.

Therefore, simulating the post-peak failure or post-damage of coal is a critical concern that can considerably influence the design and structural assessment of pillars. A number of approximations were reported on simulating the post-peak behavior of coal under static loading. However, the reported documents lack of a solid scientific approach; thus, they cannot be taken into account as a generic approach. Furthermore, as the simulation of the coal burst is directly related to dynamic and/or quasi-static analysis, the high strain rates play an important role in the modelled material properties. Table 1 presents the basic material properties used for overburden and coal. Table 2 presents the changes in cohesion, friction and dilation angles applied to the strain-softening material with the associated levels of strain [16].

The numerical models which have been presented in this study are developed using the commercial software package ABAQUS/explicit. All materials, including the rock and coal were modelled with the eight-node linear brick element (C3D8R) available in the ABAQUS library. Element C3D8R relies on reducing integration and hourglass control. Its meshing is carried out with the structured technique available in ABAQUS. The solution to the nonlinear problem was sought using the explicit dynamic analysis procedure available in ABAQUS [19].

4. Modelling results

The effect of the width to height (w/h) ratio on the pillar capacity under both quasi-static and dynamic loading has been investigated to study the behavior of pillars with varying w/h ratios. The failure modes of pillars under quasi-static loading considering different w/h ratios have also evaluated. A failure criterion based on the strain dependent analysis was implemented in the ABAQUS/explicit to determine the trajectory of the cracking under different

Table 1
Numerical modelling material properties [16].

Material	Density (kg/m^3)	Young's modulus (GPa)	Poisson ratio	Friction angle (°)	Cohesion (MPa)
Overburden	2350	23.4	0.26		
Coal	1313	3.0	0.20	23	1.69

Table 2
Softening parameters used in coal [16].

Strain	Cohesion (MPa)	Strain	Friction angle (°)	Strain	Dilation angle (°)
0.00000	1.69	0.00000	23.0	0.00000	2
0.00006	1.54	0.00007	27.5	0.00007	10
0.00008	1.47	0.00010	30.0	0.01360	10
0.03500	0.20	1.00000	30.0	0.01413	2
1.00000	0.20			1.00000	2

loading and pillar geometrical conditions. Symmetric, quarter pillars with w/h ratios of 1–10 were built for the analyzes. It can be concluded that when the w/h ratios are less than four, the failure mode of pillar is either a double or a single diagonal shear failure in which the crack propagation starts from the edges and progresses toward the center of the pillar. On the other hand, when the w/h ratios are greater than four, the possible mode of failure is a combination of the shear and compression failure. In this case, the trajectory of the cracking due to the pure compression failure would be propagated from the center to the corners where a pillar gradually starts to get fully squashed.

Furthermore, as coal burst is modelled dynamically or quasi-statically, the effect of high strain rate on the material properties can be emphasised by the role of the dynamic amplitude factor (DAF) which is defined as the proportion of the dynamic stresses over the static stresses. To date, very little, if any, research discussed the consequences of dynamic responses on coal mechanical properties. This is why in the different numerical modelling research simulating the effect of coal burst, the estimated stresses as well as calculated strain energy are far away from the observed values in either in the measured field or experimental investigations. The suggested equation by Galvin and Hebblewhite which is well known as the UNSW equation was used to predict the ultimate static stress capacity of the pillar with different w/h ratios ranging from 1 to 10 [7]. The modelled dynamic and static stresses were plotted against pillar geometrical properties values which have been presented in Fig. 3.

As illustrated, there is a significant variation between the predicted static and modelled dynamic stresses in a single pillar with different w/h ratio. This can be justified by considering the dynamic amplitude factor (DAF) which is closely related the effect of the inertia forces due to the dynamic loading. Using the above results Eq. (3) can be rewritten to calculate the dynamic amplitude factor (DAF) for different w/h ratios in a single pillar to examine the effect of the dynamic and quasi-static loading conditions.

$$DAF = \left(\frac{MaxDynamic_{Stress}}{MaxStatic_{Stress}}\right) = \left|Ln\left(\frac{W}{H}\right)^{-0.6} + 2.7\right| \quad (4)$$

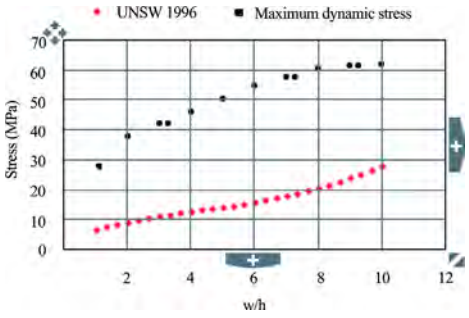

Fig. 3. Maximum static and dynamic stresses versus (w/h).

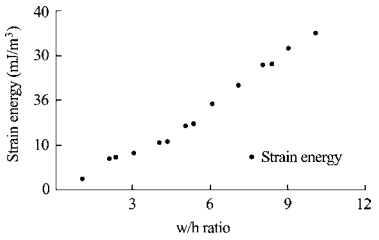

Fig. 5. Strain energy versus w/h in a single pillar.

The same trend can be extended as follows to analyze the maximum dynamic stresses in a single pillar due to the different w/h ratios.

$$MaxDynamicStress\ (\mathrm{MPa}) = \left|3 \times \left(\frac{W^{1.23}}{H^{0.2}}\right) - 29.4\right| \quad (5)$$

Furthermore, Fig. 4 provides the trajectory of the yielding surface where it starts from the corner of the single pillar toward center. One of the key aspects of the transition plastic stress is creating a strut and tie structure on the face of the pillar which has been explicitly shaped from the corner toward the center of the pillar. This may lead to a better understating about the strain energy transformation toward the plastic work which can be justified by taking into account the amount of the fracture surfaces on the pillar.

5. Strain energy quantification

Mining activities change the status of potential and strain energies stored within the coal in the vicinity of excavations. The major source of energy in the system, around the excavation is the work done by the boundary loading and body forces (e.g. gravity). Energy is dissipated in several forms, including the strain energy change, the kinetic energy, loading on the support system if it is applied. Total strain energy is the key parameter that can cause coal burst. Fig. 5 illustrates the modelled strain energy versus the proportion of w/h in a single pillar, due to the applied dynamic loading.

Eq. (6) can be used to estimate the amount of stored strain energy per volume due to the changing of the pillar geometry.

$$\left(\frac{Strain\ (\mathrm{mJ})}{Volume\ (\mathrm{m^3})}\right) = 31 \times \log\left(\frac{W}{H}\right)^{2.9} + 4.1 \quad (6)$$

6. Conclusions

Finite element model of ABAQUS/explicit was used to model the dynamic behavior of a single pillar under applied quasi-static and dynamic loading conditions. A strain based failure criterion was

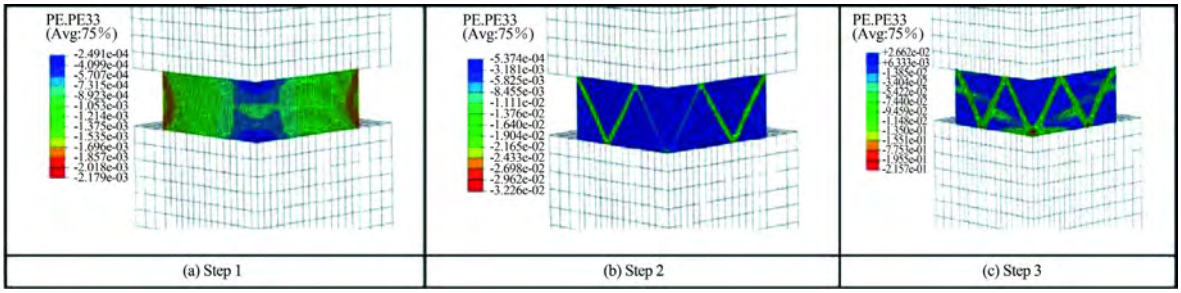

Fig. 4. Progressive yielding surfaces in a single pillar.

examined to estimate the failure modes in a single pillar with varying w/h ratios. Shear and compression failures as well as a combination of them were numerically observed. Furthermore, a number of empirical equations were examined to predict dynamic amplitude factor as well as the amount of the strain energy in a single pillar with varying w/h ratios. These findings are only preliminary and require further investigations. It is, however, indicated that a new tool can be developed to identify the coal burst risk areas in a coal mine. It is likely that the same trends may be extended to other types of the mining structures where finding critical factors to predict coal bursts is significantly important.

References

[1] Dou LM, He XQ. Prevention theory and technology of rock burst. Xuzhou: China University of Mining and Technology Press; 2001.
[2] Rice GS. Bumps in Coal Mines of the Cumberland Field, Kentucky and Virginia – Causes and Remedy, USBM RI 3267; 1935.
[3] Mark C, Gauna M. Evaluating the risk of coal bursts in underground coal mines. Int J Min Sci Technol 2016;26(1):47–52.
[4] Zhang P, Peterson S, Neilans D, Wade S, McGrady R, Pugh J. Geotechnical risk management to prevent coal outburst in room-and-pillar mining. Int J Min Sci Technol 2016;26(1):9–18.
[5] Lawson H, Weakley A, Miller A. Dynamic failure in coal seams: implications of coal composition for bump susceptibility. Int J Min Sci Technol 2016;26(1):3–8.
[6] Salamon MDG, Wagner H. The role of stabilising pillars in the alleviation of rockburst hazard in deep mines. Research Report No. 27/79. Johannesburg: Chamber of Mines of South Africa Research Organisation; 1979.
[7] Galvin JM, Hebblewhite BK. UNSW pillar design methodology. Sydney, Australia: University of New South Wales, School of Mining Engineering; 1995.
[8] Wang JA, Park HD. Comprehensive prediction of rockburst based on analysis of strain energy in rocks. Tunnell Underground Space Technol 2001;16(1):49–57.
[9] Li CW, Jie BJ, Cao GL, Wang TT, Wang XY. The energy evaluation model of coal and gas outburst intensity. J China Coal Soc 2012;37:1547–52.
[10] Ortlepp WD, Stacey TR. Rockburst mechanisms in tunnels and shafts. Tunnell Underground Space Technol 1994;9(1):59–65.
[11] Cook NGW. The failure of rock. Int J Rock Mech Min Sci Geomech Abstracts 1965;2:389–403.
[12] Salamon MDG. Energy considerations in rock mechanics; fundamental results. J South Afr Inst Min Metall 1984;84:233–46.
[13] Maleki H, Aggson J, Miller F. Mine layout design for coal bump control. In: Proceedings 6th international conference on ground control in mining. Morgantown, West Virginia; 1987. p. 32–46.
[14] Heasley KA. An examination of energy calculations applied to coal bump prediction. In: Proceedings of symposium on rock mechanics. Norman, Oklahoma; 1991. p. 481–90.
[15] Sears MM, Heasley KA. An application of energy release rate. In: Proceedings 28th international conference on ground control in mining. Morgantown: West Virginia University; 2009. p. 10–16.
[16] Poeck E, Zhang K, Garvey R, Ozbay U. Energy concepts in the analysis of unstable coal pillar failures. In: Proceedings 34th international conference on ground control in mining. Morgantown: West Virginia University; 2015. p. 8–13.
[17] Heasley KA, Zelanko JC. Pillar design in bump-prone ground using numerical models with energy calculations. In: Proceedings of the workshop on coal pillar mechanics and design. BuMines IC 9315; 1992. p. 50–60.
[18] Jager AJ, Ryder JA. A handbook on rock engineering practice for tabular hard rock mines. Johannesburg: Safety in Mines Research Advisory Committee; 1999.
[19] Tahmasebinia F, Ranzi G, Zona A. Beam tests of composite steel–concrete members: a three dimensional finite element model. Int J Steel Struct 2012;12(1):37–45.

International Journal of Mining Science and Technology 27 (2017) 49–55

Contents lists available at ScienceDirect

International Journal of Mining Science and Technology

journal homepage: www.elsevier.com/locate/ijmst

Coal and gas outburst dynamic system

Fan Chaojun [a], Li Sheng [a,b,c,*], Luo Mingkun [a], Du Wenzhang [a], Yang Zhenhua [a]

[a] College of Mining Engineering, Liaoning Technical University, Fuxin 123000, China
[b] State Key Laboratory for GeoMechanics and Deep Underground Engineering, China University of Mining & Technology, Xuzhou 221116, China
[c] State Key Laboratory of Coal Resources and Safe Mining, China University of Mining & Technology, Xuzhou 221116, China

ARTICLE INFO

Article history:
Received 3 June 2016
Received in revised form 19 August 2016
Accepted 12 October 2016
Available online 7 December 2016

Keywords:
Coal and gas outburst
Dynamic system
Coal-gas medium
Geology dynamic environment
Mining disturbance
Stress-seepage-damage coupling model

ABSTRACT

Coal and gas outburst is an extremely complex dynamic disaster in coal mine production process which will damage casualties and equipment facilities, and disorder the ventilation system by suddenly ejecting a great amount of coal and gas into roadway or working face. This paper analyzed the interaction among the three essential elements of coal and gas outburst dynamic system. A stress-seepage-damage coupling model was established which can be used to simulate the evolution of the dynamical system, and then the size scale of coal and gas outburst dynamical system was investigated. Results show that the dynamical system is consisted of three essential elements, coal-gas medium (material basis), geology dynamic environment (internal motivation) and mining disturbance (external motivation). On the case of C13 coal seam in Panyi Mine, the dynamical system exists in the range of 8–12 m in front of advancing face. The size scale will be larger where there are large geologic structures. This research plays an important guiding role for developing measures of coal and gas outburst prediction and prevention.

1. Introduction

Coal and gas outburst is a complicated mine gas dynamic phenomenon, which seriously threats coal mine safety production [1]. Since the first-recorded coal and gas outburst happened in Isaac Coal Mine in Lule coal field in 1843, more than 40 thousand outbursts have occurred in the world. China ranks first place in the aspects of frequency and strength of outburst. In recent 20 years, China averagely increases 37 pairs of coal mine and more than 280 times outburst accident every year [2,3]. The coal and gas outburst occurred on October 20, 2004 in Daping Coal Mine, Zhengzhou Coal Group, and has caused serious gas explosion accident, which pushed 1894 tons of coal into the working face and caused 148 deaths [4]. In recent years, despite taking a lot of control measures, coal and gas outburst still occurred frequently with the increase of the depth and mining intensity.

Outburst mechanism is summed up in the following four aspects: the gas leading role hypothesis, the geostress leading role hypothesis, the chemical effect hypothesis, and combination hypothesis. And the last hypothesis has won the acceptance of most scholars, which considered that the outburst is the result of combined effect of stress, gas and coal [5].

Numerous experimental measurements and numerical simulations were conducted to investigate permeability and damage evolution process in coal seam. Sobczyk et al. carried out a laboratory research of the influence of sorption processes on gas stresses leading to coal and gas outbursts [6]. Wang et al. conducted laboratory experiments to investigate the rapid decompression and desorption induced energetic failure in coal using a shock tube apparatus [7,8]. Xu et al. developed a coupled gas flow and solid deformation numerical model and applied to simulate the coal and gas outbursts in underground collieries using RFPA2D-gasflow [9]. An and Xue analyzed major parameters and the effect of gas desorption on outburst initiation, and established a model of gas migration and mechanical processes during excavation [10,11].

Meanwhile, some scholars have taken measures to forecast and prevent coal and gas outburst. Zhang and Li developed a multifactor pattern recognition technique to certain the possibility of coal and gas outburst [12]. Li and Zhao designed a simplex positioning algorithm for microseism monitoring and established a mine microseism monitoring system to canalize mine microseism [13]. Aguado and Nicieza established site measurements using some critical parameters for risk assessment and analyzed the gas behavior of subvertical coal seams in deep mines in order to prevent gas outburst [14]. The protective seam mining and gas drainage technique applied to strong coal and gas outburst dangers coal mine [15].

* Corresponding author. Tel.: +86 13941811946.
E-mail address: lisheng76@139.com (L. Sheng).

http://dx.doi.org/10.1016/j.ijmst.2016.11.003
2095-2686/

However, coal and gas outburst is much complex, and there are so many influencing factors. Coal and gas outburst has different patterns in the condition of different areas, different coal seams, different structures and different mining disturbances [12]. It is still a great topic to build a convincing and perfect cognition of coal and gas outburst.

In this paper, we propose the concept of coal and gas outburst dynamic system, and analyze interaction relationship of coal-gas medium, geological environment and mining disturbance in the dynamic system. A stress-seepage-damage coupling model will be established. And the size scale of the dynamic system will be analyzed by numerical simulation using this coupling model.

2. Dynamic system of coal and gas outburst

Coal is a porous medium, which contains a lot of gas. Under certain conditions geological environment and mining disturbance, the coal-gas medium will lose its stability and finally generate coal and gas outburst. Dynamic system of the coal and gas outburst consists of coal-gas medium, geological environment and mining disturbance (Fig. 1).

2.1. Coal-gas medium

Coal-gas medium composed of coal, water, air and other materials is the material basis and the necessary condition of coal and gas outburst. Its physical factors include coal thickness, firmness coefficient, porosity, permeability, gas pressure, gas content, initial speed of gas diffusion, ground water, etc. [12].

The adsorbed gas in the coal seam takes more than 80% of the total, while the content of adsorbed gas mainly depends on the porosity of coal, gas pressure and temperature. The gas in coal seam contains a large amount of internal energy, which will dramatically expanse under high pressure gradient and could throw out the broken coal. Generally speaking, the higher the gas pressure, the greater the gas content, the lower initial gas emission, the higher possibility of coal and gas outburst will be.

According to the fragmentation degree, coal structure is divided into primary constructional coal, ruptured coal, mortar coal and mylonitic coal [16]. The ruptured coal does not induce coal and gas outburst, but mylonitic coal and mortor coal can do it easily. Tectonic coal has a large porosity and a poor permeability, which benefits the gas preservation and will lead to relatively high gas pressure. The firmness coefficient of tectonic coal is significantly lower than primary constructional coal, and can be destroyed and thrown out easily [17]. Usually, the larger porosity and thickness of coal seam, the higher outburst risk will be. On the contrary, the larger permeability and firmness coefficient of coal seam, the lower outburst risk will be.

Water in the coal seam will fill the fractures and inhibit the gas desorption, diffusion and seepage. Generally, greater water content generates lower outburst risk.

2.2. Geological dynamic environment

Geological dynamic environment refers to the various geological factors which affect the properties of coal, and is the interior motivate of the coal and gas outburst. Geological dynamic environment includes geological structures (faults, folds, magmatite intrusion, and coal seam thickness variation), tectonic movement, coal seam depth. Han et al. discovered that coal and gas outburst usually occurred near the geological structures, such as the soft layer, faults, folds, igneous intrusion, and coal seam thickness variation [18].

Geological structure has a reconstruct function on the structure and mechanical properties of coal-gas medium, namely the damage effect. The coal structure in complex geological structure area is damaged seriously, with low strength and ability to resist coal and gas outburst. At the same time, tectonic stress in complex geological structure can often concentrate, which will increase the elastic potential energy in coal. Meanwhile, geological structure may lead to gas accumulation and high gas pressure. And high gas pressure gradient will cause tensile fracture of coal and increase the outburst risk.

Coal and gas outburst is the result of the interaction of the original crustal stress field and mining stress field caused by human activities [19]. Tectonic movement is the mechanical movement of the deformation and displacement of the lithosphere in the earth. The tectonic stress caused by tectonic movement is the maximum principal stress in coal-series strata. Horizontal extrusion stress often exceeds the vertical extrusion stress caused by the gravity of the overlying strata [16]. The nappe structure, syncline structure and structural depressions tend to have higher horizontal tectonic stress which provides a dynamic foundation for coal and gas outburst. In the process of tectonic evolution, these structures will compact and close the fractures and pores in the coal (rock) bodies and limit gas migration and dissipation, which has the sealing function to the coal and gas system. Therefore, the coal body

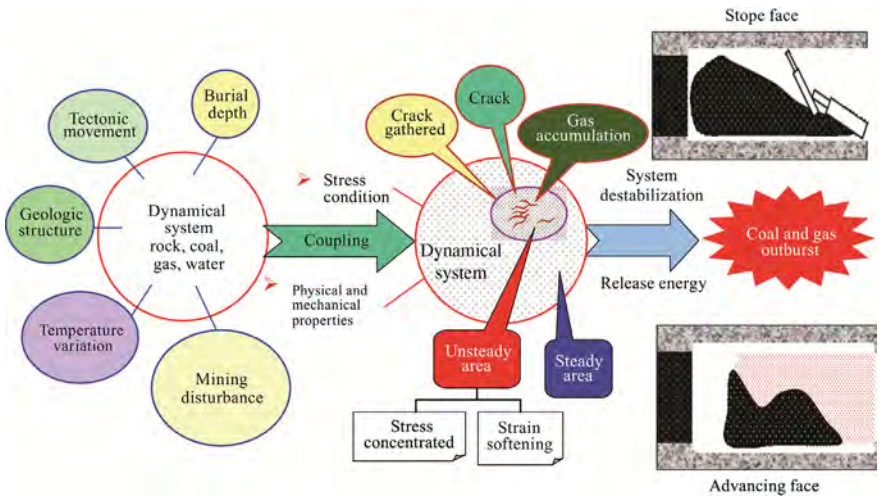

Fig. 1. Dynamic system of coal and gas outburst.

with high gas content, pressure and low strength forms the material condition for coal and gas outburst.

In the syncline structure (Fig. 2), for example, the rock bends under bending moment *M*. By the neutral layer, the lower part bears tensile stress and the upper part bears compressive stress [20]. And the farther from the neutral layer, the larger the tensile stress will be. The maximum value is located at the top and bottom edges. In the stress state of the rock formation, the maximum and minimum compressive stresses (σ_1 and σ_3) are perpendicular or parallel to the surface of the rock, and are perpendicular to the synclinal axis. The middle stress should be parallel to the rock layer and synclinal axis. Overall, syncline structure's high pressure zone is located above the two wings of syncline axis and neutral layer. The maximum shear stress in coal seam is the smallest in the syncline axial and largest in the wings.

Pingdingshan mining area is located in the southwest of Likou syncline (Fig. 3). The direction of the mining area distribution is parallel to Likou syncline. The Nos. 8, 10 and 12 coal mines in the eastern part of mining area are nearby Likou syncline, Niuzhuang syncline. The Nos. 1, 4 and 6 coal mines in the middle of the mining area are nearby some smaller faults. The Nos. 5, 7 and 11 coal mines in the west are closed to Guodishan fault, Jiulishan fault and the middle Haotang syncline. The statistics shows that gas outburst has a characteristic of regional distribution. Three pairs of coal mines in the eastern part are outburst mine with 43 times outburst and coal mine in the western part only has a few outburst appearances. There is no outburst in the middle of the mine area. Overall, coal and gas outburst in Pingdingshan is macroscopically controlled by syncline.

2.3. Mining disturbance

The coal-gas medium is stable without the external function. The mining disturbance means that human activities will break the original stress state, cause stress redistribution of the coal and rock mass around the mining. Different mining methods, mining process causes the disturbance effect that will have different forms of expression.

Under the combination of crustal stress (gravity stress and tectonic stress) and mining stress, coal-gas medium around the advancing (mining) face will deform. As shown in Fig. 4, when stress of coal-gas medium in the high stress area exceeds the peak strength, the medium will generate plastic deformation area. The coal-gas medium surrounding this area will form the elastic deformation and storage elastic energy [21]. Coal-gas medium unloads at the coal wall and causes tensile failure of coal. And then, the microcrack continues to develop to raise the coal seam permeability. At the same time, a large amount of gas desorbs and gathers at the local area to form high pressure. When the high pressure exceeds a limitation, the gas will rapidly emit out and damage the nearby coal wall. The damaged coal and high pressure gas will suddenly eject into the mining space, cause outburst. Mining disturbance is the external motivate, which provides sufficient energy source and space condition for coal and gas outburst.

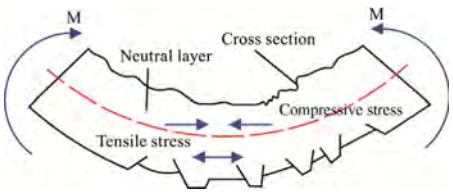

Fig. 2. Mechanics of syncline structure.

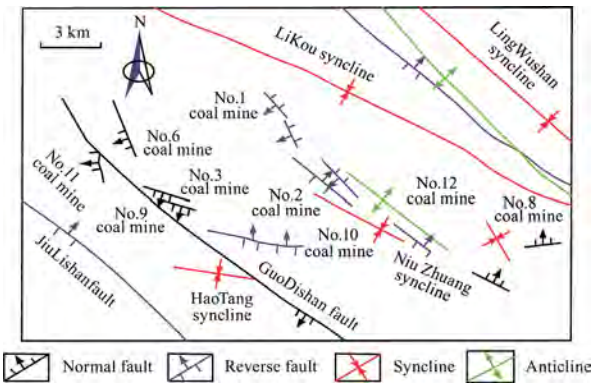

Fig. 3. Distribution of geological structure in Ping Dingshan mining area.

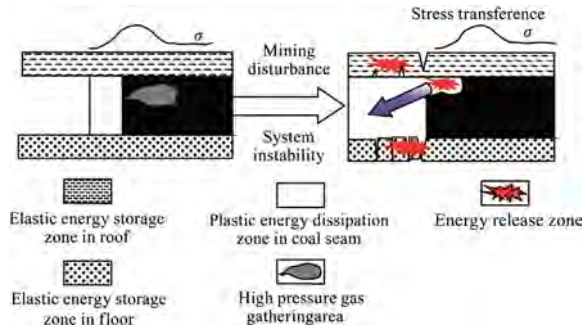

Fig. 4. Effect of mining disturbance on coal and gas outburst.

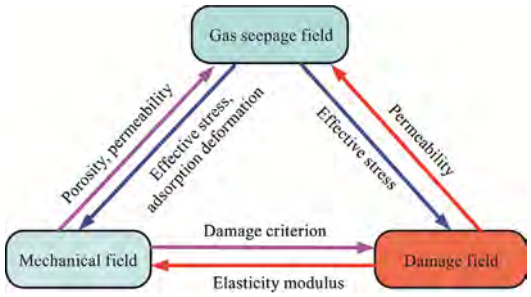

Fig. 5. Coupled interaction and the governing equations of the dynamical system.

In the coal and gas outburst dynamic system, coal-gas medium is material basis; geology dynamic environment is the internal motivation; mining disturbance is the external motivation. Coal and gas outburst is actually the stress-seepage-damage coupling catastrophe process in the dynamic system

3. Stress-seepage-damage coupling model in dynamic system

In the following, a set of governing equations are defined to govern the coal deformation and the gas transport, as shown in Fig. 5. These derivations are based on the following hypotheses: (1) the representative element volume (REV) within the coal seam is used; (2) strains of coal are infinitesimal; (3) the gas exists and migrates in pores; (4) the gas migration in the coal seam is closely related to the pore structure; (5) gas agrees with the ideal gas state equation and adsorbs/desorbs; (6) the volume force of gas is not considered; and (7) tensile stress is positive, while pore pressure is negative [22,23].

3.1. Governing equation of mechanical field

By taking strain induced by gas pressure and shrinkage/swelling strain induced by gas desorption/adsorption into consideration, the constitutive relations for coal seams can be expressed as [24]:

$$Gu_{i,jj} + \frac{G}{1-2\upsilon}u_{j,ji} - \alpha p_{,i} - K\varepsilon_{a,i} + f_i = 0 \tag{1}$$

where $G = E/2(1+\nu)$; $K = E/3(1-2\nu)$; $K_s = E_s/3(1-2\nu)$; $\varepsilon_a = \alpha_{sg}V_{sg}$; $\alpha = 1\text{-}K/K_s$; G the shear modulus, Pa; K the bulk modulus, Pa; K_s the skeleton bulk modulus, Pa; E the elastic modulus, Pa; E_s the skeleton elastic modulus, Pa; ν the Poisson's ratio; ε_a the volumetric strain induced by gas desorption; α the Biot coefficient; α_{sg} the strain coefficient induced by gas adsorption, kg/m; V_{sg} the absorbed gas content, m^3/kg; and p the gas pressure, Pa [25].

The absorbed gas content can be expressed as:

$$V_{sg} = \frac{V_L p}{P_L + p} \tag{2}$$

where V_L is the Langmuir volume constant, m^3/kg; and p_L the Langmuir pressure constant, Pa.

We use the elastic damage model to describe deformation and failure behavior of coal and rock. The strain equivalence principle defines that the material strain of damaged materials induced by real stress is equal to which of nondestructive materials induced by effective stress, which can be described as

$$\sigma = E\varepsilon = E_0(1-D)\cdot\varepsilon \tag{3}$$

where E_0 and E are the initial elastic modulus and damaged elastic modulus of coal, MPa, respectively; and D the damage variable, $0 \leqslant D \leqslant 1$, in which $D = 0$ expresses that the coal is undamaged, and $D = 1$ completely damaged.

Two strength criterions are adopted to describe the state of coal: coal will generate tensile damage when the stress state matches the maximum tensile-stress criterion; while coal will generate shear damage when the stress state matches the Mohr-Coulomb Criterion [26]. The maximum tensile-stress criterion can be expressed as:

$$\sigma_3 \leqslant -\sigma_t \tag{4}$$

The damage variable can be defined as:

$$D = \begin{cases} 0(\varepsilon < \varepsilon_{t0}) \\ 1 - \frac{\sigma_{tr}}{E_0\varepsilon}(\varepsilon_{t0} \leqslant \varepsilon < \varepsilon_{tu}) \\ 1(\varepsilon_{tu} \leqslant \varepsilon) \end{cases} \tag{5}$$

where $\varepsilon_{t0} = \sigma_{t0}/E_0$ is the ultimate elastic strains of coal under tensile condition; σ_{t0} the tensile strength, MPa; σ_{tr} the residual tensile strength, MPa; and ε_{tu} the maximum tensile strain. When tensile strain exceeds the maximum tensile strain, coal (rock) will be in a state of completely damaged.

The Mohr-Coulomb Criterion can be defined as:

$$F = \sigma_1 - \sigma_3\frac{1+\sin\phi}{1-\sin\phi} \geqslant \sigma_c \tag{6}$$

where φ is the internal friction angle, °; and σ_c the uniaxial compressive strength, MPa.

When shear stress exceeds the uniaxial compressive strength, the damage variable can be defined as:

$$D = \begin{cases} 0(\varepsilon < \varepsilon_{c0}) \\ 1 - \frac{\sigma_{cr}}{E_0\varepsilon}(\varepsilon_{c0} \leqslant \varepsilon \leqslant \varepsilon_r) \end{cases} \tag{7}$$

where σ_{cr} is the residual compressive strength, MPa; $\varepsilon_{c0} = \sigma_{c0}/E_0$ the maximum compressive strain; and ε_{c0} the compressive strength; and ε_r the residual strain.

3.2. Governing equation of seepage field

Mass conservation equation in coal-gas medium can be expressed as:

$$\frac{\partial m}{\partial t} + \nabla\cdot(\rho_g u_g) = 0 \tag{8}$$

where m is the gas content in coal-gas medium, kg/m^3; t the time, s; u_g the velocity of gas, m/s; and ρ_g the gas density, kg/m^3.

Gas content in coal-gas medium, consisting of absorbed gas and free gas components, can be defined as:

$$m = V_{sg}\rho_c\frac{M_g}{RT_s}p_s + \phi\frac{M_g}{RT}p \tag{9}$$

where V_{sg} is the absorbed gas content, m^3/kg; ρ_c the density of coal skeleton, kg/m^3; $p_s = 101$ kPa the standard atmospheric pressure, Pa; $T_s = 273.5$ K the temperature under standard condition; ϕ the porosity; M_g the gas molar mass, kg/mol; $R = 8.314$ J·mol/K the gas molar constant; and T the temperature in coal seam, K.

Based on generalized Darcy's law, the gas velocity can be defined as:

$$u_g = -\frac{k}{\mu_g}\left(1+\frac{b}{p}\right)\nabla p \tag{10}$$

where k is the permeability of coal-gas medium, m^2; μ_g the gas dynamic viscosity Pa·s; and b the Klinkenberg factor, Pa.

By substituting Eqs. (9) and (10) into (8), the governing equation of seepage field can be derived as:

$$\frac{\partial}{\partial t}\left(V_{sg}\rho_s\frac{M_g}{RT_s}p_s + \phi\frac{M_g}{RT}p\right) + \nabla\cdot\left[-\frac{M_g}{RT}\frac{k(p+b)}{\mu_g}\nabla p\right] = 0 \tag{11}$$

3.3. Cross coupling

Porosity and permeability, characterized as the key factor for coal and gas outburst, are sensitive to the stress state and material property. According to the previous work, the general porosity model can be expressed as [19].

$$\phi = \alpha - (\alpha - \phi_0)\exp\left\{-\left[(\varepsilon_v + \frac{p}{K_s} - \varepsilon_a) - \left(\varepsilon_{v0} + \frac{p_0}{K_s} - \varepsilon_{a0}\right)\right]\right\} \tag{12}$$

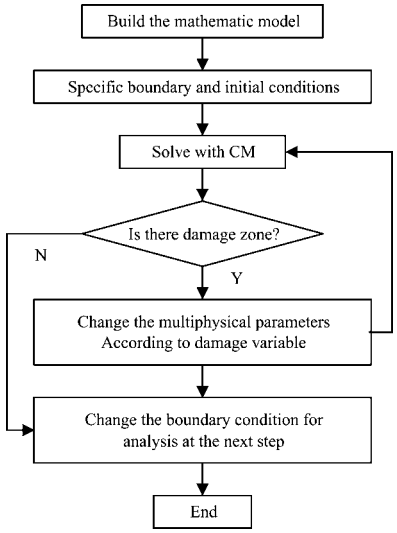

Fig. 6. Basic process for numerical simulation.

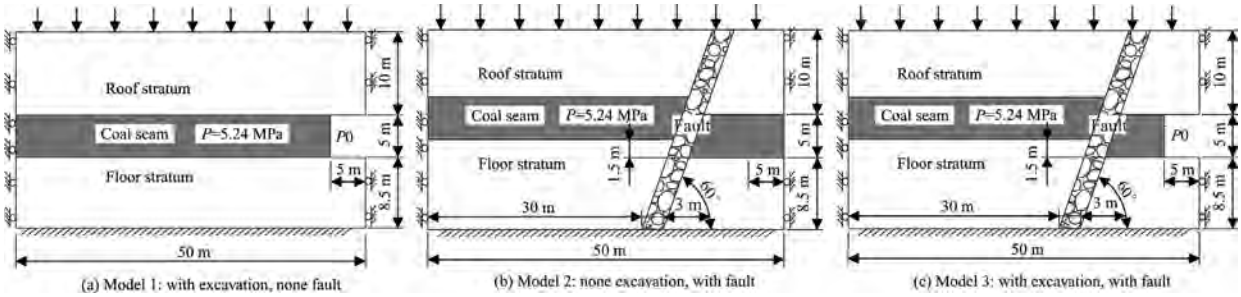

Fig. 7. Physical model for the numerical simulation.

Table 1
Related parameters used in the numerical simulation.

Variable	Parameter	Value
p_0	Initial gas pressure in coal seam	5.24 MPa
k_{m0}	Initial permeability in coal seam	2.8×10^{-15} m^2
k_{r0}	Initial permeability in floor and roof stratum	2.8×10^{-17} m^2
k_{f0}	Initial permeability in fault	2.8×10^{-14} m^2
E	Young's modulus of coal matrix	2713 MPa
E_s	Young's modulus of coal skeleton	8410 MPa
E_r	Young's modulus of floor and roof stratum	18,469 MPa
E_f	Young's modulus of fault	1552 MPa
ν_m	Poisson's ratio of coal	0.35
ν_r	Poisson's ratio of floor and roof stratum	0.27
ν_f	Poisson's ratio of fault	0.35
σ_{cm}	The compressive strength of coal seam	20.0 MPa
σ_{cr}	The compressive strength of floor and roof stratum	60.0 MPa
σ_{cf}	The compressive strength of fault	15.0 MPa
σ_{tm}	The tensile strength of coal seam	2.0 MPa
σ_{tr}	The tensile strength of floor and roof stratum	5.0 MPa
σ_{tf}	The tensile strength of fault	1.2 MPa
Φ_{m0}	Initial porosity of coal	0.05
Φ_{r0}	Initial porosity of floor and roof stratum	0.02
Φ_{f0}	Initial porosity of fault	0.12
μ_g	Gas dynamic viscosity	1.84×10^{-5} Pa·s
P_L	Langmuir pressure constant	3.03 MPa
V_L	Langmuir volume constant	0.036 m^3/kg
α_{sg}	Coefficient for sorption-induced volumetric strain	0.06 kg/m^3
b	Klinkenberg factor	0.76 MPa

where ε_v is the volumetric strain of coal-gas medium; and the subscript '0' the initial value.

The cubic law is used to express the relationship between permeability ratio and porosity ratio in coal seams.

$$\frac{k}{k_0} = \left(\frac{\phi}{\phi_0}\right)^3 \tag{13}$$

where k_0 is the initial permeability in the stress-free state, m^2.

Substituting Eqs. (12) into (13) yields Eq. (14).

$$k = k_0\left\{\frac{\alpha}{\phi_0} + \left(1 - \frac{\alpha}{\phi_0}\right)\exp\left[\left(\varepsilon_{v0} + \frac{p_0}{K_s} - \varepsilon_{a0}\right) - \left(\varepsilon_v + \frac{p}{K_s} - \varepsilon_a\right)\right]\right\}^3 \tag{14}$$

Combining Eqs. (1), (5), (7) and (11), the stress-seepage-damage coupling mathematical model can be achieved. These governing equations are nonlinear second-order partial differential equations (PDEs) in both the space and time domain, and are difficult to solve theoretically. We combine the MATLAB and the COMSOL Multiphysics to obtain numerical solution and achieve the evolution process of coal and gas outburst dynamic system [27]. The basic procedure is shown in Fig. 6.

4. Size scale of coal and gas outburst dynamical system

4.1. Simulation case and models

Panyi Coal Mine is located in Huainan area in Anhui province, China. The mine began to product coal in 1983 and the production is 3×10^6 tons per year. The trend longwall mining method is adopted in Panyi Coal Mine. The primary mineable coal seams are C_{13}, B_{11} and B_8. Among them B_{11} has no coal and gas outburst risk with an average thickness of 2 m, and C_{13} has coal and gas outburst risk with an average thickness of 5 m and has occurred gas outburst and explosion accidents many times. Gas pressure in C_{13} coal seam is 5.24 MPa, and the permeability is 2.8×10^{-15} m^2.

As shown in Fig. 7, three plane strain models were adopted to comparatively analyze the size scale of outburst dynamical system.

Model 1: the size is 50 m × 13.5 m, with thickness of floor strata 8.5 m, roof strata 10 m and coal seam 5 m. The burial depth of C_{13} coal seam is 500 m. The bottom boundary is fixed and a slip boundary was applied for other sides. The load from the weight of overlying strata with an average density of 2500 kg/m^3 is applied to the top boundary. All the external boundaries are insulated for gas transport. Coal seam excavates 5 m from right to left to simulate mining disturbance.

Model 2: the basic parameters are the same as model 1, however with none excavation. There is a small fault in this model with 1.5 m of fault throw, 3 m of shattered zone width and 60° arranges with coal seam.

Model 3: on the basis of model 2, coal seam is excavated 5 m from right to left, in order to simulate mining disturbance.

Other parameters used in the numerical simulations are listed in Table 1.

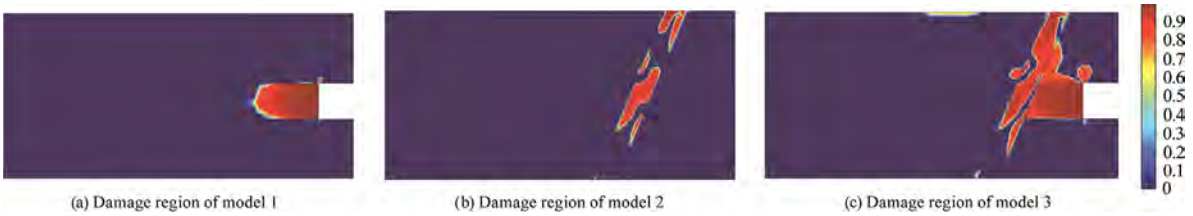

Fig. 8. Damage region of different models.

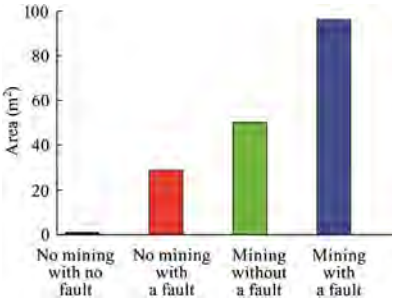

Fig. 9. Statistics of damage area under different geological environment and mining disturbance conditions.

4.2. Size scale of dynamical system

We define the damage region as the size scale of the dynamical system of coal and gas outbursts. Fig. 8 shows the damage region of different models. The damage region of model 1 is mainly distributed in the range of 8 m in front of advancing face in coal seam. There is a small amount of damage region in the roof and floor stratum near the advancing face. In model 2, the damage region is developed in the fault fracture zone, especially where close to the seam. There are both excavation and fault in front of the advancing face in model 3. Damage region is developed near the fault zone due to stress concentration and transfixion of damage region caused by excavation and the fault is occurred. The size of this region is larger than the sum of the size of model 1 and model 2, and reaches to 12 m in front of the advancing face.

The size of the damage region can be calculated via the integral function of COMSOL Multiphysics. In Fig. 9, damage area when there is a fault in front of the advancing face is the largest, about 96.26 m^2. The following is 50.17 m^2 when there is no fault in front of the advancing face. And the damage area is 29.11 m^2 when a fault exists without excavation.

Different combinations of geological environment and mining disturbance have different models of coal and gas outburst. In general, the damage region, risk and strength of coal and gas outburst will be larger if geologic structures occurred in front of the mining and advancing face. If we assume that roadway width is 4 m, the volume of coal and gas outburst dynamical system is about 385.04 m^3 on the case of there is a small fault in front of the advancing face, and is about 200.68 m^3 without a fault. It also explains that the strength of most outbursts is less than 500 tons of coal.

It should be noted that the damage region of model 2 is not the size scale of outburst dynamical system, because the dynamical system must be composed of three indispensable elements: coal-gas medium, geological environment and mining disturbance. The purpose of carrying on the simulation of model 2 is to facilitate comparative analysis. In addition, this article only simulated the fault among geological structures. In the following researches, we will take more factors, such as coal seam thickness variation, fold and mining intensity, into consideration to perfect this study.

5. Conclusions

(1) The coal and gas outburst dynamical system consists of three essential elements, coal-gas medium, geology dynamic environment and mining disturbance. Coal-gas medium is the material basis and requirement; geology dynamic environment can weaken the mechanical properties of coal-gas medium and also provide the internal motivation; mining disturbance is the external motivation, which provides the enough energy source and space condition.

(2) Coal and gas outburst is the catastrophe process with the stress-seepage-damage coupling effect in the dynamical system. A stress-seepage-damage coupling model is established which can be used to simulate the evolution of the dynamical system.

(3) The damage region is defined as the size scale of coal and gas outburst dynamical system. On the case of C_{13} coal seam in Panyi Mine, the dynamical system exists in the range of 8–12 m in front of advancing face. In general, the damage region, risk and strength of outburst will be larger if geologic structures occurred in front of the mining and advancing face.

Acknowledgments

The work was funded by the National Natural Science Foundation of China (No. 51674132), the State Key Research Development Program of China (No. 2016YFC0801407-2), the Open Projects of State Key Laboratory for GeoMechanics and Deep Underground Engineering of China (No. SKLGDUEK1510), the Open Projects of State Key Laboratory of Coal Resources and Safe Mining of China (No. SKLCRSM15KF04) and the Research Fund of State and Local Joint Engineering Laboratory for Gas Drainage & Ground Control of Deep Mines (Henan Polytechnic University) (No. G201602). These supports are gratefully acknowledged.

References

[1] Zhou AT, Wang K, Wu ZQ. Propagation law of shock waves and gas flow in cross roadway caused by coal and gas outburst. Int J Min Sci Technol 2014;24(1):23–9.
[2] Yu BH, Su CX, Wang DM. Study of the features of outburst caused by rock cross-cut coal uncovering and the law of gas dilatation energy release. Int J Min Sci Technol 2015;25(3):453–8.
[3] Yan JW, Zhang XB, Zhang ZM. Research on geological control mechanism of coal-gas outburst. J China Coal Soc 2013;38(07):1174–8.
[4] Zhang ZM, Zhang YG. Investigation into coal gas outburst occurred in Daping Coalmine by using theories of gas-geology. J China Coal Soc 2005;30(2):137–40.
[5] Yu QX. Mine gas prevention and control. Xuzhou: China University of Mining and Technology; 1992.
[6] Sobczyk J. The influence of sorption processes on gas stresses leading to the coal and gas outburst in the laboratory conditions. Fuel 2011;90(3):1018–23.
[7] Wang SG, Elsworth D, Liu JS. Permeability evolution during progressive deformation of intact coal and implications for instability in underground coal seams. Int J Rock Mech Min Sci 2013;58:34–45.
[8] Wang S, Elsworth D, Liu J. Rapid decompression and desorption induced energetic failure in coal. J Rock Mech Geotech Eng 2015;7(3):345–50.
[9] Xu T, Tang CA, Yang TH, Zhu WC, Liu J. Numerical investigation of coal and gas outbursts in underground collieries. Int J Rock Mech Min Sci 2006;43(6):905–19.
[10] An F, Cheng Y, Wang L, Li W. A numerical model for outburst including the effect of adsorbed gas on coal deformation and mechanical properties. Comput Geotech 2013;54:222–31.
[11] Xue S, Yuan L, Wang Y, Xie J. Numerical analyses of the major parameters affecting the initiation of outbursts of coal and gas. Rock Mech Rock Eng 2014;47(4):1505.
[12] Zhang HW, Li S. Pattern recognition and possibility prediction of coal and gas outburst. Chin J Rock Mech Eng 2005;24(19):3577–81.
[13] Li ZB, Zhao BT. Microseism monitoring system for coal and gas outburst. Int J Comput Sci Iss 2012;9:5.
[14] Aguado MBD, Nicieza CG. Control and prevention of gas outbursts in coal mines, Riosa-Olloniego coalfield, Spain. Int J Coal Geol 2007;69(4):253–66.
[15] Zhou H, Yang Q, Cheng Y, Ge C, Chen J. Gas drainage and utilization in coal mines with strong coal and gas outburst dangers: a case study in Luling mine, China. J Nat Gas Sci Eng 2014;20:357–65.
[16] Zhang XB, Yan JW. Physical conditions and process of gas outburst coal forming. J Saf Sci Technol 2014;10(11):48–53.
[17] Shao Q, Wang EY, Wang HW, Yin Qiuchao, Huo Guangsheng, Li Fengliang. Control to coal and gas outburst of tectonic coal distribution. J China Coal Soc 2010;35(2):250–4.
[18] Han J, Zhang HW, Zhang PT. Nappe structure's kinetic features and mechanisms of action to coal and gas outburst. J China Coal Soc 2012;37(02):247–52.
[19] Han J, Zhang HW, Zhu ZM, Song JC. Controlling of tectonic stress field evolution for coal and gas outburst in Fuxin basin. J China Coal Soc 2007;32(09):934–8.

[20] Han J, Zhang HW, Huo BJ. Discussion of coal and gas outburst mechanism of syncline. J China Coal Soc 2008;33(08):908–13.
[21] Pan YS. Integrated study on compound dynamic disaster of coal-gas outburst and rockburst. J China Coal Soc 2016;41(1):105–12.
[22] Zhu WC, Wei CH, Liu J, Qu HY, Elsworth D. A model of coal-gas interaction under variable temperatures. Int J Coal Geol 2011;86(2):213–21.
[23] Xia T, Zhou F, Gao F, Kang JH, Liu JS, Wang JG. Simulation of coal self-heating processes in underground methane-rich coal seams. Int J Coal Geol 2015;141:1–12.
[24] Li S, Fan C, Han J, Luo M, Yang Z, Bi H. A fully coupled thermal-hydraulic-mechanical model with two-phase flow for coalbed methane extraction. J Nat Gas Sci Eng 2016;33:324–36.
[25] Biot MA. General theory of three-dimensional consolidation. J Appl Phys 1941;12(2):155–64.
[26] Yang TH, Xu T, Liu JX, Tang ST, Tang CA, Yu QX, et al. Coupling model of stress-seepage-damage and its application to the investigation of instantaneous seepage mechanism for gas during unloading in coal seam with depth. Chin J Rock Mech Eng 2005;24(16):2900–5.
[27] Comsol AB. COMSOL multiphysics version 4.3: User's Guide and Reference Guide; 2012. <www.comsol.com>.

International Journal of Mining Science and Technology 27 (2017) 57–64

Contents lists available at ScienceDirect

International Journal of Mining Science and Technology

journal homepage: www.elsevier.com/locate/ijmst

Assessment of potential impacts to surface and subsurface water bodies due to longwall mining

Christopher Newman, Zacharias Agioutantis *, Gabriel Boede Jimenez Leon

Department of Mining Engineering, University of Kentucky, Lexington, KY 40506, USA

ARTICLE INFO

Article history:
Available online 29 December 2016

Keywords:
Streams
Aquifers
Ground strain
Coal mining

ABSTRACT

Ground movements due to longwall mining operations have the potential to damage the hydrological balance within as well as outside the mine permit area in the form of increased surface ponding and changes to hydrogeological properties. Recently, the Office of Surface Mining, Reclamation and Enforcement (OSMRE) in the USA, has completed a public comment period on a newly proposed rule for the protection of streams and groundwater from adverse impacts of surface and underground mining operations (80 FR 44435). With increased community and regulatory focus on mining operations and their potential to adversely affect streams and groundwater, now there is a greater need for better prediction of the possible effects mining has on both surface and subsurface bodies of water. With mining induced stress and strain within the overburden correlated to changes in the hydrogeological properties of rock and soil, this paper investigates the evaluation of the hydrogeological system within the vicinity of an underground mining operation based on strain values calculated through a surface deformation prediction model. Through accurate modeling of the pre- and post-mining hydrogeological system, industry personnel can better depict mining induced effects on surface and subsurface bodies of water aiding in the optimization of underground extraction sequences while maintaining the integrity of water resources.

1. Introduction

The utilization of high-recovery underground mining methods, such as longwall or high-extraction room-and-pillar operations, has the potential to cause adverse impacts to both surface and subsurface bodies of water as strata movement and deformations propagate from the mined seam through the overburden to the surface [1].

Previous research has indicated that mining induced strains are the most damaging to surface streams as well as greatly affecting the integrity of subsurface bodies of water and groundwater flow conditions [2,3]. On the surface, adverse effects to the stream can occur due to the development of either tensile or compressive strain in the stream bed. The development of tensile cracks along the bedrock allows for a potential loss of stream flow through developed fissures. The potential impact of longwall mining on the hydrogeological environment typically results in a drop in the groundwater table culminating in water loss to the surface by altering water flow paths [4]. In fact, water flow in the Cataract River of Australia ceased in 1994 as a result of mining-induced strains from longwall operations in the Bulli Seam 430 m below the river gorge [5]. On the other hand, the development of compressive strains within the rock layers can cause rupturing or buckling of the stream bed, blocking stream flow and/or diverting flow into the fractures at the base [6]. While these localized fractures can contribute to the loss of stream flows, given time, damaged streams have the ability to self-heal through the regeneration of near-surface aquifers as well as the sealing of mining-induced fractures with rock debris, gravel, sand, clay or other soil particles carried from upstream sources and deposited in the river bed [7].

Below the surface, mining-induced strains can initiate subsidence and fracturing of the strata, causing changes to the hydraulic conductivity and affecting flow paths within the overburden [8]. Recently, the Office of Surface Mining Reclamation and Enforcement (OSMRE) in the USA has completed the public comment period on a newly proposed rule for the protection of streams and groundwater from the adverse impacts of surface and underground mining operations (80 FR 44435). These proposed regulations call for an increase in baseline data collection, pre- and post-mining monitoring and mitigation/restoration practices, as well as increased focus on possible mining-induced damages to the hydro-

* Corresponding author.
E-mail address: zach.agioutantis@uky.edu (Z. Agioutantis).

http://dx.doi.org/10.1016/j.ijmst.2016.11.016
2095-2686/

geological balance within the mine permit area, which includes both surface and subsurface bodies of water. With an increase in environmental scrutiny from both local communities and regulatory agencies, this paper investigates the application of a numerical modeling approach for a more realistic evaluation of mining impacts to both surface and subsurface bodies of water.

Since the determination of the strain regime above an underground mine is integral to this investigation, the Surface Deformation Prediction Software (SDPS), a package developed at Virginia Tech, USA will be utilized to calculate mining-induced strains at different elevations above the seam as well as on the surface [9]. Surface strain calculations now include the effect of varying topography, while subsurface strain outputs from SDPS will be used to assess changes to the hydraulic conductivity of affected strata. An assessment of the post-mining hydrogeological system using a hypothetical case study will be presented through the application of MODFLOW, a groundwater modeling software package available through the United States Geologic Survey (USGS) [10].

This paper presents two conceptual case studies that demonstrate: (a) the effect of variable surface topography on ground strains in the vicinity of a linear surface body (e.g., a stream) and (b) the effect of horizontal strain magnitude in the overburden on the hydraulic conductivity of different formations potentially impacted by underground mining.

2. Background

2.1. Importance of strain in assessing potential impacts to the surface and subsurface

The influence function method, as implemented by SDPS, for the calculation of ground deformations is a mature methodology widely used by academic, industry and regulatory personnel [9]. Through the application of this Gaussian bell-shaped influence function in SDPS, one is able to calculate horizontal displacement as a linear function of the first derivative of subsidence and horizontal strain as the first derivative of horizontal displacement. Recent advances in the SDPS package allow for the calculation of directional strain and ground strain along a profile as well as ground strain for random prediction points by calculating the 3D distance between neighboring surface points [11,12]. The influence function formulation can accurately calculate deformations at any point in 3D space and, therefore, at any point on the surface and at any elevation between the seam and the surface. This is conceptually depicted in Fig. 1, where a typical horizontal strain distribution across a transverse profile line over a rectangular panels of 2 m extraction height at a depth of 150 m. Additionally, a horizontal strain curve is calculated within the overburden at depth equal to half the overburden height or 75 m. Although strain magnitudes increase as the distance from the extracted panel decreases, the inflection point of the strain curve remains above the rib.

These calculations can be easily utilized to determine potential surface impacts or used to derive other physical parameters for surface or groundwater modeling [13].

It should be emphasized, however, that further adjustments are necessary when these ground strain calculations or strain calculations within a given formation are applied to man-made structures in contact with the ground, such as buildings or pipelines [14].

2.2. Relating horizontal strain magnitudes to changes in hydraulic conductivity

While the majority of research has focused on mining-induced strain damages at the surface, strain magnitudes within the overburden can also cause detrimental impacts to the strata overlying a mined panel. Overburden strains discussed in this paper refer to the maximum horizontal strains developed within the geologic strata and, as already mentioned, can be calculated by SDPS at any point between the seam and the surface. Similar to the effects of increased strains at the surface, strains within the overburden can cause mining-induced fracturing of the overburden leading to the dewatering of both surface and subsurface bodies of water through the subsequent and large increase in hydraulic conductivity [15]. While academic and industry research acknowledges that changes to the hydraulic conductivity within the overburden material can alter the groundwater system, few studies have investigated the interaction between mining-induced strata deformations and the modifications to hydraulic conductivity [16–18].

In lieu of tedious and time-consuming groundwater monitoring regimes, groundwater flow models are often used to evaluate the impact of mining operations on the hydrogeological system through the prediction of groundwater flows and transportation processes. The three-dimensional finite-difference groundwater flow model, MODFLOW, provides users with a mathematical description of groundwater flows as well as surface-groundwater interaction through the application of Darcy's equation for fluid flow in porous material [10]. Distributed to users through the USGS web site, MODFLOW is widely used within the mining industry to simulate groundwater seepage into mine openings or shafts [19]. As with any numerical model, realistic model estimations are closely tied to input parameters; therefore, it is important that users have detailed information on site-specific geology, water quality, recharge, river locations, water levels, hydraulic parameters, etc., as well as a clear understanding of numerically embedded assumptions within the numerical modeling code such as boundary conditions, layer types, etc.

In order to accurately simulate groundwater flow paths, it is important that users can accurately quantify the hydraulic conductivity of the overburden strata material. Typically determined through borehole slug tests, hydraulic conductivity is the proportionality constant of Darcy's equations (K), which relates the amount of flow through a unit cross-sectional area (A) of an aquifer under a unit gradient of hydraulic head ($\Delta h/\Delta L$).

$$Q = KA\frac{\Delta h}{\Delta L} \tag{1}$$

In reviewing the literature, a wide range of pre- and post-mining hydraulic conductivities have been documented (as summarized in Table 1). These values have been determined through a series of in-situ borehole slug tests and/or back calculations from groundwater monitoring regimes. In reviewing the values presented in Table 1, all testing seems to indicate pre- and post-mining hydraulic conductivities within similar ranges. For shale materials in the overburden, the data suggests a pre-mining hydraulic conductivity in the order of 10^{-8} to 10^{-9} m/s with post-mining conductivities increasing by one or two orders of magnitude. For sandstone materials, the data suggests typical pre-mining hydraulic conductivity values ranging in the order of 10^{-4} to 10^{-5} m/s with post-mining conductivities again increasing by 10- or 100-fold. Limestone channels within the overburden material have pre-mining hydraulic conductivities ranging in the order of 10^{-8} to 10^{-10} m/s; post-mining hydraulic conductivity were not available.

While the majority of the literature reviewed points to the same range of pre- and post-mining hydraulic conductivity for overburden strata materials, the data published by Li et al. has significantly higher conductivities for all materials [21]. In further reviewing this publication, it is believed that the units may have been mislabeled (ft/day instead of m/s). Under this assumption, conductivity values collaborate well with the other published data. The change in hydraulic conductivity between pre- and post-mining activity is

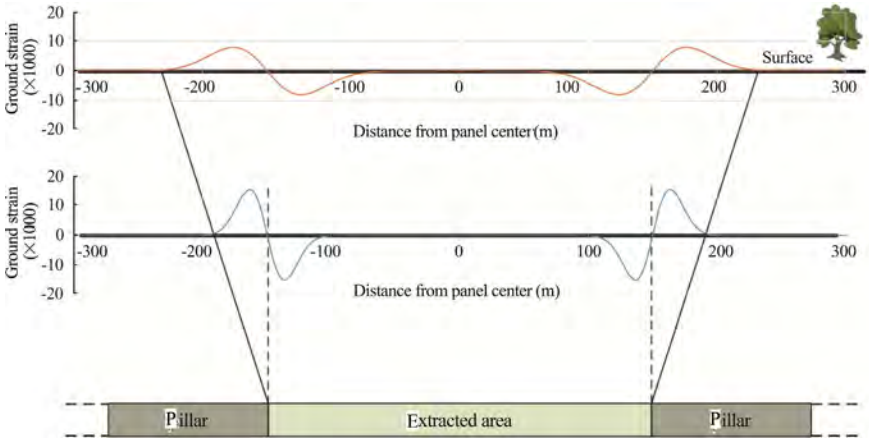

Fig. 1. Distribution of horizontal strains at and below the surface over an underground extraction area.

Table 1
Hydraulic conductivity values (m/s).

	Shale		Sandstone		Limestone	Coal seam		Aquifer	
	Pre-mining	Post-mining	Pre-mining	Post-mining	Pre-mining	Pre-mining	Post-mining	Post-mining	
Horizontal	7.01E−08 to 7.01E−09	7.01E−06 to 7.01E−08	7.01E−05	7.01E−03					Matetic et al. [20]
Vertical	7.01E−08 to 7.01E−09	7.01E−07 to 7.01E−08	7.01E−05	7.01E−04					Matetic et al. [20]
Horizontal	1.13E−07 to 9.53E−08	2.89E−05 to 3.53E−07	1.14E−06 to 4.23E−08	2.85E−05 to 3.42E−06	1.76E−09	1.76E−09			Li et al. [21]
Horizontal								1.65E−03 to 6.1E−06	Toran and Bradbury [22]
Vertical		6.1E−09 to 6.1E−11							Toran and Bradbury [22]
Horizontal							1.74E−06 to 3.47E−07		McCoy et al. [23]
Horizontal			1.0E−04 to 1.0E−05						Rapantova et al. [24]
Horizontal	8.89E−09 to 2.28E−09				1.09E−08 to 5.43E−10				Karacan and Goodman [8]

similar in magnitude change (10- to 100-fold), the data seems to suggest that there were previous impacts to the overlying strata causing such high pre-conductivity values.

According to the work of Ouyang and Elsworth, after determining the mining-induced strain field around a given panel, one can approximate the post-mining hydraulic conductivity of overburden material using the following equations [25]:

$$K_x = K_{xo} \times \left[1 + \frac{b + S(1 - R_m)}{b} \Delta\varepsilon_y\right]^3 \quad (2)$$

$$K_y = K_{yo} \times \left[1 + \frac{b + S(1 - R_m)}{b} \Delta\varepsilon_x\right]^3 \quad (3)$$

where K_x and K_y are the post-mining hydraulic conductivities in the horizontal and vertical directions determined as a function of the pre-mining conductivity in the horizontal and vertical directions (K_{xo} and K_{yo}), the fracture aperture (b) and spacing (S), a modulus reduction ratio (R_m), and the mining-induced strains in the horizontal ($\Delta\varepsilon_x$) and vertical ($\Delta\varepsilon_y$) directions.

Thus, using the predicted, calculated, and/or measured mining-induced strains within the overburden strata, one is able to approximate the post-mining hydraulic conductivity. Table 2 was generated using assumed values for the geometric parameters S (0.33 m), b (1 mm or 0.001 m) and R_m (0.8) of Eq. (3). Post-mining hydraulic conductivity increases as the strain magnitude increases by a factor of 1.2 for a strain value of 1 mm/m to a factor of 82.3 for a strain value of 50 mm/m.

Following the determination of changes in hydraulic conductivity with respect to mining-induced strains, the post-mining hydrogeological system may subsequently be defined through the application of a groundwater model [15].

A summary of the steps required are shown in the brief flowchart depicted in Fig. 2. Users can input mine and surface geometry and overburden parameters into the influence function method of the SDPS package and calculate strain at any point within the overburden with respect to the defined mine layout. Taking the horizontal strain outputs from SDPS and averaging them over specific regions, one can then estimate the post-mining hydraulic conductivity with respect to Eq. (3). Finally, by implementing the post-mining hydraulic conductivity values as input parameters to a hydrogeological model, one can effectively approximate the changes in groundwater flow with respect to mining-induced strains in the overburden.

2.3. Conceptual case studies

2.3.1. Case study 1: the effect of variable topography on ground strains in the vicinity of a linear water body

To highlight the differences in the horizontal and ground strain calculations, the following case study was developed in SDPS to evaluate strain magnitudes with respect to stream location, stream orientation, and topographic relief. For each scenario presented in

Table 2
Approximation of vertical post-mining hydraulic conductivity with respect to mining-induced horizontal strain based on the formulation by Ouyang and Elsworth [25].

ε_x	S	b (m)	R_m	K_{yo}		K_y		K_y/K_{yo}
				(m/s)	(m/day)	(m/s)	(m/day)	
0.001	0.33	0.001	0.8	5.00E−08	4.32E−03	6.07E−08	5.25E−03	1.2
0.010	0.33	0.001	0.8	5.00E−08	4.32E−03	2.33E−07	2.01E−02	4.7
0.020	0.33	0.001	0.8	5.00E−08	4.32E−03	6.41E−07	5.54E−02	12.8
0.050	0.33	0.001	0.8	5.00E−08	4.32E−03	4.12E−06	3.56E−01	82.3

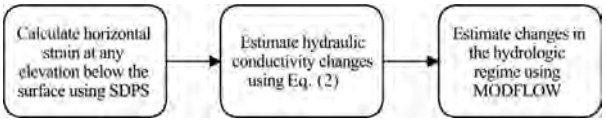

Fig. 2. Flow chart for the approximation of groundwater flow with respect to mining-induced strains in the overburden material.

case study 1 a stream was defined within the vicinity of or overlying a longwall panel at a depth of 150 m, extraction thickness of 2 m, supercritical subsidence factor of 50%, and an edge effect of 0 m. Default parameters were assigned by the SDPS program for defining the ground response. A discussion regarding the difference between horizontal and ground strains is available in Agioutantis and Karmis and also in Agioutantis et al. [11,13]. Positive horizontal or ground strain values correspond to tension, while negative strain values correspond to compression.

In Scenario 1a, horizontal and ground strains were calculated along a transverse line (stream) which bisects the longwall across the full extent of the subsidence trough without any subsidence influence from either end of the panel. Prediction points were defined along a transverse line as shown in Fig. 3. From the results of Scenario 1a, one finds similar horizontal strain (Em) and ground strain (EGA) profiles with the ground strain calculation having slightly lower magnitudes for the peak compressive and tensile strains. These differences in the strain profiles are attributed to the integration of the total displacement from pre- and post-mining surface elevations.

In Scenario 1b horizontal and ground strains were determined along a stream which again, was defined such that it bisects the longwall panel across the full extent of the subsidence trough. Prediction points for Scenario 1b were defined such that the stream dips at a 5° angle from west to east (Fig. 4). Given the sloping terrain, there is an overall strain increase on the downhill side of the stream and an overall strain decrease on the uphill side. As previously stated in Scenario 1a, differences in the strain profiles are due

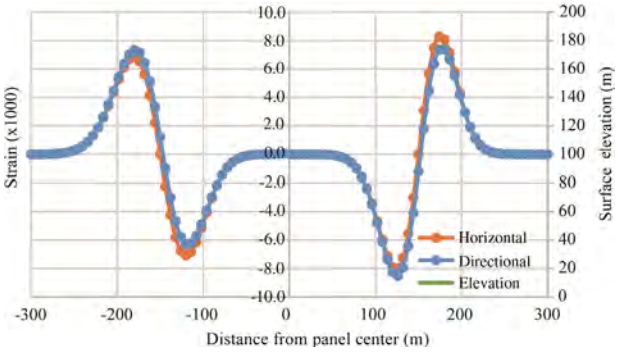

Fig. 4. Case 1 Scenario 1b–transverse profile, surface sloped at 5 degrees.

to the incorporation of the pre- and post-mining surface elevations. From these results, one finds that the ground strain calculation provides lower strains in the tensile downhill region and compressive uphill regions of the subsidence trough in comparison to the horizontal strain calculation.

In Scenarios 1c and 1d horizontal and ground strains were determined along a stream, which crosses the full extent of the subsidence trough at a 45° angle (Fig. 5). The prediction points for Scenario 1c were defined along a flat lying horizontal plane. From the results of Scenario 1c, one finds that the maximum horizontal strain magnitude is much larger than that determined by the ground strain calculation. By evaluating strain magnitudes with respect to the change in pre- and post-mining surface elevations as well as the directional strain vectors between consecutive points along the stream path, the ground strain calculation provides a more accurate depiction of the strain developed along the defined stream bed.

In Scenario 1d prediction points were redefined such that the stream dips at a 5° angle from west to east crossing the subsidence trough at a 45° angle (Fig. 6). From the results of Scenario 1d one

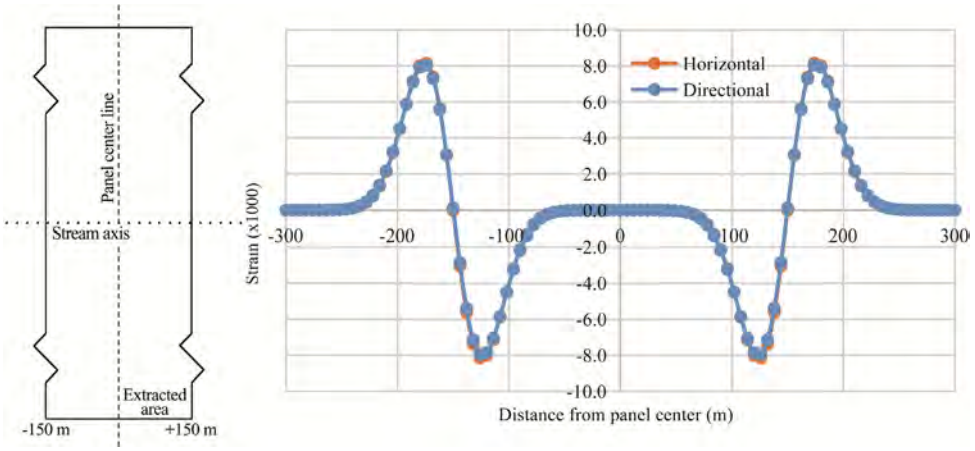

Fig. 3. Case 1 Scenario 1a–transverse profile, flat lying stream.

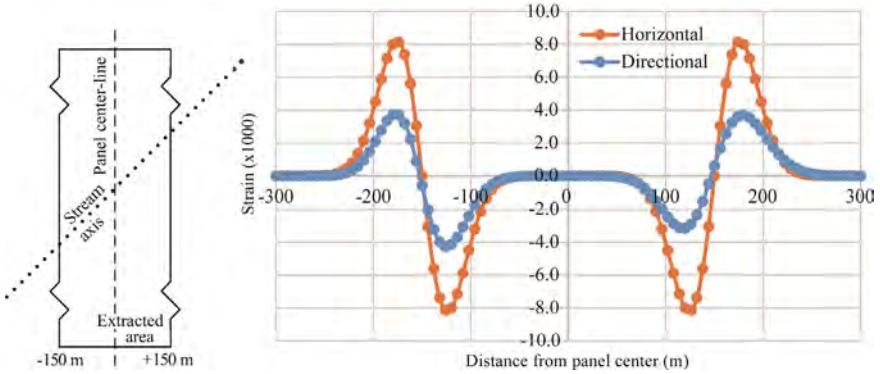

Fig. 5. Case 1 Scenario 1c–angled profile, flat lying stream.

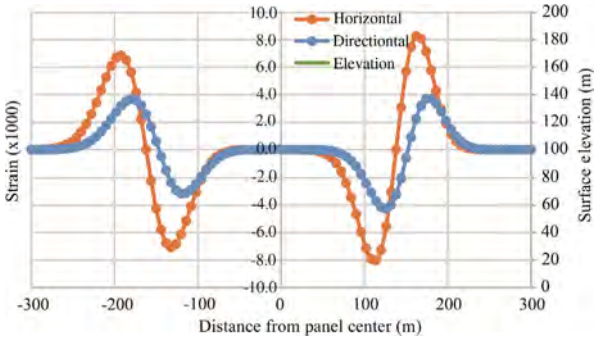

Fig. 6. Case 1 Scenario 1d–angled profile, surface sloped at 5 degrees.

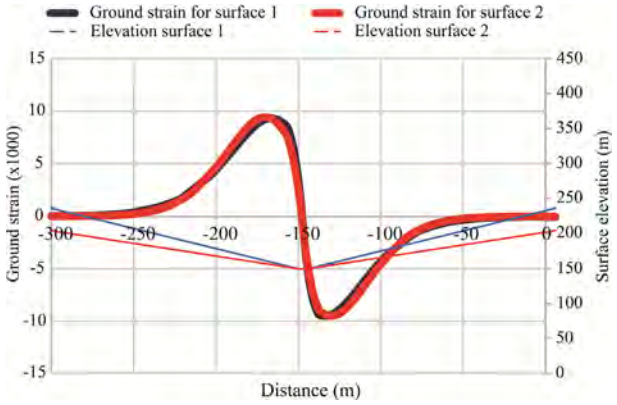

Fig. 8. Ground strain profiles on a transverse line above a longwall panel with respect to varying topography.

finds, through the incorporation of changes to the pre- and post-mining surface elevations and directional strain values, that the ground strain calculation determines strain magnitudes which are significantly less than that of the horizontal strain magnitudes in the maximum compression and tensile zones providing a more realistic evaluation of the strain developments along the stream bed.

Scenario 1e through Scenario 1k further investigate the effect of varying topography over and in the vicinity of the high extraction area. The geometry of the extracted longwall panel and the transverse prediction line are shown in Fig. 7a. The elevation profile presented in Fig. 7b simulates a stream flowing at the bottom of a valley along the longitudinal axis of a longwall panel. Starting from the west side of the panel, elevations gradually decrease to a minimum point that represents the stream bed and then increase again towards the eastern side of the panel.

Fig. 8 shows the distribution of strain along the transverse profile shown in Fig. 7b. Positive horizontal or ground strain values correspond to tension, and negative strain corresponds to compression. Two ground strain profiles are plotted: one corresponds to a surface inclination of 20°, and the other to a surface inclination of 30°. Ground strain magnitudes are comparable for both profiles.

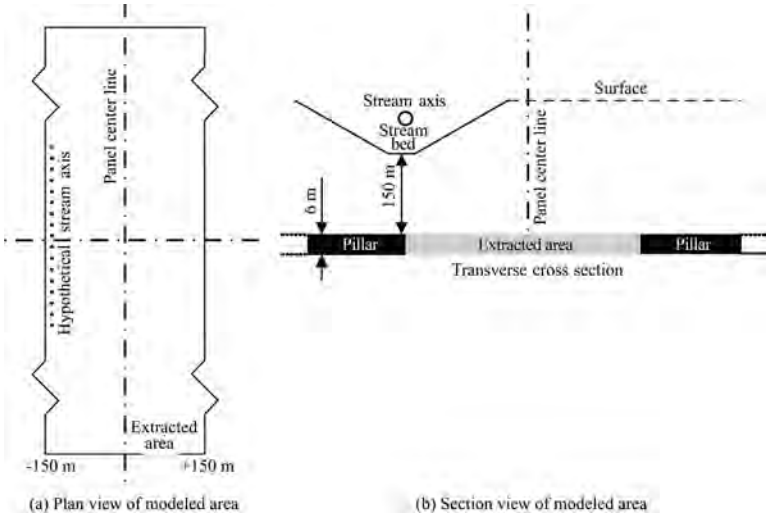

Fig. 7. Case 1 Scenario 1e–1k geometry and location information.

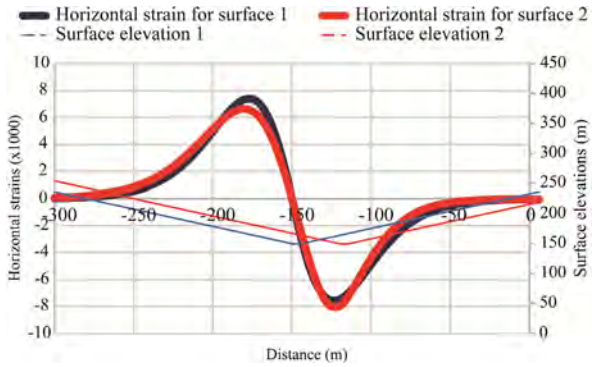

Fig. 9. Horizontal strain profiles on a transverse line above a longwall panel.

The zero strain point has slightly moved inby due to the ground strain adjustment.

As shown in Fig. 8, surface 1 corresponds to 30° and Surface 2 to 20°.

Fig. 9 presents the distribution of horizontal strain along two similar transverse profiles that differ only with respect to the horizontal location of the minimum elevation area. Strain magnitudes are again similar, and the slight differences can be attributed to the elevation differences between the two curves.

As noted in Fig. 9, surfaces 1 and 2 are both sloping 30° to the horizontal, but with a different location of the minimum elevation.

Fig. 10 shows the distribution of ground strain along three transverse profiles; the difference between the profiles is the location of the stream bed with respect to the rib of the extracted area. The inflection point of the ground strain curve is displaced with respect to the rib, depending on the surface curve. Ground strain magnitudes are similar although the shape of the peak tensile regime and peak compressive regime may differ.

As is evident in Fig. 10, the stream bed in surface 1 is close to the rib, the stream bed in surface 2 is inby and in surface 3 it is outby.

Results presented above show that the maximum ground strains expected on a stream bed can be mitigated as a function of the relative location of the stream axis to the rib of the excavation.

2.3.2. Case study 2: the effect of horizontal strain on groundwater flow

To evaluate the effect of mining-induced strains on the hydrogeological system, a conceptual model containing a subsurface aquifer overlying an active longwall panel was developed using MODFLOW. With an excavation height of 2 m, the caving zone, as defined by Peng and Chiang, extends up to 20 m (up to 10 times the seam thickness) from the coal seam into the overburden strata

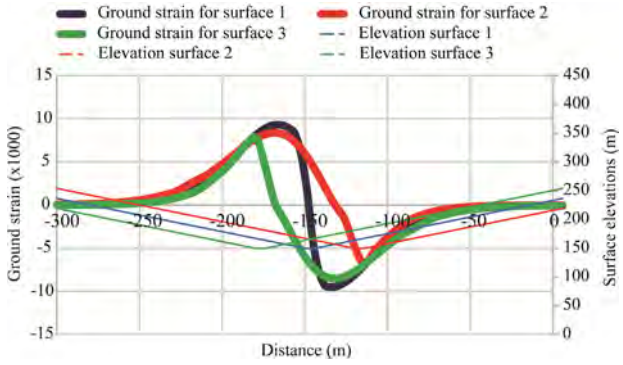

Fig. 10. Ground strain profiles on a transverse line above a longwall panel with respect to varying stream bed locations.

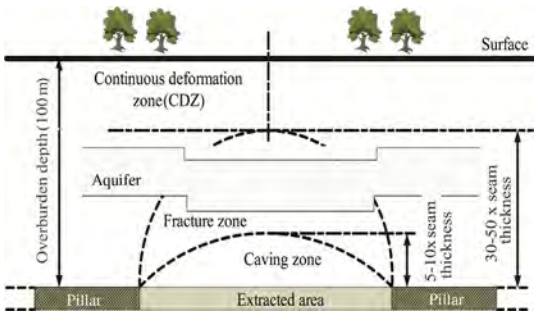

Fig. 11. Aquifer location with respect to the fracture and caving zones [26].

[26]. As shown in Fig. 11, the subsurface aquifer is therefore located in the fractured zone (30–50 times the seam thickness). In order to evaluate the effect of mining-induced strains on groundwater flow conditions, pre- and post-mining groundwater models were developed simulating water flows through a simplistic three-dimensional block 1380 m wide (138 elements), 2000 m long (200 elements) and 100 m deep. Each model was developed such that it simulates water flow over a year, given 12 (time) stress periods each spanning 30 days.

Each model is comprised of four layers (Fig. 12) corresponding to four stratified geological formations. Their respective geometric as well as pre- and post-mining hydraulic properties are given in Table 3. Layer 1 was defined as an unconfined shale formation 40 m thick with a hydraulic conductivity of 0.0864 m/day (1.00E−06 m/s) in both the horizontal and vertical directions as interpreted from the literature. Layer 2 was defined as an unconfined aquifer (sandstone) with variable transmissivity layer type that is 20 m thick with a pre-mining vertical and horizontal hydraulic conductivity of 8.64 m/day (1.00E−04 m/s) and a post-mining vertical and horizontal conductivity of 86.4 m/day (1.00E−03 m/s) correlating to a strain value of 0.01723. Since Layer 2 represents an unconfined water-bearing sandstone aquifer, an initial head of 60 m was defined for Layer 2 while Layers 1, 3, and 4 of the model were defined with initial heads of zero.

Layer 3 was defined as a confined shale formation 40 m thick with a pre-mining vertical and horizontal conductivity of 0.0866 m/day (1.00E−06 m/s) and a post-mining vertical and horizontal conductivity of 0.864 m/day (1.00E−05 m/s), correlating to a strain value of 0.01723. Layer 4 was defined as a confined coal seam which is 2 m thick with a pre-mining vertical and horizontal conductivity of 0.864 m/day (1.00E−05 m/s) and a post-mining vertical and horizontal conductivity of 8.64 m/day (1.00E−04 m/s).

As MODFLOW operates with differences in head and/or elevation, an arbitrary datum of zero elevation was assumed to lie at the top of Layer 4 such that the cumulative thickness of layers 1–3 represents the overburden depth over the coal seam. All layers within this model were defined with default values for specific storage (0.0001 m^{-1}) and specific yield (0.25). Post-mining hydraulic conductivities were defined in the areas of mining disturbance, and their magnitude was estimated based on horizontal strains

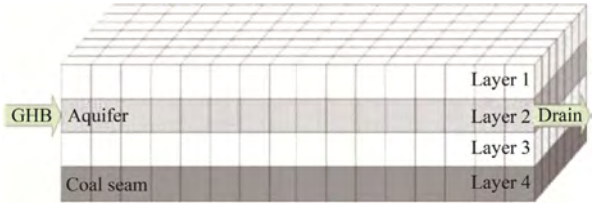

Fig. 12. Pre-mining groundwater model (not to scale).

Table 3
MODFLOW input parameters and change in mining-induced horizontal strain.

Layer	Thickness (m)	Hydraulic head (m)	Pre-mining hydraulic conductivity		Change in Horizontal strain	Post-mining hydraulic conductivity		Change ratio in hydraulic conductivity	Comment
			(m/s)	(m/day)		(m/s)	(m/day)		
Layer 1	40	0	1.00E−06	0.0864	0	1.00E−06	0.0864	1	Overburden assumed impermeable
Layer 2	20	60	1.00E−04	8.6400	0.0172	1.00E−03	86.4000	10	Aquifer assumed unconfined
Layer 3	40	0	1.00E−06	0.0864	0.0172	1.00E−05	0.8640	10	Overburden assumed impermeable
Layer 4	2	0	1.00E−05	0.8640	0.0172	1.00E−04	8.6400	10	Coal seam

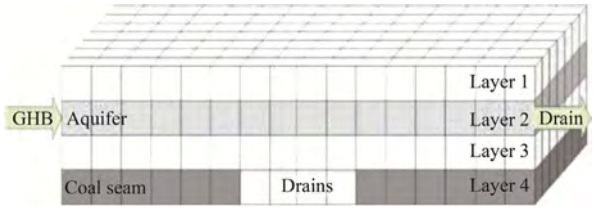

Fig. 13. Post-mining groundwater model (not to scale).

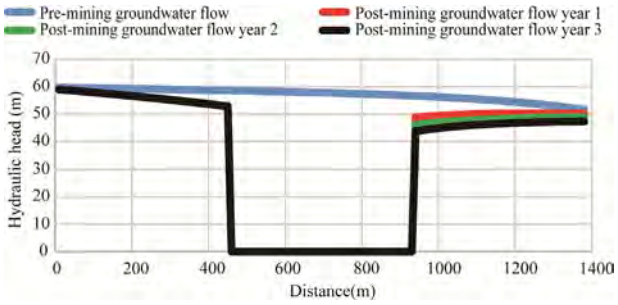

Fig. 14. Effect of mining on groundwater flow through an aquifer.

determined by the influence function method of the SDPS package (Table 3). Recharge of the groundwater system due to precipitation was not considered in this model, nor was the removal of water from the system with respect to plant transpiration or evaporation.

As shown in Figs. 12 and 13, two boundary conditions were applied to the sandstone aquifer (Layer 2) for both pre- and post-mining groundwater models. A general head boundary with a conductance of 34.25 m^2/day (3.96E−04 m^2/s) was defined on the eastern edge of the aquifer, while a drain with a conductance of 34.25 m^2/day (3.96E−04 m^2/s) was defined along the western boundary of the aquifer. In defining these boundary conditions, water flow through the aquifer can be simulated by the model. In order to simulate the post-mining flow of groundwater into the mine with respect to the excavation of coal by the longwall, drains with a conductance of 0.5 m^2/day (6.00E−06 m^2/s) were defined for element 46–92 in Layer 4, as shown in Fig. 13.

3. Results and discussion

Comparing the MODFLOW results of the pre- and post-mining head of the aquifer for this hypothetical case study, one is able to evaluate the impact of mining-induced strains on groundwater conditions. Before mining occurs, the water level within the aquifer gradually decreases from an initial head of 60 m to a head of 51 m across the simulated area, as represented by the blue line shown in the cross-section presented in Fig. 14. Note that unconfined aquifers may show either a head decrease or a constant head along a specific length.

These results are then compared to that of the post-mining water levels within the aquifer. In these cases, groundwater flow simulations start after all mining has been completed, while pumping (water loss) at mine level continues. Here, one finds that the increase in hydraulic conductivity with respect to mining-induced strains in the overburden results in the dewatering of the aquifer in the area directly overlaying the mined-out panel. The simulation is performed for periods of one, two, and three years for a constant water removal rate.

As shown in Fig. 14, for all simulated time periods, the hydraulic head within the aquifer gradually decreases as it approaches the longwall panel. In the overburden area directly above the longwall panel, water within the aquifer is lost to the lower geologic layers due to the mining-induced increase in hydraulic conductivity for years one, two, and three. Similar results were found by Guo et al., while monitoring the water levels of piezometers located above a longwall district in the Pittsbugh #8 coal seam [27]. From the data collected from monitored piezometers located over the mined area the authors found that the water levels decreased to immeasurable levels indicating a dry well. The water levels of piezometers outside the zone of mining induced overburden impacts mined area remained relatively constant during the entirety of the mining process encountering only slight water loss before recharging to its pre-mining water level [27].

On the eastern side of the modeled longwall panel, in the area of non-impacted overburden material, the hydraulic head gradually decreases from the eastern boundary to the eastern edge of the gob panel as groundwater flows into the mine workings. As simulation time increases to years two and three, the water level at the eastern side tends to decrease as pumping continues and there is no recharge applied to the model. These graphs are indicative of aquifer behavior since simulation results depend on model assumptions regarding formation permeability and storativity, as well water input and outputs. Furthermore, once mining operations cease and aquifer water is not removed from the system, simulations show that the aquifer will recover to its original levels. In addition, Guo et al. observed that the piezometer outside the affected overburden area not only stabilized to its pre-mining water level, but over the course of two years water levels were observed to be higher than the pre-mining levels [27]. This is similar to observed downstream waters level recovery in surface streams [28]. Mining-induced surface cracks can potentially drain streams in areas above underground longwall panels. The water is diverted through these cracks into subsurface aquifers. Given time, these aquifers will become full and force water back to the surface downstream from where the original water loss occurred.

4. Summary and conclusions

Increases in environmental scrutiny from community and regulatory agencies have created significant obstacles for mining companies to obtain mining and reclamation permits [16]. Currently, the Office of Surface Mining Reclamation and Enforcement (OSMRE) is looking to impose new regulations in 2016 for the pro-

tection of streams and groundwater from adverse impacts of surface and underground mining operations (80 FR 44435), which could possibly sterilize large amounts of coal reserves.

This paper examines the implementation of a general methodology for operations personnel to evaluate mining-induced impacts on surface and subsurface bodies of water. Through the utilization of the influence function formulation in SDPS, one is able to predict mining-induced ground deformations at any point in the three-dimensional space and, therefore, at any point along the surface topography or at any elevation within the overburden strata.

A hypothetical case study simulating a stream in a hill/valley system is utilized for calculating the distribution of ground strain along linear surface water bodies under simple geometrical considerations. Calculations indicate that the maximum ground strains expected on a stream bed can be mitigated as a function of the relative location of the stream axis to the rib of the excavation as well as the orientation of the stream with respect to the longwall panel. More work needs to be done for quantifying the effect of stream orientation, overburden topography to panel orientation and edge effect offset.

A second hypothetical case study was investigated where subsurface strain outputs from SDPS were used in the assessment of mining-induced changes to the hydraulic conductivity of the overburden strata and, therefore, changes to the hydrogeological system above a high-extraction area. Results show that in overburden areas disturbed by underground mining operations, groundwater levels at an aquifer will gradually decrease while water is removed from the underground working through pumping or other means. When water outflows at mine level cease then the aquifer present in the overburden will rebound. These results were further compared to the field work of Guo et al., which indicated the similar outcomes to those obtained by the MODFLOW model [27]. While the results of the model presented in this paper point to a promising methodology for the evaluation of mining-induced impacts on subsurface bodies of water, further research is needed for validating hydraulic conductivity changes and water head distribution above high-extraction areas.

Acknowledgments

This study was sponsored by the Appalachian Research Initiative for Environmental Science (ARIES). The views, opinions and recommendations expressed in this paper are solely those of the authors and do not imply any endorsement by ARIES employees or other ARIES-affiliated researchers. The authors would also like to thank the reviewers of this paper for their diligence in technically reviewing this work.

References

[1] Peng SS. Coal mine ground control. 3rd ed. Morgantown, West Virginia: West Virginia University; 2008.
[2] Singh MM. Mine subsidence, section 10.6. SME mining engineering handbook. Colorado: Littleton: SME; 1992.
[3] Booth CJ. Strata-movement concepts and the hydrogeological impact of underground coal mining. Ground Water 1986;24(4):507–15.
[4] Bian ZF, Inyang HI, Daniels JL, Frank OT, Struthers S. Environmental issues from coal mining and their solutions. Mining Sci Technol 2009;20(2):215–23.
[5] McNally G, Evans R. Impacts of longwall mining on surface water and ground water, southern coalfield NSW. Australia: NSW Department of Environment and Climate Change. Water Cooperative Research Center; 2007.
[6] Iannacchione A, Tonsor S, Witkowski M, Benner J, Hale A, Shendge M. The effects of subsidence resulting from underground bituminous coal mining on surface structures and features and on water resources: 3rd ACT 54 five-year report. University of Pittsburg; 2010.
[7] Waddington AA, Kay DR. Research into the impacts of mine subsidence on the strata and hydrology of river valleys and development of management guidelines for undermining cliffs, gorges, and river systems–stage 2. Brisbane, Australia: Australian Coal Association Research Program (ACARP). ACARP Research Report Project C9067; 2002.
[8] Karacan CÖ, Goodman G. Hydraulic conductivity changes and influencing factors in longwall overburden determined by slug tests in gob gas ventholes. Int J Rock Mech Min Sci 2009;46(7):1162–74.
[9] Karmis M, Agioutantis Z, Andrews K. Enhancing mine subsidence prediction and control methodologies. In: Proceedings, 27th international conference on ground control in mining, Morgantown, West Virginia. p. 131–6.
[10] McDonald MG, Harbaugh AW. A modular three-dimensional finite-differences groundwater flow model. In: Techniques of water-resources investigations. Reston, Virginia: US Geological Survey; 1988.
[11] Agioutantis Z, Newman C, Böde Jimenez Leon G, Karmis M. Minimizing impacts on streams due to underground mining by predicting surface ground movements. Min Eng 2016;68(3):28–37.
[12] Agioutantis Z, Karmis M, Kirby L. Application of subsidence prediction methodologies for sizing barrier pillars for stream protection in Appalachia. In: Craynon JR, editor. Proceedings, symposium on environmental considerations in energy production. Charleston, West Virginia: SME; 2013. p. 319–35.
[13] Agioutantis Z, Karmis M. Recent developments on surface ground strain calculations due to underground mining in Appalachia. In: Proceedings, 32nd international conference on ground control in mining, Morgantown, West Virginia. p. 214–9.
[14] Deck O, Harlaka A. Study of soil-structure interaction phenomena within mining subsidence areas, post-mining 2008, February 6–8, Nancy, France.
[15] Liu J, Elsworth D, Matetic RJ. Evaluation of the post-mining groundwater regime following longwall mining. Hydrol Process 1997;11(15):1945–61.
[16] Booth CJ. Groundwater as an environmental constraint of longwall coal mining. Mater Geoenviron 2006;50(1):49–52.
[17] Hawkins J, Smoyer JJ. Hydrologic impacts of multiple-seam underground and surface mining: a northern Appalachia example. Mine Water Environ 2011;30(4):263–73.
[18] Karacan CÖ. Prediction of porosity and permeability of caved zone in longwall gobs. Transp Porous Media 2010;82(2):13–439.
[19] Zaidel J, Markham B, Bleiker D. Simulating seepage into mine shafts and tunnels with MODFLOW. Ground Water 2010;48(3):390–400.
[20] Matetic RJ, Liu J, Elsworth D. Modeling the effects of longwall mining on the ground water system. USBM RI 9561. Bureau of Mines, Pittsburgh, Pa; 1995.
[21] Li Y, Peng SS, Zhang J. Impact of longwall mining on groundwater above the longwall panel in shallow coal seams. J Rock Mech Geotech Eng 2015;7(3):298–305.
[22] Toran L, Bradbury KR. Groundwater flow model of drawdown and recovery near an underground mine. Ground Water 1988;26(6):724–33.
[23] McCoy KJ, Donovan JJ, Leavitt BR. Estimation of hydraulic conductivity of coal mine barriers, Pittsburgh coal, Northern West Virginia, 1992-2000. In: Proceedings, 25th West Virginia surface mine drainage task force, Lexington, Kentucky. p. 1218–26.
[24] Rapantova N, Grmela A, Vojtek D, Halir J, Michalek B. Ground water flow modeling applications in mining hydrogeology. Mine Water Environ 2007;26(4):264–70.
[25] Ouyang Z, Elsworth D. Evaluation of groundwater flow into mined panels. Int J Rock Mech Min Sci 1993;30(2):71–9.
[26] Peng SS, Chiang HS. Longwall mining. New York: Wiley; 1984.
[27] Guo WB, Zou YF, Hou QL. Fractured zone height of longwall mining and its effects on the overburden aquifers. Int J Mining Sci Technol 2012;22(5):603–6.
[28] Tieman G, Rauch H. Study of dewatering effects at a longwall mine in northern West Virginia. In: 3rd Workshop on surface subsidence due to underground mining, West Virginia: Morgantown.

International Journal of Mining Science and Technology 27 (2017) 65–69

Contents lists available at ScienceDirect

International Journal of Mining Science and Technology

journal homepage: www.elsevier.com/locate/ijmst

Ground control monitoring of retreat room–and–pillar mine in Central Appalachia

Erik C. Westman *, Ryan J. Molka, William J. Conrad

Mining and Minerals Engineering Department, Virginia Tech, Blacksburg, VA 24061, USA

ARTICLE INFO

Article history:
Received 15 May 2016
Received in revised form 18 August 2016
Accepted 28 September 2016
Available online 9 December 2016

Keywords:
Retreat mining
Stress measurement
Microseismic monitoring
Pillar stability

ABSTRACT

In order to study pillar and overburden response to retreat mining, a ground control program was conducted at a Central Appalachian Mine. The program consisted of several monitoring methods including a seismic monitoring system, borehole pressure cells in the pillars, and time-lapse photogrammetry of the pillar ribs. Two parallel geophone arrays were installed, one on each side of the panel with the sensors mounted 3 m into the roof. A total of fourteen geophones recorded more than 5000 events during the panel retreat. A MIDAS datalogger was used to record pressure from borehole pressure cells (BPCs) located in two adjacent pillars that were not mined during retreat. A series of photographs were taken of the pillars that had the BPCs as the face approached so that deformation of the entire rib could be monitored using photogrammetry. Results showed that pillar stability and cave development were as expected. The BPCs showed an increase in loading when the face was 115 m inby and a clear onset of the forward abutment at 30 m. The photogrammetry results displayed pillar deformation corresponding to the increased loading. The microseismic monitoring results showed the overburden caving inby the face, again as expected. The significance of these results lies in two points, (1) we can quantify the safe manner in which this mine is conducting retreating operations, and (2) we can use volumetric technologies (photogrammetry and microseismic) to monitor entire volumes of the mine in addition to the traditional point-location geotechnical measurements (BPCs).

1. Introduction and background

Excavation of underground openings is a difficult job in a challenging environment. The rigor of the process is compounded by the lack of a method that allows quantification of changes within the rock mass as excavation progresses. Statistics kept by the Department of Labor, Mine Safety and Health Administration show that 16% of fatalities and lost time incidents in the underground mining industry are due to unexpected rock mass failure [1]. A recent example is the Crandall Canyon, Utah, coal mine accident caused by the vertical collapse of a longwall coal mine on August 6, 2007 [2].

Point-location measurements of deformation and change in stress form the basis for understanding ground control. There are several recent examples of the use of point-location geotechnical measurements in underground coal mines. Oyler et al. provided an excellent description of several case studies of point-location geotechnical measurements including vibrating wire stress cells used to show stress change in longwall panels and abutment pillars as the face retreated and extensometers reporting roof deformation [3]. Another example documents closure meters and borehole pressure cells being used to monitor load and deformation associated with pre-driven recovery rooms at a longwall mine [4]. Finally, the ground and tailgate support interaction was quantified at two longwall mines using instrumented tailgate supports so that numerical models could be calibrated. These numerical models provided the means for calculating the ground reaction curve [5].

Laser scanning of underground openings can provide relative measurements of convergence over much of an underground mine. This method has become more commonly used in the past decade. Huber and Vandapel reported on a demonstration of scanning an underground coal mine for mapping accuracy [6]. The information can be used to increase the accuracy of maps for active or abandoned mines. Building on this, an autonomous mobile robot has been developed to provide a 3D volumetric map of underground mines [7]. Finally, convergence measurements in an underground potash mine have also been mapped with laser scanning [8,9].

* Corresponding author. Tel.: +1 540 2317510.
E-mail address: ewestman@vt.edu (E.C. Westman).

http://dx.doi.org/10.1016/j.ijmst.2016.11.008
2095-2686/

One of the great challenges in the field of rock mechanics is imaging and understanding stress redistribution resulting from human activity. Seismic monitoring can be used to track changing conditions within a rock mass by monitoring the occurrence of mining-induced fracturing near the face. As the earth is perturbed by the excavation process, stress redistribution results in failure along new and/or previously existing faults or joints. The seismic energy produced by these relatively small failures is termed "induced seismicity" and typically has a local magnitude (M) between −3 and 2 [10].

An integrated suite of monitoring methods at a retreat room-and-pillar mine under 300 m of cover showed that pillar stability and cave development were progressing safely. Also, new methods offer additional insight into ground control conditions.

2. Methods and procedures

Ground monitoring instrumentation was installed in a retreat room-and-pillar mine in Central Appalachia. Cover depth above the monitored panel varied from 200 m to more than 300 m as shown in Fig. 1. Additionally, the immediate roof varied from a shale to a sandy shale with two sandstone channels in the panel. There were seven entries in the panel, and the row of pillars nearest to the subsequent panel was left unmined. When retreating, a slabbing cut is taken from the barrier pillar that separates the current panel from the previously mined panel. The panel was the fourth panel in its section to be mined, so there were three previously mined panels on one side of the monitored panel but no mining or development on the other side. The panel was retreated over a two-month period at a typical rate of one row per every day of production.

As noted in Fig. 1, solid line is 300 m cover depth contour and dashed line is 200 m cover contour and tan areas are location of sandstone channels.

The instrumentation installed at the mine included borehole pressure cells in two adjacent pillars. Pressure cells were installed at the midpoint of each pillar. The cells were grouted in place and initially pressurized to 10.3 MPa. The pressure transducers were wired into a MIDAS data acquisition unit, which is MSHA-approved for use in return air [11]. The pressure readings were written to the memory card in the MIDAS unit every two hours, and all data were downloaded via wireless transmission every two weeks.

The photogrammetry procedure was straightforward. A pillar was photographed using a Sony CyberShot camera when the face was 12 rows inby and then again when the face was 3 rows inby the pillar of interest. The process included starting at the stopping in one crosscut, moving along the entry around the pillar, and finishing at the stopping in the opposite crosscut. A straight-line method was used to photograph the pillar, in which photos were taken at regular intervals with the camera directed orthogonal to the pillar. The interval distance should allow for each photo to overlap the previous photo by 1/3–2/3 so as to capture features of the pillar in multiple photos. At each interval, three photos were taken: one orthogonal to the pillar to capture the full rib, one angled upward to include the roof, and the last one angled downward to include the floor. This process was repeated until the pillar-seal border was met at the next crosscut.

A three-dimensional point cloud of the pillar's exterior was created from the collection of pillar photos using a free software program, Autodesk 123D Catch. The program was then used to export the point cloud as a three-dimensional surface mesh. Two surface mesh models were created, one representing the pillars during November 30 and another during December 11. The models were then imported into another free software program, MeshLab, for scaling, alignment, and mesh difference measurement. The pillar meshes were scaled to the dimensions of the rib bolt pans supporting the pillar, which were 46 cm across. The two meshes were then overlapped so that any displacement over the twelve-day span could be measured. This required that the meshes were oriented so that identical locations on the pillar were overlapped. However, if the reference locations were displaced due to stress redistribution, this could have caused an unwanted error along the rest of the pillar. The rib bolts were used as the reference points for the surface meshes, because it was assumed that the bolts would be displaced significantly less than the coal around them. The distance between the scaled, aligned meshes was then found by using the Hausdorff distance sampling tool in MeshLab. The color quality tool was then used to create a color scale for the sampled points generated by the Hausdorff distance to show the displacement of the pillar over the twelve-day span.

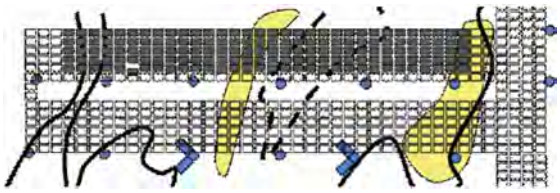

Fig. 1. Panel layout and geophone locations.

Two arrays of geophones were installed 3 m into the roof at approximately 100 m intervals for microseismic monitoring. One array, consisting of six uniaxial geophones was located in the previously-mined panel, while the second array, consisting of four uniaxial geophones and two triaxial geophones, was located in the current panel. An additional two geophones were located in the main entry (Fig. 1). The uniaxial geophones were placed in 3.2 cm diameter holes, while the triaxial geophones were placed in 5.7 cm diameter holes. Intrinsic safety barriers allowed the geophones to be installed in return air, while the data collection was near the power center near the main entries. Cable was strung from the geophones to the data collection center and hung from the roof. The system recorded continuously, and the data files were transferred from the underground location to a surface hard drive every three days.

When processing the seismic records to determine event locations, a uniform velocity was assumed and a simplex location method was used. It is preferred to conduct calibration events so that a correct velocity model is used when processing the data. In this study a calibration event from the surface above the mine was conducted; however, it was later determined that on the day the calibration was conducted the seismic system was not receiving power and so did not record data. Additionally, event locations would be the most precise if a velocity model was used that included the low-velocity caved zone retreating with the face on a daily basis.

3. Results and discussion

Borehole pressure cells, photogrammetry, and microseismic monitoring were used to monitor response to retreat mining. Results of the BPC monitoring are shown in Fig. 2. Pressures at three specific face locations are highlighted. They are when the face is: four pillar rows inby, two pillar rows inby, and at the monitored location. The results from the further inby pillar show a small increase in pressure cell readings of approximately 0.7 MPa when the face is three rows inby, followed by another 0.7 MPa when the face is one row inby, and then an increase of 3.5 MPa when the face moves one row outby the monitored pillar. Results

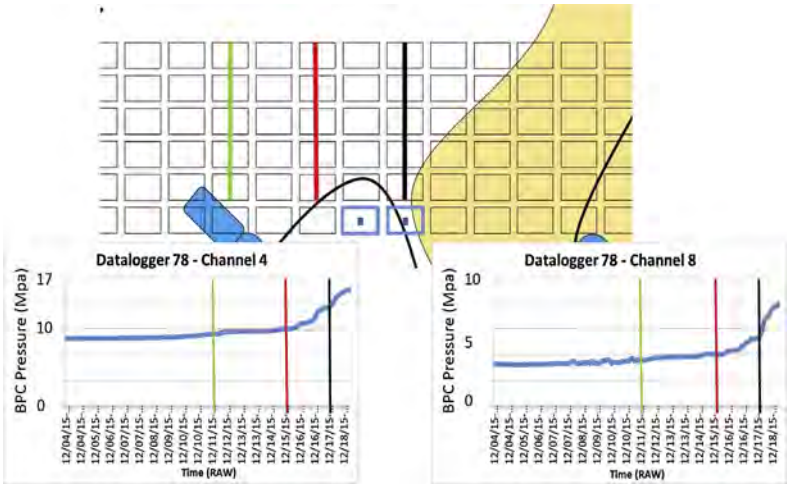

Fig. 2. Results of borehole pressure cell monitoring.

at the outby pillar were similar in behavior but lower in magnitude, increasing only from 9.2 MPa when the face was four rows inby to 9.7 MPa when the face was at the pillar. The lower pressure readings in the outby pillar are likely due to installation issues.

As shown in Fig. 2, three face locations are shown with green, red, and black lines.

The goal of photogrammetry monitoring was to see whether the method was repeatable and then, by comparing the results obtained at two different times, to see whether a reasonable difference (indicating deformation) was obtained. Fig. 3 shows the difference between the two meshes where the lighter shades are from the nearer face location. The difference is made more evident with a color scale, as shown in Fig. 4. The results show that upper meter of the inby end of the pillar deformed out into the entry. However, on the further outby portion of the pillar the deformation out into the entry was more distributed across more locations.

As is evident in Fig. 3, lighter shades are from nearer face location.

The photogrammetry results show that there is variation in deformation along a pillar, and so point-location measurements are incomplete and may misrepresent actual conditions. The results show that the deformation is relatively limited indicating that, for the loading conditions, the roof and rib bolts are providing the necessary support. Additionally, the information obtained by photogrammetry can help calibrate numerical models. The data collection and processing were inexpensive and did not require much time. These initial results indicate that there is potential for further development of this method.

The microseismic monitoring showed the rate and magnitude of the seismicity induced by the retreat mining. Although data were recorded continuously and transferred to an external data storage device every few days, there were still several time periods when the data were not properly recorded and stored. There were three time periods when data from all fourteen geophones were recorded and stored. The face locations during these three time periods are shown in Fig. 5: location 1 is under 275 m of cover and has a sandstone channel in the immediate roof, location 2 is under 250 m of cover with shale in the immediate roof, and location 3 is under 300 m of cover with shale in the immediate roof. All three locations are well after the retreating distance exceeds the panel width, so the caved zone should be mature.

The locations of the microseismic events during the three time periods are shown in Figs. 6 and 7 in both plan view and horizontal cross section. Only the events with a location error of less than 30 m are included in the analysis. The surface topography is shown

Fig. 3. Difference between two photogrammetry meshes.

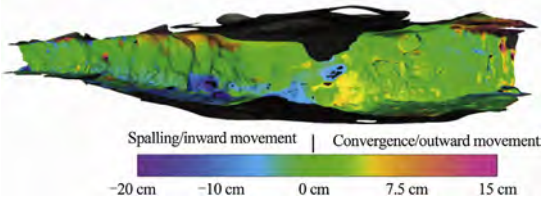

Fig. 4. Deformation measured from two photogrammetry meshes in which the face moved from 12 crosscuts inby to 3 crosscuts inby.

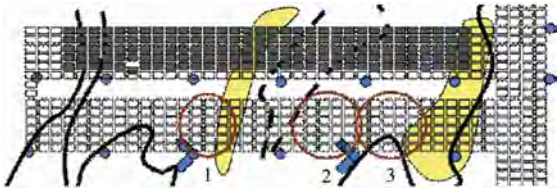

Fig. 5. Three time periods when data from all fourteen geophones were recorded and stored.

on Figs. 6 and 7, and some events are located above the surface because of the uniform velocity model that was assumed during processing. The plan views of the results show the events moving along the panel as the face retreats, while the vertical cross sections show the events extending throughout the overburden and occurring further inby at greater distances above the seam. Additionally, the vertical cross sections show that during the first time period the majority of the events occur above the seam, while during the second time period approximately the same number of events occur above the seam as below, and during the final time period the majority of the events occur below the seam.

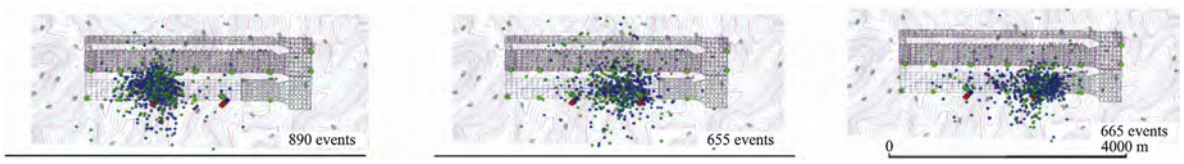

Fig. 6. Locations of the microseismic events during the three time periods in plan view.

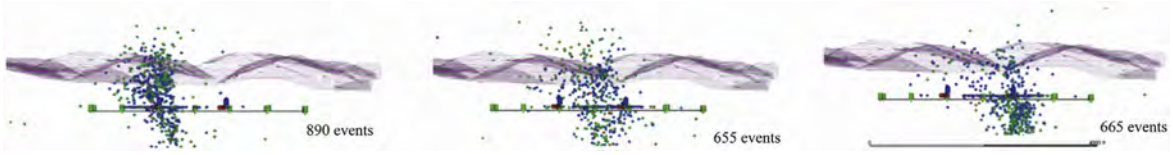

Fig. 7. Locations of the microseismic events during the three time periods, in vertical cross section.

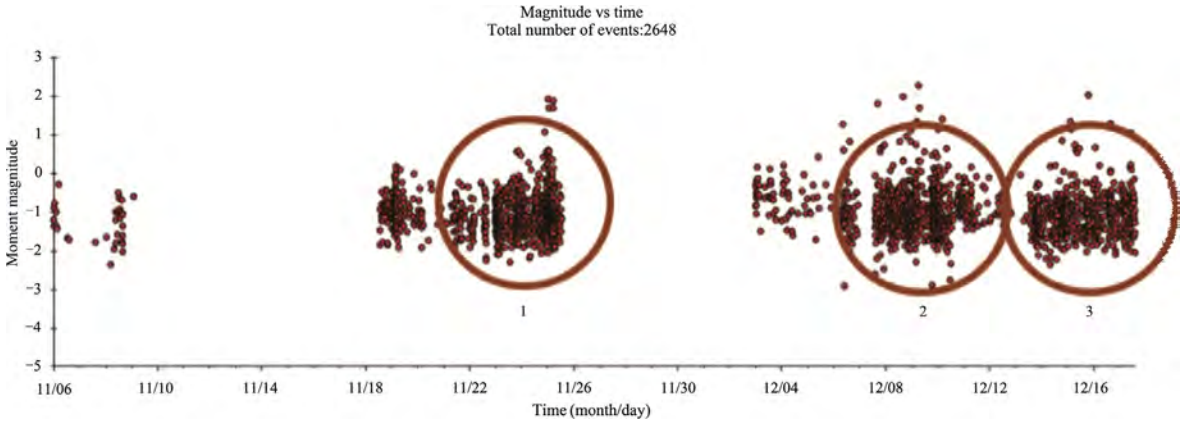

Fig. 8. Moment magnitudes of seismic events during three time periods.

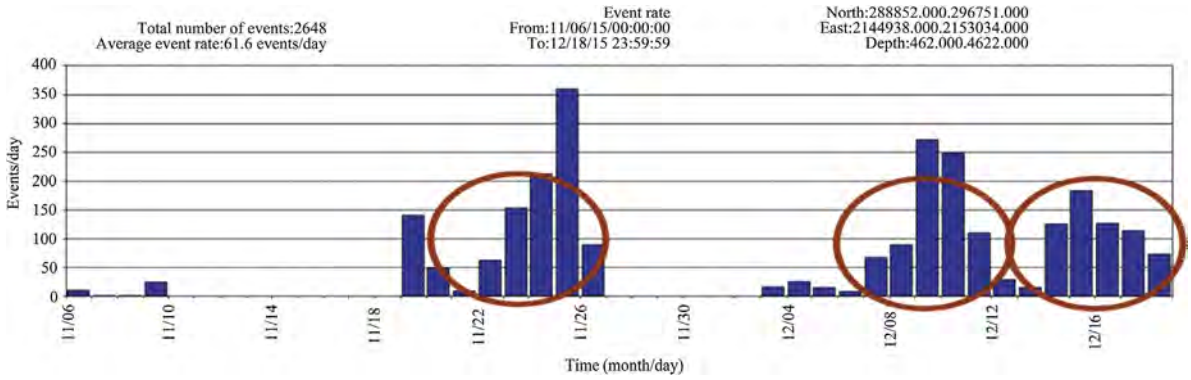

Fig. 9. Daily event rate of seismic events during three time periods.

The event rates vary with depth of cover and immediate roof material, but the event magnitudes do not. Fig. 8 shows that the magnitudes of the events are approximately consistent during the three time periods. However, Fig. 9 shows that the number of events per day is approximately the same for the first two time periods (under 275 m and 250 m of cover), while fewer events occurred per day during the third time period (under 300 m of cover).

Mining occurred during the day shift and the evening shift. Fig. 10 shows that most of the events occurred beginning halfway through the day shift and continued through the end of the evening shift. Even though mining began at the beginning of the day shift, because the mine was typically extracting a row of pillars per day, there was little seismic activity while the first pillar was extracted at the beginning of the day shift. However after the first pillar was mined, the seismic activity increased.

By combining the results from the BPCs and the microseismic monitoring, the observed conditions underground are quantified. The operators report that the loading on the pillars is relatively low in magnitude and distribution because there is a good cave,

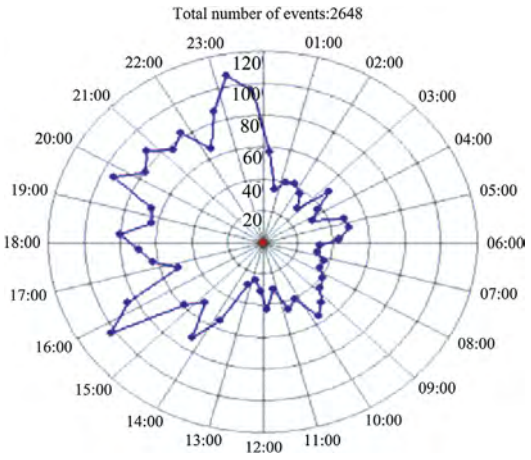

Fig. 10. Time of day in which events occurred.

that the loading is observed primarily on the current row of pillars being mined plus one row outby, and that the loads are not very high.

4. Summary and conclusions

An integrated ground monitoring study including borehole pressure cells, photogrammetry, and microseismic monitoring was conducted at a retreat room-and-pillar coal mine in order to quantify conditions observed underground. The results from integrating the three methods show some clear conclusions and some interesting potential. The clear conclusions include:

(1) BPC readings show very moderate stress increase.
(2) BPCs show that only one row of pillars outby face is under an increased load. This matches what is observed underground where miners state that it is the immediate pillar line plus one break outby that are loaded (the active mining zone is described as being about a break and a half).
(3) Photogrammetry shows deformation along the entire pillar. This can help calibrate numerical models, and provide better understanding of pillar behavior and pillar design.
(4) Magnitude of seismicity changes little with cover and immediate roof geology. This result is significant because it contrasts with the typical expectation of greater energy release under increased depth of cover.
(5) Event rates vary with cover and immediate roof geology.
(6) The combination of the seismic monitoring and BPC measurements provide data to support underground observations, which are that good caving results in little loading on pillars.
(7) Retreat mining occurred from 8 a.m. to midnight, but most events were recorded from noon to midnight, perhaps because less ground was opened up before noon.

In addition to these clear conclusions, there were also some observations that show interesting potential including:

(1) Photogrammetry is an easy, useful tool but needs further development and calibration.
(2) Photogrammetry shows convergence on the top half of the pillar because the bottom 0.3–0.6 m are rock.
(3) Events occurring above and inby the face are not necessarily forming gob, they might just be fracturing the overburden or shearing along bedding planes induced by strata bending (this is also true for events above adjacent panels). Future studies will analyze waveform data to determine failure mechanisms.

Acknowledgments

This project was supported by a NIOSH Ground Control Capacity Building grant and could not have been completed without the outstanding support of the employees of the mining company.

References

[1] MSHA; 2015. <www.msha.gov>.
[2] Dreger DS, Ford SR, Walter WR. Source analysis of the Crandall Canyon, Utah, mine collapse. Science 2008;321:217.
[3] Oyler DC, Mark C, Dolinar DR, Frith RC. A study of the ground control effects of mining longwall faces into open or backfilled entries. Geotech Geol Eng 2001;19(2):137–68.
[4] Tadolini SC, Zhang P. The unpredictable life cycle of a coal pillar. In: Proceedings of the 26th int'l conf on ground control in mining. West Virginia University, Morgantown, West Virginia; 2007. p. 90–6.
[5] Dolinar DR. Ground and standing support interaction in tailgates of western U. S. longwall mines used in the development of a design methodology based on the ground reaction curve. In: Proceedings of the 29th int'l conf on ground control in mining. West Virginia University, Morgantown, West Virginia; 2010. p. 152–60.
[6] Huber DF, Vandapel N. Automatic 3D underground mine mapping. Field Serv Robot, Springer Tracts Adv Robot 2003;24:497–506.
[7] Nuchter A, Surmann H, Lingemann K, Hertzberg J, Thrun S. 6D SLAM with an application in autonomous mine mapping. Robotics and automation. In: Proceedings of proc ICRA'04, 2004 IEEE international conference; 2004, vol. 2, p. 1998–2003.
[8] Errington AFC, Daku BLF, Prugger A. Closure monitoring in potash mines using LiDAR. In: Proceedings of IECON 2010–36th annual conference on IEEE industrial electronics society. Glendale, Arizona, USA; 2010. p. 2823–7.
[9] Slaker BA, Westman EC. Time-lapse photogrammetric monitoring of an underground stone mine. In: Proceedings of 34th international conference on ground control in mining. Morgantown, WV; 2015.
[10] Hazzard JF, Young RP. Dynamic modeling of induced seismicity. Int J Rock Mech Min Sci 2004;41:1365–76.
[11] Jones TH. Knowledge is power: introducing the Midas, a new permissible datalogging system for use in mines. In: Proceedings of 31st international conference on ground control in mining. Morgantown, WV; 2012.

International Journal of Mining Science and Technology 27 (2017) 71–76

Contents lists available at ScienceDirect

International Journal of Mining Science and Technology

journal homepage: www.elsevier.com/locate/ijmst

Void fill and support techniques to stabilize drift excavated through a transition zone mined by a TBM at the Stillwater mine

Johnson Josh [a,*], Jacobs Curt [a], Ferster Mark [a], Tadolini Stephen [b]

[a] Stillwater Mining Company, Nye, MT 59061, USA
[b] Minova, Georgetown, KY, USA

ARTICLE INFO

Article history:
Received 21 June 2016
Received in revised form 29 August 2016
Accepted 19 October 2016
Available online 21 December 2016

Keywords:
TBM
Ground
Dike
Cutterhead

ABSTRACT

Stillwater Mining Company is the only U.S. producer of platinum group metals (PGMs) and the largest producer outside of South Africa and Russia. The company controls a considerable portion of the J-M reef and is currently developing the "Blitz Project," which will provide a main haulage level, ore pass systems, backfill plants, and flow-through ventilation to increase production and ensure sustainable extraction of this critical strategic mineral. While driving two sub-parallel footwall laterals 8125 m in length, one of the development drifts experienced a massive fall in a geologically disturbed area created by a mafic dike intrusion. Combinations of a void fill material (Tekseal), polyurethane injection, fore poling coupled with steel arches, and supplemental bolting allow safe and efficient advance through this geologically disturbed zone. This paper presents the details of this project.

1. Introduction

Stillwater Mining Company is the only U.S. producer of platinum group metals (PGMs) and the largest producer outside of South Africa and Russia. The Company controls a considerable portion of the J-M reef and is currently developing the "Blitz Project," which will provide a main haulage level, ore pass systems, backfill plants, and flow-through ventilation to increase production and ensure sustainable extraction of this critical strategic mineral.

Tunnel boring machines (TBMs), shown in Fig. 1, have been used extensively at both the Stillwater Mine and the East Boulder Mine to develop access to the J-M Reef. The J-M Reef is a PGM-bearing reef deposit located in the Stillwater Complex near Nye Montana. The mining properties and location are shown in Fig. 2.

The Blitz Project is named after the Blitz mining claim and is designed to develop the Eastern extent of the J-M Reef. Project consists of a 5.5 m diameter TBM drive on the 50E (1562 m above sea level) and a 4.7 m × 4.7 m drill and blast heading on the 56E (1750 m above sea level). The Benbow Decline will be completed running perpendicular to the TBM by drilling and blasting methods. The TBM drift will be used for exploration drilling, ventilation, and will serve as the main haulage level. The 56E will be used for ventilation and exploration drilling. The Benbow decline will serve as the exhaust drift.

1.1. Geology

The Stillwater Complex is a 27-million-year-old, layered, ultramafic, intrusive rock exposed to the surface for 47 km along the Beartooth Range of South-Central Montana. The deposit, originally emplaced sub-horizontal, now sits dipping anywhere from 42° to the North, to overturned 80° to the South. The complex can be broken down into three major units: the basal series, the ultramafic series, and the banded series. The basal series averages 160 m in thickness and is a bronzite-rich unit with pods of massive sulfide. The ultramafic series ranges in thickness from 840 to 2000 m and is primarily composed of alternating layers of bronzitite, harzburgite, and dunite, with bands of chromite. Finally, the banded series has over 4500 m of layered norites, gabbros, and anothosites. The J-M Reef, the primary host for the platinum group mineralization within the deposit, sits in the lower portion of the banded series, 200–400 m above the ultramafics. A visual graphic of the Stillwater Complex Formation is shown in Fig. 3.

The excavations for the Blitz project have been designed to mine near the top of a major norite unit (norite zone 1) and the base of a banded gabbro, norite, and anorthosite unit (gabbro zone 1) roughly halfway between the ultramafic contact and the J-M Reef. This massive norite unit provides the most dependable ground conditions for mining but can become compromised by regional crosscutting structures and crosscutting mafic dikes of varying thickness. The mafic-rich rocks of the complex are prone to serpentine and talc alteration along fractures and joints. The

* Corresponding author. Tel.: +1 303 579 9330.
E-mail address: jjohnson@stillwatermining.com (J. Johnson).

http://dx.doi.org/10.1016/j.ijmst.2016.11.007
2095-2686/

Fig. 1. Robbins Main Beam (TBM) during setup.

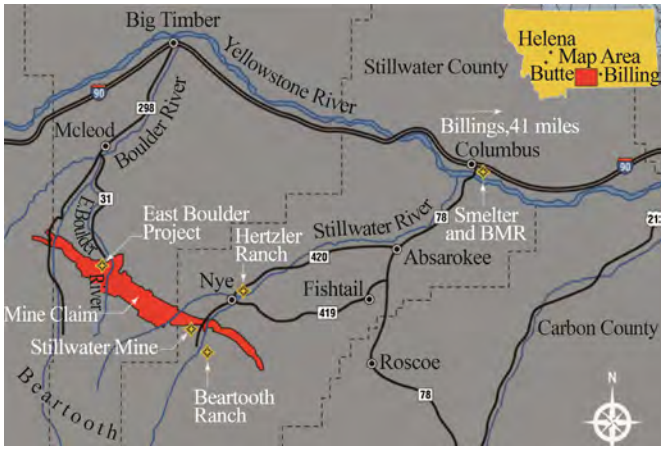

Fig. 2. JM Reef & Stillwater Mining properties.

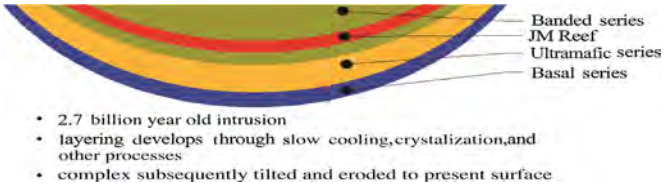

Fig. 3. Stillwater complex formation.

mafic dikes are typically associated with major structures, which can create difficult ground conditions with small block size and serpentinized contacts over distances of just a few meters to a few hundred meters.

1.2. Ground instability

Geotechnical and exploration drilling is completed on regular intervals. Core drills are used to identify the J-M Reef to the North, the ultramafic series to the South, and expected ground conditions straight ahead of the TBM. Probes vary from 156 to 312 m, depending on conditions. In April 2014, the drilling revealed faulting and altered ground straight ahead of the TBM. That fault zone was intercepted in May by the TBM and drastically slowed advance rates. In July, more probes were completed and 94 m of highly fractured dike was identified straight ahead of the TBM. Limited maneuverability of the TBM required direct advance through the dike.

Until August 2014, only one crew operated the TBM four days a week due to the limited availability of experienced manpower. A second crew was added in August. Crews were scheduled Monday through Thursday for day and night shifts, which allowed for maintenance of the TBM over the weekend. By August, ground convergence in the fault zone, shown in Fig. 4, was so great that the steel ventilation ducting on the trailing decks had to be cut off and replaced with smaller oval ductwork to allow the machine to pass.

Poor ground conditions continued to slow the advance. In January 2014, one crew was able to mine 180 m of drift, but, in October 2014, two crews were only able to mine 28 m. By late October, the TBM was within 9.4 m of the dike contact. The dike was dipping away from the TBM creating a wedge consisting of low strength altered joint rock under high stress. The conditions in September 2015 are shown in Fig. 5. Note the folding of the roof; mesh and bolt installations stabilized the immediate roof. Fig. 6 shows the small block size and the geological alterations of the immediate roof.

Several times, the crew attempted to shotcrete the back with a high-strength accelerated-set polyfiber mix. Shotcrete was allowed to set up for 72 h before bolt installation and advance attempts were made. The shotcrete and ground failed due to the vibrations from drill hammers during bolting and cutterhead during advance. The failed shotcrete is shown in Fig. 7.

Ground failure continued until advance was no longer an option, and the void was filled. Fig. 8 shows the void. The wedge of poor rock continued to chimney up until the total height was over 18.7 m and was no longer measureable.

After the first void was filled and the TBM advanced through that zone, there were two smaller sections of fallout; one of which required filling before advance could continue. A schematic of the initial and subsequent failure zones is shown in Fig. 9. After investigating the situation, an error in the Program Logic Controller (PLC) was found that showed that all six drive motors were pulling full load amps, while, in reality, only half of the motors were working as designed. The lack of torque applied to the cutterhead required operators to back the head off of the active face to get the head to turn. This allowed ground to start failing. As the head was pulled back, muck would fail against the head and continually "chase" the head back. The lack of adequate torque to the cutterhead was the reason the second section required void fill.

Fig. 4. Drift convergence August 2014 (mesh was installed tight to rock surface).

Fig. 5. September 2014 roof conditions.

Fig. 6. October 2014, small block size and alteration are clearly visible.

Fig. 7. October 2014 shotcrete failure.

2. Solution

The final engineered solution was combinations of a comprehensive void fill procedure combined with steel arches, supplementary bolting, and change in workday schedule.

Fig. 8. Void October 11, 2014 picture taken from above cutterhead.

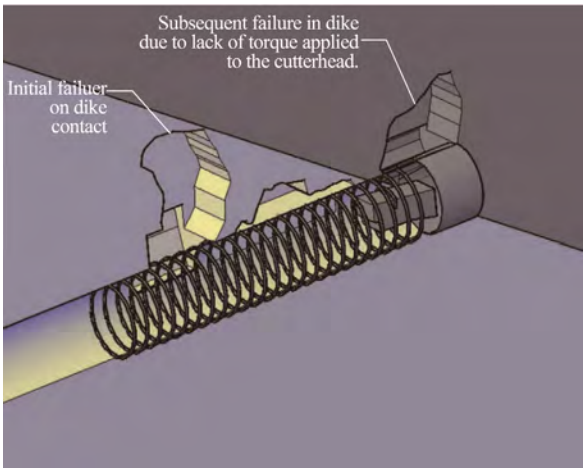

Fig. 9. Dike contact and associated fallout.

2.1. Void fill procedure

Concrete, neat cement grout, and aerated cementitious grouts were evaluated as options for backfill media. Concrete would have to be brought in via Moran cars, requiring constant operation of the mines batch plant and long duty cycles. Additionally, the delay in material placement would allow cold seam joints to form due to the large volume required to fill the void. Concrete fill would have created a heavy block suspended above the drift after excavation. Staff was concerned about the ability of the abutment rock to support the weight of the concrete block. Neat cement grout would allow for a continuous pour but cold seams could still form as with concrete. Cement fill also had the potential to create a heavy block above the finished excavation.

Various aerated cementitious grouts were evaluated, but Tekseal was chosen as the desired product due to the high volume pour rate, lack of cold seams, the lightweight material, fast set time, and controllable consistency.

Pallets were staged at a cross cut in the TBM drift, and a pump was staged just off of the trailing decks of the TBM about 156 m back from the void. High Density Polyethylene (HDPE) pipe and Polyvinyl Chloride (PVC) pipe were used to deliver the product. A bulkhead made from vent bag prevented Tekseal from infiltrating the cutterhead. Tekseal was mixed using 9 bags (21 kg bags) per cubic meter to achieve the highest strengths. The void filling in November 2014 is shown in Fig. 10. Samples were taken throughout the filling process to determine actual placed strength. Uncon-

Fig. 10. Void filing in November 2014 (view from above cutterhead).

Fig. 11. Back of drift after mining through the Tekseal and rock conglomerate.

fined compressive strengths and indirect tensile testing were completed on samples at 40 and 76 days. Testing was completed to ensure the material had adequately cured, and the design strengths were achieved. To complete the testing program, cylinders were filled throughout the placement process and remained at the site to simulate in situ curing conditions. The samples were tested in accordance with ASTM D1266 for compressive strength and ASTM C496 for indirect tensile strengths (Brazilian test) strength [1,2]. Table 1 shows the results after 40 days and 76 days. No indirect tensile testing was completed at the 76 day interval. Sample #10 resulted in a low value attributed to sample damage during mold removal. The entire testing suite resulted in an average of 3231 kg or 6763 kPa. If you exclude sample 10, the average load was 3480 kg or 7287 kPa. The desired design strength was 6894 kPa, so the material was at a satisfactory strength, and mining could proceed. The consistency of the Tekseal was manipulated to allow material to flow through the muck pile and adjusted further if it started flowing out past the bulkhead. Nevertheless, the 9-bag mixture provided the desire results, and the material flowed through the muck pile, and strengthened it for the TBM advance.

2.2. Steel arches and supplementary bolting

W6×15 curved steel sets were installed on 1.25 m centers to provide additional support in the backfilled zone and for the rest of the dike. Steel sets consisted of 4 equal length curved sections and a Dutchman shim designed to expand to 5.6 m. Fig. 11 illustrates the steel arches and the mining of the Tekseal and rock conglomerate; notice the ring profiles as the cutters created tension cracks. In places of extreme fallout, steel beams were installed perpendicular to the ring steel and rock surface to provide more even loading of the steel, reducing deformation of steel sets under load. A cross-section of the ring steel is shown in Fig. 12. The TBM was designed so that rebar slats could be installed in the steel finger sleeves, anchored, and would then be pulled out of the sleeves on advance, becoming pinned to the back by the ring steel. However, the rebar slats were unable to hold up to loading conditions and the practice was abandoned.

Additionally, 15.6 m long, 15 mm cable bolts were used through the backfilled zone to reach past the Tekseal and into the rock to maintain a compressive load on the backfill media. Then 2.5 m friction bolts and 3.75 m resin-anchored continuous threaded (CT) rebar bolts were installed on a 0.9 m × 0.9 m pattern when possible. Fig. 13 shows the tight conditions that existed to install the ground support.

The crew attempted to use hollow core injection bar (IBO rod) to spile and pre-support rock on front of the cutterhead.

This method was abandoned due to lack of overall effectiveness. Drilling of the IBO rod may have caused enough stress on the rock above the cutterhead support to create failure, which created additional fallout. This required additional time and resources. Fig. 14 shows the support mechanisms that were installed and the location of the ground falls.

Polyurethane grout was applied to the rock to further consolidate loose material. Polyurethane grout could be installed quickly and achieved high strengths almost immediately. Approximately 9072 kg of polyurethane grout was used to achieve desired rock consolidation (see Fig. 15).

Table 1
Physical property testing of Tekseal material (40 and 76 d).

Tekseal sample #	Load (kg)	Compressive strength (kPa)	Indirect tensile strength (kPa)	Load (kg)	Compressive strength (kPa)
	40 days			76 Days	
1	4667	9735		3706	7763
2	841		917	5470	11,459
3	969		1089	3883	8129
4	3963	8322		3493	7302
5	779		848	3221	6743
6	711		807	3089	6467
7	2426	5075		3270	6833
8	4985	10,384		3003	6274
9	2922	6102		3765	7874
10	3245	6771		494	1034
11	2451	5123		2159	4516
12				3180	6660
Average	2542	7359	915	3228	6755

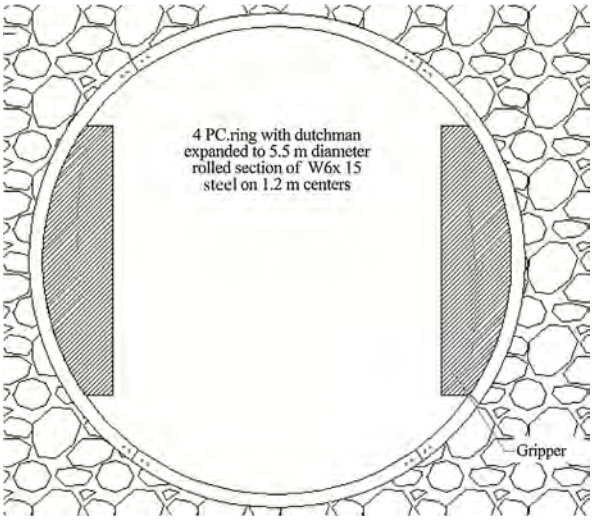

Fig. 12. Ring steel cross section with TBM grippers.

Fig. 13. Ground support installation.

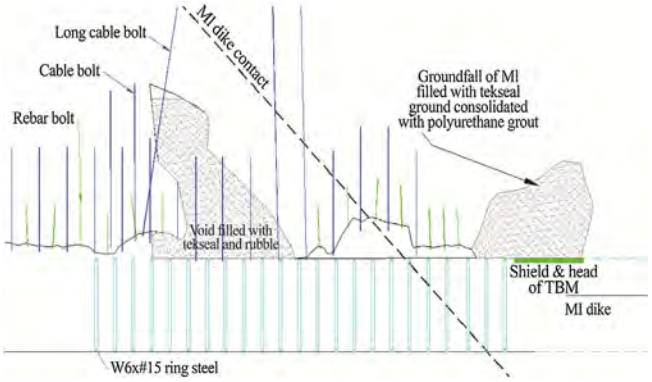

Fig. 14. Support mechanisms.

2.3. Schedule

Additional experienced operations support was brought in, and the crew schedule was changed so that the machine was manned straight days every day rather than 24 h a day 4 days a week. Schedule change reduced unsupported time of ground from 72 h every 7 days to 12 h every day. Reduction in time that ground was unsupported allowed for increased effectiveness of the support system, safer conditions, and faster advance rates.

Fig. 15. View looking east of completed tunnel.

2.4. Cutterhead torque

After repairs were made to the TBM, and all motors were working correctly, the crews were able to advance the TBM without pulling the cutterhead back off the face as far. Keeping constant pressure against the face prevented ground from failing, which improved conditions.

3. Results

Tekseal worked well in this application. Material filled the voids quickly without the need for a major bulkhead and provided the necessary strengths to mine through. The long support and steel sets worked very well in preventing additional ground falls. Application of polyurethane grout also worked well to consolidate ground before there were any major voids to fill. Schedule change greatly reduced ground control issues.

Spilling and the rebar slats did not prove to be beneficial in this specific application. The spilling may have made conditions worse due to the required set time of the cement and the percussion on small block-sized material above the cutterhead. The rebar slats were not robust enough; wire mesh proved to be just as effective.

In hindsight, identifying the PLC issues, scheduling a crew seven days a week, and starting ring steel installation earlier may have prevented or reduced the challenges faced with these poor ground conditions.

4. Conclusions

The Blitz Project is a major development project at the Stillwater Mine that will provide access to the J-M Reef. The project uses a 5.6 m diameter TBM to mine a main haulage level, vent drift, and exploration drift. The project requires development through very complex geology that includes multiple major fault structures and dikes that alter the ground.

During development of the TBM drift, the ground failed while approaching a dike contact. Multiple factors played a role in the ground failure: TBM drive motor performance, crew schedule, and ground support system. The ground failure was large enough that the void had to be backfilled before advance could continue. An aerated cementitious grout (Tekseal) was used to fill the voids. Crews were able to continue advance after filling voids, changing

the operating schedule, and increasing the ground support to include steel sets and long cable bolts.

Acknowledgments

We would like to thank the exceptional talent, leadership, and experienced operations staff at the Stillwater Mine and Minova for their hard work in providing a safe and effective solution that allowed the project to continue. From Stillwater: Curt Jacobs (Project Superintendent), Tom Cecil (Supervisor), Steve Kurschner (Foreman), Roland Marchand (Supervisor).From Minova: Casey Thomas provided excellent technical support and product procurement.

References

[1] ASTM. ASTM C496/C496M: standard test method for splitting tensile strength of cylindrical concrete specimens. West Conshohocken, PA: ASTM International; 2011. , http://www.astm.org/Standards/C496.htm.
[2] ASTM. ASTM C495/C495M: standard test method for compressive strength of lightweight insulating concrete. West Conshohocken, PA: ASTM International; 2012. , http://www. astm.org/Standards/C495.htm.

International Journal of Mining Science and Technology 27 (2017) 77–81

Contents lists available at ScienceDirect

International Journal of Mining Science and Technology

journal homepage: www.elsevier.com/locate/ijmst

Application of new void detection algorithm for analysis of feed pressure and rotation pressure of roof bolters

Liu Wenpeng [a], Jamal Rostami [b,*], Eric Keller [c]

[a] Department of Energy and Mineral Engineering, The Pennsylvania State University, State College, PA 16802, USA
[b] Earth Mechanics Institute, Department of Mining Engineering, Colorado School of Mine, Golden, CO 80401, USA
[c] Electro-Mechanical Systems Laboratory, The Pennsylvania State University, State College, PA 16802, USA

ARTICLE INFO

Article history:
Received 25 June 2016
Received in revised form 9 October 2016
Accepted 18 October 2016
Available online 9 December 2016

Keywords:
Roof bolter
Void detection
Feed pressure
Rotation pressure
CUSUM algorithm
Ground support optimization

ABSTRACT

Roof and rib instability is an important issue in underground mining. To optimize ground support design, enhance ground stability, and reduce the possibility of roof or rib failure with minimal use of artificial ground support, it is essential to have an accurate understanding of ground conditions. This includes the location of voids, cracks, and discontinuities, as well as information about the different strata in the immediate roof. This paper briefly introduces ongoing research on void detection by using the roof bolter feed and rotation pressure. The goal of this project is to improve the sensitivity of detection programs to locate smaller joints and reduce the number of false alarms. This paper presents a brief review of the testing procedures, data analysis, logic, and algorithms used for void detection. In addition, this paper discusses the results of preliminary laboratory tests and statistical analysis of the data from these two drilling parameters used for void detection.

1. Introduction

Roof falls are one of the most serious and frequent accidents in underground mining. Each year, personnel are injured or killed because of roof falls. Equipment can also be damaged when this occurs. According to Mine Safety and Health Administration statistics collected from 1999 to 2008, ground falls were the largest cause of fatal accidents in underground coal mining, causing around 40% of all fatalities [1]. Out of 8 to 10 fatalities and over 800 injuries are recorded each year in underground mines, there are nearly 2000 reportable non-injury ground falls every year [2]. From literature review of published paper from other countries, although there were some differences of total numbers of injuries caused by ground falls in underground mining and tunneling, it showed similar trend in the world [3,4].

Certain features in the ground, such as voids, cracks, and discontinuities, are significant factors that cause roof support failures and roof fall accidents. The detection of those geological features are essential for design of effective ground support in underground support. Void detection in underground space can be performed by various techniques including bore scoping, visual observation and geophysical loggings, rock mass rating of the roof and ribs. However, these techniques also offer many shortcomings. For instance, although the bore scoping is widely applied in field for the identification of the rock types, voids, cracks and formation boundaries, it is a time-consuming method for stability analysis, and it requires pre-training on operators. In addition, visual observation and geophysical loggings usually failed to provide sufficient geological features information of the ground. Rock mass rating method typically cannot be performed in advance of mining activities, because some on site observation and measures are required. Thus, it seems that these methods could not provide sufficient geological information for support strategy improvement in a timely manner [5].

Many researchers have worked on this problem using instrumented drilling machines. For instance, Itakura et al. instrumented a pneumatic drill to monitor the torque, thrust, rotational speed, and stroke; both in the laboratory and the field. Fig. 1 shows typical patterns corresponding of torque to discontinuities [6,7]. From the laboratory tests, this system could identify locations of discontinuities, but it could not discriminate between cracks and layer boundaries. To achieve in-situ evaluation of roof rock, Itakura et al. developed a measurement while drilling (MWD) system to locate discontinuities by monitoring drilling parameters of torque, thrust, rotation speed, and stroke [8]. They state that torque and

* Corresponding author. Tel.: +1 2022471336.
E-mail addresses: wpl5038@psu.edu (W. Liu), rostami@mines.edu (J. Rostami).

http://dx.doi.org/10.1016/j.ijmst.2016.11.009
2095-2686/

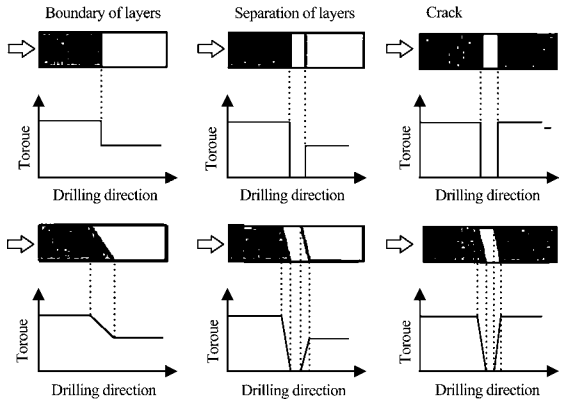

Fig. 1. Typical patterns corresponding to discontinuities [6].

thrust data had better performance in detecting geological structures in field tests. However, the MWD system still could not detect discontinuities with small size.

A research team at West Virginia University applied the J.H. Fletcher & Co.™ HDDR Model Walk-Thru Dual Head Roof Bolter to detect the location of voids, joints, bed separation, fractures, and formation interfaces by analyzing several drilling parameters. These drilling parameters included rotational speed, thrust, torque, and penetration rate values [9]. They note that the specific energy of drilling, SED in short, is a good indicator of ground features for identifying fractures. SED, which was calculated using drilling parameters, indicated a significant variation in the same material. Finfinger conducted a series of laboratory tests to use the primary drilling parameters, including thrust, torque, rotational velocity and penetration rate, to identify voids, joints and fractures, and mentioned that those features could be determined by "thrust valleys" when the penetration rate was preset (Fig. 2) [10]. A real time drilling display system for the J.H. Fletcher HDDR Dual Head Roof Bolter was developed and tested in the field to detect voids or fractures in the roof [11]. While successful in some cases, the sensitivity of this system still needed to be improved to detect joints or fractures with small aperture. After this, Anderson and Prosser developed a new software with improved algorithms to indicate void or separation locations in real time during the drilling process, but it could not detect hairline or vertical cracks [12].

More recently, Bahrampour et al. at the Pennsylvania State University research group installed vibration and acoustic sensors on the J.H. Fletcher drill unit to monitor vibration and acoustic signals for void detection [13]. Similar to previous studies, voids with openings smaller than 0.318 cm could not be successfully detected. There were also some false alarms in the detection process [14,15]. Rostami et al. also mentioned that these geological feature information collected by instrumented drills can be applied for roof characterization to offer an instant mapping of roof conditions before mining activities [16].

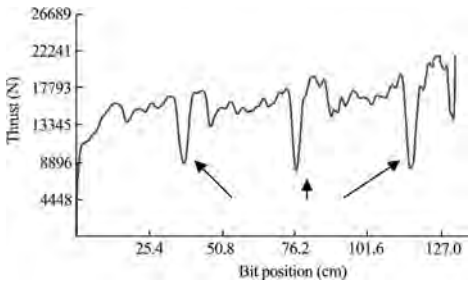

Fig. 2. "Thrust valleys" associated with fractures in concrete block [9].

Currently, several manufacturers provide smart roof bolters with limited capabilities for void detection. While successful in many instances, in laboratory experiments, the existing void detection systems have limited success in detecting void openings that are less than 0.318 cm. This limited success was observed in testing concrete blocks with gaps in between, simulating a rock medium with voids. Detection programs have missed some voids, while, in some cases, they have shown false detection. These algorithms need to be revised in sensing voids to improve the capabilities of these programs. This paper focuses on void detection by using a new algorithm to analyze the feed pressure and rotation pressure, which comes from thrust and torque correspondingly. This paper will also provide statistics on their void detection performances. The laboratory results indicate the feasibility of this new detection programs for void detection purposes.

2. Instrumented J.H. Fletcher drilling system

As shown in Fig. 3, a drill control unit, DCU in short, had been developed by J.H. Fletcher to record drilling parameters including torque, thrust, rotation rate, drill bit position, and vacuum pressure during the drilling processes. In this study, a DCU was used for laboratory tests on various samples at the Fletcher testing facility in Huntington, WV. For void detection purposes, a set of concrete blocks were made by casting grout with designed strengths. This included soft (S, approximately 20 MPa), medium (M, approximately 50 MPa), and hard (H, approximately 70 MPa) grout samples to represent various rock types and sequences of strata. The dimension of each block was approximately 0.5 m × 0.5 m × 0.75 m.

To simulate the void, each testing sample was set up by placing one block on top of another block. This left a gap of less than 2 mm between two blocks and was considered the void. Nine different combinations of rock strength sequences were tested, including soft to hard (S-H), hard to soft (H-S), and other possible scenarios (M-H, H-H, H-M, M-S, S-M, M-M, and S-S). Moreover, the drilling facilities used a sampling rate of 100 Hz to monitor drilling parameters.

3. Void detection by using the cumulative sum (CUSUM) algorithm

As discussed above, various pattern recognition systems have been studied for detecting joints using different drilling parameters. The most promising of the parameters seem to be the drilling thrust or feed pressure, and the rotation pressure, representing torque. Other parameters, including vibration and acoustic data, have also been considered and used in previous stages of this study [13]. While working on various pattern recognition systems, different mean change detection algorithms have been examined. Among the algorithms used for void detection, the CUSUM algorithm has been most promising and was used to evaluate recorded data for void detection. The CUSUM algorithm is a sequential analysis technique, introduced by Page, which is typically used for detection of abrupt changes in streaming data [17]. While drilling, the feed pressure and rotation pressure show sudden changes at the location where the drill bit encounters a void or a crack. This sudden drop is hidden in the monitored parameters and noises of the signal and is often difficult to locate. The CUSUM algorithm can be used to sense these changes and locate the features representing the open joint or void in the rock strata. Because of this, new void detection programs were developed based on the CUSUM algorithm to improve capabilities to detect the location of void.

Fig. 4 is an example of three drilling parameters that were recorded while drilling into a hard to hard (H-H) concrete block

Fig. 3. J.H. Fletcher drill control unit.

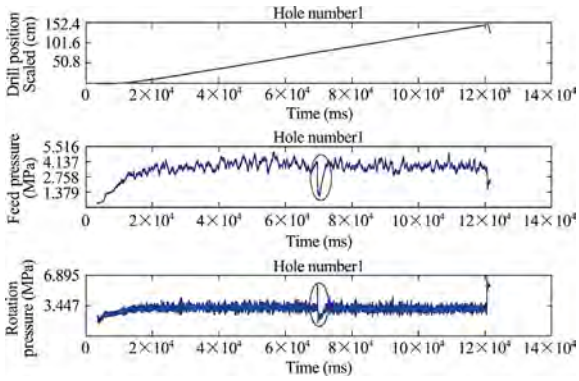

Fig. 4. Position, feed pressure and rotation pressure signals obtained from Hole #1.

specimen. In this combination of strata hardness, 18 holes were drilled. The top chart shows drill bit position signal during the drilling test, the middle is the feed pressure, and the lower chart is the plot of rotation pressure. The red circles show the detected location of the joint using the feed pressure and rotation pressure signal. In Fig. 4, feed pressure and rotation pressure signals indicate a significant change at around 76.2 cm, which was the location that the drill bit encountered the void in the specimen.

The CUSUM algorithm was applied in all specimen settings to detect the location of the void in each hole. Fig. 5a presents the result of void detection based on feed pressure on H-H specimen setting. In Fig. 5a, the orange markers present the detected location of the joint or void, and the majority of the voids had been located at the depth of approximately 76.2 cm. However, a false alarm was generated in hole #4 (blue marker) where no void seems to exist. Also, no void was detected in hole #10 by new void detection programs.

Fig. 5b illustrates void detection results using new void detection programs based on the analysis of rotation pressure signal on H-H specimen setting. In Fig. 5b, most of the voids were identified at the depth of about 76.2 cm, which indicates similar void detection results as in the case of feed pressure. However, a false alarm was generated in hole #3 (blue marker), and no void information was detected in holes #10, #11, and #12 by the new void detection programs.

4. Summary of void detection analysis in different blocks

To estimate the capability of the new void detection program based on the CUSUM algorithm, many laboratory tests have been conducted by drilling into various concrete block samples. Since the concrete blocks had three different strengths, there were nine different combinations of concrete blocks (Table 1).

As shown in Table 1, the average void detection rate was about 92.9% on feed pressure signals with 12 false alarms generated in all concrete block settings; however, the new void detection programs also had some misses and some false alarms. Besides, the void detection rates based on the CUSUM algorithm on feed pressure signals varied from 77.8% to 100% in all of these nine different combinations of concrete blocks.

Table 2 shows the average void detection rate was about 91.8% based on rotation pressure signals in all concrete block settings. The void detection rates ranged from 76.5% to 100% in different combination of concrete blocks. Similarly, in some boreholes, the voids could not be identified in some concrete block settings. However, up to 100 false alarms were also created during void detection based on rotation pressure signals. Therefore, the sensitivity of new void detection programs needs to be further improved.

To improve the accuracy of the void detection program, composite indices have been developed to eliminate some of the excessive variations and noise in the input data. Another approach to increase the sensitivity of the programs is the use of various digital filtering techniques to eliminate certain reoccurring frequencies to clean up the ambient noise in the data. One of the successful indices has been the ratio of torque/thrust/penetration. Fig. 6 shows the variation of this index versus time and notably lower noise in the data. The preliminary review of the data shows that

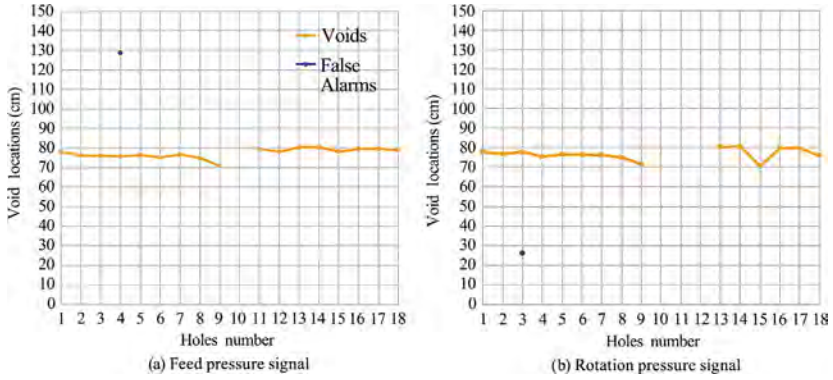

Fig. 5. Void detection of new void detection programs on a H-H block setting.

Table 1
Summary of void detection of feed pressure signal.

Concrete combination	S-H	H-S	M-H	H-H	H-M	M-S	S-M	M-M	S-S
Number of effective holes	15	17	17	18	21	18	18	18	16
Number of holes no void information	2	2	0	1	0	0	2	4	0
Detection rate (%)	86.7	88.2	100	94.4	100	100	88.9	77.8	100
False alarms	1	1	0	1	2	2	2	1	2

Table 2
Summary of void detection of rotation pressure signal.

Concrete combination	S-H	H-S	M-H	H-H	H-M	M-S	S-M	M-M	S-S
Number of effective holes	15	17	17	18	21	18	18	18	16
Number of holes no void information	1	4	0	3	1	0	2	2	0
Detection rate (%)	93.3	76.5	100	83.3	95.2	100	88.9	88.9	100
False alarms	6	4	5	1	16	17	19	10	22

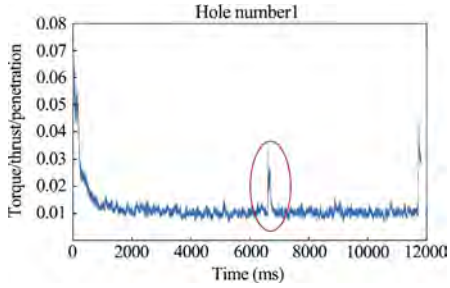

Fig. 6. A composite indices of torque/thrust/penetration.

use of the composite indices can improve the detection rate. Additional analysis of variable combination of parameters are underway to optimize the combination of different input parameters and their relative power in the formula for development of more suitable combined index for further analysis with the pattern recognition algorithms to enhance the current void detection capabilities.

5. Conclusions

The results of laboratory testing on an instrumented roof bolter drilling unit have shown that the new void detection programs based on the CUSUM algorithm could improve the capability of void detection, by showing reasonably good success when drilling across voids with aperture of around 2 mm. This system can help in identification of voids, bed separation, and open joints and allow for incorporation of data in evaluating ground and rock mass conditions. There are still several issues that must be resolved to further improve the capabilities and accuracy of these new void detection programs. In particular, void detection rates need to continue to improve, and the number of false alarms needs to be reduced. Moreover, additional laboratory tests with more complicated void conditions are underway for enhancing the capabilities and accuracy of the new void detection programs for a variety of applications.

References

[1] NIOSH. Mining topic: geologic characterization. National Institute for Occupational Safety and Health; 2015a. <http://www.cdc.gov/niosh/mining/topics/GeologicCharacterization.html>.
[2] NIOSH. Mining topic: roof support. National Institute for Occupational Safety and Health; 2015b. <http://www.cdc.gov/niosh/mining/topics/RoofSupport.html>.
[3] Mark C. Ground control in the underground coal mines of Colombia. In: Proceedings of the 33rd international conference on ground control in mining. West Virginia University, Morgantown, WV.
[4] Oraee K, Oraee N, Goodarzi A, Khajehpour P. Effect of discontinuities characteristics on coal mine stability and sustainability: a rock fall prediction approach. Int J Min Sci Technol 2016;26(1):65–70.
[5] Rostami J, Kahraman S, Naeimipour A, Collins C. Rock characterization while drilling and application of roof bolter drilling data for evaluation of ground conditions. J Rock Mech Geotech Eng 2015;7:273–81.
[6] Itakura K, Sato K, Deguchi G, Ichihara Y, Matsumoto H, Eguchi H. Development of a roof-logging system by rockbolt drilling. Trans Inst Min Metall Sect A: Min Technol 1997:A118–23.
[7] Itakura K. Current drill monitoring system using mechanical data of drilling machine and estimation of roof rock structure. In: Proceedings of Australia-Japan technology exchange workshop in coal mining '98. Brisbane (Australia): Commonwealth Scientific & Industrial Research Organisation; 1998. p. 8–10.
[8] Itakura K, Sato K, Deguchi G, Ichihara Y, Matsumoto H. Visualization of geostructure by mechanical data logging of rockbolt drilling and its accuracy.

In: Proceedings of 20th international conference on ground control in mining. West Virginia University, Morgantown, WV. p. 184–90.
[9] Finfinger G, Peng S, Gu Q, Wilson G. An approach to identifying geological properties from roof bolter drilling parameters. In: Proceedings of 19th international conference on ground control in mining. West Virginia University, Morgantown, WV. p. 11.
[10] Finfinger G. A methodology for determining the character of mine roof rocks. Ph.D. Dissertation. Morgantown, WV: West Virginia University; 2003.
[11] Collins CM, Wilson G, Tang D, Peng S. Field testing of a real time roof mapping drilling display system in a limestone mine. In: Proceedings of 23rd international conference on ground control in mining. West Virginia University, Morgantown, WV. p. 8–55.
[12] Anderson R, Prosser LJ. Improving the capability for real time assessment of roof conditions through intelligent roof bolt drilling operations. In: Proceedings of 26th international conference on ground control in mining. West Virginia University, Morgantown, WV. p. 87–292.
[13] Bahrampour S, Rostami J, Naeimipour A, Collins C, Kahraman S. Instrumentation of a roof bolter machine for void detection and rock characterization. In: Proceedings of 32nd international conference on ground control in mining. West Virginia University, Morgantown, WV. p. 73–281.
[14] Kahraman S, Rostami J, Naeimipour A. Review of ground characterization by using instrumented drills for underground mining and construction. Rock Mech Rock Eng 2016;49:585–602.
[15] Bahrampour S, Rostami J, Ray A, Naeimipour A, Collins C. Ground characterization and roof mapping: online sensor signal-based change detection. Int J Min Sci Technol 2015;25(6):905–13.
[16] Rostami J, Naeimipour A, Bahrampour S, Dogruoz C. Logging of roofbolt boreholes for ground characterization in underground construction. In: Proceedings of world tunneling conference. Iguasso Falls, Brazil.
[17] Basseville M, Nikiforov IV. Detection of abrupt changes: theory and application. Englewood Cliffs (NJ): Prentice Hall; 1993. p. 469.

International Journal of Mining Science and Technology 27 (2017) 83–90

Contents lists available at ScienceDirect

International Journal of Mining Science and Technology

journal homepage: www.elsevier.com/locate/ijmst

A practical application of photogrammetry to performing rib characterization measurements in an underground coal mine using a DSLR camera

Brent A. Slaker *, Khaled M. Mohamed

Mining Engineer Ground Control Branch NIOSH, Office of Mine Safety and Health Research, Pittsburgh, PA, USA

ARTICLE INFO

Article history:
Received 19 July 2016
Accepted 9 September 2016
Available online 5 December 2016

Keywords:
Photogrammetry
Coal mining
Underground
Rib characterization

ABSTRACT

Understanding coal mine rib behavior is important for inferring pillar loading conditions as well as ensuring the safety of miners who are regularly exposed to ribs. Due to the variability in the geometry of underground openings and ground behavior, point measurements often fail to capture the true movement of mine workings. Photogrammetry is a potentially fast, cheap, and precise supplemental measurement tool in comparison to extensometers, tape measures, or laser range meters, but its application in underground coal has been limited. The practical use of photogrammetry was tested at the Safety Research Coal Mine, National Institute for Occupational Safety and Health (NIOSH). A commercially available, digital single-lens reflex (DSLR) camera was used to perform the photogrammetric surveys for the experiment. Several experiments were performed using different lighting conditions, distances to subject, camera settings, and photograph overlaps, with results summarized as follows: the lighting method was found to be insignificant if the scene was appropriately illuminated. It was found that the distance to the subject has a minimal impact on result accuracy, and that camera settings have a significant impact on the photogrammetric quality of images. An increasing photograph resolution was preferable when measuring plane orientations; otherwise a high point cloud density would likely be excessive. Focal ratio (F-stop) changes affect the depth of field and image quality in situations where multiple angles are necessary to survey cleat orientations. Photograph overlap is very important to proper three-dimensional reconstruction, and at least 60% overlap between photograph pairs is ideal to avoid unnecessary post-processing. The suggestions and guidelines proposed are designed to increase the quality of photogrammetry inputs and outputs as well as minimize processing time, and serve as a starting point for an underground coal photogrammetry study.

1. Introduction

The stability of underground mine ribs has been a safety concern for underground coal mines for decades. Unfortunately, the average rib fatality rate has been about 1.3 per year between 1996 and 2013 [1]. In an effort to better understand coal rib behavior, photogrammetry is being investigated in this study as a measurement tool for surveying ribs in an underground coal mine environment.

Photogrammetry is a method of image measurement used to derive the shape of an object as determined from multiple photographs. Photographs themselves, being two-dimensional representations of three-dimensional space, have an inherent loss of information, but measurements can be inferred by analyzing the shape of an object with the relative camera positions [2]. This paper specifically deals with close-range digital photogrammetry (CRDP), which is typically limited to objects or scenes less than 100 m from the camera [3]. In recent years, the practice of photogrammetry has seen increased applications to research in underground mines, such as work characterizing fracture networks and establishing a pillar rating system, rock mass and support monitoring, and an assessment of pillar spalling in unstable limestone mine workings [4–9].

The use of this technology in underground coal mines has been severely limited, in large part due to the lack of Mine Safety and Health Administration (MSHA) approved options for photography equipment in the potentially explosive atmosphere. Additionally, the visible features in an underground coal mine are markedly different from those of other underground mines. The goal of this

* Corresponding author. Tel.: +1 412 3866546.
E-mail address: yww7@cdc.gov (B.A. Slaker).

http://dx.doi.org/10.1016/j.ijmst.2016.09.032
2095-2686/

study is to determine what photogrammetry methodology, camera settings, and lighting scenario will work in an underground coal mine environment, considering the potential equipment limitations.

2. Experiment methodology

Three sites were selected at the NIOSH Safety Research Coal Mine, shown in Fig. 1, to test the best methods for applying photogrammetry as a measurement tool for rib characterization in underground coal mines. The mine entries are approximately 4.3 m wide and average 2 m in height. Several objectives were identified: determining cleat orientation and spacing, measuring rib displacement, and performing routine length measurements. Ideally the measurements could be performed quickly and easily, so the experiments tested methods of photography that vary in data collection time and complexity.

A Nikon D5500 DSLR camera was used with an AF-S NIKKOR 35 mm 1:1.8G lens. This camera is not purposefully configured for photogrammetry. The following camera settings were common to all the experiments: fine image quality, 6000 × 4000 resolution, automatic bracketing, HDR off, automatic active d-lighting, auto white balance, standard picture control, automatic focus, auto-area (AF) mode, point metering, 0 flash compensation, and 0 exposure compensation. The settings that were changed on an experiment-specific basis, to compensate for lighting and depth of field changes, are detailed in their respective sections.

Two lighting systems were independently investigated: the camera's onboard flash and an external LED lighting system. The LED lighting system is currently under development by NIOSH for use in underground coal environments and consists of twelve small LEDs mounted to a singular circular frame with an attached handle. The LEDs are angled in a way to evenly distribute light across a coal rib. The even distribution of light allows the lighting system to be moved along with the camera without significantly changing the rib's appearance. When necessary, cap lamp lighting was also used to allow the camera to automatically focus.

2.1. Site A

The purpose of the Site A (Fig. 1) experiments was to obtain enough detail on a rib to measure cleat spacing and orientation. This was attempted using both the onboard flash for the Nikon camera and the external NIOSH LED lighting system. The camera settings used for each experiment at this location are shown in Table 1. All the reference objects used in these experiments are shown in Fig. 2.

Using the Nikon's onboard flash or an LED lighting system, hereafter called the LED lighting or simply LED, photographs were taken at varying heights and angles surrounding the corner of a pillar (Fig. 3). The perpendicular photographs were taken approximately 3 m from the rib, while the high-angle photographs were taken about 1.5 m from the rib. An area of rib visible in several of these photographs was selected for a measurement comparison between photogrammetry and traditional methods using six different features, labeled as M1 through M6. Most of these photographs were taken at an orientation perpendicular to the rib surface. However, several were taken at high angles-of-incidence to better capture the depth of the rib. These high angle-of-incidence photographs were taken at different F-stops to compare the changing depth of field focus. The shutter speed and ISO were adjusted to account for this change in light sensitivity. Additionally, a set of photographs was collected using an intentionally more haphazard approach without evenly spaced or angled photographs, with no regard for overlap, and using the camera's automatic settings. This was done to emulate a casual approach where the camera operator is minimally instructed on an ideal photogrammetry methodology. The regimented sets of photographs required

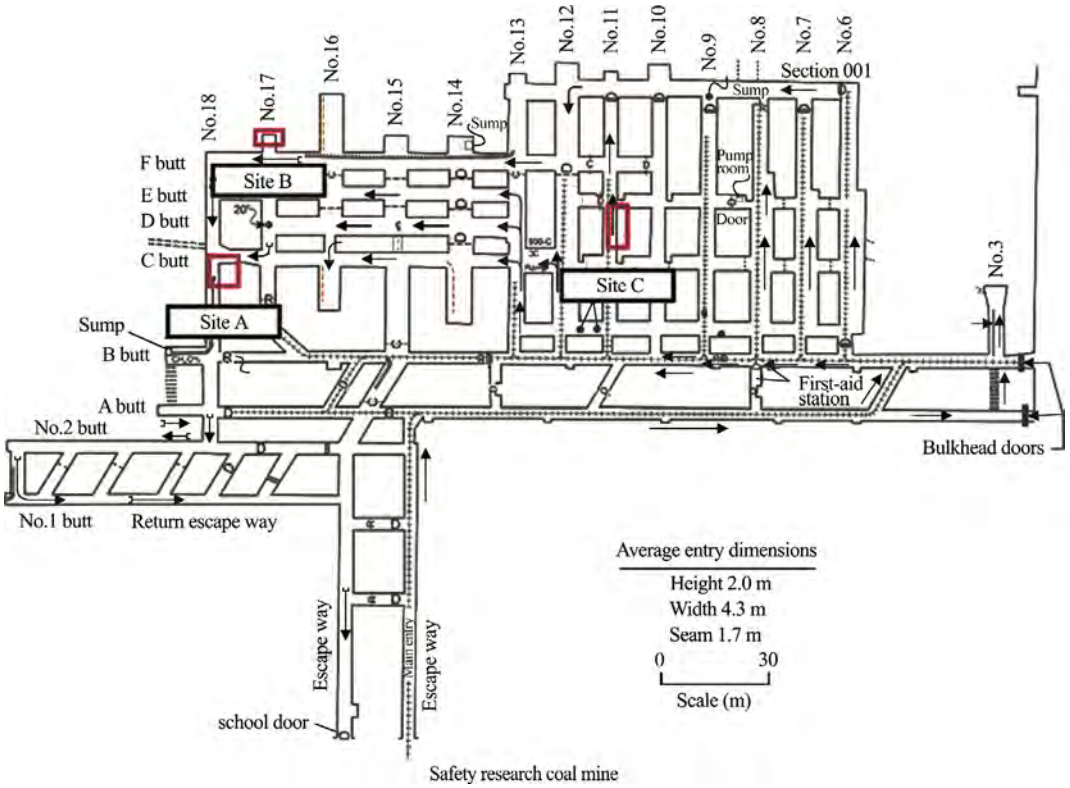

Fig. 1. Study sites at the safety research coal mine.

Table 1
Camera settings for Site A experiments.

Experiment	F-stop	Shutter speed (s)	ISO	Number of photograph
Flash	5	1/100	100	62
Flash w/F-stop adjust	5, 8	1/30	100, 200	62
LED	5	1/6	400	62
LED w/F-stop adjust	5, 8	1/6, 1/2	400	62
Automatic	1.8, 2	1/60	800–6400	23

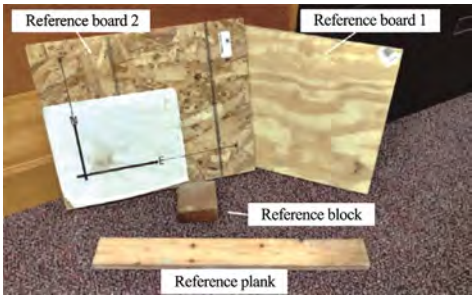

Fig. 2. Reference objects.

21 min each to collect while the automatic settings method required only 3 min.

2.2. Site B

The purpose of the experiment at Site B (Fig. 1) was to measure the coal rib displacement between photograph sets at varying lighting and distance conditions. For each of the conditions described, a set of photographs was collected prior to and after pieces of coal were removed from the photographed coal face. The camera settings used in this experiment are shown in Table 2.

A close set of photographs at approximately 3–4 m from the face and a far set of photographs at approximately 7–8 m from the face were collected using both lighting scenarios. The camera locations as well as the features that were measured are shown in Fig. 4. At both locations the camera height was varied by 0.3 m. The distance from the face for the farther set was chosen as the minimum distance where the entire face is visible in each photograph. With a 35 mm lens that minimum distance was between 7 and 8 m. The close experiment required 4 min while the far experiment required 2 min.

As shown in Fig. 4, the area of the rib that would be displaced is highlighted in red in the "before" photograph.

Table 2
Camera settings for Site B experiments.

Experiment	F-stop	Shutter speed (s)	ISO	Number of photograph
Far flash (FF)	5	1/100	100	6
Far LED (FL)	5	1/4	400	6
Close flash (CF)	5	1/100	100	14
Close LED (CL)	5	1/4	400	14

2.3. Site C

The purpose of the experiment at Site C (Fig. 1) was to determine how many photographs are necessary to adequately reconstruct a rib face. Ideally, as few photographs as possible would be taken to reduce data collection and processing time if more photographs being taken would result in insignificant changes to reconstruction accuracy. This experiment follows a methodology that is likely to be most practical when photographing long sections of mine travel ways because it consists of a simple, quick, and consistent procedure. Photographs of a 17.5 m length of rib were taken at approximately 4 m from the rib face, moving parallel

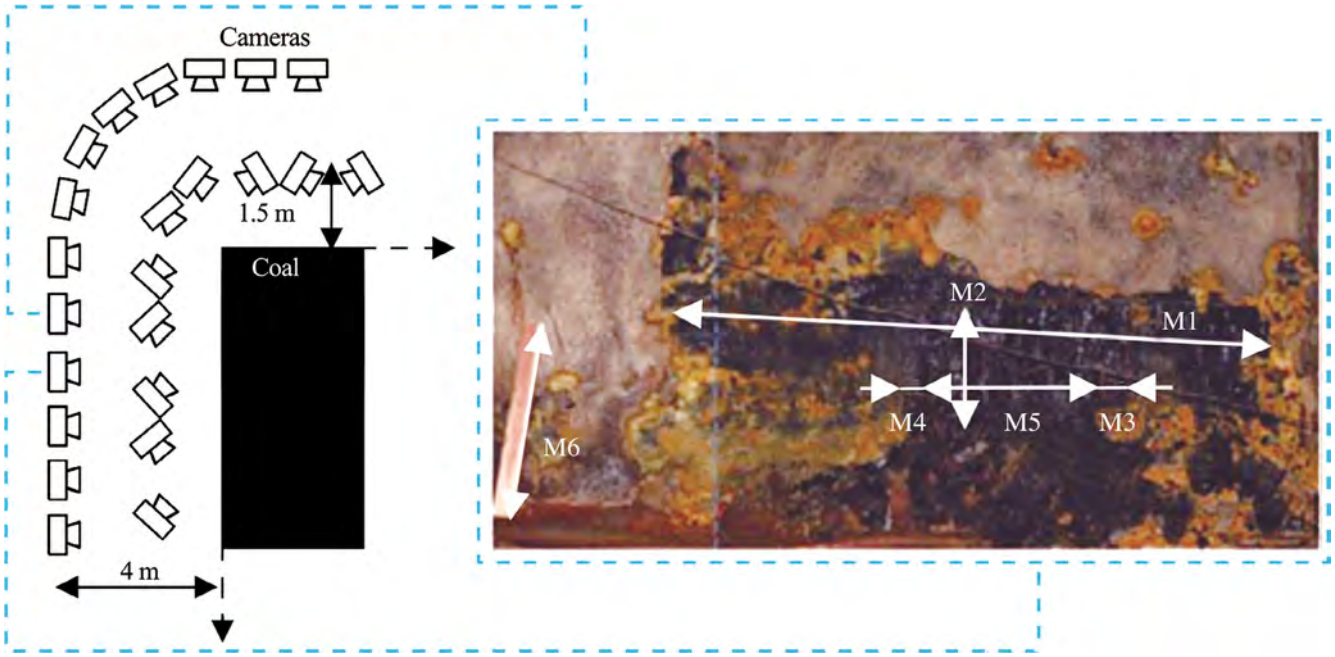

Fig. 3. Camera locations at Site A along with a composite photograph containing the distances selected for measurement comparison.

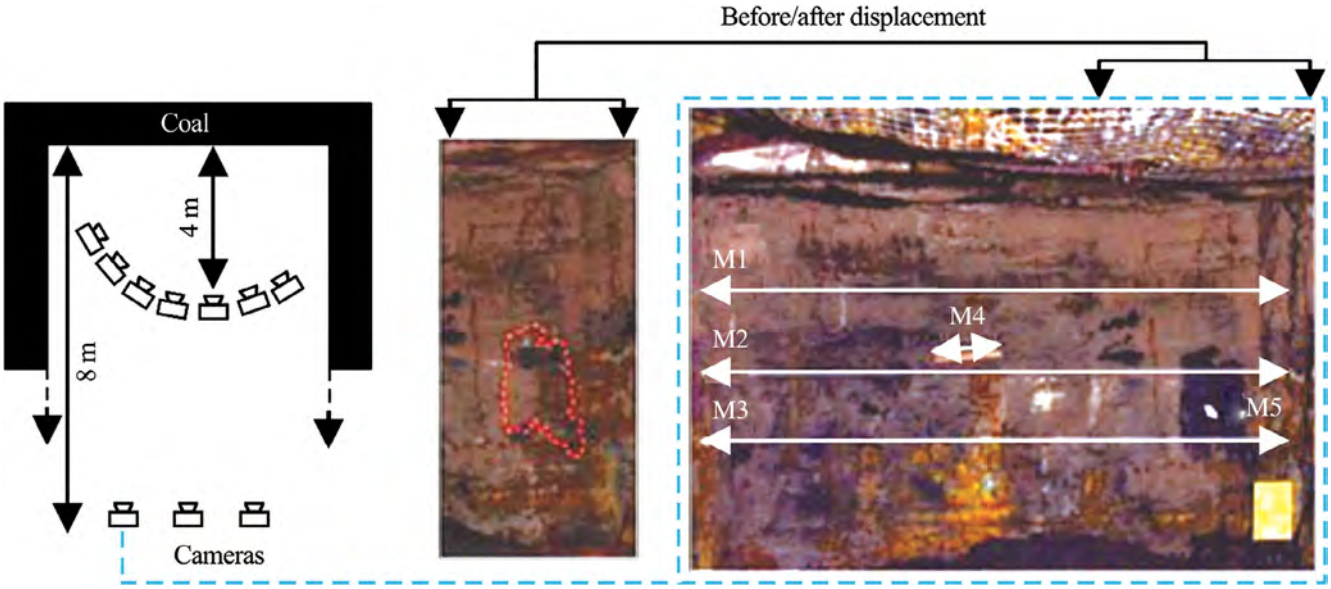

Fig. 4. Camera locations and photographs at site B showing the features selected for measurement comparisons.

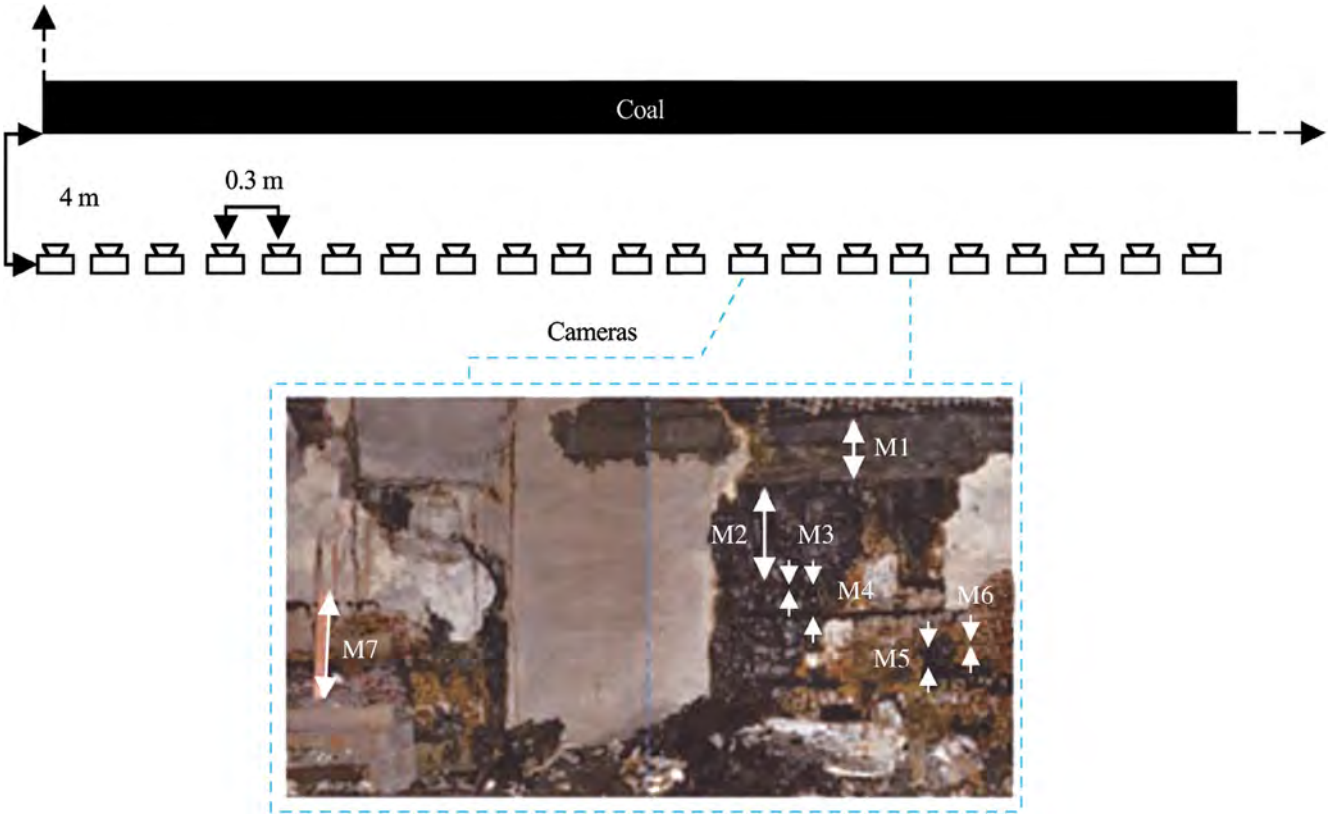

Fig. 5. Camera locations at Site C along with a composite photograph containing the distances selected for measurement comparison.

to the rib approximately 0.3 m for each camera location, as illustrated in Fig. 5. Seven features are shown that were selected for measurement comparisons. The camera settings used in this experiment are shown in Table 3.

Photographs were taken with both lighting conditions (flash and LED) and viewing angles perpendicular to the rib and camera positions following a line parallel to the rib. Capturing the entire roof-to-floor extent was not possible with a 35 mm lens and DX sensor. To correct for this, a line of photographs was taken angled slightly toward the floor and another line of photographs was taken angled slightly toward the roof. The roof photograph line was positioned approximately 0.3 m above the floor photograph line. Approximately 17 min was required to collect each of the flash and LED lighting sets.

Table 3
Camera settings for Site C experiments.

Experiment	F-stop	Shutter speed (s)	ISO	Number of photograph
Flash	5	1/100	100	84
LED	5	1/3	400	93

3. Results

Point cloud reconstructions were generated for all three sites using Agisoft Photoscan professional edition [10]. Agisoft Photoscan is a stand-alone software product that performs photogrammetric processing of digital images and generates 3D spatial data. Reference boards (Fig. 2) were used to scale the scenes. The scenes were initially reconstructed on an arbitrary coordinate system, using a corner of the board as the origin. This arbitrary coordinate system is sufficient for measuring lengths, but undesirable when time-lapse monitoring is being performed or geologic feature orientation is important. To address this common need, all the reconstructions were set to the same coordinate system by picking four (three are required, but more points reduce error) common features and assigning the same coordinates to each. The average error in the reference points ranges from 0.5 to 1.5 mm.

The measurements were made first in the software and later in the field. This approach allowed for marking measurement points on photographs and reproducing that measured length underground with more precision than would be possible by simply estimating locations or marking the rib. It should be noted that many features, such as a shale layer near the roof, have varying dimensions depending on where they are measured, and small changes in the measurement location may affect results. Efforts were made to pick the same location in all of the photogrammetric reconstructions; however, there is an error with manual picking due to imprecise point selection and the point cloud density, likely in the range of several millimeters for similar applications. Differences between tape or laser range meter measurements and photogrammetry measurements may be significant due to tape bending or sag, slight inconsistencies in measured location, difficulties in obtaining laser line-of-sight, and precision of the measuring device. These inconsistencies could range from less than one millimeter for shorter measurements to several centimeters for longer measurements.

Table 4
Length measurements of different coal rib features at Site A under different lighting conditions.

Feature	Flash experiment (cm)	LED experiment (cm)	Field (cm)
M1	195.7 (+1.1%)	195.7 (+1.1%)	193.5*
M2	32.5 (+0.9%)	32.6 (+1.2%)	32.2
M3	5.9 (−11.9%)	6.4 (−4.4%)	6.7
M4	5.8 (−6.4%)	5.3 (−14.5%)	6.2
M5	61.6 (+2.7%)	61.6 (+2.7%)	60.0
M6	55.0 (+0.7%)	55.0 (+0.7%)	54.6

Note: * means that field measurement was performed with a laser instead of tape measure.

3.1. Site A

Several features were selected for measurement due to their prominence and relevance to coal rib characterization. Most features are shown in Fig. 3, and their lengths are shown in Table 4. Additionally, a face cleat orientation at location M3 was calculated, and was compared to compass measurements. The face cleat orientation at M3 was measured with a Brunton compass and calculated by fitting a plane through three points manually chosen from the point cloud. The calculated dip was 89.24° and the measured dip was 89°. The calculated strike was 127.35° and the measured strike was 130°. The calculated angles are considered to be within the margin of error for the compass angle measurement method. Features M3 and M4 are cleat spacing measurements, and have among the highest margin of error when represented by a percentage of the total length. However, these results and those presented later suggest that the difference in measured and calculated distances is a function of errors that are minimally related to the magnitude of measurement span.

The automatic flash method did work for the reconstruction, but not reliably. The automatic flash method is distinctly different from the manual flash method, reported as "flash experiment" in Table 4, in that it allows the camera to select appropriate settings for controlling exposure. Several photographs were often discarded in the reconstruction process and required manual alignment. The two most probable reasons for this are the cap lamp obscuring sections of the photograph, as shown in Fig. 6, and the intentionally haphazard camera locations resulting in insufficient overlap. A cap lamp directed on the rib surface may be necessary when using an automatic focus, which can cause that part of the photograph to become overexposed. When using manual settings, the exposure can be changed to mitigate the effect of the cap lamp. It may also be beneficial, regardless of method, to reduce the cap lamp intensity when an automatic focus is being used.

The F-stop setting becomes more relevant as the depth of field of the scene grows, as low F-stops will cause objects far from the focus to become blurred. This effect is highlighted in Fig. 7 where a segment of the photograph from the foreground is compared across two different F-stops. If the rib is the only subject, and photographs are being captured perpendicular to it, low F-stops may be used. If the roof and floor are also being analyzed, or high angle-of-incidence photographs are being taken, a higher F-stop will be necessary to improve the detail across the scene. This may not be immediately apparent when viewing previews on a

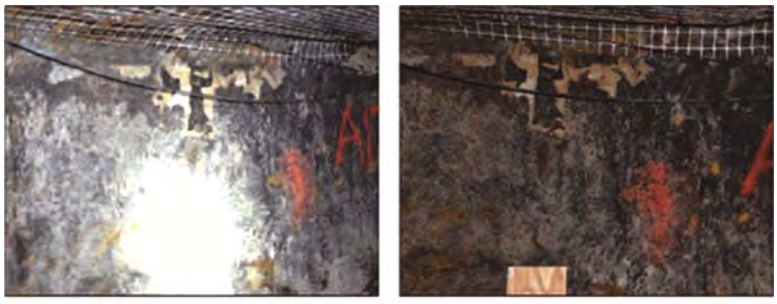

(a) Automatic flash (b) Manual flash

Fig. 6. Exposure comparison for automatic and manual modes when using a cap lamp to focus.

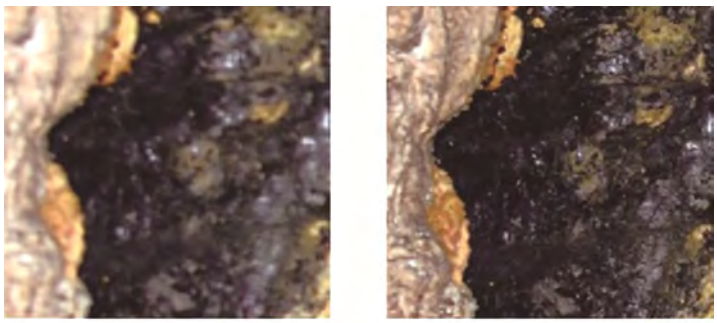

Fig. 7. F-stop comparison using flash lighting.

camera underground, but will be obvious during post-processing. This effect is difficult to quantify, but comparing the reconstructions using the higher F-stop and lower F-stop, the higher F-stop point cloud shows a higher-quality dense reconstruction with a larger reconstructed area.

As shown in Fig. 7, photograph segments are both natively 480×560 pixels, from the foreground of a 6000×4000 pixel image.

3.2. Site B

Five different features were measured and reported at Site B, including: entry width measurements (M1, M2, and M3), a reference plank measurement (M4), and a displacement depth measurement (M5), as shown in Fig. 4. These measurements were made for the far flash (FF), close flash (CF), far LED (FL), and close LED (CL) scenarios before and after coal was removed from the face to simulate spalling. Roof-to-floor measurements were also performed, but these were difficult to reproduce reliably in the photogrammetry due to a dip in the roof which blocked line of sight to the rib/roof intersection beyond. The variability of mine roof, floor, and rib geometries makes any comparison of dimensions only useful for determining changes in that surface.

Displacement magnitude is reported as one point, but each reported measurement consists of three points sampled in a horizontal line across the center of the displaced area, which were measured to obtain an average displacement. Additionally, three control points at the same height above the floor approximately 2 m away from the displaced area, where no change should have occurred, were measured in the same way. The irregular area that was created by removing coal from the face was difficult to measure in the field by hand, but an approximate depth measurement of 6 cm into the displaced area was made. This roughly matches the average displacements measured in photogrammetry shown in Tables 5 and 6.

The difference between the field and calculated distances for features M1, M2, and M3 are expected because the same point was not used for both measurements. The purpose of this comparison, then, is to determine if entry width measurements can be reasonably determined through photogrammetry. If tape measure or laser measurements are otherwise trusted, the magnitude and range of distances obtained through photogrammetry are reasonably similar, considering the natural variation in coal rib depth.

First considering the control points, there is an inherent error to the photogrammetric measurements. This error is likely due to: reconstruction, orientation and scaling, point cloud density, and point selection precision. Reconstruction error will be dependent on the software and quality of input photographs. Most software packages will not allow significant modification of the underlying algorithms, so improving this source of error will require careful setting selection and ensuring that input photographs are acceptable. Orientation and scaling error can be minimized by choosing more reference points. Point cloud density is affected by the software and its settings, number of photographs, resolution of photographs, and distance to the subject. The point cloud density could have been increased in the Agisoft Photoscan software; however, this was not done, so as to maintain consistent reconstruction settings across all experiments.

Given the number of tests and closeness of the results, it is difficult to conclude definitively that there is a difference between the close-to-far and flash-to-LED scenarios; however, any difference appears to be small compared to the magnitude of typical convergence or displacements. An average absolute difference of 0.56 cm is observed between the close and far experiments, while an average absolute difference of 0.08 cm is observed between the flash and LED light scenarios. These measurements suggest that the difference between a consistent LED lighting and the camera flash is very small, with 0.08 cm being within acceptable limits for many underground measurements.

One possible explanation for the larger difference of 0.56 cm is the ratio of camera-to-camera distance to the rib-to-camera distance, also known as the base/height ratio. As the height grows significantly larger than the base, the accuracy of resolving the rib depth is reduced [2]. The point cloud density may also be respon-

Table 5
Length measurements of different coal rib features at Site B under different lighting conditions (cm).

Feature	FF	CF	FL	CL	FF time 2	CF time 2	FL time 2	CL time 2	Field
M1	445.2	447.6	446.6	NM	441.5	445.2	440.7	441.5	433.4*
	+2.7%	+3.2%	+3.0%		+1.9%	+2.7%	+1.7%	+1.9%	
M2	441.5	437.3	436.5	NM	445.1	437.5	444.4	444.6	432.8*
	+2.0%	+1.0%	+0.8%		+2.8%	+1.1%	+2.7%	+2.7%	
M3	437.1	NM	443.0	NM	436.6	NM	436.8	437.3	442.0*
	−1.1%		+0.2%		−1.2%		−1.2%	−1.1%	
M4	54.9	55.2	54.8	55.1	54.9	55.2	54.7	55.1	54.6
	+0.5%	+1.1%	+0.4%	+0.9%	+0.5%	+1.1%	+0.2%	+0.9%	

Note: Time 2 represents the photographs taken after coal was removed from the rib; NM signifies that the measurement was not performed; and * means the field measurement was performed with a laser instead of tape measure.

Table 6
Depth of the induced displacement occurring at M5 (cm).

Feature	FF to FF2	CF to CF2	FL to FL2	CL to CL2
M5	7.15	6.51	7.05	6.57
Control	0.23	0.14	0.21	0.06

sible for the difference in measurements because the distance being measured is point-to-point, which is illustrated in Fig. 8. Sparser point clouds are less likely to contain points at the precise location. The point cloud density on the rib is approximately 1,000,000 points/m^2 for the close set of photographs and 130,000 points/m^2 for the far set of photographs.

3.3. Site C

Seven features were evaluated at Site C (Fig. 5; Table 7). The ½ flash and ½ light data represent measurements from a reconstruction that excludes every other photograph from the original set. All of the features were chosen because they are easily identifiable in the photographs. The photographs from the two lighting scenarios, flash and constant LED, were subsampled to determine the minimum number necessary, which was a 50% reduction in this experiment. Anything less resulted in a loss of connectivity between the photographs and an incomplete reconstruction.

The resulting distance measurements are comparable to those found at the other sites with the exception of M1. Nothing in the photographs, photogrammetric reconstruction, or points selected indicates that there is an error associated with that calculated distance, and a difference of approximately 6 cm is outside the range of expected error. It is most likely that this feature was incorrectly measured or recorded in the field. Feature M7, the reference board, has a very similar calculated and measured length, which can also be seen in feature M6 in Table 4 and M4 in Table 5. This object has the highest field measurement precision because it can be handled, cannot be easily deformed, and can be repeatedly measured. The consistent overestimation of its length suggests a systematic scaling error of around 0.5%.

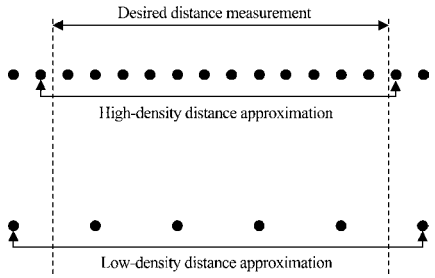

Fig. 8. Example of high-density point clouds yielding more precise distance measurements.

A redundant number of photographs for the flash and LED lighting scenarios, 84 and 93 respectively, were captured. These were then reduced to determine the minimum amount of overlap required for a reconstruction, and the approximate distance that could be traveled between each photograph. Reducing the number of photographs by 50% appeared to yield the most consistent results. Reconstruction using fewer photographs was possible; however, it required more manual effort on the part of the researcher in post-processing, which is far less time-efficient than taking more photographs.

It was hypothesized that decreasing the number of photographs would decrease the precision of the results. After processing the photographs, the number of photographs appeared to negligibly affect the precision of measurements. Table 7 shows the measurements calculated for the full and reduced photograph sets. The differences found between the 50% photograph reduction and the full photograph set are similar to the differences found in the previous experiments, suggesting that the reduction in photographs does not introduce significant additional error. In the reduced photograph set, the percentage overlap between photographs varies between approximately 55% and 75%. Typically, overlaps of greater than 60% are ideal; however, increasing overlap will be necessary if the edges of the photograph are poorly exposed or out of focus. If photographs are taken using a similar approach to that described for Site C, a simpler method would be to ensure that every third photograph shares points with the two photographs preceding it.

Another noteworthy finding was the difficulty of obtaining level photographs. Counter intuitively, a tripod may decrease the consistency of the photographs, creating gaps in the reconstruction. The uneven floor, especially as the tripod nears the far rib, requires constant leveling to ensure orderly photographs. If the lighting condition permits a fast shutter speed, taking photographs by hand may be the optimal method. Level photographs are not essential, and any orientation may be used if it best suits the mine geometry, but it is typically easier to ensure sufficient overlap by orienting the long axis of the photograph with the long axis of the opening.

3.4. Exposure considerations

Managing the camera exposure is one of the most important components of the photogrammetry survey. As shown in Figs. 6 and 7, the decision to use automatic camera settings or choosing the wrong settings can have a significant impact on photograph quality. Shutter speed, ISO speed, and aperture (specified by F-

Table 7
Length measurements of different coal rib features at Site C under different lighting conditions and with different numbers of images at each site (cm).

Feature	Flash	LED	1/2 flash	1/2 LED	Field
M1	32.7	32.7	32.7	32.6	38.6
	−15.3%	−15.3%	−15.3%	−15.5%	
M2	56.9	57.0	57.3	57.0	56.7
	+0.3%	+0.5%	+1.1%	+0.5%	
M3	16.1	15.8	16.1	16.1	15.7
	+2.5%	+0.6%	+2.5%	+2.5%	
M4	8.5	8.4	8.5	8.4	8.9
	−4.5%	−5.6%	−4.5%	−5.6%	
M5	1.6	1.6	1.5	1.5	1.9
	−15.8%	−15.8%	−21.0%	−21.0%	
M6	0.8	0.8	1.1	0.6	1.3
	−38.5%	−38.5%	−15.4%	−53.8%	
M7	54.8	54.6	54.8	55.1	54.6
	+0.4%	0	+0.4%	+0.9%	

stop) are the most important settings for controlling exposure. In the practical experience of the authors, the following guidelines for camera settings should be applied in an underground coal mine environment:

(1) *Shutter speed:* a shutter speed faster than 1/60 s has been ideal for handheld photography with a 35 mm lens, while higher speeds are necessary with longer focal lengths and much lower speeds are acceptable with a tripod. A lower shutter speed will usually not have an effect on exposure when using the camera flash as a light source.
(2) *Focal ratio:* F-stop values should be set as high as lighting conditions allow. Most tests during this research were performed at an F-stop between 5 and 8 as a compromise between lighting and clearness of the foreground. Different lenses may perform optimally at different F-stops, and should be experimented with to find a focal ratio that provides the most image clarity. Lower F-stops are certainly usable, but care must be taken for photographs where the subject extends toward or away from the camera.
(3) *ISO speed:* lower ISO speeds are always preferable if lighting allows, with minimal graininess occurring in the 100–400 range.

As shown in Tables 1 and 2, a fully automatic camera setting may choose extreme F-stop and ISO values to compensate for the low light environment. If the camera allows, limiting the range of automatic settings will likely be beneficial. The values suggested previously should be loosely applicable to a wide range of cameras, but they will vary slightly depending on camera model and lens focal length.

4. Conclusions

A suite of experiments were performed at varying test sites to determine a strategy that best works for performing photogrammetry with a commercially available DSLR camera in an underground coal mine. These experiments were performed at the NIOSH Safety Research Coal Mine using a Nikon D5500 with a 35 mm lens. Three-dimensional reconstruction was performed using Agisoft Photoscan professional edition. Measurements were made from the reconstructed scene and those measurements were compared to measurements made in-mine with a tape measure and laser rangefinder.

Different factors were hypothesized to affect the measurement accuracy: lighting scenario, distance to subject, and overlap between photographs. There were seventeen experiment pairs where photographs were taken in the same manner using both LED and flash lighting. Changing the light condition between these two did not appear to cause a meaningful difference in measurement accuracy when using the LED lighting scenario or onboard flash lighting scenario. The average difference between flash and hand measurements was −0.07 cm with a standard deviation of 1.67 cm. The average difference between LED and hand measurements was −0.12 cm with a standard deviation of 1.67 cm. The average difference between flash and LED measurements was 0.05 cm with a standard deviation of 0.21 cm.

The distance to subject was tested in four different experiment pairs, all at Site B. Decreasing subject distance was found to increase the point density of the coal surface, due to a higher pixel density per unit area of the subject. The increased point density, however, did not significantly affect measurement precision at this photograph resolution. Given the physical constraints of an underground coal mine, it is likely that any modern DSLR camera will have a sufficient resolution at the maximum allowable perpendicular distance to a rib face for all but the smallest or most precise measurements.

The overlap between photographs that is necessary for a three-dimensional surface to be reconstructed was indirectly tested at Site C. The overlap was inconsistent between photographs due to the uneven terrain, so an approximate required overlap was inferred. The linear distance between camera locations was approximately 0.3 m for the full sets, and 0.6 m for the half sets. There does not appear to be a fixed amount of overlap required between the photographs, but with similar entry geometries, 0.6 m between photographs at 5 m away from the rib would be ideal as a "good practice" guideline to allow for greater than 2/3 overlap in successive photographs.

Photogrammetry has been effective across a variety of camera settings, distances, and orientations, with the largest limiting factor being the amount of overlap between photographs. Differences between measurements from 3D reconstructions and hand measurements may serve to highlight the inaccuracy of traditional tape measure or laser measurements more than they show the inaccuracy of photogrammetry. Unfortunately, it would be difficult to quantify the error associated with more traditional measurements, as they will vary with the person performing them. As a result, this work is not intended to show the precision of photogrammetry, but rather to show that photogrammetry can be used in an underground coal mine environment and delivers comparable results to measurement techniques already being performed. Methodology and exposure guidelines presented here should be sufficient to perform a photogrammetry survey in most underground coal mining situations where DSLRs are approved for use.

Disclaimer

The findings and conclusions in this report are those of the authors and do not necessarily represent the views of the National Institute for Occupational Safety and Health.

References

[1] Jones T, Mohamed K, Klemetti T. Investigating the contributing factors to rib fatalities through historical aAnalysis. In: Proceedings of the 33rd international conference on ground control in mining. Morgantown, West Virginia; 2014. p. 113–22.
[2] Luhmann T, Robson S, Kyle S, Boehm J. Close-range photogrammetry and 3D imaging. 2nd ed. Walter de Gruyter; 2014.
[3] Atkinson KB. Close range photogrammetry and machine vision. Dunbeath (Caithness, Scotland): Whittles Publish; 1996.
[4] Styles TD, Zhang Y, Stead D, Elmo D, Robert D, Yanske T. A photogrammetric approach to brittle fracture characterization in mine pillars. In: Proceedings of 44th US Rock mechanics symposium and 5th US-Canada rock mechanics symposium. Salt Lake City, Utah; 2010.
[5] Kim J, Kim D, Won K. Measurement of joint orientations of tunnel working face using a new photogrammetric technique. In: Proceedings of the 40th US symposium on rock mechanics; 2005.
[6] Petteri Somervuori ML. Modern 3D photogrammetry method for rock mechanics. Geological Mapping 3D Model and Documentation of Open Pit Faces and Tunnels; 2010.
[7] Benton DJ, Iverson SR, Martin LA, Johnson JC, Raffaldi MJ. Volumetric measurement of rock movement using photogrammetry. Int J Min Sci Technol 2016;26(1):123–30.
[8] Slaker B, Westman E, Ellenberger J, Murphy M. Determination of volumetric changes at an underground stone mine: a photogrammetry case study. Int J Min Sci Technol 2016;26(1):149–54.
[9] Slaker B, Westman E, Fahrman B, Luxbacher M. Determination of volumetric changes from laser scanning at an underground limestone mine. Min Eng 2013;65:11.
[10] AgiSoft LLC. Agisoft PhotoScan Professional Edition (Version 1.2.3). Retrieved from <www.agisoft.com>; 2015.

International Journal of Mining Science and Technology 27 (2017) 91–99

Contents lists available at ScienceDirect

International Journal of Mining Science and Technology

journal homepage: www.elsevier.com/locate/ijmst

Analysis of the design and performance characteristics of pumpable roof supports

Batchler Timothy *

NIOSH, Office of Mine Safety and Health Research, Pittsburgh, PA 15236, USA

ARTICLE INFO

Article history:
Received 9 June 2016
Received in revised form 1 September 2016
Accepted 10 October 2016
Available online 16 December 2016

Keywords:
Pumpable
Roof support
Performance characteristics
Secondary support

ABSTRACT

Pumpable roof supports are currently being used to provide a safe working environment for longwall mining. Because different pumpable supports are visually similar and installed fundamentally in the same manner as other supports, there is a tendency to believe they all perform the same way. However, there are several design parameters that can affect their performance, including the cementitious material properties and the bag construction practices that influence the degree of confinement provided. A full understanding of the impact of these design parameters is necessary to optimize the support application and to provide a foundation for making further improvements in the support performance. This paper evaluates the impact of various support design parameters by examining full-scale performance tests conducted using the National Institute for Occupational Safety and Health (NIOSH) Mine Roof Simulator (MRS) as part of manufacturers' developmental and quality control testing. These tests were analyzed to identify correlations between the support design parameters and the resulting performance. Based on more than 160 tests over 7 years, quantifiable patterns were examined to assess the correlation between the support dimensions, cementitious material type, wire pitch, and single-wall vs. dual-walled bag designs to the support capacity, stiffness, load shedding events, and yield characteristics.

1. Introduction

Developed in the 1990s, the first major use of pumpable supports systems in U.S. longwall operations was in the support of bleeder entries [1]. Since then, they have been utilized as yieldable concrete supports to provide a safe working environment for longwall mining gateroads, bleeders, and emergency escapeways while also maintaining adequate ventilation pathways. The basic structure of pumpable roof supports has remained unchanged over the years. Formed in place with a two-part fast-setting grout, the support material can be pumped into a containment bag from several thousand feet away, often through surface boreholes. The containment bag then acts as a form to fill the support and provides confinement to the grout during loading and after failure. Pumpable roof supports provide full contact with the mine roof and floor, which eliminates the need for secondary material to establish proper roof contact (see Fig. 1). They provide a high peak load capacity and a sustained, confinement-controlled yield behavior while maintaining stable ground conditions, which is essential to underground mining operations.

Over the years, considerable research has been conducted to develop pumpable support technologies and to evaluate their performance characteristics to improve the support design. Performance traits, installation patterns, and ground control observations in various geological and mining conditions were evaluated to determine the support performance characteristics and correlation to observed ground responses [2–4]. To examine performance, the load displacement characteristics of the pumpable roof support can be determined from full-scale testing conducted using the National Institute for Occupational Safety and Health (NIOSH) Mine Roof Simulator (MRS) located in Bruceton, PA [1].

Because pumpable supports all look similar, the tendency is to think that they all perform the same. However, several design parameters can affect the performance characteristics of the pumpable support system. This paper evaluates the impact of various support design parameters by examining full-scale performance tests conducted at the NIOSH MRS as part of various product development and quality control testing. These tests were analyzed to identify correlations between the support design parameters and the resulting performance. Based on more than 160 tests over 7 years, quantifiable patterns were examined to assess the correlation of the support dimensions, cementitious material type, wire

* Tel.: +1 412 3866844.
E-mail address: tbatchler@cdc.gov

http://dx.doi.org/10.1016/j.ijmst.2016.10.003
2095-2686/

Fig. 1. Pumpable roof supports in a longwall recovery room.

pitch, and single-wall vs. dual-walled bag designs to the support capacity, stiffness, load shedding events, and yield characteristics.

2. Design features

For many years, pumpable roof supports have been installed in mines to support the roof. The supports are designed to be installed in place using a pumpable cementitious grout. Typically, a two-component material is pumped from a surface installation through an access borehole into a containment bag to form the support, with the capability to pump the material a distance of over 5486 m [3]. The unfilled support bags are transported into the mine in a collapsed configuration, minimizing the transportation needs to the installation site. During installation, the bags are secured to the mine roof and then extended down to the floor. The solidified grout material captured by the containment bag provides a full support column between the mine roof and floor without the need for any additional materials, providing a significant advantage over most other support designs.

Pumpable roof support systems have evolved during the last 20 years, with improvements made to the bag design and several variations of cementitious materials in an effort to optimize cost and performance. Currently, there are two basic types of material used: calcium-sulfo-aluminate (CSA) and Portland-based cementitious grouts. The CSA grout contains no Portland material and generally has an inherently faster setup time and strength gain than Portland grouts without the use of accelerating additives. Both materials are pumped in separate two-part mixes such that the reactive chemistry only occurs once the materials are mixed together just prior to entering the support bag. One interesting physical difference between the two materials is that some samples of the Portland-based materials severely decompose (lose structural integrity) when exposed to air, while the CSA grout once cured is insensitive to air and does not physically deteriorate. The primary performance difference is that the supports made with the higher-modulus CSA material achieve peak compressive strength with less displacement, providing increased support stiffness compared to the supports constructed from Portland-based material.

Temperature can play a significant role in the support installation process. Most grouts are temperature-sensitive in terms of the reactive chemistry, which affects both the setup time and the material strength when the water temperature used to make the grout slurries falls beyond the required specifications. Typically, a water heater at the surface pumping station is used to ensure the water is the proper temperature in colder weather. Depending on the setup time, supports are often filled in several lifts. If the grout does not set up fast enough, the bag will tend to bow outward from the roof to the floor, potentially degrading the capacity of the support by as much as 10% [1].

A high loading stiffness with a sustainable residual load through several centimeters of convergence is one of the universal design features of pumpable supports. The high loading stiffness causes the support to reach a peak load capacity within a short amount of convergence. For a passive roof support, this is beneficial to roof control as the support resistance is mobilized quickly to work to control the roof deformation. The peak load is typically followed by a sequence of load shedding events, which results in sharp drops in load. These sudden drops in load are caused by the brittle grout fracturing induced from the stress of convergence. The subsequent residual load behavior is dependent on the confinement and integrity of the support bag. A full understanding of the impact of these design features is necessary to optimize the support applications and to provide a foundation for making improvements in the support performance.

3. Performance characteristics

The performance characteristics for pumpable roof support entail four main factors, as illustrated in Fig. 2, namely stiffness, peak load capacity, load shedding events, and residual load characteristics.

Stiffness is defined as the resistance offered by an elastic body to deformation. The pumpable support loading stiffness is calculated using the linear portion of the loading cycle prior to grout failure and load shedding events (see Fig. 2). It measures the capacity of the support to develop load as a function of convergence. Stiffness is important in designing supports since, as passive supports, the load resistance is only developed through convergence of the mine opening, and excessive convergence leads to unstable ground conditions. Therefore, high load stiffness is desirable.

Peak load capacity is the maximum capacity of the support and is often referred to as the support strength. The compressive strength of the cementitious grout and the confinement pressure provided by the pumpable support bag control the peak load capacity. When the compressive strength of the grout is exceeded, the grout will fracture and the support will abruptly shed some of its load capacity.

As with most structures made from brittle material, failure is associated with a major drop in load once the compressive and shear strength of the material are exceeded. This is common in all pumpable supports. As illustrated in Fig. 2, the support quickly recovers from the initial load shedding event, restoring a loading stiffness that is very close to the pre-failure loading stiffness. It is believed that the restoration of the support stiffness following a load shedding event is attributed to reestablishment of confining pressure caused by the dilation of the support body and resistance provided by the bag and wire wrap system. As shown in Fig. 2, this restoration of confinement and subsequent loading stiffness may be sufficient to allow continued development of load capacity. The peak load capacity occurs when this confining pressure can

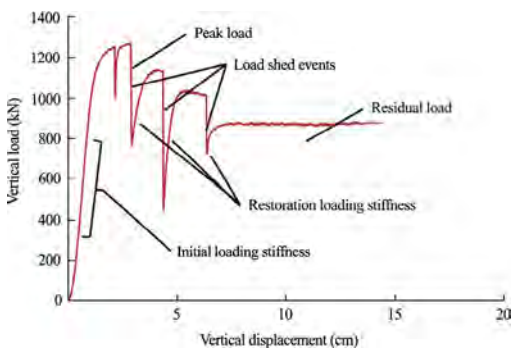

Fig. 2. Illustration of performance characteristics for a pumpable roof support loading profile.

no longer be fully restored. The load shed associated with the peak load is generally, but not always, the largest of the set. As illustrated in Fig. 2, the restoration loading stiffness following the peak load shedding event is reduced. The residual load will vary depending on the severity of the grout fracturing and the capability of the bag and wire to maintain confining pressure.

A progressive failure behavior occurs through a series of subsequent load shedding events following the peak loading. The continued bulking of the fractured grout material stretches the bag and wire wrap, resulting in a tendency of continued decreased stiffness during load restoration following the load shed events (Fig. 2). A load shed event is defined as a sudden drop of load capacity of over 222 kN within less than 0.76 cm of displacement. This action of successive load shedding and declining load restoration continues until the wire breaks, which generally occurs after several centimeters of convergence. Once the wire breaks, the bag will generally rip open, causing spillage of material out of the bag containment system and culminating in a more severe load shedding with little and often no increase in load following the event. The residual loading beyond this point depends on the severity of damage to the bag and wire containment system. The support often can provide a useful sustained loading through a few more centimeters of convergence once the wire is broken, but the capacity of the support is definitely compromised and less reliable that it was prior to the wire breaking event.

4. Design parameters

There are several design parameters that affect the performance characteristics of the pumpable support system. Based on more than 160 full-scale tests of various pumpable supports in the NIOSH MRS as part of various vendor developmental and quality control testing, quantifiable patterns were examined to assess the impact of the following design parameters: (1) cementitious material type, (2) support dimensions, (3) wire pitch, and (4) single-wall vs. dual-wall bag construction. It is important to note that a controlled experimental plan was not executed, and as such there is some potential for performance bias based on the variability in support designs included in the study population.

4.1. Cementitious material type

There is a strong relationship between the support performance and the cementitious material used for the support construction. Two different cementitious grouts (CSA and Portland) were evaluated in this study. Fig. 3 shows the mean and standard deviation of peak load capacities for supports constructed from the two cementitious grouts, along with the mean and standard deviation of the convergence at peak load capacity. In general, the peak load capacity of the CSA supports was higher than for the equivalent Portland supports. The mean peak load capacity of a standard 76-cm-diameter support with a 10-cm wire containment bag constructed from CSA material was 2389 kN. This compares to the mean peak load of the Portland-based material supports of 1735 kN. Therefore, for a 76 cm-diameter support, the CSA support provided about 38% more capacity than the Portland-based support. However, this magnitude of higher load capacity for CSA was not consistent for all the support sizes. The CSA material provided only 17% more capacity than the Portland-based material for the 69 cm-diameter and 76 cm-diameter supports. Conversely, the Portland material provided 10% more capacity than the CSA material for the 61 cm-diameter support. The likely reason for the higher peak load capacity for the 61-cm Portland supports was an increase in confinement of the bag system due to a closer wire wrapping around the support circumference. These tests provide

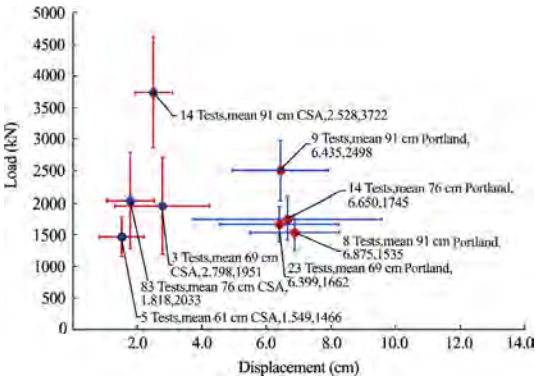

Fig. 3. Comparison of the peak loading capacity of the CSA and Portland-based supports.

some insight into the impact of the different cementitious materials on the peak load capacity of pumpable supports.

The pre-peak loading stiffness of the supports constructed from the CSA material was consistently higher than for the Portland material for all support sizes as documented in Table 1. Fig. 3 shows the mean and standard deviation of the convergence at peak load for each of the cementitious type pumpable roof supports. The supports constructed with CSA material exhibited a higher stiffness that resulted in the peak load being reached at much less displacement. The CSA supports reached peak loading between 1.5 and 2.8 cm of convergence compared between 6.3 and 6.9 cm for the Portland supports to reach peak loading.

Load shed events are sudden drops in support load capacity as the grout fractures from the induced stress from convergence. A major load shed event is defined as a sudden drop of load capacity of over 222 kN within less than 0.76 cm of displacement. Fig. 4 illustrates the number of load shed events generated prior to the peak load capacity for the CSA-based and Portland-based supports. These values represent the distribution of the percentage of the number of load shed events during a full-scale test using the full complement of tests available in this study. By far, the most common behavior is no load shed events prior to the peak loading. Since the peak loading is controlled by the grout strength, this would be the expected behavior. The lower occurrences of CSA load sheds prior to peak load could be attributed to the fact that the convergence at peak load capacity for CSA based material was 1.5–2.8 cm compared to 6.4–6.9 cm for the Portland-based material. The lower stiffness of the Portland-based supports gives more opportunity for a grout fracture to occur, resulting in a load shedding event.

Fig. 5 shows the distribution of the number of load shed events that occurred during a loading cycle following the peak load capacity and through 15.25 cm of convergence for the two cementitious grouts. It was rare for the CSA supports to exhibit no load shedding

Table 1
Comparison of support loading stiffness for CSA and Portland-based supports.

Diameter (cm)	Stiffness (kN/cm)	Peak load (kN)
(a) CSA-based material		
61	2250	1468
69	2270	1953
76	2338	2033
91	3888	3723
(b) Portland-based material		
61	904	1535
69	1114	1664
76	1228	1744
91	1308	2500

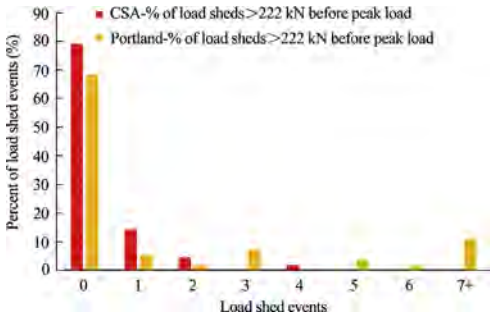

Fig. 4. Distribution of the percentage of the number of load sheds occurring prior to the peak load capacity for CSA and Portland-based supports.

events following peak loading (5%). Conversely, Portland supports exhibited no load shedding events 24% of the time. The most common number of load sheds for the Portland supports was one, which occurred 41% of the time, compared to the CSA material, which had two load shed events occurring 25% of the time. Similar to the trend showing fewer load sheds prior to peak load capacity, the higher number of load sheds for the CSA material could be attributed to the fact that the peak load capacity was achieved at a lesser displacement.

Fig. 6 shows the distribution of the number of load shed events (percentage) within the first 15.25 cm of convergence for both cementitious grouts. The highest percentage of load shed events for both materials was three. The Portland-based supports experienced three load shed events for 28% of the tests, and the CSA-based supports experienced three load shed events for 25% of the tests. The most common distribution of the number of load shed events was 1–3 for the Portland-based supports and 2–5 for the CSA-based supports. Overall, more load shed events occurred with the CSA-based supports than the Portland-based supports, suggesting that the CSA material tends to be more brittle than the Portland material.

One of the design features for a pumpable support system is to maintain a useful residual load carry capacity through several centimeters of convergence. Fig. 7 shows the representative average loading performance through 18 cm of convergence for a 76 cm-diameter CSA and Portland support with a 10-cm wire pitch construction in the support bag. The curve shows that the support load averaged over each 2.54 cm of displacement. For example, the average load for a CSA support between 11 and 14 cm was 1334 kN (see Fig. 7). This averaging process essentially diminishes the load shed events. These average performance curves are developed from the average load displacement response of 11 tests for the CSA curve and 9 tests for the Portland curve. Both support loading performances are characterized by an initial rapid increase in load

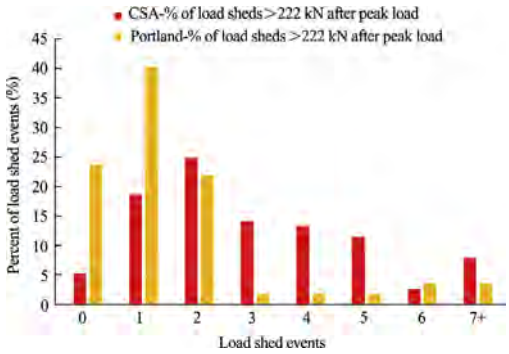

Fig. 5. Distribution of the percentage of the number of load sheds occurring after the peak load capacity for CSA and Portland-based supports.

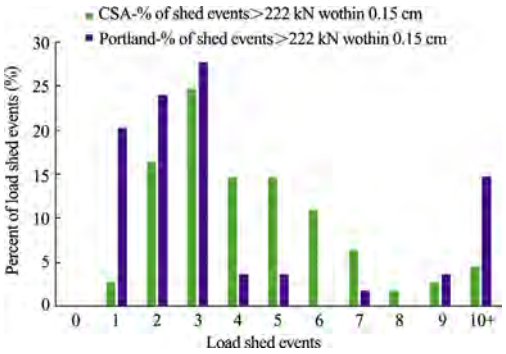

Fig. 6. Distribution of the percentage of the number of load sheds occurring from 0 to 15.25 cm of displacement for CSA and Portland-based supports.

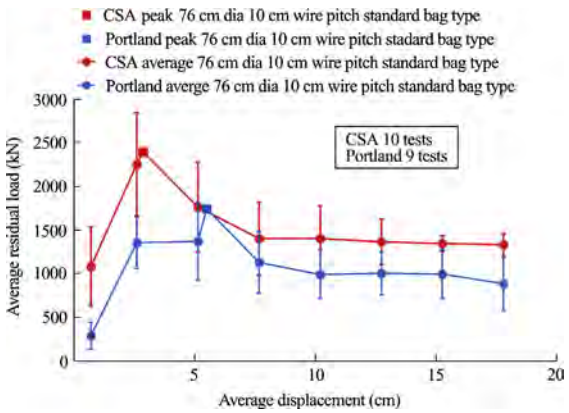

Fig. 7. Representative average loading performance for a 76 cm-diameter CSA and Portland support.

capacity, indicating high stiffness, followed by an extended residual load. The average residual load for the CSA-based supports was 1334 kN compared to 1001 kN for the Portland-based supports. This pattern showed a higher residual load for CSA supports, but this trend was not consistent with all the support design variations. The average residual load for Portland supports was higher by as much as 24% for both the 69 cm-diameter and 76 cm-diameter supports with a 15 cm wire pitch. This response is inconsistent with the established trends above and is likely the result of an insufficient number of direct comparison tests of grout materials and bag construction types.

Pumpable supports are often used in higher convergence environments where an extended residual load is required. Fig. 8 illustrates the representative average loading performance for a 76 cm-diameter CSA support with a 15-cm wire pitch construction in the support bag through 30 cm of convergence. The residual load capacity is highly dependent on the confinement provided by the containment bag and functions until the bag is severely damaged and the crib material starts to fall out. A well-designed pumpable support will generally maintain a fairly high residual load through about 25 cm of displacement as seen in Fig. 8.

4.2. Support dimensions

The support dimension controls several factors including peak capacity, stiffness, and residual loading. Theoretically, the peak capacity and stiffness should be directly proportional to the support area, while stiffness should be inversely proportional to the support height. The area relationships were evaluated, but there were not enough height test variances to enable a proper assessment of the

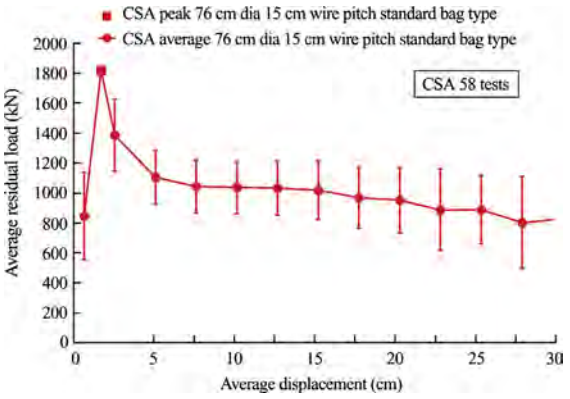

Fig. 8. Representative average loading performance for a 76 cm-diameter CSA support through 30 cm of displacement.

impact of the support height. There is no simple theoretical relationship to examine residual loading behavior relative to support area or height, but the hypothesis is that higher peak loading will result in higher residual loading as well. This hypothesis is examined from the full-scale support testing.

When using a specific cementitious grout with a consistent elastic modulus and compressive strength, the peak load capacity and stiffness should be directly related to the support area. Four different diameters of pumpable roof supports were evaluated in this study. Fig. 9 shows the mean peak load capacities of 61, 69, 76, and 91 cm-diameter pumpable roof supports. Fig. 9 illustrates the linear relationship of capacity increase with support diameter, and also shows an increase in peak load capacity of 69% for the 91 cm-diameter support compared to a 61-cm-diameter Portland support with a 10-cm wire pitch. The 7 cm wire pitch performance for the Portland supports was the least consistent in terms of the linear relationship between peak capacity and support diameter. This inconsistency is most likely driven by the limited number of tests (2–3) for each support diameter in this test configuration.

The loading stiffness of the pumpable roof supports is also proportionally related to the diameter of the pumpable roof support. For example, an increase of 61% in loading stiffness was observed when comparing a 91 cm-diameter Portland pumpable support with a 10-cm pitch bag construction with a 61 cm-diameter support. Fig. 10 illustrates the loading stiffness of 61, 69, 72, and 91 cm-diameter supports. The Portland 7 and 10 cm wire pitch had some inconsistency again due to the limited number of tests, but overall a reasonable linear relationship was observed for all test configurations. The graph also shows that the wire pitch can strongly influence the support stiffness. The impact of the wire design will be discussed later in the paper. The slopes of the stiffness lines are similar for all support configurations with the exception of the 15 cm wire pitch for the CSA supports, which had a steeper slope indicating there was an elevated increase in capacity due to the support diameter for the larger diameter supports in this configuration.

The impact of support area on load shedding prior to the support reaching peak loading is shown in Figs. 11 and 12 for diameters of 61, 69, 76, and 91 cm. Overall, the occurrence of load shed events prior to peak loading is minimal. CSA supports tended to have more load shed events prior to peak loading for the larger-diameter (76 and 91 cm) supports, while Portland-based supports tended to have more load shedding events prior to peak loading for smaller-diameter (61 and 69 cm) supports.

Figs. 13 and 14 document the number of load shed events after the peak load capacity for the 61, 69, 76, and 91 cm diameter supports. Similar to the pre-peak load capacity trend for load sheds, the CSA supports tended to have more load sheds after the peak load capacity occurred for the larger-diameter supports. The most common of load sheds was 1–3 for the smaller-diameter supports (61 and 69 cm) and 2–5 for the two larger-diameter supports (76 and 91 cm). The Portland supports tended to have 0–2 load shed events after peak load capacity occurred.

There is some correlation between the support diameter and the residual loading of the support. As hypothesized, residual loading tended to be greater for the larger-diameter supports. An example is shown in Fig. 15, which compares the relationship for Portland supports with a 10 cm wire pitch construction in the support bag. The curve shows that the support load averaged 2.54 cm of displacement over each. For example, the average load for a 61 cm-diameter support between 11 and 14 cm was 725 kN (see Fig. 15). The average residual load between 10 and 23 cm of displacement was also compared. The average residual load for the 61 cm-diameter support was 641 kN compared to 1205 kN for the 91 cm-diameter support. This trend was also consistent with the CSA supports.

4.2.1. Wire pitch

Confinement plays a significant role in support performance, influencing both the peak load and residual load behavior. The bag is used as a form to fill the support in place underground and integrates a spiraled wire, as shown in Fig. 16, around the support to increase confinement of the fill material. When the strength of the grout is exceeded, the grout bulks through successive fracturing, and as convergence continues to stretch the bag, the bulking of the fractured grout inevitably causes a tear in the bag

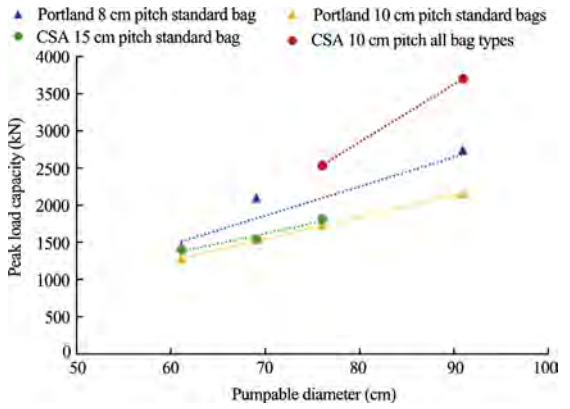

Fig. 9. Trend showing increase in peak load capacity in relationship to the support diameter.

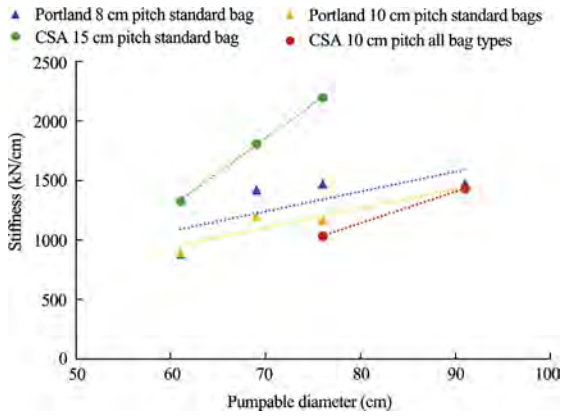

Fig. 10. Trend showing increase in stiffness in relationship to the support diameter.

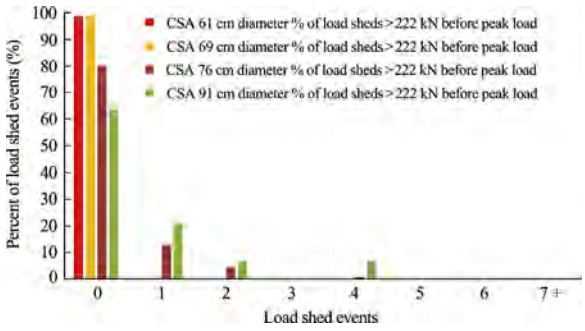

Fig. 11. Distribution of the percentage of the number of load sheds occurring prior to the peak load capacity for 61, 69, 76, and 91 cm diameter CSA pumpable roof supports.

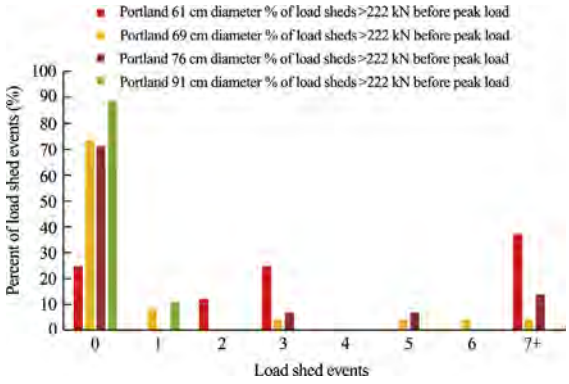

Fig. 12. Distribution of the percentage of the number of load sheds occurring prior to the peak load capacity for 61, 69, 76, and 91 cm diameter Portland pumpable roof supports.

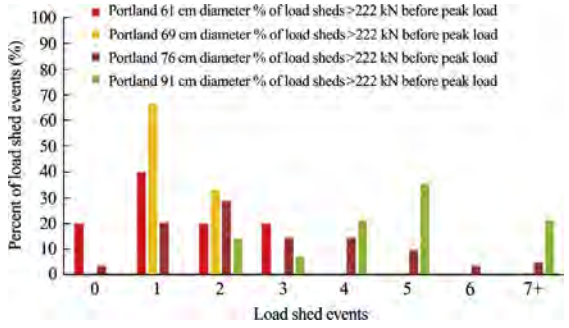

Fig. 13. Distribution of the percentage of the number of load sheds occurring after the peak load capacity for 61, 69, 76, and 91 cm-diameter CSA pumpable roof supports.

fabric. Without the spiraled wire to contain the bulking material, the bag would not have sufficient strength to provide enough confinement to preserve the residual loading. Eventually, after enough convergence causes excessive bulking of the fractured grout segments, the wire confinement will fail and the support experiences a sudden, unrecoverable drop in load capacity (see Fig. 17).

Any confining pressure will have a positive impact on the effective grout strength and resulting support capacity. Confining pressure can be generated by the grout pumping pressure, providing the support bag can provide the necessary resistance. This "preload" confinement can add to the peak capacity of the support. One cause for the CSA support capacity being less than what would be expected from the material compressive strength is the existence of hairline pre-existing fractures. These hairline fractures

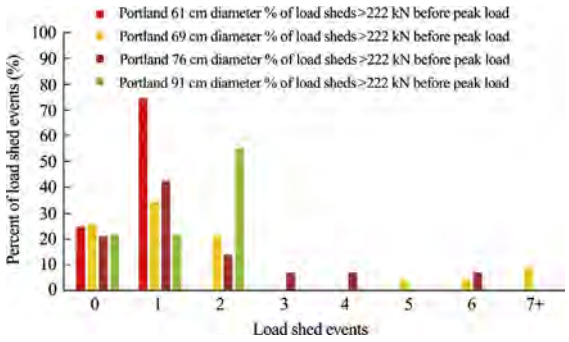

Fig. 14. Distribution of the percentage of the number of load sheds occurring after the peak load capacity for 61, 69, 76, and 91 cm-diameter Portland pumpable roof supports.

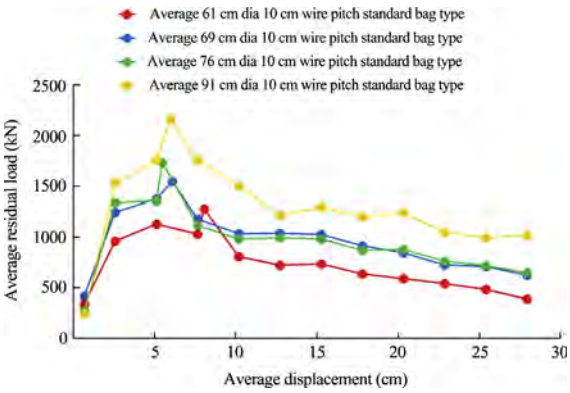

Fig. 15. Representative average loading performance for 61, 69, 76, and 91 cm-diameter Portland pumpable roof support.

Fig. 16. Containment bag seam securing a metal reinforcement wire that is spiraled from the top to the bottom of the bag.

may come from the expansion of the grout material during the hydration of the cement components as the grout cures and hardens in the support bag [5]. These pre-existing fractures can be seen on the surface of the support if the bag is removed, and they appear to control the fracture behavior of the grout during loading. Confining pressure will help to control the shear stress and subsequent fracture development. Fig. 18 shows results from two full-scale tests comparing the maximum support capacity with

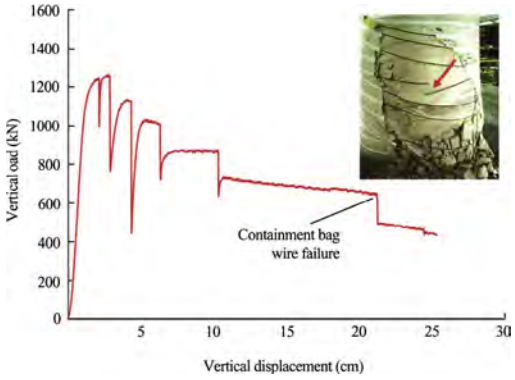

Fig. 17. Failure of the wire confinement within the pumpable containment bag.

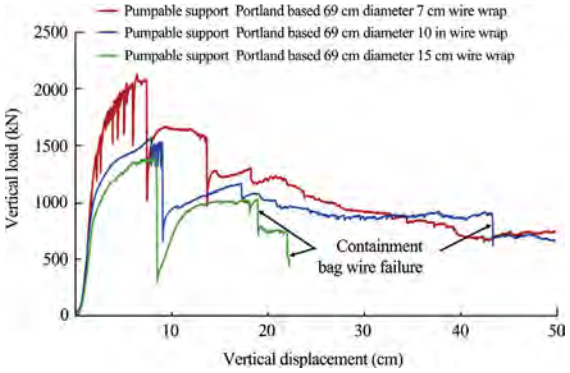

Fig. 19. Performance comparison displaying the increased load capacity due to increased confinement from closer wire spacing.

the containment bag as normal and with the containment bag removed after the support was pumped and the grout fully cured. The support peak capacity was increased by 94% by the confinement of the bag, and the residual loading without the bag was quickly lost following the load shedding after the peak capacity was obtained.

As previously indicated, confinement is largely provided by the wire wrap integrated into the support bag. One way the confinement of the support can be increased is by reducing the spacing (pitch) of the spiral wire. Fig. 19 shows the increase in support capacity of a 69 cm-diameter Portland-based support by comparing a 7, 10, and 15 cm wire pitch. The benefit of the closer wire spacing can be seen as the performance of a bag with the 7 cm wire pitch has a 54% higher peak load capacity than the 15 cm wire pitch bag. Capacity improvements for other support configurations due to wire pitch can also be seen in Fig. 9.

Table 2 compares the average loading stiffness of the 69 cm-diameter, Portland-based supports. A 36% increase in the loading stiffness was observed with a change in the wire pitch from 15 to 10 cm for the support. A 61% increase in loading stiffness was observed when changing the wire pitch spacing from 15 to 7 cm. However, this magnitude of elevated loading stiffness was not consistent with every size of Portland-based supports. When comparing the 15 to 10 cm wire pitch for the 76 cm-diameter and 91 cm-diameter supports, the increase in loading stiffness was 26% and 3%, respectively.

Table 2
Comparison of support loading stiffness for 7, 10, 15 cm wire spacing Portland-based supports.

Diameter (cm)	Wire pitch (cm)	Stiffness (kN/cm)	Peak load (kN)
69	8	1425	2108
69	10	1198	1548
69	15	883	1414

4.3. Single-wall vs. dual-wall bag construction

The majority of tests evaluated (73%) used a standard single-wall, wire-wrapped (external) containment bag for the full-scale evaluation of the pumpable supports. The rest of the tests consisted of various prototype bags (11%) and dual-wall containment bags (16%). The dual-wall construction containment bag includes an internal cylindrical mesh with a spiral wire reinforcement within the bag (Fig. 20). The inner mesh is located about 4–7 cm inside the external bag. This design allows the cementitious fill material to encapsulate the mess reinforcement and fill the external bag during installation. The design goal of the dual bag is to increase the residual load capacity of the support and was used only in conjunction with CSA supports in the NIOSH tests.

The mean peak load capacities of the dual-wall support constructions were higher than the equivalent single-wall support constructions in the majority of the tests. Fig. 21 compares the peak load capacity for 76 cm-diameter supports with standard single-wall and dual-wall constructions with a wire pitch spacing of 10 and 15 cm. In this example, the mean peak load capacity of a dual-wall support with a 10 cm wire pitch was 2713. This compares to the mean peak load capacity of single-wall support of 2389. Therefore, for a 76 cm-diameter support with a 10 cm wire pitch, the dual-wall containment bag provided about 14% more capacity than the single-wall support.

The average loading stiffness of the dual-walled pumpable supports with a 10-cm wire pitch was 2718 kN/cm compared to 2317 kN/cm for the equivalent single-walled supports (Table 3). This resulted in the dual-wall supports being on average 17% stiffer

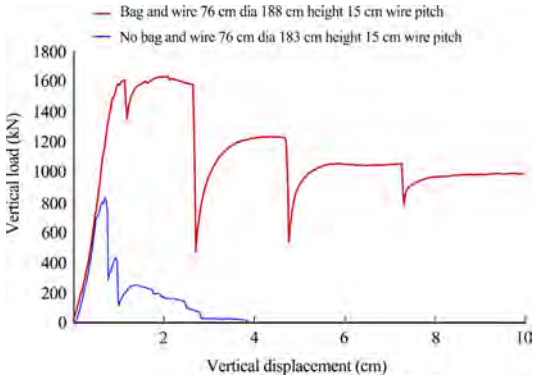

Fig. 18. Comparison of support capacity with and without the containment bag.

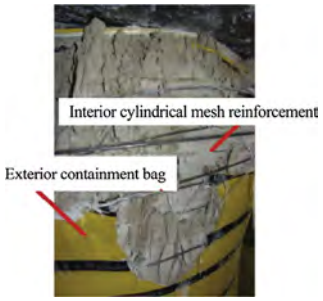

Fig. 20. Bag construction showing inner mesh that ripped open during performance testing in NIOSH Mine Roof Simulator.

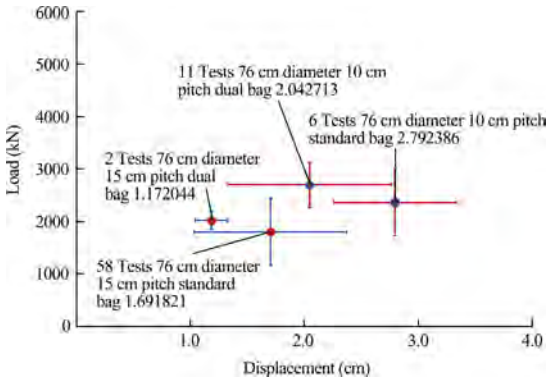

Fig. 21. Comparison of the peak loading capacity of single-wall vs. dual-wall supports.

Table 3
Comparison of support loading stiffness for single-wall and dual-wall supports of CSA-based material.

Bag type	Diameter (cm)	Wire pitch (cm)	Stiffness (kN/cm)	Peak load (kN)
Single-wall	76	10	2317	2389
Dual-Wall	76	10	2718	2713
Single-wall	76	15	2196	1819
Dual-wall	76	15	2949	2046

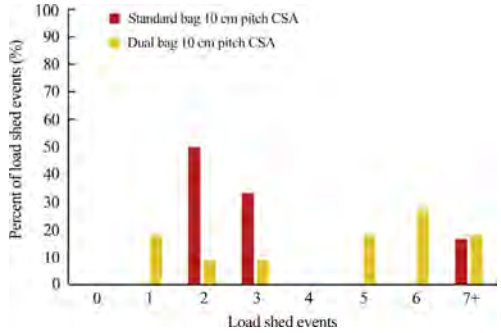

Fig. 22. Distribution of the percentage of the number of load sheds occurring after the peak load capacity for single-wall and dual-wall pumpable roof supports.

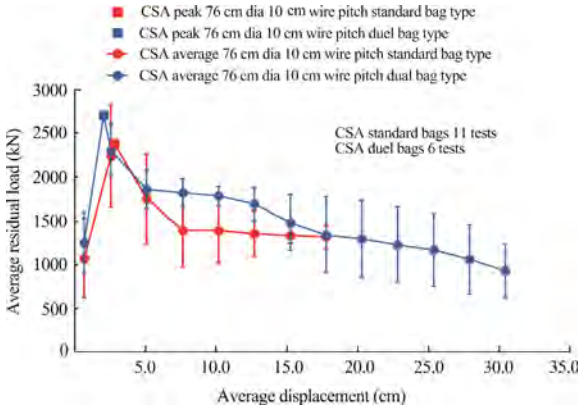

Fig. 23. Representative average loading performance for single-wall and dual-wall pumpable roof supports.

than the single-wall supports. This trend was also consistent with the 15 cm wire-pitch supports, which showed a stiffness increase of 34% from a dual-wall to single-wall construction.

The 76 cm-diameter, 10 cm wire pitch CSA supports were examined to determine the effect of dual-wall vs. single-wall construction on load shedding. The dual-wall construction does not significantly affect the number of load shed events generated prior to the peak load capacity being reached, since the initial load shed events are largely controlled by the compressive and shear strength of the grout instead of the confinement. Both the single-wall and dual-wall supports experienced load shed events prior to the peak load capacity only 18% of the time. Dual-wall support constructions tended to have more load shed events post-peak loading than the single-wall containment bags (see Fig. 22).

The dual-wall supports maintained a higher residual load on average than the single-wall supports. Fig. 23 compares the representative performance between 0 and 18 cm of displacement, showing the load averaged over each 2.54 cm of displacement. The average residual load for the dual-wall supports was 1379 kN compared to 1001 kN for the single-wall supports—a 38% increase. The results further confirm that the residual load capacity is influenced by the confinement provided by the containment bag.

5. Conclusions

In this study, the stiffness of the supports constructed from CSA material was significantly higher than for the Portland material for all support sizes. Likewise, the peak load capacities of the CSA supports were mostly higher than the equivalent Portland supports.

Confinement also plays a significant role in the support performance, influencing both the peak load and residual load behavior. The bag is used as a form for filling the support in place underground and integrates a spiraled wire that wraps around the pumpable support to increase confinement of the fill material. There is a direct relationship between the wire spacing (pitch) and the capacity of the support, with increased capacity provided by the added confinement of closer wire spacing. Wire spacings of 7, 10, and 15 cm are utilized in current pumpable support constructions. The wire diameter and material properties were not evaluated in this study, but the variances in these factors among the bag constructions are believed to be relatively minor.

The failure behavior of pumpable supports, like all brittle material, occurs when the support stress exceeds the compressive and shear strength of the material, causing a load shed event. A sequence of significant load shedding events occurs during loading and the support typically fails progressively while providing a sustained residual loading through several centimeters of displacement (typically 18–25 cm) before the wire breaks. Once the wire breaks, the confinement is significantly compromised, which, in combination with the bag ripping open and grout material spilling out, causes a more rapid deterioration of useful residual loading and yielding capability. A well-designed pumpable support can provide a useful residual load through 25–41 cm of convergence.

Currently, progressive load shedding is a common and unavoidable consequence of the material used for this type of support construction. Therefore, reducing load shedding behavior with this type of support construction will have to be achieved by altering the fill materials' properties to eliminate the brittle failure and highly bulked behavior of the failed material. NIOSH is planning to conduct additional studies that evaluate other less brittle and more crushable materials to determine the feasibility of reducing load shedding with the current containment bag constructions.

References

[1] Barczak TM, Tadolini SC. Pumpable roof supports: an evolution in longwall roof support technology. Transactions of the Society for Mining, Metallurgy, and Exploration, Inc, vol. 324. p. 19–31.

[2] Dolinar D. Ground and standing support interaction in tailgates of western U.S. longwall mines used in the development of a design methodology based on the ground reaction curve. In: Proceedings of 22nd international conference on ground control in mining. West Virginia University; 2010. p. 152–60.
[3] Campoli AA. Selection of pumpable cribs for longwall gate and bleeders entries. In: Procedures of 34th international conference on ground control in mining. West Virginia University; 2015. p. 80–2.
[4] Zhang P, Milam M, Mishra M, Hudak WJ, Kimutis R. Requirements and performance of pumpable cribs in longwall tailgate entries and bleeders. In: Proceedings of 31st international conference on ground control in mining. West Virginia University; 2012. p. 1–11.
[5] Barczak TM, Chen J, Bower J. Pumpable roof supports: developing design criteria by measurement of the ground reaction curve. In: Proceedings of 22nd international conference on ground control in mining. West Virginia University; 2003. p. 283–93.

International Journal of Mining Science and Technology 27 (2017) 101–106

Contents lists available at ScienceDirect

International Journal of Mining Science and Technology

journal homepage: www.elsevier.com/locate/ijmst

Laboratory and field testing of bolting systems subjected to highly corrosive environments

Meikle Tom [a,*], Tadolini Stephen C. [b], Sainsbury Bre-Anne [c], Bolton John [a]

[a] Minova Richmond Vale, NSW 2327, Australia
[b] Minova Georgetown, KY 43204, USA
[c] Mining and Resource Engineering Monash University, VIC 3800 Caulfield, Australia

ARTICLE INFO

Article history:
Available online 29 December 2016

Keywords:
Corrosion
Coatings
Galvanised
Salt spray
Accelerated corrosion testing

ABSTRACT

The capacity of ground support components which have been affected by corrosion is reduced and may ultimately lead to dynamic failure of the component and the strata. In order to maintain an effective, long-term ground support system, significant campaigns of rehabilitation are often required in corrosion affected areas which also expose the workers to hazardous conditions. The most common corrosion protection for steel ground support utilises sacrificial systems such as galvanising. Galvanising has previously been proven to be susceptible to some corrosion processes. Stainless steel is the most effective in resistance to corrosion, but can be cost prohibitive, and its mechanical properties often make it unsuited to use in ground support components. Providing an outer protective plastic coating to bolts has proven to be an effective means of protecting the inner steel bar from corrosion. However, these support systems tend to be susceptible to coating damage, and require post cement grouting to provide full encapsulation. In comparison to a standard bolt/resin system, they can be slow to install and expensive. These systems have also been shown to reduce overall load transfer performance of the bolting system. In order to provide a higher level of corrosion protection whilst maintaining current installation practices and bolting cycle times, Minova has developed the Enduro™ steel ground support range. The Enduro™ range consists of standard Minova steel ground support components which have been treated with a unique coating process. The Enduro™ coating has been tested in the harshest of conditions, in laboratory controlled conditions and in underground trials. It has been proven to effectively resist or completely eliminate the formation of corrosion, even in the most aggressive environments. This paper explains the process and provides the details of the laboratory and underground corrosion performance testing carried out on Enduro™ ground support products.

1. Introduction

Traditionally, the most common form of corrosion protection in steel ground support consists of a sacrificial protective coating such as galvanising [1]. Such coatings have proven to be ineffective in extreme high and low pH conditions with corrosion of the support system commonly encountered [2–4]. There is also evidence that common forms of galvanising may actually increase the rate of corrosion in certain pH environments. Fig. 1 shows typical corrosion and failure of a standard re-bar roof bolt.

In order to provide additional protection, double corrosion protected (DCP) systems were introduced. These systems, although effective in providing additional corrosion protection, have proven to be expensive, complex to manufacture, bulky and difficult to handle. They are normally slow to install which leads to a reduction in development rates. The outer layer can also be damaged during careless installations, permitting the coalescence of corrosive solutions on selected areas. Additionally flexible polymer coatings have been attempted in highly acid ground in two underground gold mines in Nevada, USA [5]. In addition to the challenges described above, Clarke and Sieders identified that the plastic "smooth" layer between the steel bolts may impact the axial load stiffness or friction of the installed ground support systems [6].

Due to these limitations in the double corrosion protection systems, Minova developed the Enduro™ range of steel ground support products. The Enduro™ bolt, whether it be a solid bolt or friction bolt, is installed like any other common bolting system.

* Corresponding author. Tel.: +1 740 3594076.
E-mail address: tom.meikle@orica.com (T. Meikle).

http://dx.doi.org/10.1016/j.ijmst.2016.11.017
2095-2686/

Fig. 1. Corroded and failed roof bolt.

It is no heavier than a standard bolt and requires no additional training or special equipment to be installed.

2. Endure coating

There are two components to the Enduro™ coating:

(1) The Enduro™ or base coat which covers entire surface area of the bolt. The Enduro™ coating is a unique and protected Minova application to ground support components.
(2) An optional top coat applied to either the entire surface area or selected sections (i.e. exposed tail of bolt).

The Enduro™ Coat is applied using the cathodic dip coating (CDC) process. In this process the system applies a direct current (DC) charge to the component, which is immersed in a bath of oppositely charged coating particles. The particles are drawn to the component surface and are deposited forming an even, continuous film over the surface (including every crevice) until the coating reaches the desired thickness, typically 20 μm.

An optional top coat is applied using a thermoplastic powder coating process and is suitable for most metals that can withstand 180 °C oven temperatures that are required for curing the powder. The thickness of thermoplastic powder coating is typically 150–250 μm. The top coat can be used to provide extra confidence in the protection of the steel, particularly where physical damage through extreme handling may be encountered. It is also effective in UV protection to the Enduro™ coat should the tail be exposed after installation.

The thickness of either the Enduro™ or top coat can be increased, or the coating process repeated to provide even greater confidence in the corrosion protection for extremely difficult environments.

3. Laboratory testing and results

In order to validate the performance of the Enduro™ product, a series of controlled laboratory tests have been completed.

3.1. Corrosion resistance acetic acid salt spray (AASS)

The corrosion resistance performance of the Enduro™ product in acetic acid salt spray (AASS) has been observed over 1000 h and compared to a traditional galvanised bolt. A total of three bolts were tested that included a 'standard' galvanised bolt, a bolt with an Enduro™ base coat and a bolt with a Enduro™ base coat and a topcoat. The salt spray chamber used to perform the tests is presented in Fig. 2.

Test conditions were pH 3.1–3.3@ + 35 °C. The test results for each of the three coating types are provided in Table 1.

Despite galvanised bolts being used extensively to protect against corrosion in saline conditions, laboratory testing conducted herein presents obvious signs of corrosion (see Fig. 3). Better corrosion resistance has been observed (when compared to the galvanised bolt) by the two Enduro™ variant coated bolts. The product with both base and topcoat provided the best resistance to corrosion under saline conditions.

3.2. Acid bath immersion

The acid resistance of the Enduro™ product in a low acid environment has been observed and compared to traditional bolt materials. A total of three bolts were tested that included a 'standard' hot-dip galvanised bolt, a bolt with an Enduro™ base coat and a bolt developed from raw steel.

A straight forward test procedure has been used whereby each of the products were placed in an acidic solution (dilute sulphuric acid with a pH of 1.69) for a period of 50 days. The visual appearance was observed and recorded at 30 min, 5, 21 and 50 day increments for each of the bolt types. The acid bath and pH measuring instrument is presented in Fig. 4.

Immediately upon immersion, the hot-dip galvanised bolt (grey colour Fig. 4, part A) commenced 'fizzing' (reacting). The raw steel bolt (charcoal colour Fig. 4, part B) commenced reacting after approximately 30 min. Over a period of testing, there was no apparent reaction with the black Enduro™ base coated bolt (Fig. 4, part C).

After 5 days of immersion, a pH of 2.25 was measured. Sheets of corroded material can be seen on the galvanised and raw steel bolt. There was no corrosion observed on the Enduro™ bolt (Fig. 5 left). After 21 days, additional corrosion was observed on the raw steel and galvanised bolts (Fig. 5 right).

After 50 days (Fig. 6) both the raw steel and galvanised bolts have corroded significantly with the nut on the galvanised bolt completely corroded. There were still no obvious signs of corrosion on the Enduro™ bolt.

From the observations, it is clear that the galvanised and the raw steel bolts are severely corroded after 50 days of immersion.

The Enduro™ bolt still looks 'intact' with no apparent corrosion evident. The dissolution pattern of the raw and galvanised bolt appears different: (1) the raw bolt appears to be dissolving uniformly with the nut showing severe corrosion, and (2) the galvanised bolt shows severe pitting and complete dissolution of the nut.

Fig. 2. Salt spray chamber used for Enduro™ product testing.

Table 1
Testing results of Enduro™ bolt and traditionally galvanised bolts.

AASS testing hour	257	518	722	1012
Description	Corrosion observations after elapsed hours			
Required specifications	No visible corrosion observed for acceptable performance result			
Galvanised bolt	Severe white rust, some red rust	Severe white rust, some red rust	Severe white & red rust	Severe white & red rust
Observed result	Fail	Fail	Fail	Fail
Enduro™ bolt (base coat only)	No visible corrosion	No visible corrosion	Minor red rust spots	Minor red rust spots
Observed result	Pass	Pass	Fail	Fail
Enduro™ bolt (base coat and topcoat)	No visible corrosion	No visible corrosion	No visible corrosion	No visible corrosion
Observed result	Pass	Pass	Pass	Pass

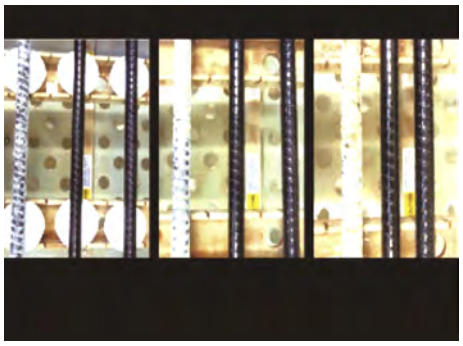

Fig. 3. Corrosion observations during AASS testing at 257, 518 and 722 h.

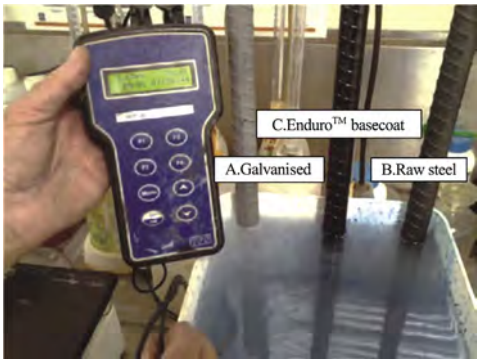

Fig. 4. Acid bath and pH monitoring instrument used during Enduro™ product testing.

In both cases, the threaded areas of the raw steel and galvanised bolt area have been significantly reduced in diameter. The Enduro™ nut and thread is observed to be unaffected showing no signs of corrosion (Fig. 6).

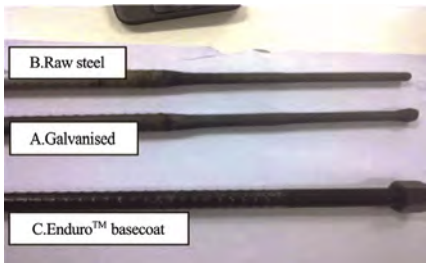

Fig. 6. Acid bath immersion testing results after 50 days.

3.3. Accelerated corrosion tests

Monash University has conducted accelerated corrosion tests (ACT) to provide a rapid comparison of the corrosion resistance of the Enduro™ product to other products currently being used to determine corrosion expected from 2 to 100 years (specifically thickness loss data in mm/year).

To complete the tests, a test solution of 3.5 (%, by weight) NaCl, was prepared by dissolving 35 g of NaCl in 1 L of distilled water. This solution has a normal pH of approximately 7.8. For the development of other pH solutions, 0.1 N solutions of HCl or NaOH were added to achieve pH environments of 2, 7 and 9 for testing. The accelerated corrosion testing procedure used included taking potentiodynamic polarization measurements using a typical three-electrode electrochemical cell that was connected with a Bio-Logic potentiostat. Prior to each corrosion test the open circuit potential (OCP) was measured to confirm stability over a period of time of 1000 s.

A total of five bolt materials were tested that included; Enduro™ with basecoat, black (e.g. ungalvanised), hot dip galvanisation, thermally diffused galvanisation (TDG) and stainless steel. Results for each of the products at a pH 2 are presented in Fig. 7.

The Enduro™ product specimens provided the best observed corrosion resistance in acidic conditions (3.5% NaCl at pH 2) fol-

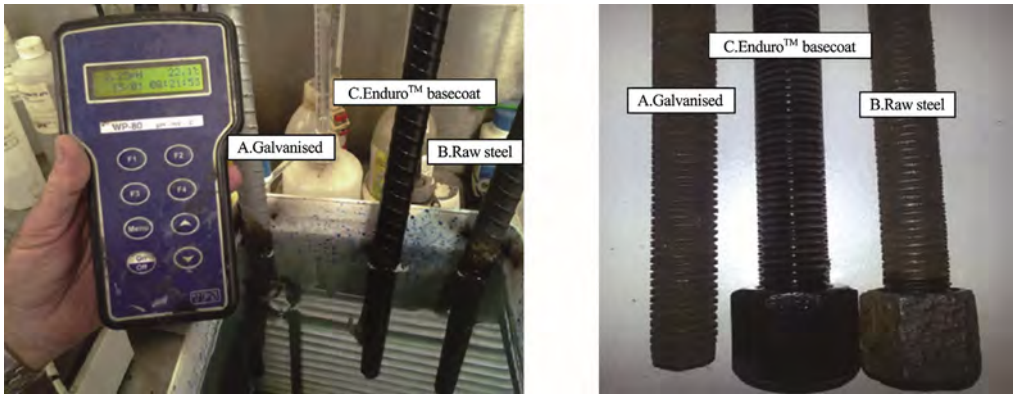

Fig. 5. Acid bath test results after 5 and 21 days.

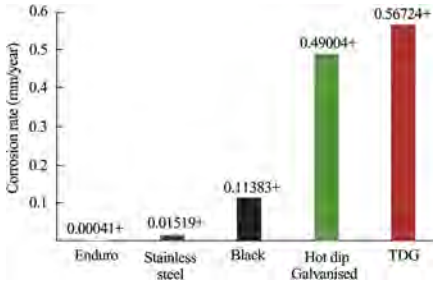

Fig. 7. Average calculated corrosion rate of Enduro™ and comparison samples in 3.5% NaCl solution, pH 2.

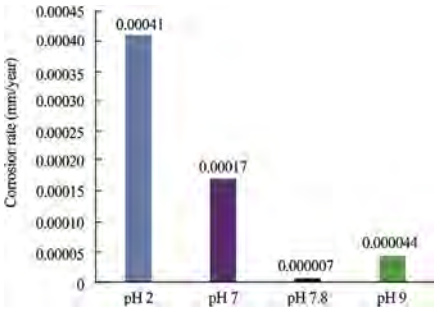

Fig. 8. Enduro corrosion (mm/year) calculated at various pH levels.

lowed by stainless steel and then the other products tested. It can be observed that HDG and TDG coatings have extremely low resistance to corrosion from low pH solutions.

The corrosion performance of the Enduro™ product (base coat only) over a range of pH conditions are provided in Fig. 8 for the purposes of estimating service life.

4. Field testing and results

A series of underground tests on the Enduro™ product were carried out to determine the durability of the bolt when exposed to highly acidic mine water. A summary of the in situ trials are provided below.

4.1. Mine A

Six sections of Enduro™ bolts (Type A) and six sections of hot dip galvanised bolts (Type B) were selected for using in this trial. Each section was 600 mm in length. The bolts were placed Fig. 9.

Fig. 9. Mine A bolt in situ test conditions.

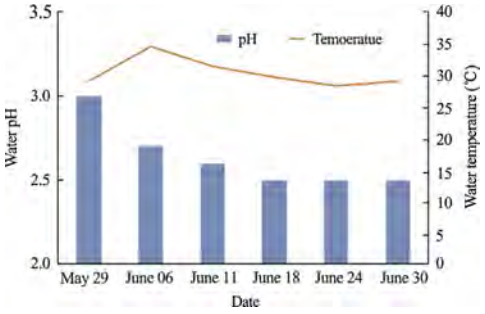

Fig. 10. The pH measured weekly at Mine A.

The pH was measured 6 times over a 33 days period. The dates and results of those measurements are provided in Fig. 10.

After 330 days, a section of each bolt type was extracted from the acidic water, the excess build-up was removed, and the level of corrosion observed (Fig. 11). It can be seen, that under the highly acidic mine water conditions at Mine A, the Enduro™ bolt outperforms the hot dip galvanised bolt in resisting the effects of the corrosive mine water.

Fig. 12 presents a solid Enduro™ bolt that has been installed for six weeks at Mine A. At this point discoloration is observed but no corrosion is evident on the bolt. The galvanised mesh surrounding the Enduro™ bolt is eight weeks old.

4.2. Mine B

At Mine B, in situ trial sites for the Enduro™ product were selected based on a significant observed degradation in the existing galvanised friction bolt support which had been installed approximately 3 years previously. Fig. 13a shows a heavily corroded friction bolt and plate that has been installed for approximately two weeks. Visual observations regarding the corrosion of the bolts have been made in addition to corrosion assessments of the inside of the bolts using a hand-held wand camera (Fig. 13b).

The performance of the Enduro™ product was measured along with red bolt over a two-month period whereby exposure of the bolts was maximised by placing them on the floor under dripping mine water (Fig. 14).

In order to replicate mining conditions the bolts were extensively scratched and scoured on the inside and outside. The extent of corrosion on the bolts was recorded every month. The red bolt and the black Enduro™ bolt showed minimal evidence of corrosion over a two-month period.

4.3. Underground installation at Mine C

Minova was approached regarding the support system currently being installed in Mine C's surface to underground declines. Mine C were having issues complying with the geotechnical design criteria to fully encapsulate the bolt prior to the application of shotcrete. At the time Minova got involved, this issue was severely hindering development rates and had led to a substantial amount of re-support having to be carried out.

Minova proposed using the Enduro™ solid bolt along with our standard resin anchor to overcome this issue. Having proved the durability of the Enduro™ bolt, the system was adopted. With the Enduro™ bolt Mine C was able to accept a less than 100% encapsulation with traditional resin anchors due to its effective resistance to corrosion. Implementing this system also eliminated manual handling issues and exposure to cement dust encountered while using the previous post grouting system. As a result of the application of the Enduro™ product, advance rates increased significantly and no further re-support was required.

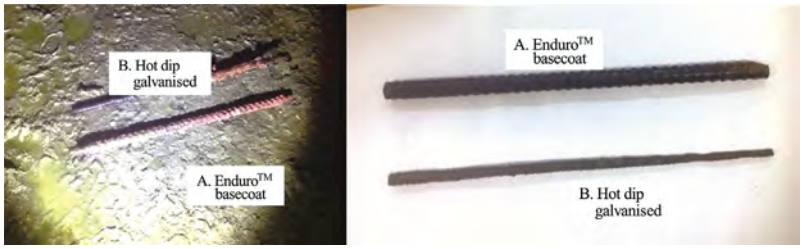

Fig. 11. Mine A after 30 days (left) bolts observed underground (right) excess build up removed from bolt.

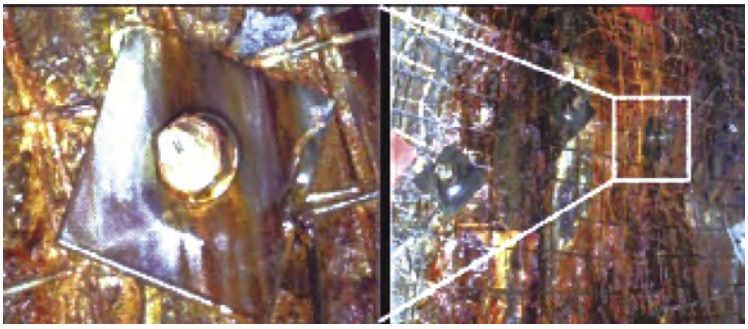

Fig. 12. In situ observations of the performance of an Enduro™ bolt in comparison to galvanised mesh in acidic mine groundwater conditions.

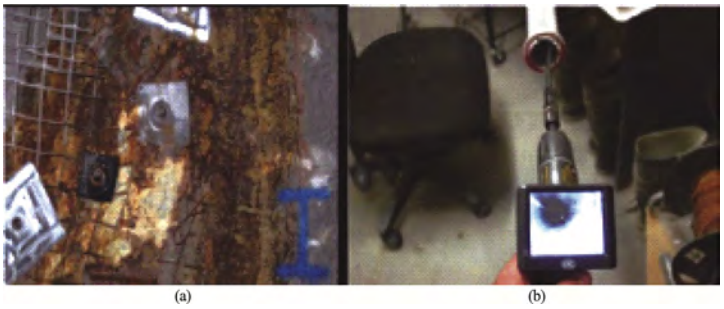

Fig. 13. Observed corrosion of existing galvanised ground support through surface and penetrating visual means at Mine B.

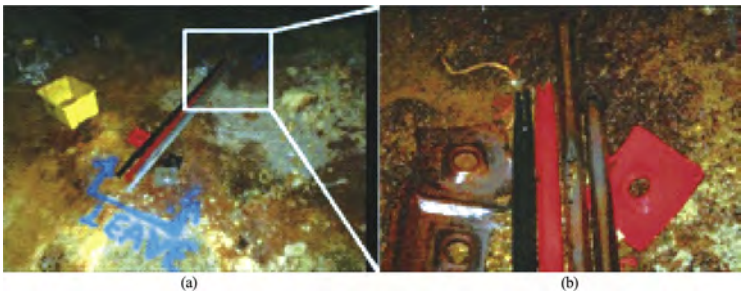

Fig. 14. Observed corrosion of Enduro™ (black) and red bolt at Mine B.

5. Conclusions

Corrosive ground control conditions can be difficult to control and be extremely hazardous to workers. Previous developments have been partially successful in extending the service life of support bolts and fixtures. Both field and laboratory testing of Enduro™ rockbolts and ground support components have shown significant reductions in rates of corrosion compared to other traditional corrosion resistant steel ground support systems. Additionally, Enduro™ bolt installation offers significant efficiency benefits over other 100 year design life rockbolts. The authors believe that project designers and geotechnical engineers now have a viable option for ground support systems to consider where long service life is required and/or extreme corrosion potential exists.

Acknowledgments

The authors would like to acknowledge the following people who have contributed significantly to the development and testing

of the Enduro™ rockbolt range who include; Steve Burgess, Evan McKay, David Cuello, Peter Keall, and Professor Raman Singh.

References

[1] Aziz N, Craig P, Mencik J, F Hai. Rock bolt corrosion – an experimental study. In: Proceedings of the coal operators conference. Wollongong, Australia: University of Wollongong; 2013. p. 144–51.
[2] Craig P, Serkan S, Hagan P, Hebblewhite B, Vandermaat D, Crosky A, et al. Investigations into the corrosive contributing to premature failure of Australian coal mine rock bolts. Int J Min Sci Technol 2016;26(1):59–64.
[3] Barnard C, Kallu RR, Warren S, Thareja R. Inflatable rock bolt bond strength versus rock mass rating (RMR): a comparative analysis of pull-out testing data from underground mines in Nevada. Int J Min Sci Technol 2016;26(1):19–22.
[4] Ghafar N. Corrosion control in underground concrete structures using double waterproofing shield system (DWS). Int J Min Sci Technol 2013;236(4):603–11.
[5] Clark S, Sieders G. Comparison of glass fibre reinforced polymer rock bolts with double corrosion protection steel rock bolts for use in tunnel applications. In: Proceedings of the 15th Australasian tunnelling conference. Sydney; 2014. Paper 051.
[6] Oler R, Chen J. Introduction of a new superior coating on ground control products. In: Proceedings of the 33rd international conference on ground control in mining. Morgantown, WV; 2014. p. 189–92.

International Journal of Mining Science and Technology 27 (2017) 107–113

Contents lists available at ScienceDirect

International Journal of Mining Science and Technology

journal homepage: www.elsevier.com/locate/ijmst

Preventing roof fall fatalities during pillar recovery: A ground control success story

Mark Christopher *, Gauna Michael

MSHA, Pittsburgh Safety and Health Technology Center, Pittsburgh, PA 15236, USA

ARTICLE INFO

Article history:
Received 28 May 2016
Received in revised form 9 August 2016
Accepted 15 September 2016
Available online 20 December 2016

Keywords:
Retreat mining
Roof support
Room-and-pillar
Ground control

ABSTRACT

For decades, pillar recovery accounted for a quarter of all roof fall fatalities in underground coal mines. Studies showed that a miner on a pillar recovery section was at least three times more likely to be killed by a roof fall than other coal miners. Since 2007, however, there has been just one fatal roof fall on a pillar line. This paper describes the process that resulted in this historic achievement. It covers both the key research findings and the ways in which those insights, beginning in the early 2000s, were implemented in mining practice. One key finding was that safe pillar recovery requires both global and local stability. Global stability is addressed primarily through proper pillar design, and became a major focus after the 2007 Crandall Canyon mine disaster. But the most significant improvements resulted from detailed studies that showed that local stability, defined as roof control in the immediate work area, could be achieved with three interventions: (1) leaving an engineered final stump, rather than extracting the entire pillar, (2) enhancing roof bolt support, particularly in intersections, and (3) increasing the use of mobile roof supports (MRS). A final component was an emphasis on better management of pillar recovery operations. This included a focus on worker positioning, as well as on the pillar and lift sequences, MRS operations, and hazard identification. As retreat mines have incorporated these elements into their roof control plans, it has become clear that pillar recovery is not "inherently unsafe." The paper concludes with a discussion of the challenges that remain, including the problems of rib falls and coal bursts.

1. Introduction

Pillar recovery has always been an integral part of underground coal mining in the US. When room-and-pillar methods are employed, large blocks of coal in the form of pillars are initially left in place to support the weight of the overburden. Unless these pillars are subsequently recovered, the coal they contain will never be mined.

During the retreat mining process the roof above the worked-out area caves and the overburden subsides (Fig. 1). Because premature caving can cause hazardous roof falls while the miners are still present, pillar recovery has historically been less safe than other underground mining methods. A century ago, Rice found that of 317 miners that were killed by roof falls in one year in Pennsylvania, 98 perished while attempting to recover pillars, showing that "Drawing pillars is plainly most dangerous work" [1].

As noted in Fig. 1, the gob is the area where the pillars have been extracted and the roof has caved.

2. Demographics of pillar recovery

No official statistics are available on the prevalence of retreat mining. Indeed, collecting such data would be difficult, since many mines switch back and forth from development to retreat mining. Fortunately, through the years a number of "snapshots" have been taken of the retreat mining segment of the industry.

Kauffman, Hawkings and Thompson developed a retreat mining manual which included a survey of roof control plans from all over the US [2]. They found that out of the 4166 underground coal mines operating during the late 1970's, 1093 (26%) included pillar recovery in their roof control plans. The regions with highest rates of retreat mining plans were PA (pillar extraction included in 70% of plans), Northern WV (60%) and the Western US (56%). In the Central Appalachia coalfields, which covers Southern WV, Eastern KY, Western VA, and Northeastern TN, only 23% of the roof control plans included pillar recovery. But because there were so many mines located in Central Appalachia, a large majority (79%) of all US retreat mines were located there. Kauffman, Hawkings and Thompson made no attempt to determine the production or the number of miners at the pillar recovery mines [2]. A NIOSH study

* Corresponding author. Tel.: +1 412 3866522.
E-mail address: mark.christopher@dol.gov (C. Mark).

http://dx.doi.org/10.1016/j.ijmst.2016.09.030
2095-2686/

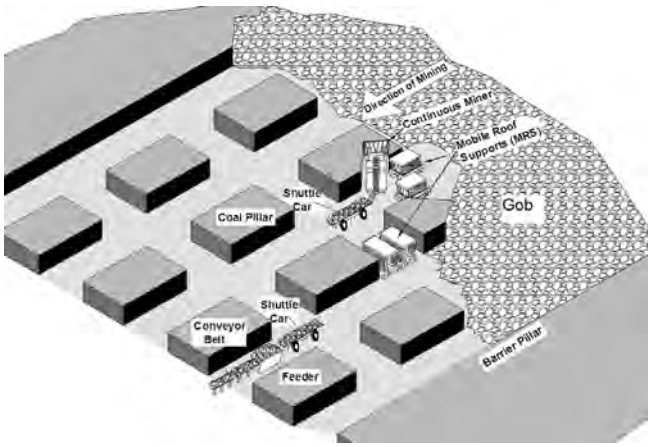

Fig. 1. Retreat phase of room-and-pillar mining showing pillar recovery.

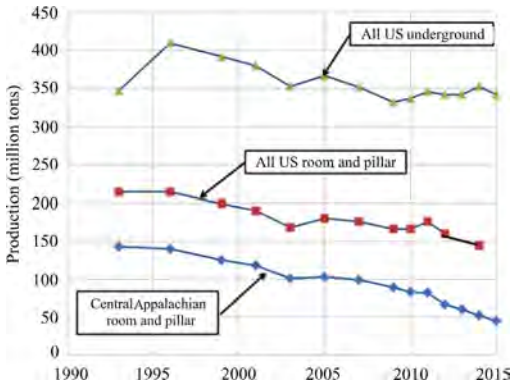

Fig. 2. Trends in US underground coal production, 1993–2015 cited in Energy Information Agency in 2015.

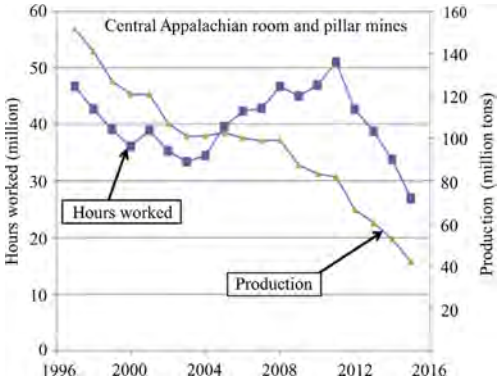

Fig. 3. Coal production and worker hours for Central Appalachian room-and-pillar mines, 1993–2015, cited in Energy Information Agency in 2015.

made use of a 1993 MSHA survey of gob ventilation and bleeder systems in US underground mines [3]. The MSHA survey found that 367 non-longwall mines had gob areas, about evenly split between "active" and "inactive" gob areas. The NIOSH study linked only the mines with active gob areas to the MSHA accident and employment data base, and found that they employed 9,100 miners and produced 61.7 million tons, while the totals for all room and pillar mines were 33,100 miners and 214.3 million tons. NIOSH also found that about two-thirds of the active retreat mining was taking place in Central Appalachia, with some of the remainder coming from every other coalfield except Western KY. However, the NIOSH study significantly underestimated the total size of the retreat mining sector because it excluded the mines with inactive gobs. A mine was not counted unless it was actively extracting pillars at the moment the MSHA survey was conducted, even if it contained inactive gobs and was developing pillars for later extraction. In particular, small single-section mines in Central Appalachia were probably underrepresented.

A few years later, NIOSH surveyed MSHA roof control specialists about the pillar recovery practices in the mines they inspected [4]. The data was again linked to the MSHA accident and employment data base. This study found that in 2001, 370 retreat mines produced 108 million tons of coal, about two-thirds of the total non-longwall underground production. At this time more than 90% of the retreat mine production came from Central Appalachia, with about 9% coming from Northern West Virginia. There was essentially no pillar recovery taking place in the Midwest or in Alabama.

Pillar extraction waned rapidly in Northern Appalachia after 2001. In recent years, the total number of retreat mines anywhere outside of Central Appalachia can be counted in single digits.

While retreat mining has largely disappeared from the other coalfields, the 2003 NIOSH survey found that in Central Appalachia mines that practiced pillar extraction accounted for about 75% of the non-longwall production in the region. A 2015 survey of MSHA roof control supervisors confirmed that ratio was still valid. So while no precise data on retreat mining has been collected since 2001, data from all Central Appalachian room and pillar mines can be considered a good proxy for the pillar recovery sector of the US underground coal industry.

Fig. 2 shows that Central Appalachian room and pillar production declined slowly between 2001 and 2011, from 108 to 82 million tons. During this same period, however, productivity also declined, from 3.12 to 1.59 tons per worker hour. Therefore, the number of miners exposed to pillar recovery likely increased during this period, peaking in 2011 (Fig. 3). NIOSH estimated in 2001 that about 10% of all underground hours were engaged in pillar recovery, and this estimate was probably valid through 2011. The number of both mines and miners in Central Appalachia has greatly declined since then.

3. Ground fall fatalities during pillar recovery

Retreat mining has long been considered the most hazardous type of underground mining. During the first decade of the 2000's, three separate studies on the safety of pillar recovery were commissioned by the state of WV, the State of KY, and by the US Congress [5–7].

Historically, roof falls have been the most significant hazard faced by miners on pillar recovery sections. Mark found that between 1978 and 1986, out of 328 total roof fall fatalities, 67 (20%) were associated with pillar recovery [8]. For the period 1989 to 1996, Mark et al. found that out of a total of 111 roof and rib fatalities, 33 (30%) took place during pillar recovery [3]. Mark et al. estimated that a coal miner on a pillar recovery section was approximately three times more likely to be fatally injured in a roof fall than a miner on an advancing section [4].

In recent years, the number of roof falls during pillar recovery has been dramatically reduced, however. As shown in Fig. 4, there has been just one roof fall fatality in the eight years since 2007. This compares to a total of 19 in the prior decade. Since the total exposure to retreat mining has only recently fallen, it seems that a retreat miner's risk of being killed by a roof fall was reduced by a factor of 16 (for the ten-year period 1998–2007, DOE statistics show that an average of 38.44 million hours were worked each year in Central Appalachian room and pillar mines. For the eight-year period 2008–2015, the annual average was 41.44 million hours. Therefore, there was one roof fall fatality during pillar

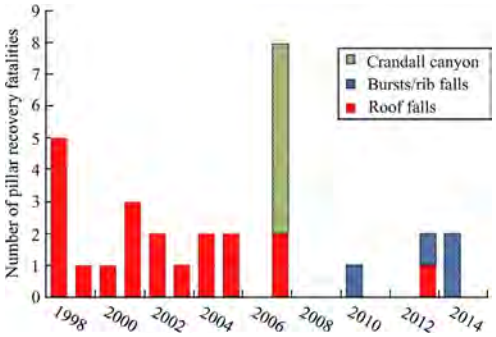

Fig. 4. Ground fall fatalities during pillar recovery, 1998–2015.

Fig. 5. A final stump.

recovery for every 20 million hours worked in decade prior to 2008, and one for every 331 million hours in the eight years since.). The focus of this paper is on how this historic improvement was achieved.

Unfortunately, roof falls are not the only hazard faced by miners engaged in pillar recovery. The 2007 Crandall Canyon Mine Disaster, which was caused by a pillar collapse, initially cost six miners their lives, and then three additional miners were killed during the rescue attempt. In 2010 one retreat miner was killed in a rib fall, and three miners were killed by two separate coal burst incidents in 2013 and 2014. Each of these hazards will be discussed as well.

Previous studies have found that the roof/rib non-fatal injury rate has been slightly lower in pillar recovery mines than it is in other room and pillar mines [3]. The explanation was that while the process of bolting freshly-exposed mine roof is normally a major source of rock fall injuries, retreat mining typically requires relatively little roof bolting. However, NIOSH found that the subset of deep-cover retreat mines (cover greater than 300 m), had a much greater rib fall non fatal injury rate than other mines [7]. During the period 2006–2008, nearly one-quarter of all the rib fall injuries in the entire U.S. underground coal industry occurred in the small group of deep cover retreat mines that accounted for less than 10% of all hours worked underground.

4. Rock mechanics of pillar recovery

Throughout much of the 20th century, mining engineers had a relatively simple understanding of the rock mechanics involved in pillar recovery. This traditional theory was expressed clearly in the 1973 edition of the SME Mining Engineering Handbook [9]:

> "As complete recovery as possible is the No. 1 goal in pillar mining. Nothing should be left large enough to prevent proper caving and subsidence of the roof, which should follow immediately or very shortly after mining of each final stump. If necessary, posts and cribs should be removed, stumps shot as needed and other steps taken as required to insure proper caving and minimum transfer of weight to the mineral being mined. In extreme circumstances, this may involve drilling and shooting the overlying material to induce caving. Among the hazards and handicaps of roof hanging up on pillars or supports left in the gob are squeezing and crushing of the coal or other material or complete collapse at some point in the mining process, endangering men and equipment and causing loss of mineral."

One result of the traditional emphasis on complete extraction was the large number of miners killed while extracting the final pushout stump (Fig. 5). Montague found that 50% of the 67 retreat mining fatalities, and he analyzed occurred during the mining of the pushout [8]. Similarly, Mark et al. found that final stumps accounted for 45% of the 26 retreat mining fatalities between 1989 and 1996 [3]. These numbers are particularly staggering when one considers that only a small fraction of the total time spent during pillar recovery is devoted to the pushout extraction.

When Mark and Zelanko analyzed MSHA fatality reports from 25 pillar recovery incidents that occurred between 1992 and 2005, they found that two-thirds of the mines where the fatalities had occurred had been following their approved roof control plans. In other words, the plans themselves were inadequate, not the implementation [10]. Since the traditional emphasis on total recovery was providing designs, procedures, and practices that were insufficient to protect miners, a new paradigm was needed.

The new risk reduction strategy for pillar extraction developed by Mark and Zelanko included three components: (1) global stability: prevention of section-wide pillar failure, (2) local stability: prevention of roof falls in the working area, and (3) work procedures and worker location: minimizing exposure to hazardous areas [10].

During the past decade, these new concepts have been incorporated into roof control plans for pillar recovery, with dramatic results. The MSHA roof control plan review and approval handbook reflects the new approach, and contains guidance documents and checklists that have been developed regarding retreat mining safety [11].

5. Global stability

Proper pillar design is the key to ensuring global stability, because the pillars normally carry the weight of hundreds of meters of overlying rock. In contrast, artificial supports like roof bolts or posts can carry just a few meters of rock, and so can only provide local stability to the roof directly above the miners. Without global stability, no local support strategy can be effective.

Mining engineers have known about the need for proper pillar sizing for more than a century. For example, Bunting wrote that "to mine without leaving adequate pillar supports will result, sooner or later, in a squeeze" [12]. Unfortunately, pillar design remained more of an art than a science for most of the 20th century. In particular, none of the popular empirical techniques considered the effect of the abutment loads generated by pillar extraction on the pillar line.

The 2007 Crandall Canyon Mine Disaster was a tragic reminder of the importance of global stability. The MSHA report on the disaster concluded that "it was obvious, at the most fundamental level, that the accidents at Crandall Canyon Mine were precipitated by pillar failures" [13]. The report further cited the "flawed pillar design" which allowed the stress level to "exceed the strength of a pillar or group of pillars near the pillar line," resulting in a local failure that triggered a widespread collapse.

MSHA's standard at 30 CFR 75.203 (a) states that "pillar dimensions shall be compatible with effective control of the roof, face and ribs and coal or rock bursts." In the wake of the Crandall Canyon

disaster, MSHA distributed a series of program information bulletins (PIBs) and other documents that described the technical and engineering data related to pillar design that mine operators must submit as part of their roof control plans. Subsequently, MSHA incorporated these PIBs into its roof control plan review and approval handbook ("the Handbook"). The Handbook states that "in order to comply with 30 CFR 75.203 (a), the retreat mining portion of the roof control plan submittal should include an engineering design and supporting analysis" [11].

Fortunately, reliable techniques for designing coal pillars are now readily available. The analysis of retreat mining pillar stability (ARMPS) is the most widely used pillar design method in the U.S. ARMPS is an empirical method that was originally developed by NIOSH in the mid-1990s [14]. Statistical analysis was used to derive design guidelines that separate the "successful" case histories (those where the entire panel was mined without pillar failure) from those that were "unsuccessful."

The original ARMPS database consisted of approximately 150 case histories, representing a broad range of cover depths [3]. A follow-up study that focused on deep cover pillar recovery added 100 case histories from mines in Central Appalachia [15]. The latest version of ARMPS is based on 640 case histories, and it features a "pressure arch" loading model and new criteria for sizing the barrier pillars between panels [16]. Where a retreat mine may be impacted by a multiple seam mining (an all-too-common situation in Central Appalachia), the NIOSH program analysis of multiple seam stability (AMSS) is available to assist with pillar design [17].

The LaModel program can also be used for coal pillar design [18]. LaModel is a numerical model that can analyze more complex mining geometries, accounting for such factors as multiple seam interactions and variable surface topography. LaModel is unique in that it includes "laminations" allowing it to more accurately simulate the behavior of layered, sedimentary overburden. It has also been extensively calibrated to case histories [19].

The widespread application of pillar design based on engineering principles to retreat mining has apparently resulted in a dramatic reduction in the number of squeezes, wide spread propagating ground failure, and other types of pillar failures. In recent years only a handful of pillar failures have come to the attention of MSHA technical support, while the sheer number of failures included in the ARMPS and AMSS data bases attests to the prevalence of such events in the past.

In retrospect, it seems likely that most of the squeezes that occurred in past decades were due to undersized pillars, not to poor caving. Miners who experienced a squeeze in those days wanted an explanation, and "incomplete extraction" was a convenient culprit. As discussed below, today large remnants are almost always purposely left standing, and it is not unusual for the roof to stay up for some time after a pillar is fully extracted. Yet the incidence of squeezes has diminished, not increased. In fact, our modern understanding of the overburden load distribution associated with full extraction mining indicates that the traditional theory was based on a misconception. The height of an immediate roof cave is so small compared to the total weight of the overburden, and the stiffness of the freshly created gob is so low, that it is hard to see how the caving of the immediate roof could seriously affect the overburden loads carried by the pillars.

6. Local stability risk factors

Global stability is a necessary, but not sufficient, condition for creating a safe working area. Local stability depends on providing adequate support to the immediate roof. The crucial area is the active intersection just outby the pillar being extracted. Mark and Zelanko identified three key technologies for improving the level of roof support during pillar recovery: (1) leaving an engineered final stump, rather than extracting the entire pillar; (2) substituting mechanized mobile roof supports (MRS) for traditional wood timbers; and (3) using longer and stronger roof bolts on retreat sections, particularly in intersections [10].

Over the past decade, concerted efforts have been made to implement these technologies into retreat mining practice and approved roof control plans, and they are discussed in Appendix G of the Handbook [11].

Final stump: leaving the final stump is perhaps the biggest change with the new paradigm. Rather than viewing the stump as a hindrance to "necessary" caving, the stump is now seen as an essential roof support. A 2013 survey of roof control supervisors in the five Central Appalachian MSHA Districts found that 98% of retreat mining roof control plans now leave a final stump in place. In some cases these stumps are as small as 1.8 m by 1.8 m, but they are more commonly at least 2.4 m by 2.4 m (Fig. 6a).

The survey also found that in many plans no lifts at all are taken from the crosscut. In these plans the "final stump" is the entire outby end of the pillar. In two Central Appalachian MSHA Districts, apparently about 80% of the retreat pillars are mined this way (Fig. 6b).

Mobile roof supports: traditionally, timber posts provided supplemental support for pillar recovery. More than 100 roadway, turn, and breaker posts could be required to extract a single pillar [20]. But setting posts on a pillar line is a very high-risk activity. Between 1998 and 2007, six retreat miners were killed while setting posts. Timber posts also have a number of disadvantages as roof supports, and their weight and bulk can result in material handling injuries.

Mobile roof supports (MRS) are shield-type supports mounted on a crawler frame (Fig. 7). The advantages of MRS over timber supports are that they: (1) reduce miner exposure to roof falls at the pillar line since they can be operated remotely, (2) provide an active support pressure to the roof at the pillar line, (3) provide larger overall capacity (one 600 ton MRS is approximately equivalent to 12 posts), (4) maintain load through a much greater range of displacement, and (5) decrease the potential for material handling injuries.

For all of these reasons, both MSHA and NIOSH have advocated the use of MRS for pillar recovery since their introduction more than 20 years ago.

Another survey of roof control supervisors in Central Appalachia, conducted in 2015, found that about 60% of the hours worked at retreat mines were at operations that used MRS. This contrasts with the NIOSH finding that more than 80% of deep cover pillar recovery mines used MRS [7]. The explanation is likely that the deeper retreat mines tend to be in thicker seams. The operating range of MRS is usually limited to seams thicker than approximately 1.1 m, and apparently few mines with seams thinner than 1.3 m use MRS.

Roof bolts: roof bolts are the only overhead protection miners have during pillar recovery unless they are under the haulage

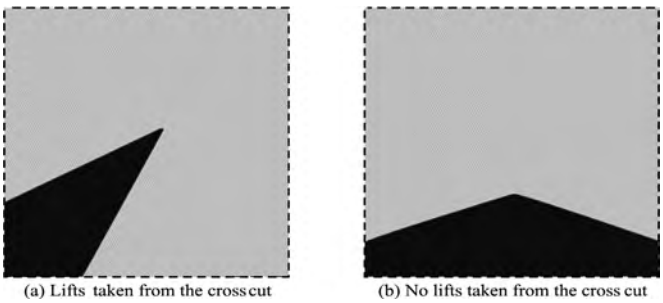

Fig. 6. Plan views of two types of final stumps.

Fig. 7. A mobile roof support.

equipment canopies. Yet in all but one of the fatal retreat mining incidents that occurred between 1996 and 2007 the victims were located beneath bolted roof.

In traditional roof control plans, retreat sections were typically supported by the same roof bolt patterns used elsewhere in the mine. Now we recognize that pillar lines, like longwall headgate and tailgate entries, are subjected to abutment loads and therefore normally require extra roof support. Typically the extra support consists of 4–6 cable bolts installed in the intersection in anticipation of the more severe conditions that will be encountered during retreat mining. NIOSH found that 87% of the retreat mines they studied incorporated such extra roof bolt support, and the authors believe that the percentage is even higher today [7].

7. Work procedures and worker location

Successful pillar extraction requires attention to detail. Fatal accidents, some involving multiple fatalities, have occurred when miners were standing unnecessarily close to the pillar line. In other cases poor mining practices have contributed to fatalities. Some of the best practices which have been developed, and which are covered in more detail in the Handbook, are discussed below.

Cut sequence: federal regulations require that the roof control plan contain drawings that show "the sequence of mining pillars." If a panel configuration differs from the one shown in the plan, such that the sequence in the drawings is no longer applicable, then a panel-specific mining sequence should be developed before the panel is retreated. This is especially important when the panel has a change of direction, a factor which contributed to a double fatality in KY [21].

Cut dimensions: a 2013 survey of MSHA roof control supervisors found that a large majority of retreat mines limit the pillar lifts to one continuous miner (CM) head width. In essence, the CM is run directly into the pillar to its maximum allowed depth, and then backed straight out. Typically, the attack angle is only about 50 degrees from the entry. One advantage of making such a cut, without turning in the lift, is that it minimizes the time spent in any one cut. Another is that the CM can quickly back out if roof conditions worsen, or it can be pulled straight out if it gets caught by a rock fall.

Where this method is used, the lifts are started just far enough back along the rib to allow the CM head to clear the mobile roof support or posts. Sometimes a thin coal fender is left between cuts at the rib line to assist in roof control. As the lift progresses into the pillar, the CM will typically cut into the previous lift to maintain ventilation.

Unfortunately, the direct attack method only allows the CM to extract 7.5 m or so of the pillar. This means that a large coal remnant is left in the middle of the block if the pillars are more than 15 m wide. Wider pillars are often necessary to support the overburden in thicker seams under greater cover. An alternative to the direct attack is to enter the pillar and then gradually work the CM to a greater angle of penetration into the pillar. In this manner pillars up to about 21 m wide can be almost entirely recovered.

The practice of starting the new lift 6–7.5 m back from previous one, and then widening it out to remove all the coal between the lifts, should be avoided. This technique was in use at a retreat mine in Utah when the roof fell in front of the MRS, killing the CM operator and injuring the helper [22]. If the cut must be widened in this manner, then a solid coal fender should be left between the lifts to help support the roof.

Worker position: the pillar line is a dangerous place, and miners should never congregate there. No one except haulage equipment operators should be inby the continuous mining machine operator while a pillar is being mined. Only those miners necessary to mine coal and/or install supports should be working or travelling in the work area, including the intersection. Under no circumstances should anyone travel inby installed breaker posts or into a region where pillar recovery has been completed.

The position of the continuous mining operator is another concern. The CM operator normally must handle the miner cable, keeping it against the pillar rib and out of the way of the shuttle cars. The CM operator must also stay clear of the CM boom, the haulage cars, and possibly hazardous ribs. For all these reasons, when taking the left-hand cut with a machine cabled on the right, the CM operator is usually located inby the CM, between the CM and the MRS (or turn posts). One disadvantage of this inby location is the potential lack of egress, particularly when the CM is just beginning its cut (Fig. 8a). When taking the right-hand cut, the CM operator usually stays close to the right rib, outby the CM, and can handle the cable from here and stay out of the way of the boom and the shuttle cars, and also is outby all previous lifts (Fig. 8b).

Mobile roof supports: while MRS can be a highly effective means of reducing the risk of pillar recovery, they must be used properly. Fatalities have resulted when workers have been standing too close to them, or did not follow standard operating procedures [23,24]. After evaluating these fatalities, MSHA released a number of best practices, including: (1) upon completion of mining in a given pillar, the units should be moved sequentially until they are between intact coal pillars, (2) at least one unit should be pressurized against the roof at all times, (3) personnel should remain at least 7.5 m away from MRS when they are being pressurized or depressurized, and (4) plans for performing maintenance in safe locations and for retrieving disabled or immobilized MRS should be formulated in advance and strictly followed.

Worker training: prior to any retreat mining, all persons engaged in retreat mining (including new crew members) should be trained in the provisions of the approved roof control plan relative to retreat mining. Training shall be conducted before retreating of a new panel begins.

Stability assessments: retreat mining imposes additional stresses and strains on a mine roof. Rock that seemed stable after development can suddenly be broken or pulled apart. Weak rock, or rock that contains pre-existing geologic fractures, is particularly susceptible.

Conducting a geologic assessment of the entire panel before retreat mining commences is an important best practice. The assessment should identify major roof fractures, which can then be marked, mapped, and supported. Some mines use paint or flags to note the presence of faults, hillseams (open joints), or other hazardous features. It is good practice to plan to skip some lifts in

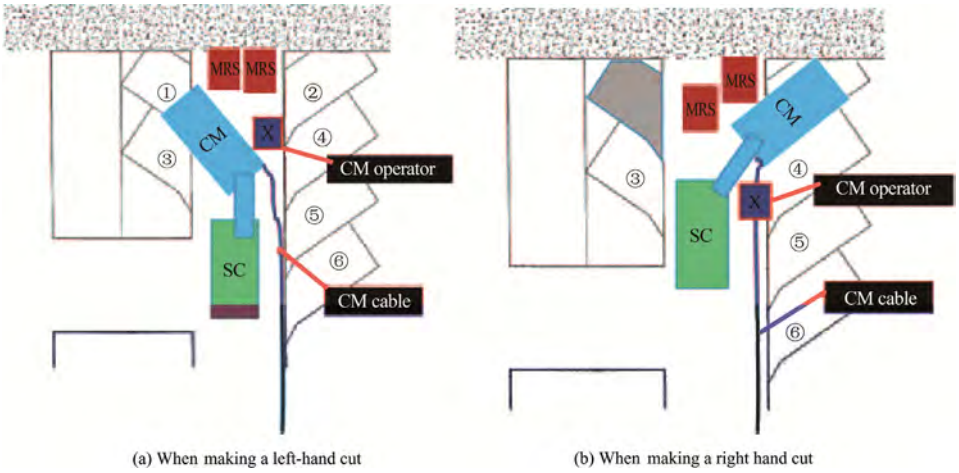

Fig. 8. Position of the continuous miner operator during pillar extraction (*X*) with a machine cabled on the right-hand side.

order to leave coal as support for such features. Appendix H of the MSHA Handbook contains further suggestions on conducting a pre-retreat mining hazard assessment.

In the past, poor conditions were often observed in the area before the retreat mining fatality occurred, but no action was taken [10]. Ideally, pre-shift and on-shift examinations should include a thorough assessment of geologic conditions, and hazards should be reported and dangered off or appropriately supported. Examinations that include areas outby the pillar line can be used to anticipate geologic conditions prior to retreat.

Test holes are useful to determine if there is roof separation, and they can be monitored during mining to see if conditions worsen. The pressures and loading rates visible on MRS gauges also provide information on roof stability. Mine-specific "trigger points" indicating anomalously high loads or loading rates can be identified, along with the procedures that should be employed to respond to them.

8. Rib falls and coal bursts

As roof fall accidents have become less frequent, bursts and rib falls have become more prominent. Hazardous roof falls can occur during pillar extraction regardless of the depth of the mining. Rib falls and coal bursts, on the other hand, are much more likely to occur under deep cover.

Rib falls are a serious hazard at deep cover pillar recovery mines. During the period 2010–2015, eight miners were killed by rib falls in room-and-pillar operations. Only one of those rib fatalities occurred on a pillar line, but another five were at mines that sometimes employed pillar extraction. The most recent rib fall fatality occurred in January of 2016 during development mining at the only active pillar retreat mine in PA.

The two main factors that lead to an increased risk of rib falls are thicker coal seams and higher stress levels [8]. For example, analysis of the eight recent fatal room-and-pillar rib fall incidents reveals that:

(1) Seven occurred where the depth exceeded 210 m and/or a multiple seam interaction was present, and
(2) The mining height exceeded 2.1 m in all but one case.

Rib bolting can be highly effective in reducing the risk of rib falls. Rib bolts should be installed using inside-control roof bolting machines, where the drill heads are between the operators and the ribs.

Coal bursts are defined as the sudden, violent ejection of coal or rock into the mine opening. Despite decades of research, the sources and mechanics of bursts are imperfectly understood, and the means to predict and control them remain elusive.

Coal bursts have long been among the most feared hazards in deep retreat mines. Eighty years ago, Rice described bursts in the coal mines of Harlan County, KY, and Wise County, VA [25]. A comprehensive database of 172 burst events that occurred between 1936 and 1993 indicated that more than 80% of the bursts reported by room-and-pillar mines occurred during the process of pillar or barrier pillar recovery [26].

The incidence of non-longwall bursts in room-and-pillar mines has decreased significantly with time. Fig. 9 shows that during the 1980 s and 1990's, there were about six bursts per year in locations other than the longwall face. The rate has fallen to less than 2 per year since then. There have been just six non-longwall bursts since 2010.

Unfortunately, three of those six bursts resulted in fatalities or permanently disabling injuries. All three were during pillar recovery, two in KY and the third in WV. None of these mines had ever reported a burst before.

Pillar design is the primary engineering control for minimizing the risk of pillar failures and coal bursts during retreat mining under deep cover. In the past, many large bursts have occurred where the barrier pillars were too small, were being extracted on retreat, or were not used at all. In some of these cases, pillar splitting operations without a barrier pillar apparently triggered the burst [7].

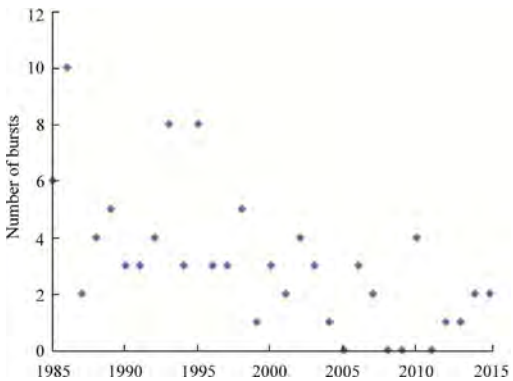

Fig. 9. Bursts in US coal mines (excluding the longwall face), 1984–2015.

Inadequate pillar design did not seem to play a role in any of the recent coal bursts, however. In one KY case, the MSHA investigation concluded that a multiple seam interaction, stronger roof geology, and an improper pillar extraction sequence contributed to the fatal burst [27]. Multiple seam interactions and geological conditions contributed to the WV burst as well [28]. Other large bursts have occurred during development mining at deep cover room and pillar mines, fortunately without injuries [29,30].

Risk management programs for the coal burst hazard in room and pillar mines have been presented [31,32]. Underground observations and monitoring are critical elements of such programs. Mining crews should be trained to observe coal burst warning signs, particularly the occurrence of small bursts, which are often the best indication that an area is becoming more burst prone. A record-keeping system should be maintained and management processes developed to ensure that warning signs receive appropriate responses. Both of the recent fatal coal bursts during pillar recovery were preceded by smaller bursts whose implications were not heeded.

9. Conclusions

Long considered "inherently" dangerous, the past eight years have shown that pillar recovery can be conducted as safely as other types of underground mining. The rate of fatal roof falls, based on exposure hours, has apparently been reduced by a factor of more than ten. This success was achieved through the widespread application of better ground control practices identified through a rigorous evaluation of past failures. The new paradigm is also based on an updated understanding of the basic rock mechanics of pillar recovery. It is built around the concepts of global and local stability, and replaces the traditional emphasis on "complete extraction." The third essential component of the new approach is an emphasis on the management of work procedures during pillar recovery operations. Remaining challenges include rib failures and coal bursts. Both hazards are most severe in the mines under deeper cover.

References

[1] Rice GS. Accidents from falls of roof and coal. Miner's Circular No. 9, US Bureau of Mines, 5th ed., 1916. p. 18.
[2] Kauffman PW, Hawkins SA, Thompson RR. Room and pillar retreat mining—a handbook for the coal industry. USBM IC 8849; 1981. p. 228.
[3] Mark C, McCall E, Pappas DM. A statistical overview of retreat mining of coal pillars in the United States. In: Proceedings of the new technology for ground control in retreat mining. Pittsburgh, PA, NIOSH IC 9446. p. 2–16.
[4] Mark C, Chase FE, Pappas DM. Reducing the risk of ground falls during pillar recovery. SME Trans 2003;314:153–60.
[5] McAteer D. Report to Governor Bob Wise on mine safety and health in West Virginia. Available at <http://www.wvminesafety.org/Mcateer.PDF>; 2001.
[6] Marshall Miller and Associates. Retreat mining practices in KY. Report to the Kentucky Department of Natural Resources. Available at <http://dnr.ky.gov/Publications%20 Library/RetreatMiningPracticesinKentucky.pdf>; 2006.
[7] NIOSH. Research Report on Coal Pillar Recovery Under Deep Cover. Report prepared in response to the FY 2008 Appropriation (Public Law 110–161); 2010. p. 79.
[8] Montague. Pillar recovery-the lost art? In: Proceedings of the American mining congress. Chicago. p. 531–48.
[9] SME. Mining engineering handbook. Cummins AB, Given, IA, editors. Section 12.4-Room and Pillar Methods; 1973(2). p 12–62.
[10] Mark C, Zelanko JC. Reducing roof fall accidents on retreat mining sections. Coal Age 2005;110(12):26–31.
[11] MSHA. Roof control plan approval and review procedures. Handbook number PH13-V-4. Available from <http://www.msha.gov/READROOM/HANDBOOK/HANDBOOK.HTM>; 2013.
[12] Bunting D. Chamber pillars in deep anthracite mines. Trans AIME 1991;42:236–45.
[13] MSHA. Report of the investigation. Fatal underground coal burst accidents, Crandall Canyon Mine. Available from <http://www.msha.gov/Fatals/2007/CrandallCanyon/FTL07CrandallCanyon.pdf>; 2007.
[14] Mark C, Chase FE. Analysis of retreat mining pillar stability. In: Proceedings of the new technology for ground control in retreat mining. NIOSH IC 9446, Pittsburgh, PA. p. 17–34.
[15] Chase FE, Mark C, Heasley KA. Deep cover pillar extraction in the U.S. coalfields. In: Proceedings of the 21st international conference on ground control in mining. Morgantown, WV: West Virginia University; 2002. p. 68–80.
[16] Mark C. Pillar design for deep cover retreat mining: ARMPS version 6 (2010). In: Proceedings of the third international workshop on coal pillar mechanics and design. Morgantown, WV. p. 106–21.
[17] Mark C, Chase FC, Pappas D. Analysis of multiple seam stability. In: Proceedings 26th international conference on ground control in mining, Morgantown, WV. p. 1–18.
[18] Heasley KA. A new laminated overburden model for coal mine design. In: Proceedings of the new technology for ground control in retreat mining. Pittsburgh, PA. Pittsburgh, PA, US: U.S. Department of Health and Human Services, Public Health Service, Centers for Disease Control and Prevention, National Institute for Occupational Safety and Health; 1997. p. 60–73.
[19] Heasley KA, Sears MM, Tulu IB, Calderon-Arteaga C, Jimison L. Calibrating the LaModel program for deep cover pillar retreat coal ming. In: Proceedings of 3rd international workshop on coal pillar mechanics and design. Morgantown, WV. p. 47–57.
[20] Chase FE, McComas A, Mark C, Goble CD. Retreat mining with mobile roof supports. In: Proceedings of the new technology for ground control in retreat mining. NIOSH Publication No. 97–122, IC 9446; 1997. p. 74–88.
[21] MSHA. Report of the Investigation. Fatal Fall of Roof, Stillhouse No. 1 Mine. Available from <www.msha.gov/FATALS/2005/FTL05c1112.asp>; 2005.
[22] MSHA. Report of the Investigation. Fatal Fall of Roof, Castle Valley No. 4 Mine. Available from <http://www.msha.gov/FATALS/2013/FTL13c08.asp>; 2013a.
[23] MSHA. Report of the Investigation, Fatal Fall of Roof, Cucumber Mine. Available from <www.msha.gov/FATALS/2007/FTL07c0203.asp>; 2007a.
[24] Urosek JE, Zuchelli DR, Beiter DA. Gob ventilation and bleeder systems in US coal mines. Soc Min Eng 1995. pp. 95–78.
[25] Rice GS. Bumps in coal mine of the Cumberland Field, Kentucky and Virginia—causes and remedy. U.S. Department of the Interior. Bureau of Mines RI 3267; 1935.
[26] Iannacchione AT, Zelanko JC. Occurrence and remediation of coal mine bumps: an historical review. In: Proceedings of the mechanics and mitigation of violent failure in hard rock mines. USBM SP 01-95, Spokane. PA, US. p. 27–67.
[27] MSHA. Report of the Investigation. Fatal Rib Burst, Huff Creek No. 1 Mine. Available from <http://www.msha.gov/FATALS/2013/FTL13c12.asp>; 2013b.
[28] MSHA. Report of the Investigation, Fatal Rib Burst, Brody Mine. Available from <http://www.msha.gov/FATALS/2014/FTL14c04-05.asp>; 2014.
[29] Newman D. A case history investigation of two coal bumps in the southern appalachian coalfield. In: Proceedings of the 21st international conference on ground control in mining. Morgantown, WV: West Virginia University; 2002. p. 90–7.
[30] Gauna M, Phillipson S. Evaluation of a multiple seam interaction coal pillar bump. In: Proceedings of the 27th international conference on ground control in mining. Morgantown, WV: West Virginia University; 2008. p. 51–9.
[31] Mark C, Gauna M. Evaluating the risk of coal bursts in underground coal mines. In: Proceedings of the 34th international conference on ground control in mining. Morgantown, WV. p. 47–53.
[32] Zhang P, Peterson S, Neilans D, Wade S, Mcgrady R, Pugh J. Geotechnical risk management to prevent coal outburst in room and pillar mining. In: Proceedings of the 34th international conference on ground control in mining. Morgantown, WV. p. 68–79.

International Journal of Mining Science and Technology 27 (2017) 115–120

Contents lists available at ScienceDirect

International Journal of Mining Science and Technology

journal homepage: www.elsevier.com/locate/ijmst

Effects of longwall-induced stress and deformation on the stability and mechanical integrity of shale gas wells drilled through a longwall abutment pillar

Daniel W.H. Su

National Institute for Occupational Safety and Health, Bruceton 15236, PA, USA

ARTICLE INFO

Article history:
Received 15 July 2016
Received in revised form 8 August 2016
Accepted 10 September 2016
Available online 24 December 2016

Keywords:
Gas well
Casing
Abutment pillar
Stability
Safety and health
Instrumentation
Numerical simulation

ABSTRACT

This paper presents the results of a comprehensive study conducted by CONSOL Energy, Marcellus Shale Coalition, and Pennsylvania Coal Association to evaluate the effects of longwall-induced subsurface deformations on the mechanical integrity of shale gas wells drilled over a longwall abutment pillar. The primary objective is to demonstrate that a properly constructed gas well in a standard longwall abutment pillar can maintain mechanical integrity during and after mining operations. A study site was selected over a southwestern Pennsylvania coal mine, which extracts 457-m-wide longwall faces under about 183 m of cover. Four test wells and four monitoring wells were drilled and installed over a 38-m by 84-m centers abutment pillar. In addition to the test wells and monitoring wells, surface subsidence measurements and underground coal pillar pressure measurements were conducted as the 457-m-wide longwall panels on the south and north sides of the abutment pillar were mined by. To evaluate the resulting coal protection casing profile and lateral displacement, three separate 60-arm caliper surveys were conducted. This research represents a very important step and initiative to utilize the knowledge and science obtained from mining research to improve miner and public safety as well as the safety and health of the oil and gas industries.

1. Introduction

Due to a recent shale gas boom, one which may enable the United States to become more energy independent, approximately 800 gas wells have been drilled through active and future coal reserves in Pennsylvania, West Virginia, Ohio, Virginia, and Tennessee over the past 10 years. These shale gas wells have penetrated many coal seams, such as the Sewickley, Pittsburgh, upper/lower Freeport, and upper/middle/lower Kittanning seams, which are either actively mined or planned to be mined in the near future. Also, these shale gas wells, whether tapped into the Marcellus or Utica formations, contain very high (approximately 2.41–20.7 MPa) gas pressure. Longwall and high-extraction-induced stresses and strata deformations could induce high stresses and deformations in the shale gas well casings, which may seriously compromise the mechanical integrity of the production, intermediate and coal protection casings. Such a compromise of mechanical integrity of the well casings would potentially introduce high-pressure, explosive gas into underground mine workings or into surface dwellings and water wells, which could seriously jeopardize underground miners as well as public safety and health. Plugging these gas wells ahead of mining not only incurs substantial cost for the mining operators, it also represents substantial loss of income for gas operators.

In 2012, upon recognizing that the 1957 Pennsylvania Gas Well Pillar Regulations were formulated without data from modern-day longwall mining, the Pennsylvania Department of Environmental Protection (PA DEP) initiated a call for research to update the outdated regulations, which have been widely used by the Mine Safety and Health Administration (MSHA) and other states to govern gas well pillar stability issues over the past 60 years. In response to this call for research, the John T. Boyd Mining and Geological Consultants Company was commissioned to conduct an analytical study to produce a preliminary safeguard distance table [1,2]. This table, by the nature of its overly simplified analytical approach, cannot take into account detailed subsurface strata deformations. In 2013 and 2014, a study was conducted in a southwestern Pennsylvania coal mine under shallow cover by the coal and gas industries, which focused primarily on the effect of strata deformations on the well casings above the mining horizon. This paper presents the results of a suite of detailed 3D finite element analyses and some

E-mail address: kxz4@cdc.gov

http://dx.doi.org/10.1016/j.ijmst.2016.09.028
2095-2686/

of the field instrumentation results (about 75% of the field instrumentation results are not able to be included pending consent from the project partners).

2. Site description and geotechnical instrumentations

The study site was located over a southwestern Pennsylvania coal mine employing longwall panels to extract from the Pittsburgh Seam. A three-entry longwall gate road system of 18.3 m × 38.1 m centers was employed at the mine. Fig. 1 illustrates the layout of the longwall panels, which are oriented approximately in the east-west direction. Fig. 1 also shows the locations of the surface and subsurface instrumentation layout, which includes four test wells designed similarly to real shale gas wells, three subsurface inclinom stations and one subsurface extensom station. Test wells were drilled to a depth of 196 m, which was about 12.2 m below the Pittsburgh Seam. The inclinom holes were drilled to different depths below the surface (0–61, 61–122 and 122–183 m), while the extensom hole was drilled to 192 m below the surface. In addition to the surface subsidence measurements, underground instrumentation consisting of borehole pressure cells (BPCs) and entry convergence meters was also installed to corroborate surface responses with subsurface and underground responses to provide a clear picture of strata reaction to longwall mining. The first panel mined by the test site in August 2013 and the second panel mined by the test site in May 2014.

3. Site geology

The overburden depth at the test site was about 183 m. Fig. 2 shows the detailed geology at the test site, which was interpreted by correlating a test site gamma log and a nearby core hole. Clearly, the overburden geology was a typical Pittsburgh Seam geology and was highlighted by many strong and weak rock interfaces, which were demonstrated to have major influences on longwall-induced stresses and deformations from ground control research conducted over the past 30 years.

4. 3D finite element simulations

Prior to the instrumentation program, which commenced in June 2013, a series of ABAQUS 3D finite element simulations were conducted and analyzed to evaluate the effect of longwall excavations on the induced stresses and deformations within the gate road abutment pillars and their effects on the stability of shale gas wells drilled through the abutment pillars. Specifically, the concerns centered on the stability of the production, intermediate and coal protection casings, since any stability compromise of these casings may potentially introduce high-pressure shale gas into mine workings, which would seriously jeopardize underground miner safety and health. The ABAQUS finite element program was selected over a number of numerical models, since it has been calibrated and verified with field data from the Pittsburgh, Pocahontas #3, and Illinois #6 seams over the past 25 years.

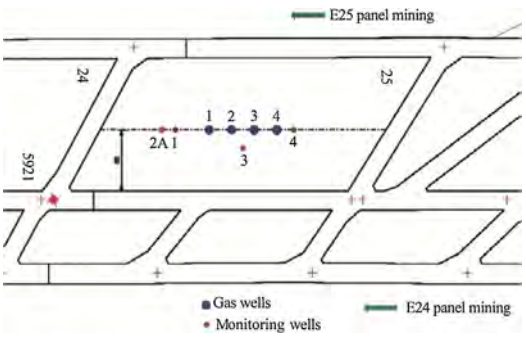

Fig. 1. Surface instrumentation layout at the test site.

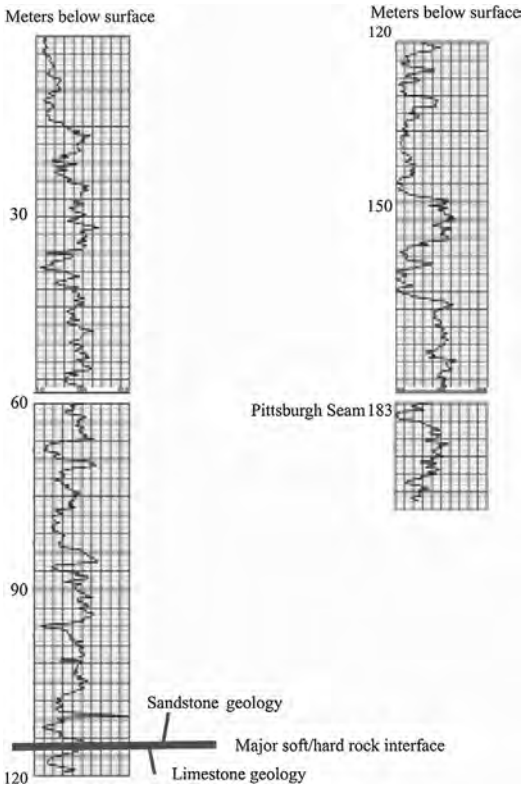

Fig. 2. Test site overburden geology as interpreted from an on-site gamma log and a nearby core hole.

5. Results of geotechnical instrumentation and 3D finite element analyses

5.1. Geotechnical instrumentation

Surface subsidence surveys were conducted as the first panel approached within 305, 153, 61, and 0 m of the test site, and 61, 153, and 305 m past the test site, which occurred in August 2013. A similar survey schedule was also implemented for mining of the second panel, and the survey was completed in June 2014. The inclinom and extensom readings were recorded continuously over the same time frame. Three 60-arm caliper surveys were conducted to evaluate the casing profile of the four test wells, and they were conducted one month prior to mining of the first panel, one month after mining of the first panel, and one month after mining of the second panel.

Fig. 3 shows the results of surface subsidence and surface horizontal movement measurements after completion of the first and second panels, respectively. Fig. 4 illustrates the plastic casing profile of one of the inclinom holes, which indicates the magnitude of movement after the first and second panel extractions. Results from the extensom monitoring are not presented, since due to the relatively shallow overburden, less than 1.3 cm of vertical movement was detected. Results from the 60-arm caliper surveys are not presented in this paper pending consent from the project partners, although the well casing profiles mimic the inclinom casing profile shown in Fig. 4.

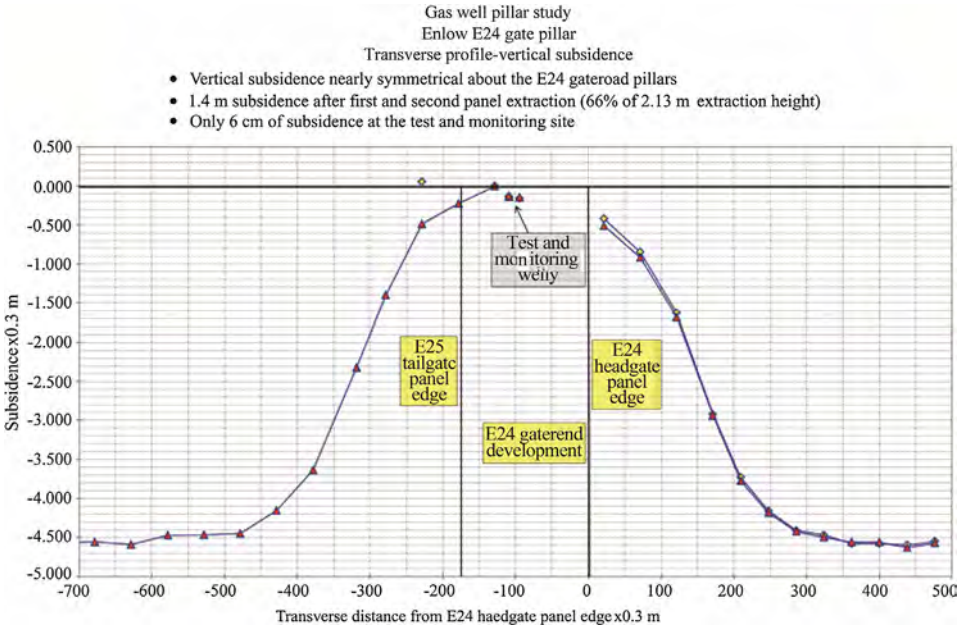

Fig. 3. Surface subsidence after first and second panel extraction.

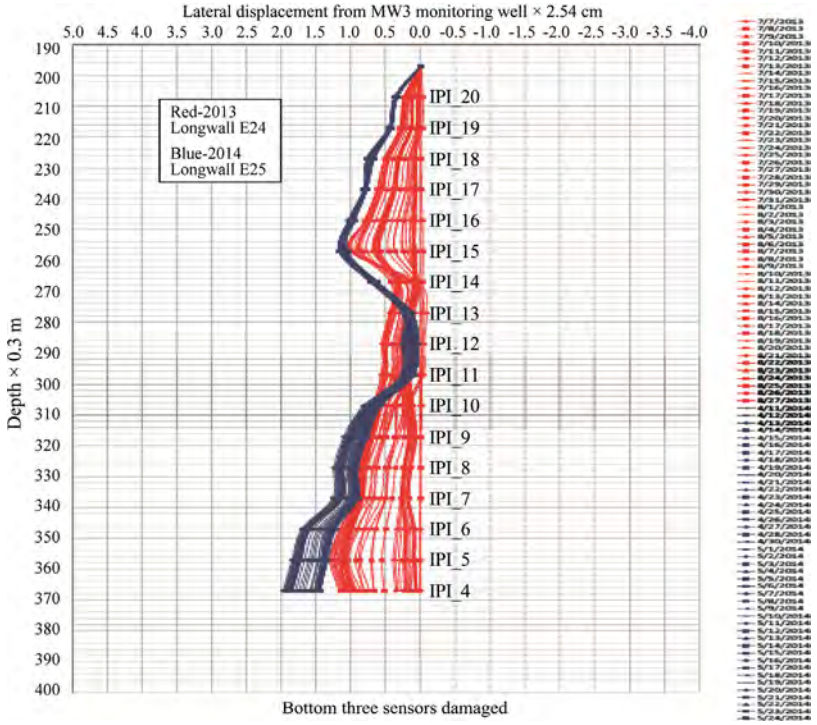

Fig. 4. Lateral displacement observed in one of the IPI monitoring wells.

5.2. 3D finite element analyses

A number of 3D ABAQUS finite element models (Fig. 5) were constructed in April 2013 to evaluate the potential effects of longwall-induced stresses and deformations on the stability of shale gas well casings drilled through longwall abutment pillars. The overburden geology used for the ABAQUS models at this early stage was based on a core hole about 213 m north of the test site. Upon test hole drilling at the test site in July 2013, a detailed gamma log was obtained and the ABAQUS models were rerun

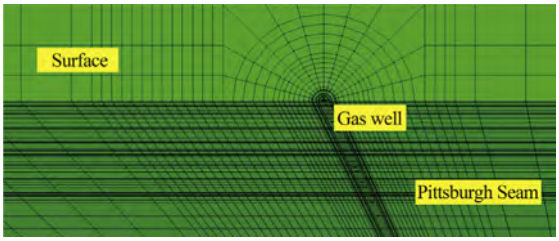

Fig. 5. 3D gas well finite element model.

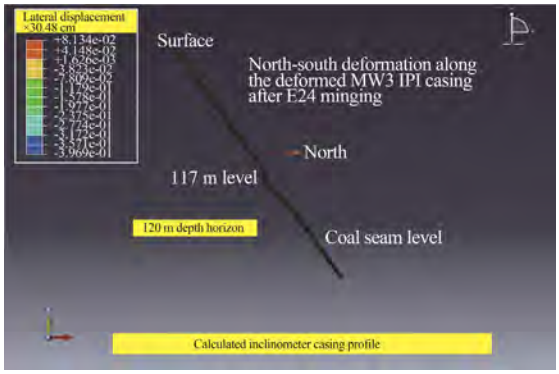

Fig. 6. Calculated inclinom casing profile.

using the interpreted overburden geology from the test site (Fig. 2). Fig. 6 shows the ABAQUS-calculated profile of the plastic inclinom casing, which closely resembles the measured profile in Fig. 4. Fig. 7 shows a calculated profile of one of the test wells, which has about an 85% match with the 60-arm caliper log measured profile.

Table 1 tabulates the comparisons of measured and ABAQUS-calculated surface subsidence and underground pillar pressure measurements. Clearly, with the detailed geologic section and with accurate modeling of the overburden interface shearing, the ABAQUS-calculated surface subsidence and underground pillar pressure increases are in excellent agreement with measured surface subsidence and pillar pressure increases. On the other hand, the ABAQUS-calculated inclinom and well casing deformations are in reasonable agreement with measured inclinom and well casing deformations. Fig. 8 shows a zoom-in ABAQUS deformation plot at 120 m below the surface, where maximum lateral shearing is present, closely resembling the TVISION image (not presented) from the 60-arm caliper survey at the same location.

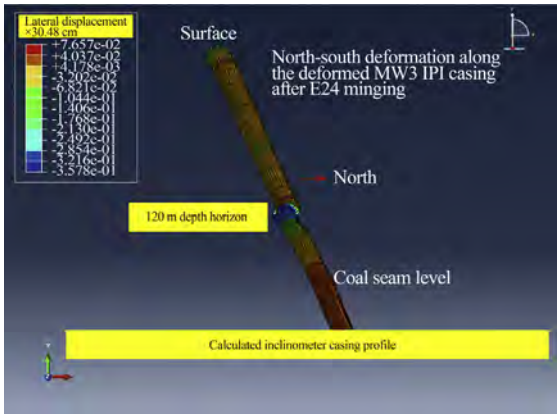

Fig. 7. Calculated test well casing profile.

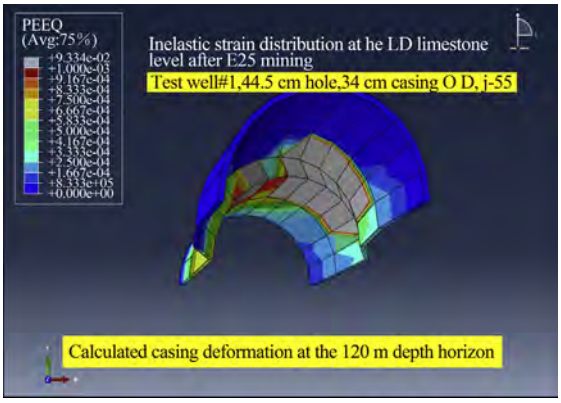

Fig. 8. Zoom-in ABAQUS plot of the 120 m-depth deformation.

6. Potential of employing the field-instrumentation-calibrated ABAQUS model to evaluate well casing stability under different overburden geology and well casing design

Since the instrumentation site described above was confined to a given overburden depth and its associated geology, two rather intriguing questions arise and need to be answered. They are: (a) will gas wells drilled into mines with deep cover behave similarly? and (b) are there any casing and cementing alternatives which can be employed to mitigate or eliminate the effect of longwall-induced stresses and deformations on the mechanical integrity of gas well casings? In this paper, the 3D ABAQUS models, which had been calibrated with the field instrumentation results, were employed to evaluate the effects of overburden depth and casing and cementing alternatives.

6.1. Effect of overburden depth

It is well known that overburden depth and its associated geology have significant influence on longwall-induced stresses and deformations. The calibrated ABAQUS 3D models were employed to evaluate the effect of deep overburden on the longwall-induced stresses and deformations and their effects on gas well casings. Fig. 9 shows that, under deep overburden, smaller strata deformation is present in the overburden above the mining horizon, while higher pressure and deformation are present at and below the coal seam, which results in a larger presence of plastic strain in the casings at the seam level (Fig. 10).

6.2. Effect of casing and cementing designs

To evaluate the effect of alternative casing and cementing designs on the coupling of longwall-induced stresses/deformations and casings, a number of 3D ABAQUS models were constructed and analyzed. Results from the analyses indicate that leaving the intermediate and production casings un-grouted from 15.3 m below the

Table 1
Comparisons of measured and ABAQUS-calculated surface subsidence and underground coal pillar pressure increase.

Center panel surface subsidence	Well site vertical subsidence	Well site horizontal movement	Coal pillar pressure
(a) Measured			
1.4 m after first panel	<6 cm	<6 cm	2.6 MPa after first panel
1.4 m after second panel			5.74 + MPa after second panel
(b) ABAQUS computed			
1.404 m after first panel	6.23 cm	4.0 cm	3.23 MPa after first panel
1.408 m after second panel			6.32 MPa after second panel

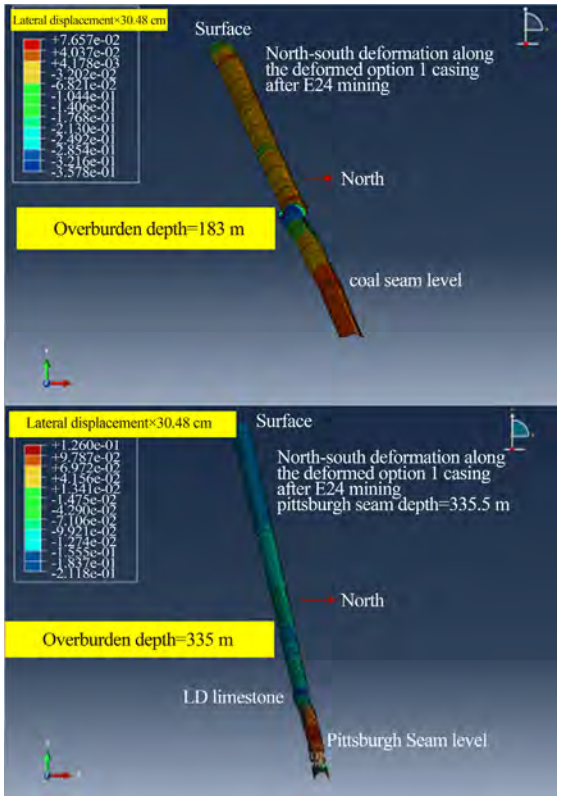

Fig. 9. Effect of overburden depth on casing deformation.

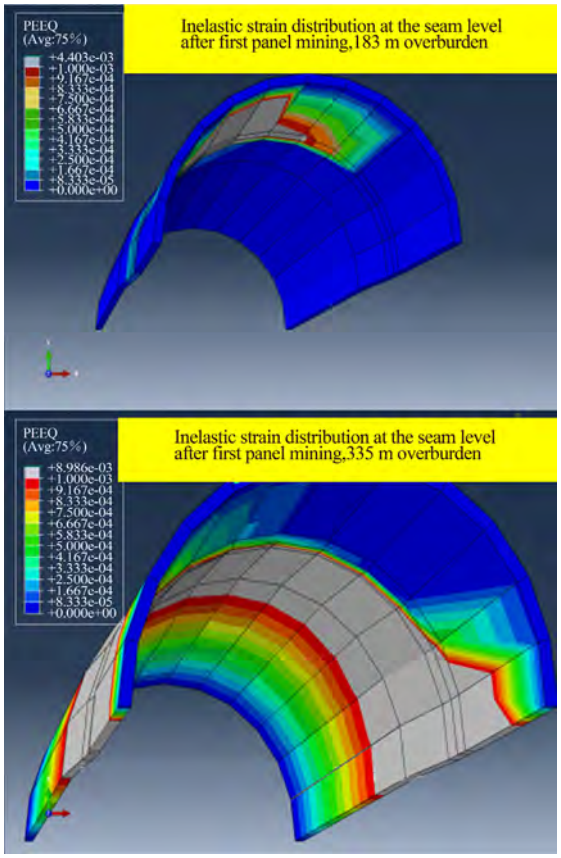

Fig. 10. Effect of overburden depth on casing strain at the seam level.

seam to the surface will effectively uncouple the ground stresses/deformations and the casings. In other words, little to no deformation and no induced strain is present in the intermediate and production casings when they are not cemented all the way to the surface.

7. Discussion

The field instrumentation as well as the numerical modeling results presented in this paper are consistent with a few previous attempts to characterize unconventional subsurface movements along the bedding planes [3–7]. Conventional subsidence engineering typically emphasizes the surface vertical displacement, surface horizontal displacement, surface horizontal strain, curvature and angle of draw induced by longwall or other high-extraction mining. Its primary objective is to assess the impact of high-extraction mining on surface structures such as buildings, water bodies, bridges, dams, streams and highways, although a few studies were designed to study the impact on shallow water wells. Vintage oil and gas wells, which are typically low pressure and which are near the end of their life cycles, are typically bought and plugged prior to longwall mining. However, due to the recent shale gas boom, many high-pressure gas well have been drilled over the past 10 years and these wells are at the beginning of their life cycles. In addition, these shale gas wells have different structures and possess much higher economic values compared to the vintage oil and gas wells. Therefore, it is imperative to understand the importance of unconventional subsurface stresses and deformations induced by longwall or other high extraction mining similar to those described in this paper.

Unfortunately, longwall-induced subsurface stresses and deformations are site-specific and more study is needed to completely characterize the induced stresses and deformations under different mining depths and geology. It is important to note that the 10.2 cm unconventional subsurface movement cited in this paper is not large enough to impact the mechanical integrity of the coal protection casing, as indicated by the consistent presence of water in the four test wells up to 122 m above the mining horizon.

Since about 800 shale gas wells have been drilled recently ahead of mining in the Pittsburgh coalfield, and since all casings of these wells are fully cemented to the surface, depending on the distance to the edge of future longwall extraction, potential casing deformation may be present. To avoid sterilizing either coal or gas reserve, these wells need to be temporarily plugged before mining. Upon completion of mining, temporary plugs can be removed and well integrity must be examined and confirmed before returning the well to production. On the other hand, for shale gas wells planned to be drilled in the future, as described in the previous section of this paper, alternative casing and cementing designs need to be considered to mitigate or eliminate potential casing deformations.

8. Conclusions

This paper demonstrates that the 3D ABAQUS finite element models, with accurate geologic information and gob behavior, can provide accurate prediction of surface subsidence and underground coal pillar pressure increases. The 3D ABAQUS models can also provide reasonable prediction of rather complex subsurface strata deformations. This is not to say that the 3D ABAQUS model is the only model capable of providing such accurate predictions; rather, results from this research suggest that numerical models can be used to predict longwall-induced stresses and deformations with reasonable accuracy, as long as they incorporate

detailed overburden geology and important strata interface and gob behaviors.

References

[1] Commonwealth of Pennsylvania, department of mines and mineral industries, oil and gas division. Joint coal and gas committee, gas well pillar study. Harrisburg, Pennsylvania; 1957.
[2] Scovazzo VA, Moran RP. Industry research into gas and oil well protective coal pillar design. In: Proceedings of the 32nd international conference on ground control in mining. Morgantown, West Virginia: West Virginia University; 2013. p. 164–8.
[3] Su WH, Hasenfus GJ. Field measurements of overburden and chain pillar response to longwall mining. In: Proceedings of the 6th international conference on ground control in mining. Morgantown, West Virginia: West Virginia University; 1987. p. 156–66.
[4] Coulthard MA, Dutton AJ. Numerical modeling of subsidence induced by underground coal mining. In: Proceedings of 29th U.S. symposium on rock mechanics. Tucson, Arizona; 1988. p. 529–36.
[5] Hasenfus GJ, Johnson KL, Su WH. A hydrogeomechanical study of overburden aquifer response to longwall mining. In: Proceedings of 7th international conference on ground control in mining. Morgantown, WV; 1988. p. 149–62.
[6] Su WH. Finite Element modeling of subsidence induced by underground coal mining: the influence of material nonlinearity and shearing along existing planes of weakness. In: Proceedings of 10th international conference on ground control in mining. Morgantown, West Virginia; 1991. p. 287–300.
[7] Hasenfus GJ, Su WH. A comprehensive integrated approach for longwall development design. In: Proceedings of first workshop on coal pillar mechanics and design. Santa Fe, New Mexico; 1992. p. 225–37.

International Journal of Mining Science and Technology 27 (2017) 121–129

Contents lists available at ScienceDirect

International Journal of Mining Science and Technology

journal homepage: www.elsevier.com/locate/ijmst

Effects of overburden characteristics on dynamic failure in underground coal mining

Lawson Heather E. *, Tesarik Douglas, Larson Mark K., Abraham Habte

NIOSH, Office of Mine Safety and Health Research, Ground Control Branch, Spokane, WA 99207, USA

ARTICLE INFO

Article history:
Received 9 May 2016
Received in revised form 10 October 2016
Accepted 29 October 2016
Available online 20 December 2016

Keywords:
Dynamic failure
Coal mining
Bumps
Bounces

ABSTRACT

Dynamic failures, or "bumps", remain an imperative safety concern in underground coal mining, despite significant advancements in engineering controls. The presence of spatially discrete, stiff roof units are one feature that has been linked to these events. However, an empirical stratigraphic review indicates that no significant difference exists in the relative commonality of discrete units between bumping and non-bumping deposits. Instead an apparent relationship exists between reportable bumping and the overall stiffness of the host rock. However, this initial study is too simplistic to be conclusive; to weight the relative impact of changes in a single variable, such as the thickness or location of sandstone members, it must be examined in isolation—i.e., in a setting where all other variables are held constant. Numerical modelling provides this setting, and the effects of variability in a stiff discrete member in a hypothetical longwall mining scenario are investigated within the context of three stratigraphic "types", Compliant, Intermediate and Stiff. A modelling experiment examines changes in rupture potential in stiff roof units for each stratigraphic type as discrete unit thickness and location are manipulated through a range of values. Results suggest that the stiff-to-compliant ratio of the host rock has an impact on the relative stress-inducing effects of discrete stiff members. In other words, it is necessary to consider both the thickness and the distance to the seam, within the context of the host rock, to accurately anticipate areas of elevated rupture-induced hazard; acknowledging the presence of a discrete unit within the overburden in general terms is an insufficient indicator of risk. This finding helps to refine our understanding of the role of individual stiff, strong roof members in bumping phenomena, and suggests that a holistic view of overburden lithology and site-specific numerical modelling may be necessary to improve miner safety.

1. Introduction

Dynamic failures, also termed "bumps", "bounces" and "bursts", may be defined as the violent ejection of coal or rock into a mine opening [1]. Despite evolving mining techniques and practices, these events continue to occur. Between 1983 and 2013, there were nearly 400 cases of reportable dynamic failure accidents in coal and nonmetal mines, resulting in 20 fatalities, 155 lost-time accidents, and an estimated 48,000 lost man hours. These events have been documented for well over 100 years within the American underground coal mining industry. Over this period of time, mining practices and support technologies have evolved considerably, resulting in an overall decrease in the rate of dynamic failure-related injuries and fatalities. However, despite this overall decrease in event rate, bump-related injuries and fatalities continue to occur. The events at Crandall Canyon, Utah, and the Brody No. 1 mine in West Virginia are two recent failure events that resulted in a total of eleven fatalities [2,3]. MSHA data further indicates that although reported incidents of these events are relatively rare, they result in worker injury up to and including death in more than 60% of cases. This is in contrast to injuries from the more common ground failure event of roof falls, which result in worker injury in less than 25% of cases (Fig. 1a and b). Clearly, dynamic failure events remain an imperative safety concern. Furthermore, their continued occurrence indicates that current engineering controls have proven inadequate at wholly mitigating the problem. The study described in this paper is part of a larger effort by NIOSH researchers that seeks to advance our current understanding of the causative factors behind dynamic failure phenomena, thereby allowing for more effective mitigation techniques.

* Corresponding author. Tel.: +1 509 3548061.
E-mail address: HELawson@cdc.gov (H.E. Lawson).

http://dx.doi.org/10.1016/j.ijmst.2016.10.001
2095-2686/

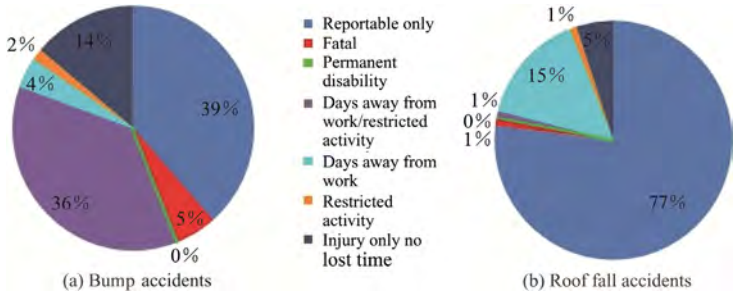

Fig. 1. Degree of injury as reported to MSHA between 1983 and 2014 by accident type.

2. Background

Many characteristics have been empirically linked to the occurrence of dynamic failure events, including design parameters, extraction techniques, and geologic factors. Identifying a set of conditions that will consistently produce bumping, however, has proven elusive; that is conditions generally associated with dynamic failure might produce an event at one site, but not another. Conversely and more troubling, dynamic failure could occur where relatively few of these factors exist.

The mechanical response of geologic structures plays a critical role in the development of dynamic failures. Regions that lack brittle strata are less prone to dynamic failure, although they may still experience roof falls, pillar failures, and other ground control difficulties. As a part of a larger effort to better define, the role of geologic risk factors in the occurrence of dynamic failure events, an empirical study was designed to examine the correlation of discrete stiff units to a reported history of bump phenomena. The role of discrete stiff units, such as massive sandstones and near-seam features, has been identified as a contributing factor to increased bump hazard.

Iannacchione and Tadolini define several fundamental factors contributing to dynamic failure occurrence [4]. Among these are strong strata surrounding the coal bed, which may "resist failure from elevated load conditions, and ... apply considerable stress and confinement to the pillars, increasing the potential for coal burst," and strata caving characteristics, in which "massive strata will often cantilever over areas...causing excessive levels of stress on coal pillars" [4]. Whyatt and Varley also describe failure of cantilevered, strong members as a significant mechanism of dynamic events [5].

Mark and Gauna provide a practical overview and generalized risk assessment matrix for bump events [6]. In their study, they describe several conditions of the overburden that have been associated with dynamic failure phenomenon, including thickness and location of near-seam strong or stiff units. They also note the lack of a quantitative, universal rating system for bump-risk identification, and identify as a qualitative intermediate risk factor, those roof conditions which are "typical Western US or Central Appalachian stratigraphy". While soft, compliant stratigraphic units are unambiguously not conducive to dynamic failure, and lithologies dominated by strong, stiff units are conducive to dynamic failure, the range of stratigraphic characteristics that pose an intermediate risk are less clearly defined.

The density of mining operations within the Western and Appalachian coalfields is illustrated in Figs. 2 and 3. Progress toward clarifying the degree of risk in these intermediate areas would benefit a significant number of active coal mines. The question, then, becomes: what are the critical thicknesses and locations of discrete stiff units, such as sandstones or competent limestones, at which they become truly hazardous to mining operations? This is by no means an easy question to answer, as influences on bump-proneness are multifaceted and identifying degrees of influence of these factors in a field setting remains elusive.

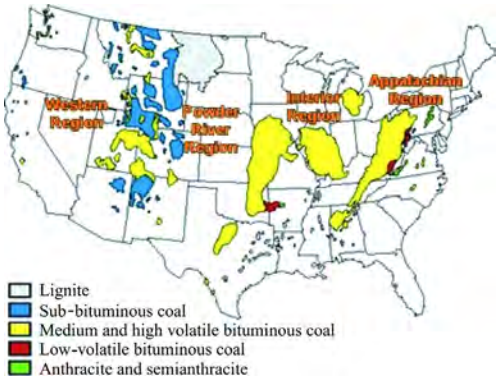

Fig. 2. Coal mining regions in the United States. (Minerals Education Coalition (MEC) of SME, 2016).

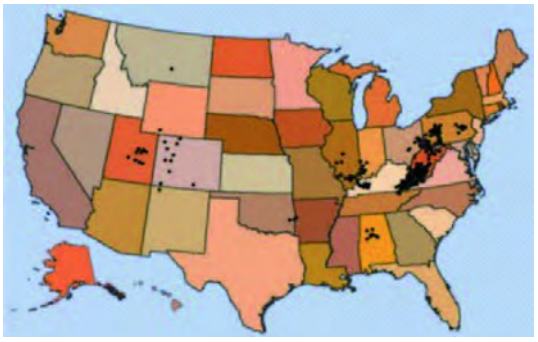

Fig. 3. Active underground coal mining operations within the United States, as of 2014.

Larson et al. demonstrate that load transfer distance correlates with different geology classifications (Fig. 4) [7]. These classifications fall into seven categories based on the proportion of sandstone (stiff) members to shale (compliant) members in the overburden, as well as the presence or absence of one or more massive or semi-massive stiff units. Strong, stiff strata may have the effect of increasing load transfer distances and resisting caving and loading of the gob, thereby increasing stresses in panel abutment.

The presence of stiff units in the overburden has the capacity to influence dynamic failure occurrence in two primary ways: First, failure of strong, brittle near-seam strata is likely to produce a seismic event. Second, bridging and cantilevering of strong strata shifts stress from gob to abutments. This paper seeks to identify the point at which these features transition from benign to hazardous. Toward this end, a review of reported failures was first compared

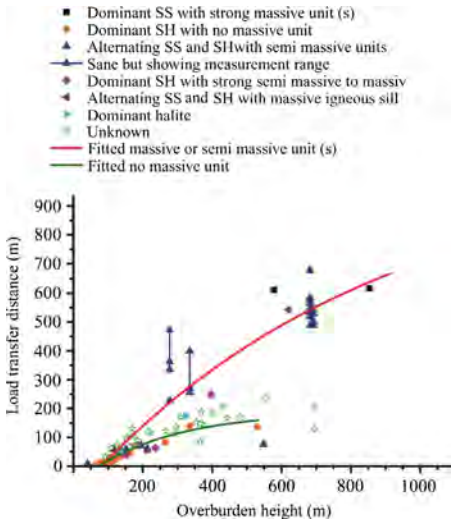

Fig. 4. Load transfer distance with respect to the geology of the overburden [7].

to typical stratigraphy for that county, and contrasted to stratigraphy in counties in which bumps have not been reported. However, this empirical portion of the study does not account for changes in mining practices, design parameters or other factors contributing to dynamic failure. Variations in any of these factors will also impact the capacity for bump occurrence. To weight the relative impact of changes in a single variable, such as the thickness or location of sandstone members, it must be examined in isolation—i.e., in a setting where all other variables are held constant. As nature defies the simplified and consistent conditions required to validate findings of the empirical study, parameter studies using numerical models of typical stratigraphic "types", as defined by the stratigraphic review, were constructed to explore how the location and thickness of strong strata influence loading.

3. Stratigraphy and dynamic failure

To begin to address this problem, core data was collected from the National Coal Resources Data System (NCRDS) [24]. The NCRDS is a compilation of core, chip, and drilling data that is made publicly available through the United States Geological Survey (USGS). Lithologic data was examined from 95 sets of log data, representing 22 different counties and 18 different coal seams or coal seam splits. These 95 core logs were then cross-referenced with a database of reported dynamic failure-related accidents and fatalities to determine the status of the seam and the county, individually, as either bump-positive or bump-negative.

The database used for identification of bump status includes 369 individual cases reported to the Mine Safety and Health Administration (MSHA) within the United States between 1983 and 2009. MSHA does not include information regarding the mined seam in these accident statistics. Consequently, an attempt was made to reconstruct this data for the 82 mines represented by the database, through publicly available lease information, MSHA Reports of Investigation, and state Coal Associations. These efforts were successful for 35 of these mines. The coal seams identified as having been excavated by mines with a history of dynamic failure phenomena were cross-referenced with the original 95 lithologic records collected through the NCRDS. Those records representing a seam correlating with a mine in which bump events had been reported were designated as "bumping." If no association existed between a given coal seam and one of these 35 mines, it was designated as "non-bumping."

There is some inherent error in identifying the bump status of records in this way, due to our inability to reconstruct seam information for each mine represented within the database of reported bump incidents. Some records identified as bump-negative, could, in fact, be bump-positive. Geographic data for both coal records and MSHA accident reports, however, is readily available. Given our ability to verify that bump-negative seams come from counties in which no bumps were reported ensures that the magnitude of this error for this study is relatively small. Likewise, identifying all seams within a county that have been associated with reported bumping allows us to exclude other seams present within the stratigraphy from "bumping" status. While error could exist in the identification of bump-negative seams, no such error exists in those that have been designated as bump-positive.

Counties were categorized independently as either "bumping," indicating a history of dynamic failure events reported to MSHA within that county, regardless of seam; or "non-bumping," that is, no reported history of dynamic failure events between 1983 and 2009 (The database of reported dynamic failure events contains event records from 1983 to 2009. If bumps have been reported in a seam before or after this range, they may be erroneously designated as non-bumping). This approach allows for isolating characteristics of the stratigraphy from those unique to the seam itself. This resulted in the following categories for the lithologic records, or cases: non-bumping seam/non-bumping county, bumping seam/non-bumping county, bumping seam/bumping county, and non-bumping seam/bumping county.

The empirical portion of this study examined log data for the presence of strong, stiff units within the overburden relative to a given seam position. Of particular interest were strong, massive units whose thicknesses exceeded 12 m, and were located at any point above the seam; and near-seam units whose thicknesses exceeded 1.2 m and whose presence was considered to be most significant within the first 8 m above the seam. Results indicated that the frequency of occurrence of these stiff members in the bumping and non-bumping sample sets was very similar. In other words, the presence of these units did not correlate with a history of dynamic failure (Figs. 5 and 6). It is important to note, however, that the log data used for this portion of the study may be widely spaced, and not directly proximal to mine workings (In several instances, logs did, in fact, indicate that the coal seam had been mined out. However, this was not a universal feature of log date). Furthermore, this portion of the study does not take into account any variables other than stratigraphy. Given the uncertainties inherent to this preliminary study, the findings are somewhat ambiguous, but provided guidance for designing more controlled studies.

Most of the factors that may influence dynamic failure occurrence could not be reconstructed using the available data. However, depth of cover was readily available with respect to seam depth. Although isolated instances of bumping behavior have been documented under relatively low cover, it is likely that exacerbat-

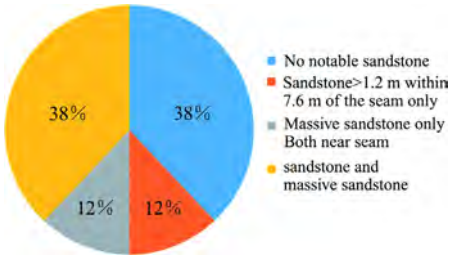

Fig. 5. Distribution of stiff unit data within the Non-Bumping Seam/Non-Bumping County data subset of the 95 USGS core logs examined during the empirical study.

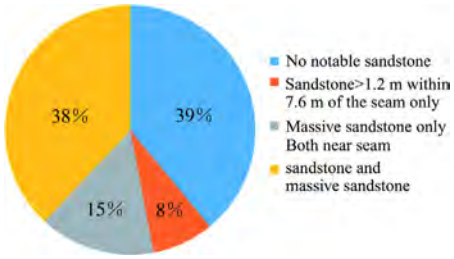

Fig. 6. Distribution of stiff unit data within the bumping seam/bumping county data subset of the 95 USGS core logs examined during the empirical study.

ing influences, such as unusual faulting conditions, existed at the event locations and that these do not represent typical dynamic failure scenarios [8]. Generally speaking, aside from these atypical cases, overburden depth may arguably be one of the most critical factors impacting the likelihood of the occurrence of dynamic failure phenomena [6]. Within the original sample set, it was found that an overlapping range of overburden depths between 244 and 423 m contained both bumping and non-bumping cases. All logs where coal seam depth fell outside of this range were eliminated from the study, leaving 21 remaining logs. Of these, three were designated as non-bumping seam/bumping county and came from very tightly spaced drill holes. These cases were eliminated from the study, as they would not have been representative of the category as a whole, but rather only the local geology at that location. Of the 18 logs remaining, there were 12 different seam-county combinations. The number of non-bumping seam/non-bumping county deposits was 11, the number of bumping seam/non-bumping county deposits was 4, and 3 were from bumping seam/bumping county deposits. While this dataset is too small to produce meaningful results using statistical methods, it does make more detailed investigation of the complete stratigraphic information for each log feasible. The log records were reconstructed in detail, and the pertinent geologic variables available through these records were examined for correlation with bump history.

In this more limited empirical study, some correlation does appear to exist between bump history and the overall ratio of stiff-to-compliant units in the overburden as a whole, and subsequently with the presence or absence of discrete stiff units (Fig. 7). However, this raises the question of whether or not the discrete units are significant in and of themselves, or rather symptomatic of the overall character of the host rock. Interestingly, a range of stiff-to-compliant values appears to exist for each sample subset; however, significant overlap exists between the non-bumping seam/non-bumping county and bumping seam/non-bumping county sample subsets. These ranges indicate that these groups represent general lithologic "types" that may be consistent across mining regions, and that it may in fact be these types that are most influential on dynamic failure phenomena, rather than the presence of discrete units alone.

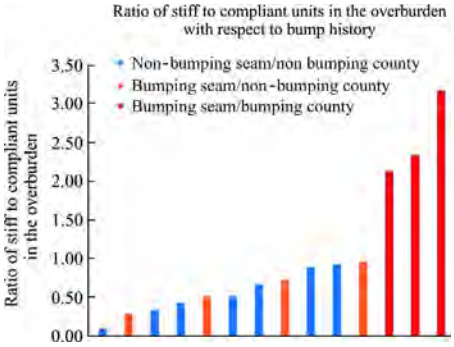

Fig. 7. Overall ratio of stiff-to-compliant stratigraphic members in the overburden as a whole for the non-bumping seam/non-bumping county dataset (blue), the bumping seam/ non-bumping county dataset (orange), and the bumping seam/ bumping county dataset (red).

From evaluation of typical stratigraphies in these core logs, three generalized stratigraphic columns were constructed: compliant-corresponding to the non-bumping seam/non-bumping county dataset; intermediate-corresponding to the non-bumping seam/bumping county dataset; and stiff-corresponding to the bumping seam/bumping county dataset. The average ratio of stiff-to-compliant members for each group was 0.06, 0.5, and 2.87, respectively. It is important to emphasize, however, the large degree of overlap in the stiff-to-compliant ratios of the non-bumping seam/bumping (intermediate) county and non-bumping seam/non-bumping (compliant) county categories. In fact, the intermediate category may only represent the upper range of the compliant stratigraphic "type." Regardless, the intermediate category provides a case study for a more transitional stratigraphy for use in numerical modelling studies. The generalized columns were modeled after the specific stratigraphies in the available USGS columns, to maintain as close a semblance to real-world conditions as possible.

To evaluate the relative influence of discrete stiff units versus lithologic stiff-to-compliant ratio, a series of numerical modelling parameter studies were designed using the generalized stratigraphic columns generated by the stratigraphic review. These examine the effects of modifying discrete member thickness and location relative to the seam within each of the aforementioned stratigraphic types, to determine how the character of the host rock will impact the capacity of discrete units to induce stress.

4. Overburden effects on stress

A parameter study using FLAC3D was conducted to determine the effect on the risk of coal bumps produced by the thickness and location of stiff members in three different coal mine roof "types": compliant, intermediate, and stiff [9]. A 0.3 m thick vertical cross section perpendicular to the gateroads of a longwall system with three 6 m wide entries, an 256 m wide longwall panel, and 43 m wide pillars was modeled. Depth of cover was set as 366 m. Vertical lines through mid-span of the longwall and middle gateroad served as symmetry lines. This configuration represents the state of stress at the completion of a developing panel, where redistributed stress from longwall extraction is directed primarily to the gateroad pillars.

Elastic and strength properties used in the numerical model were obtained from published values, and are listed in Table 1. The relationship between unconfined compressive strength and Young's Modulus is shown in Fig. 8. Poisson's ratio was 1.25 for all units. Specific density was 2403 kg/m^3 for all units, except for coal, which was 1282 kg/m^3. Reported strength values for siltstone were reduced because the siltstone was interbedded, with bed thicknesses on the scale of several meters, rather than massive, where unit thicknesses may be on the scale of tens of meters [10].

The stress-versus-strain relationship for the gob in the numerical model was calculated by using LamPre, the preprocessor of LaModel 3.0 as illustrated in Fig. 9. An 256 m wide gob was modeled at a depth of 366 m. Input parameters are listed in Table 2 [11]. LamPre default values were used for all other input parameters.

The double-yield model available in FLAC3D was then fit to the LamPre curve with the results shown in Fig. 9. All mined panel zones were assigned the double-yield material model. The gateroad adjacent to the panel was not assigned the double-yield

Table 1
Material properties for stratigraphic units used in the numerical model.

Lithology	Young's Modulus (GPa)	Unconfined compressive strength (MPa)	Friction angle (°)	Cohesion (MPa)
Strong sandstone	68.95[a]	105.41[a]	44.5[a]	22.1[a]
Limestone	54.47[b]	37.08[e]	35[e]	9.65[e]
Sandstone-dominant interbedded unit	34.47[b]	30.85[c]	34[c]	8.2[c]
Siltstone	26.27[a]	27.47[b]	30	7.93
Mudstone	20.68[c]	23.87[c]	25[c]	7.6[c]
Shale	8.34[b]	12.35[e]	12[e]	5[e]
Coal	1.64[d]	6.21[f]	30[g]	1.79[d]

Note: [a]means the conclusion got by Pariseau [23]; [b]means the conclusion got by Goodman [10]; [c]means the conclusion got by Lama and Vutukuri [21]; [d]means the conclusion got by Chi and Yuwei [20]; [e]means the conclusion got by Blyth and De Freitas [19]; [f]means the conclusion got by Mark [22]; [g]means the conclusion calculated from unconfined compressive strength and cohesion.

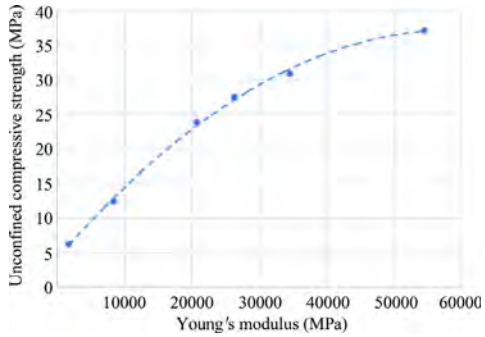

Fig. 8. Relationship between strength and stiffness for various rock types used in the numerical model.

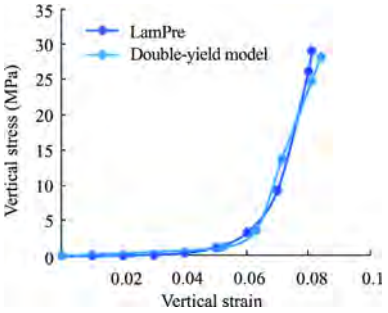

Fig. 9. FLAC3D double-yield model fit to gob stress-versus-strain curve developed by using LamPre.

Table 2
Material properties used in the numerical model.

Young's Modulus of coal seam (MPa)	1641
Unconfined compressive strength of coal seam (MPa)	6.2
Poisson's ratio of rock mass	0.25
Vertical stress gradient (MPa/m)	2.4×10^2
Element width (m)	3

model, because of lack of caving that is generally observed in this area. This observation was confirmed by many results of a caving model (FLAC3D) using a wide range of input parameters.

(1) Various thicknesses of the "strong sandstone," which is used as the stiff member variable in the different host rock settings, and whose properties are listed in Table 1, were inserted into each stratigraphic type in the numerical model at varying locations above the mine roof to determine the effect of this stiff unit on creating a bump risk factor. Placement and thickness of the stiff sandstone unit in each stratigraphic type was varied, as follows: the location relative to the coal seam of a 5 m thick stiff sandstone. The stiff beam member was moved up through the mine roof in 1.8 m increments, beginning directly overlying the seam to a maximum distance of 20 m above the coal seam.
(2) The thickness of a stiff sandstone unit located directly above, and adjacent to, the coal seam. This stiff beam member's thickness was incremented in 1.8 m increments, from 1.8 m to a maximum thickness of 29 m.

The choice to use these particular thicknesses was guided by the work of Mark and Gauna and others who cite stiff units with similar thicknesses as increasing bump risk when proximal to the mine roof [6,9,12–16].

Failure of strong strata is likely to occur suddenly and induce a seismic event. Additionally, changes in abutment and pillar loading may increase the potential for bursting in the coal seam, whether sudden or as a result of stress distribution when strong strata is intact. Failure may also induce a "shock" bump, which occurs "where a strong massive stratum, either immediately over the coal or higher up if not too far above, ruptures as a beam of flat arch and a ground wave is imparted to an already highly loaded pillar support" [17]. Rice stated that this is the principal type of bump observed in coal mines and postulated that when "the immediate roof is strong and elastic like a dense sandstone, it not only springs down and back to its former position but may also be set in vibration under certain conditions of an elastic roof layer and crushed pillars." For most of these cases, rupture of the strong member is an important factor.

The following conditions in the numerical model were used as criteria to identify the potential rupture of a strong massive stratum:

(1) Reduced thickness of a stiff member caused by partial failure, resulting in an "effective" thickness. It was assumed that risk of rupture was proportional to effective thickness.
(2) Zones of low factors of safety in stiff units.

These criteria were applied only for the case when the entries and longwall were excavated. Prior failures of stiff units were not evaluated.

5. Compliant stratigraphy

Mining of the entries and longwall without the addition of the stiff member inserted in the compliant host rock type resulted in a failure zone extending 122 m into the roof, to include the 6 m thick interbedded sandstone unit and the 3 m thick limestone unit. That is to say, this failure zone represents the failure condition of

the host rock alone, prior to the inclusion of the experimental variable.

The effect of altering the thickness and proximity to the coal seam of the stiff beam member on the potential for rupture in the compliant lithology was similar to that found for the intermediate lithology type, as discussed in greater detail in the next section. The driving factor behind this similarity is the composition of the immediate mine roof, which is shale in both cases.

When the location of the 4.8 m thick stiff member was incremented up through the stratigraphic column, it became apparent that a risk of rupture existed for a 4.8 m sandstone unit of any height above the coal seam. This is due to the partial failure of the member and reduction of beam thickness to about 1.2 m. The energy released by the rupture would decrease relative to the unit's height above the seam based on the maximum compressive stress in the unit. Put more simply, the energy decreases because of less stress on the beam.

When the thickness of the stiff member directly overlying the coal seam was incremented from 1.8 to 29 m, it was discovered that for the compliant case study, the highest risk of rupture was at a thickness of 3.7 m. This may indicate a critical thickness for this unit when it is directly on top on the seam. Intuitively, rupture risk decreased with increasing thickness beyond this point.

Several caveats are noted with regard to conducting these modelling studies within the compliant and intermediate host rock types. The introduction of a stiff member will alter the stiff-to-compliant ratio of the overburden, and this ratio will naturally increase as the thickness of this unit increases. These studies are designed to evaluate the effects of discrete, or—in other words—spatially discontinuous units in lithology that may otherwise be identified as compliant or intermediate in nature. These are intended to simulate paleochannels or other unanticipated shifts in stratigraphy, which may not become apparent during mining until they have become problematic. Furthermore, due to the experimental nature of these studies, the boundaries of these features have been pushed far beyond what would reasonably be expected in a natural setting; it is unlikely, for instance, that a unit 29 m thick would be unexpected or spatially discrete. These extremes have been included in the experimental studies in the interests of diligence and conservatism.

6. Intermediate stratigraphy

In the Intermediate host rock type, a 12 m thick limestone unit was located above the massive shale roof, and positioned between shale units with lower elastic moduli. This hypothetical stratigraphic case study was influenced by core log data examined during the stratigraphic review in which a massive or semi-massive limestone unit was found in the overburden above the seams of interest. This condition was unique to Eastern deposits, or those within the Appalachian coalfields. However, strong sandstone units commonly associated with Western coalfields would, in theory, produce similar outcomes. It was determined that for the intermediate host rock type that this geological configuration may contribute to a bump, independent of the introduction of a variable stiff member and based on the assumed criteria that rupture of overlying strata facilitates bumping behavior in coal mines. This limestone feature was fairly common in the available core log data, and is representative of an authentic stratigraphic condition. Failures induced during modelling experiments in the limestone unit reduced its effective intact thickness to 3.4 m as shown in Fig. 10, which then subsequently increased the potential of the remaining intact portion to rupture. The horizontal extent of the failed zones plot in Fig. 10 is limited to two gate roads, one pillar, and part of the gob section of the mined panel.

As shown in Fig. 10, colors other than blue background or white gateroads denote a failure zone.

6.1. Effect of a 4.8 m thick, stiff sandstone unit in intermediate stratigraphy

A 4.8 m thick, stiff sandstone unit was inserted into the intermediate stratigraphy above, and adjacent to the coal seam, and then moved up through the mine roof in 1.8 m intervals. The effect of this unit on bump potential was highest when it was located directly above the coal seam and in the path of redistributed stress from the mined longwall. This location resulted in two failed zones, which reduced the effective thickness of the stiff sandstone unit to 1.8 m, as shown in Fig. 11. The presence of the stiff sandstone unit adds to the bump potential that is already posed by the limestone unit. Instantaneous failure in the stiff sandstone unit remains feasible as the distance between the stiff unit and the coal seam increases, but less energy would be released as indicated by the decrease in maximum compressive stress in this unit as shown in Fig. 12.

6.2. Effect of a stiff unit with increasing thickness in intermediate stratigraphy

Two geological configurations were critical in producing possible ruptures when a stiff sandstone unit of increasing thickness was placed on the coal seam. The first case was for a 3.7 m thick unit placed directly above the coal seam. The risk of rupture in the stiff unit decreased as the unit became thicker, as illustrated by the increase in effective thickness as shown in Fig. 13. However, the risk of rupture in the limestone unit increases as the thickness of the stiff unit increases—even though the rupture potential of the stiff member itself decreases. Location of imminent failure based on effective thickness changes from the stiff unit to the limestone unit when the initial thickness of the stiff unit is 5.5 m, as shown in Fig. 13.

6.3. Stiff stratigraphy

A stiff lithology is less inherently likely to contribute to a potential rupture, based on the established rupture criteria compared to an intermediate stratigraphy, because the effective thickness of the siltstone is 27 m, as shown in Fig. 14, compared to 3.4 m for the limestone in the intermediate lithology, as shown in Fig. 10. Development of this stratigraphic column was influenced by two Western deposits and one Eastern deposit, all of which have experienced bumps. It seems likely that real-world bumps in these settings may be the result of pressure, as well as other dynamic failure-inducing mechanisms. As this study examines the potential

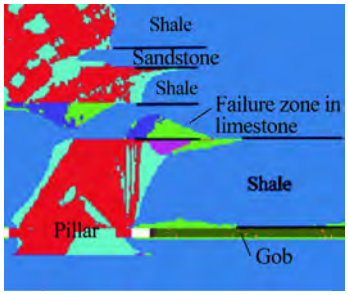

Fig. 10. Produced by the model for intermediate stratigraphy.

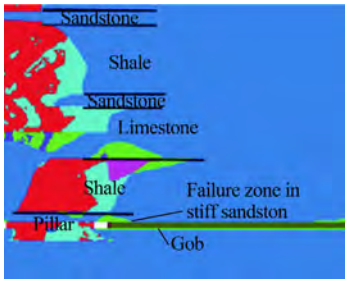

Fig. 11. Failed zones (any color differing from background blue) produced for Intermediate stratigraphy with a 4.8 m thick sandstone unit inserted directly above the coal seam.

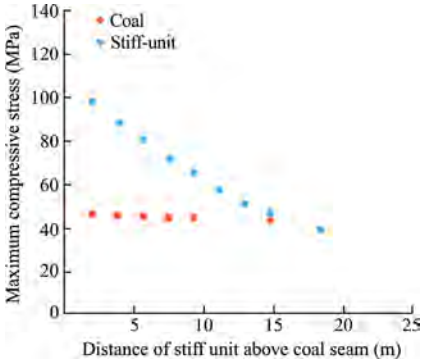

Fig. 12. Maximum compressive stress in a 4.8 m thick, stiff sandstone unit and coal seam for intermediate stratigraphy.

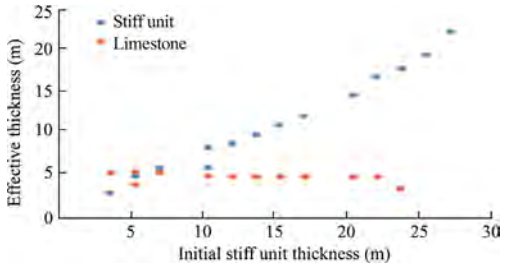

Fig. 13. Reduction in thickness of stiff unit caused by partial failure of the unit in intermediate stratigraphy.

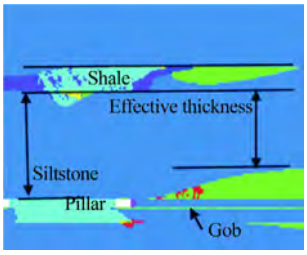

Fig. 14. Failed zones produced by the numerical model for stiff stratigraphy.

for the rupture mechanism only, pressure-induced bumps may not be represented in the numerical models. As such, it can be stated that this particular case study may be at low risk for rupture of roof units prior to introduction of the stiff member variable, but this does not discount the potential for other types of dynamic failure events.

As noted in Fig. 14, colors other than dark blue or white gateroads denote a failure zone.

6.4. Effect of a 4.8 m thick, stiff unit in stiff stratigraphy

The effect of inserting a 4.8 m thick stiff sandstone unit into stiff stratigraphy was assessed by using factors of safety zones less than 1.1, because failure did not occur in the 4.8 m units and there was little failure in the massive siltstone roof. Absence of failure in the 4.8 m thick, stiff unit can be attributed to the relatively high stiffness of the immediate mine roof carrying some of the redistributed stress from longwall excavation. In Figs. 15–21, factors of safety from 1.0, up to but not including 1.1, are denoted by color gradation from orange to background blue. Background blue denotes factors of safety greater than or equal to 1.1.

The most significant effect of the stiff sandstone unit on the factor of safety occurred when the stiff unit was directly on the coal seam as shown in Figs. 15–18. The low factor-of-safety zone that was introduced into the siltstone by the stiff unit was caused by the limitation of vertical displacement, resulting in a shift of horizontal stress from compression to tensile. The effect of the stiff sandstone unit on factors of safety less than 1.1 decreased as the 4.8 m-thick unit was moved up through the stratigraphy and above the redistributed stresses from longwall excavation.

The area of factor of safety less than 1.1 in the massive siltstone roof increases with increasing thickness of a stiff sandstone unit placed directly above the coal seam, as shown in Figs. 19–21. Areas of low safety factor adjacent to failed zones are susceptible to microseismic activity, which could trigger complete failure of the siltstone roof [18]. The upper and lower factor of safety zones in the siltstone became contiguous when the thickness of the stiff unit was 7.3 m. The height of the contiguous zone was 35 m. This scenario, illustrated in Fig. 21, shows a zone of failure spanning up through the overburden from the stiff member to the shale unit. This zone grows progressively larger as the thickness of the stiff member variable increases in thickness up to 7.3 m. At this point, failure becomes nearly continuous with the zone of failure in the overlying shale unit, effectively severing the massive siltstone roof from the overburden. This would have the potential to cause a large shock bump, were this siltstone to fall, and would stress the pillars as the weight previously supported by this stratum is

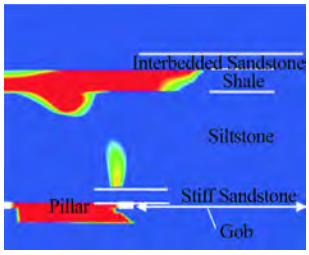

Fig. 15. Factors of safety for stiff stratigraphy with a 4.8 m stiff sandstone unit inserted on the coal seam.

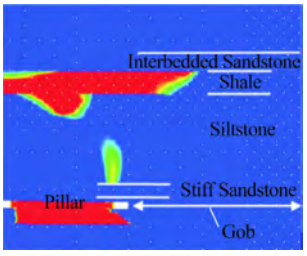

Fig. 16. Factors of safety for stiff stratigraphy with a 4.8 m stiff sandstone unit inserted 1.8 m above the coal seam.

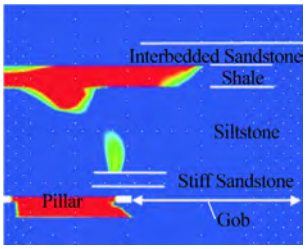

Fig. 17. Factors of safety for stiff stratigraphy with a 4.8 m stiff sandstone unit inserted 3.7 m above the coal seam.

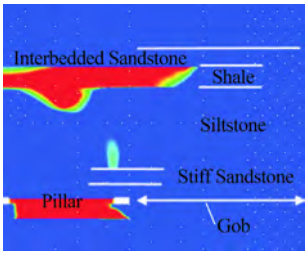

Fig. 18. Factors of safety for stiff stratigraphy with a 4.8 m stiff sandstone inserted 5.5 m above the coal seam.

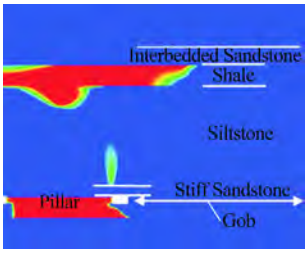

Fig. 19. Factors of safety for stiff stratigraphy with a 3.7 stiff sandstone unit inserted on top of the coal seam.

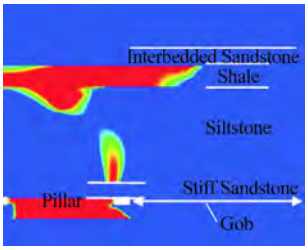

Fig. 20. Factors of safety for stiff stratigraphy with a 5.5 m stiff sandstone unit inserted on top of the coal seam.

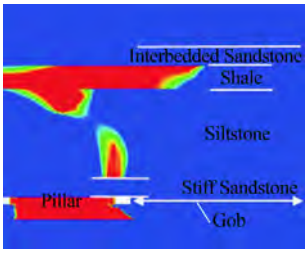

Fig. 21. Factors of safety less than or equal to 1.1 for stiff stratigraphy with a 7.3 m thick stiff sandstone unit inserted on top of the coal seam.

redistributed. This example illustrates one potential mechanism for bump development in stiff host rock settings where a weaker more compliant bed may also be present.

7. Conclusions

The relationship of coal bump potential to the ratio of the overall stiff-to-compliant strata thickness could not be explained solely by the stress state produced by a two-dimensional numerical model of a longwall system. However, when a stiff sandstone unit of various thicknesses and locations was inserted into three different lithologies, the numerical model was useful in identifying areas that were near failure, which, if ruptured, could possibly produce a coal bump. The effect of the stiff sandstone unit on large-scale roof failure and potential coal bumps associated with this failure depended on the location of the unit in the stratigraphic column, the relative stiffness and strength of other structural members, and stress concentrations caused by mining.

Failure zones developed in a 4.8 m stiff sandstone unit inserted into a relatively compliant shale roof, producing a risk of rupture in the sandstone. This risk existed for all heights of the sandstone above the coal seam, but maximum compressive stress in the sandstone, and probable energy released by its rupture, decreased with its height above the coal seam. The risk of rupture of the sandstone was coupled with the risk of rupture of a stiff limestone above the massive shale. On the other hand, failure zones developed above a 4.8 m stiff sandstone beam inserted into a relatively stiff siltstone roof. The risk of rupture of the siltstone deceased as the sandstone unit moved up and away from the coal seam, and the stress concentration caused by longwall panel extraction.

The risk of a rupture of a stiff sandstone unit inserted on top of a coal seam in massive shale mine roof decreased as the unit became thicker. Failures occurred in units of all thicknesses but the effective thickness of these units also increased, which reduced rupture potential. The critical thickness of a stiff sandstone unit inserted on top of a coal seam in a massive siltstone roof was 7.3 m. The presence of the sandstone created a 35 m thick zone of low safety factors in the siltstone.

Parameter study findings suggest that, for the experimental scenario, bump risk factor generally correlates with stiff-to-compliant ratio. The introduction of a very stiff member into the geological setting causes a concentration of stresses in stiffer strata, frequently resulting in a band of low factors of safety through the entire thickness of these members. This effect depends on the thickness of the introduced beam, the location of this beam in the geological setting, and the stiffness of the surrounding strata. When a stiff member delays caving, the risk of a dynamic event increases, either through eventual failure of the stiff member so that coal away from the fulcrum of the cantilever is dynamically impacted, or coal near the fulcrum is loaded to the point that strain bumping occurs. The ability to store potential energy increases the risk of a dynamic event. In this parameter study, a large stiff-to-compliant thickness ratio generally has a higher risk of bumps than a small stiff-to-compliant thickness ratio, but individual cases of stratigraphy need to be considered for bump risk factor. Results suggest that the stiff-to-compliant ratio of the host rock has an impact on the relative stress-inducing effects of discrete stiff members. In other words, it is necessary to consider both the thickness and the distance to the seam, within the context of the host rock, to accurately anticipate areas of elevated rupture-induced hazard; acknowledging the presence of a discrete unit within the overburden in general terms is an insufficient indicator of risk. The case studies used in this experiment are modelled after common stratigraphies associated with non-bumping or bumping scenarios and can be expected to be realistic. Failure of stiff beam members

may trigger strain-or strata-failure-driven bumps in stiff host rock [6]. Results shed light on the relative stress-inducing effects of individual stiff beam members relative to the nature of the host rock. However, the significance in these results is not that these critical thicknesses and distances should be applied outside of the case studies used here; rather, through modelling of anticipated changes in the placement and dimensions of discrete units within their stratigraphic setting, elevated bump hazard can be anticipated on a case by case basis. Were similar modelling studies conducted in tandem with tracking of problematic discrete stiff units, it may be possible to anticipate areas of elevated risk in advance of mining.

This study represents a beginning stage for the accurate weighting of dynamic failure risk factors, and with further research, ultimately predictive capability. Developing this predictive capability beyond identifying rupture potential in discrete roof members is essential to the eventual elimination of dynamic failure related worker injuries and fatalities. As stress is a necessary component in the occurrence of dynamic failure events, this finding helps to refine our understanding of the role of individual stiff, strong roof members in bumping phenomena, and suggests that a more holistic view of overburden lithology, combined with site-specific numerical modelling, may be necessary to achieve greater miner safety. Stress analysis conducted with detailed geology and combined with the monitoring of bumps offers a possible tool for more accurate risk assessment of bump potential in underground coal mining.

References

[1] Peng SS. Coal mine ground control. 3rd ed. West Virginia: Department of Mining Engineering, West Virginia University; 2008.
[2] MSHA. Report of investigation-fatal underground coal burst accidents, August 6 and 16, 2007, Crandall Canyon mine, Genwal Resources Inc, Huntington, Emery County, Utah. CAI-2007-15-17, 19–24. U.S. Department of Labor, MSHA; 2008.
[3] MSHA. Report of investigation-underground coal mine, fatal rib burst accident, May 12, 2014, brody mining, LLC, brody mine no. 1, Wharton, Boone County, WV. CAI-2014–05. U.S. Department of Labor, MSHA; 2014.
[4] Iannacchione AT, Tadolini SC. Occurrence, predication, and control of coal burst events in the US. Int J Min Sci Technol 2016;26(1):39–46.
[5] Whyatt J, Varley F. Regional bumps: case studies from the 1958 bump symposium. In: Proceedings of SME 2009 annual meeting and exhibit. Denver, CO. p. 7.
[6] Mark C, Gauna M. Evaluating the risk of coal bursts in underground coal mines. Int J Min Sci Technol 2016;26(1):47–52.
[7] Larson MK, Lawson HE, Tesarik DR. Load transfer distance measurements at two mines in the Western U.S. In: Proceedings of 34th international conference on ground control in mining. West Virginia University, Morgantown, WV. p. 54–64.
[8] Peperakis J. Mountain bumps at the sunnyside mines. Min Eng 1958;10(9):982–6.
[9] Itasca Consulting Group. FLAC3D—fast lagrangian analysis of continua in 3 dimensions, ver. 5.0. Minneapolis: Itasca Consulting Group, Inc.; 2013.
[10] Goodman RE. Introduction to rock mechanics. 2nd ed. New York: John Wiley & Sons; 1989.
[11] Heasley KA. LaModel, ver. 3.0. Morgantown, WV: West Virginia University; 2010.
[12] Maleki H. Caving, load transfer, and mine design in western U.S. mines. In: Proceedings of golden rocks 2006, The 41st U.S. symposium on rock mechanics (USRMS): 50 years of rock mechanics — landmarks and future challenges. Golden, Colorado. Paper No. 06-931; 2006. P. 10.
[13] Maleki H, White B. Geotechnical factors influencing violent failure in U.S. mines. In: Proceedings of international symposium on rock support—applied solutions for underground structures. Lillehammer, Norway. p. 208–21.
[14] Iannacchione A. Behavior of a coal pillar prone to burst in the southern appalachian basin of the United States. In: Proceedings of rockbursts and seismicity in mines. Minneapolis, Minnesota. p. 295–300.
[15] Maleki H. An analysis of violent failure in U.S. coal mines—case studies. In: Proceedings of mechanics and mitigation of violent failure in coal and hard-rock mines. U.S. Department of the Interior, Bureau of Mines (USBM); 1995. p. 5–25. Special publication.
[16] Agapito JFT, Goodrich RR. Five stress factors conducive to bumps in Utah, USA, coal mines. In: Proceedings of 19th international conference on ground control in mining. West Virginia University, Morgantown, WV. p. 93–100.
[17] Rice GS. Bumps in coal mines—theories of causes and suggested means of prevention or of minimizing effects. Trans Am Inst Min Metall Eng 1936;119:11–39.
[18] Andrieux PP, Hudyma MR, O'Connor CP, Li H, Cotesta L, Brummer RK. Calibration of large-scale. In: Proceedings of ree-dimensional non-linear numerical models of underground mines using microseismic data. Proceedings of continuum and distinct element numerical modeling in geo-engineering – 2008. Proceedings of the 1st international FLAC/DEM symposium. Itasca Consulting Group, Inc., Minneapolis, MN. p. 343–50.
[19] Blyth FGH, de Freitas MH. A geology for engineers. 7th ed. New York: Elsevier; 1984.
[20] Ai C, Li YW. The model for calculating elastic modulus and poisson's ratio of coal body. Open Fuels Energy Sci J 2013;6:36–43.
[21] Lama RD, Vutukuri VS. Handbook on mechanical properties of rocks—testing techniques and results, vol. 4. Clausthal, Germany: Trans Tech Publications; 1978. p. 534.
[22] Mark C. The evolution of intelligent coal pillar design: 1981-2006. In: Proceedings of 25th international conference on ground control in mining. Morgantown, WV. p. 325–34.
[23] Pariseau WG. Design analysis in rock mechanics. 2nd ed. London: Taylor and Francis; 2012.
[24] USGS. National coal resources data system (NCRDS). Department of the Interior, U.S. Geological Survey (USGS); 2015.

International Journal of Mining Science and Technology 27 (2017) 131–137

Contents lists available at ScienceDirect

International Journal of Mining Science and Technology

journal homepage: www.elsevier.com/locate/ijmst

Unanticipated multiple seam stresses from pillar systems behaving as pseudo gob–case histories

Gauna Michael *, Mark Christopher

Pittsburgh Safety and Health Technology Center, Mine Safety and Health Administration (MSHA), Pittsburgh, PA 15236, USA

ARTICLE INFO

Article history:
Received 9 June 2016
Received in revised form 18 August 2016
Accepted 28 September 2016
Available online 8 December 2016

Keywords:
Underground mining
Coal
Multiple seam
Gob
Ground control

ABSTRACT

Underground coal mining in the U.S. is conducted in numerous regions where previous workings exist above and/or below an actively mined seam. Miners know that overlying or underlying fully extracted coal areas, also known as gob regions, can result in abutment stresses that affect the active mining. If there was no full extraction, and the past mining consists entirely of intact pillars, the stresses on the active seam are usually minimal. However, experience has shown that in some situations there has been sufficient yielding in overlying or underlying pillar systems to cause stress transfer to the adjoining larger pillars or barriers, which in turn, transfer significant stresses onto the workings of the active seam. In other words, the overlying or underlying pillar system behaves as a "pseudo gob." The presence of a pseudo gob is often unexpected, and the consequences can be severe. This paper presents several case histories, summarized briefly below, that illustrate pseudo gob phenomenon: (1) pillar rib degradation at a West Virginia mine at 335 m depth that contributed to a rib roll fatality, (2) pillar rib deterioration at a Western Kentucky mine at 175 m depth that required pillar size adjustment and installation of supplemental bolting, (3) roof deterioration at an eastern Kentucky mine at 400 m depth that stopped mine advance and required redirecting the section development, (4) coal burst on development at an eastern Kentucky mine at 520 m depth that had no nearby pillar recovery, and (5) coal burst on development at a West Virginia mine at the relatively shallow depth of 335 m that also had no nearby pillar recovery. The paper provides guidance so that when an operation encounters a potential pseudo gob stress interaction the hazard can be mitigated based on an understanding of the mechanism encountered.

1. Introduction

The U.S. underground coal mining industry has conducted mining in multiple seam environments, where the active mining has underlying or overlying old workings at varying interburden distances, throughout its history. Often no serious consequences arise from the multiple seam mining. However, sometime mines have been confronted with hazards from underlying or overlying workings that include localized roof and rib failure, pillar system failures through propagating roof falls and floor heave, and also pillar bursts.

The major underground coal mining basins in the U.S. are shown in Fig. 1. Historically, the Central Appalachian region, consisting of southern West Virginia, eastern Kentucky, and southwestern Virginia has encountered the most significant multiple seam mining issues. This is attributable to the more than 100 years of underground mining, existence of numerous mineable seams in the respective stratigraphic sequences, and the predominant use of pillar recovery that concentrates mining stresses. While less frequent, multiple seam interactions occur in all the other coal mining regions as well [1].

2. Evaluation of multiple seam interaction

For decades the stresses that arise from multiple seam mining scenarios and the impact on the seam being mined has been the subject of much research. In 2007 the National Institute for Occupational Safety and Health (NIOSH) developed the analysis of multiple seam stability (AMSS) program to help reduce the risk of ground failures from potential interactions. The NIOSH study reviewed previous multiple seam mining research, established an extensive database of multiple seam mining case histories, applied LaModel 2D to establish multiple seam stress levels, and incorporated these stress levels to analysis of retreat mining pillar stability (ARMPS) and analysis of longwall pillar stability (ALPS) computations. The computations and statistical analyses of the database

* Corresponding author. Tel.: +1 304 547 2311.
E-mail address: gauna.michael@dol.gov (M. Gauna).

http://dx.doi.org/10.1016/j.ijmst.2016.11.015
2095-2686/

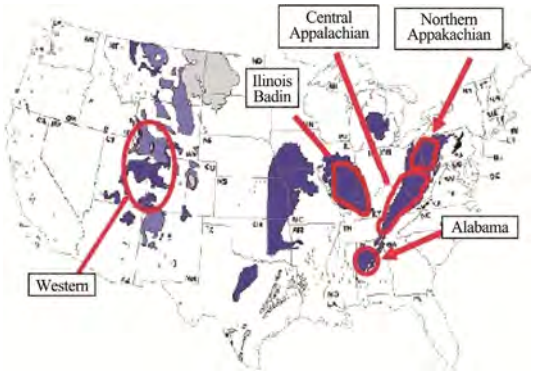

Fig. 1. The U.S. major underground coal mining regions [1].

helped determine the significant parameters that need to be accounted for in a multiple seam mining environment. The AMSS program offers criteria for an appropriate pillar design and guidance for the installation of supplemental roof and rib support [1]. A significant finding from the AMSS research is that when there is no full extraction, and the past mining in an overlying or underlying seam consists entirely of intact pillars, interactions with the active seam are usually minimal unless the interburden is less than 10–15 m.

AMSS has been used extensively in the U.S., underground coal mining industry. After the Crandall Canyon Mine disaster in 2007, the Mine Safety and Health Administration (MSHA) has instituted technical review procedures to ensure that appropriate pillar designs are used in underground coal mines [2]. The most numerous category of MSHA technical review are multiple seam mining scenarios evaluated with AMSS by the operator and/or MSHA [3].

2.1. Multiple seam interaction factors

The NIOSH study found that the most important factors affecting the intensity of a multiple seam interaction were the depth of cover, whether the past mining was conducted above or below the active seam, the immediate roof geology of the active seam, the interburden thickness between the active seam and the previously mined seam (or seams), and type of remnant structure in the overlying and/or underlying seam. Remnant structures in the previously mined seam(s) are typically created when coal is left in place adjacent to areas of full extraction, also known as gob areas. Isolated remnants, with worked out areas on two or more sides, have the most hazardous stress concentration, while less severe stress concentrations occur along gob-solid boundaries [1,4].

By definition, remnant structures exist in conjunction with gob areas which are de-stressed and have transferred load to the remnants. Regions in which all the pillars are intact are usually presumed to have minimal stress concentrations. However, a number of situations have been encountered where severe stress concentrations have occurred without the presence of full extraction mining in the overlying and/or overlying seam. In these cases, smaller developed pillars in old works have apparently yielded and transferred much of their load onto larger nearby pillars or barriers. In other words, the documented pattern of roof, rib, and floor degradation observed in these situations suggests that the small pillars are behaving as a "pseudo gob."

3. Multiple seam pseudo gob case studies

The case studies presented below all involve pseudo gob situations. They illustrate the range of unanticipated multiple seam mining hazards that can be encountered.

3.1. Pillar rib deterioration-West Virginia

The mining operation is located in Boone County, West Virginia in the Central Appalachian coal mining region. In 2006, a 46-year old roof bolting machine operator was fatally injured when a large portion of the rib fell [5]. The accident was investigated by the Mine Safety and Health Administration, Technical Support (MSHA-TS).

The mining unit investigated consisted of a five entry configuration being developed to establish a pillar recovery panel. The mine portals were in the No. 2 gas seam with the mining area accessed via an in-mine slope from the No. 2 gas seam down to the Powellton Seam. The pillars on the mining unit were established on 24 m × 34 m to 46 m centers with approximately 3 m × 5.5 m mining dimensions. Depth of cover was approximately 335 m.

The section was overlain by development mining in the No. 2 gas seam with 20 m of interburden (Fig. 2). U.S. multiple seam mining research has shown that when overlying seams have no pillar recovery and consist of development mining, this interburden distance normally will have minimal stress interaction. The investigation revealed that pillars located under the No. 2 gas seam chain pillars showed no or minimal evidence of rib spall (Fig. 3). In contrast, ribs located beneath the edge of the overlying barrier pillar exhibited intense rib sloughing (Fig. 4). The accident occurred in the Powellton Seam #5 entry face area after it had advanced beneath the overlying barrier. The accident site was subjected to an elevated intensity of rib sloughing and the rib side had a thick shale parting that had a tendency to roll out as large blocks.

As shown in Fig. 4, this photo illustrates thick shale parting that tends to roll out as large blocks.

The ARMPS SF calculated for the chain pillars in the overlying No. 2 gas seam was 2.3, a value that would normally indicate a stable pillar configuration [6]. Nonetheless, it is apparent that some factor allowed the No. 2 gas seam pillar system to yield and transfer loads onto the surrounding barrier. An AMSS evaluation, not yet developed at the time of the investigation, of the Powellton Seam mining shows that if the No. 2 gas seam chain pillars are treated as gob, pillar SF = 2; however, a "condition yellow" cautionary warning is generated indicating the likelihood of rib instability.

Rib control measures were subsequently instituted in the high stress region. In-cycle rib bolting was instituted to protect the personnel. Also, the mine operator purchased "inside control" dual boom bolting machines, with drill station controls located between

Fig. 2. Powellton Seam mining completed (black) with overlying development mining in the No. 2 gas seam (red).

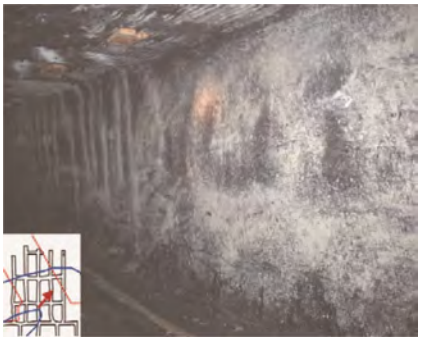

Fig. 3. Powellton Seam mining under the No. 2 gas seam chain pillars showing no evidence of rib spall; photo view shown by arrow on embedded map.

Fig. 4. Powellton Seam mining within the overlying barrier pillar exhibiting intense rib sloughing; photo view shown by arrow on embedded map.

the drill booms, so that roof bolt machine operators could work in a zone where they were protected from the rib hazard.

3.2. Pillar rib deterioration-West Kentucky

The two-seam mining operation is located in Webster County, Kentucky in the Illinois Basin coal mining region. Highly localized zones of severe rib sloughage occurred in the active workings of the overlying mine, and these were investigated in 2015 by MSHA-TS.

The operation originally started in the Springfield (West Kentucky No. 9) Seam. Upon depleting those reserves, mining moved into the overlying Baker (West Kentucky No. 13) Seam. Interburden between the two seams is roughly 30 m.

The pillars in the active, overlying mine range in size from 21 m × 21 m centers to 30 m × 30 m centers, depending on their use as production panels or mains. Mining dimensions are approximately 3 m × 6 m. The mining height involves two benches of the coal seam separated by an approximate 0.3 m mudstone layer.

At the time of the investigation, mining had generally progressed down dip from roughly 45 m depth near the access shafts to a maximum depth of 175 m to the northeast of the shafts. The mining units investigated consisted of ten entry room work without pillar recovery. A robust primary roof support system is used consisting of No. 21 mm × 2.4 m SRD fully grouted, headed rebar. Intersections have supplemental support consisting of eight 15 mm × 3.7 m cable bolts installed 4 across in conjunction with T-channel. Panels of 10 cm grid 1.5 m × 4.9 m roof mesh are installed in all entries. Wire mesh rib support was routinely installed in the belt entry and supply/travel roadway [7].

The underlying Springfield Seam mining was also mined without pillar recovery. The production pillar centers appear to range from 15 m × 15 m to 20 m × 20 m. Panels were separated by barriers that could be 30 m wide. Multiple seam interactions were being encountered above these barrier pillars. It seems likely that the Springfield Seam pillars have failed, perhaps by punching into clay floor. Consequently, due to load transfer, the Springfield Seam barrier pillars separating the smaller pillars behaved as underlying gob-solid or remnant structures that impact the active mining in the Baker Seam. The stress interactions became noticeably more significant at depths exceeding 140 m.

An example of Baker Seam mining encountering underlying remnant structure at 174 m depth is shown in Fig. 5. In the example, mining is on 24 m × 24 m centers with crosscut center increased to 37 m over an underlying remnant barrier in the Springfield Seam. As noted on Fig. 5, roof pot-outs tend to flank the perimeter of the barrier and were consistent with roof flexure from the subsidence troughs that flanked the underlying barrier [7].

As noted in Fig. 5, rib sloughing and roof pot-outs plotted from an intermittent traverse where all roadways are not mapped [7].

The roof support system did not require modification. However, pillar rib sloughing was severe and persistent directly above and in the vicinity of the underlying barrier to the extent that rib support was installed to control further deterioration using wire mesh panels secured with 1.2 m fully grouted bolts and 15 cm × 41 cm plates (Fig. 6). The investigation involved other portions of the mine and revealed that there is also a depth dependency to rib deterioration where there is an absence of multiple seam structure. As a consequence a two-phase rib support program was established [7]:

(1) Entries or crosscuts that cross a Springfield Seam barrier at any depth, or lies within 15 m of its vertical projection, have rib support installed in the upper coal bench.
(2) At depths greater than 152 m, all critical entries (defined as escapeways, intake entry, belt entry, supply/travel entry, and 1 return entry per mining unit) as well as crosscuts that host equipment caches and power centers where workers congregate, have rib support installed in the upper coal bench.

The investigation led to the operation applying AMSS to insure that the Baker Seam pillars that cross the underlying multiple seam structures have adequate pillar stability to achieve global stability. An assessment of the AMSS procedures by MSHA-TS led to estab-

Fig. 5. Baker Seam mining (black) on 24 m × 24 m centers with crosscut center increased to 37 m over underlying remnant barrier (tan) in the Springfield Seam.

Fig. 6. Typical Baker Seam rib conditions in the vicinity of an underlying barrier requiring welded wire mesh and rib bolting in the upper bench-mudstone layer of the seam [7].

lishing a site specific Baker Seam AMSS evaluation for this mine's multiple seam environments. In the example shown in Fig. 5, the 24 m × 24 m center pillar system had crosscuts extended over the barrier to 37 m center and establishes an acceptable AMSS derived stability factor. However, the AMSS warning remains that stress interaction will be significant to where robust roof and rib support will likely be required to have local stability. The conditions noted in the underground investigation validate the need for robust ground support even with increased pillar stability which is a common situation in multiple seam mining scenarios.

3.3. Roof and rib deterioration-Kentucky

The mining operation is located in Letcher County, eastern Kentucky, in the Central Appalachian coal mining region. An underground area with severe rib sloughage was investigated in 2013 by MSHA-TS. The mining unit investigated consisted of a six entry submain being developed with 26 m × 32 m center pillars to establish pillar recovery panels at 370 to 430 m depth of cover (Fig. 7).

The mine is in the Kellioka Seam (B Seam). Previous mining has been conducted in the following three seams: Imboden Seam approximately 91 m below, Low Splint Seam (F Seam) approximately 60 m above, and the Owl Seam (D Seam) approximately 25 m above. The Imboden Seam mining in the investigation area consists of four entry development and barrier pillars. The Low Splint Seam mining consists of a large barrier pillar with full extraction mining on one side. The Kellioka Seam mining showed no evidence of multiple stress interaction from either the underlying Imboden Seam or from the overlying Low Splint Seam.

However, multiple seam stress interaction became apparent from overlying owl seam workings. The Kellioka Seam submain is also in a transition zone where the development advanced under an Owl Seam barrier that adjoins a seven entry panel having 22 m × 29 m center pillars (Fig. 8). The Owl Seam panel was reported to have experienced floor failure, which would have shifted considerable load to the adjacent barrier pillar. The investigation revealed that the Kellioka Seam mining under the owl seam barrier exhibited elevated stress that generated rib spall and roof degradation (Figs. 9 and 10). In contrast, the mining under the failed Owl Seam pillar system offered a de-stressed region with a clear definition of where the de-stressed zone is and the position of the overlying edge of the barrier (Fig. 11).

The ARMPS SF calculated for the overlying Owl Seam pillars was 2.5, which would normally indicate a stable pillar configuration. However, floor failure was noted, and later adjoining mining employed larger pillars for Owl Seam development (Fig. 8). An AMSS evaluation of the Kellioka Seam mining assuming the Owl Seam failed panel as gob, indicates a stable pillar system (SF = 1.58); however, a cautionary warning exists indicating the possibility of interaction affecting roof and rib stability which did occur as noted in the investigation.

The need to install roof-to-floor support to cope with roof deterioration stopped the section advance (Fig. 9). To avoid the problem area, the mine elected to advance the development elsewhere. Kellioka Seam entries were superimposed under Owl Seam entries and mining under the intact Owl Seam barriers was avoided. Mining then advanced into the destressed zone under the overlying panel, and then tied back into the stopped entries to establish ventilation using reduced mining widths and robust roof support.

3.4. Multiple pillar burst - Kentucky

The mining area is located in Harlan County, Kentucky in the Central Appalachian coal mining region in the Kellioka Seam two adjoining mining operations encountered three multiple pillar burst events in December 1999, September 2001, and November 2002 that were investigated by MSHA-TS. The bursts events in 1999 and 2001 are attributable to a pseudo gob situation in an underlying seam at one of those operations (Fig. 12).

The 1999 and 2001 burst events occurred on five entry developments having 24 m × 24 m pillar centers at similar depths of cover of 502–518 m. The events were situated under a ridge exceeding 460 m depth of cover (Fig. 13).

Fig. 7. Kellioka Seam six entry submain being developed to establish pillar recovery panels at 370–430 m depth of cover.

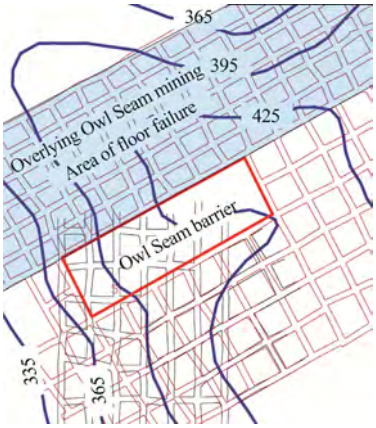

Fig. 8. Kellioka Seam six entry submain (black) overlain by Owl Seam pillars and barrier (red) showing Owl Seam panel having reported floor failure (shaded).

Fig. 9. Kellioka Seam pillar showing rib sloughing from multiple seam stress interaction (view shown by arrow on embedded map).

Fig. 10. Kellioka Seam roof geologic structure, small drag fold, degradation and pillar rib sloughing from multiple seam stress interaction.

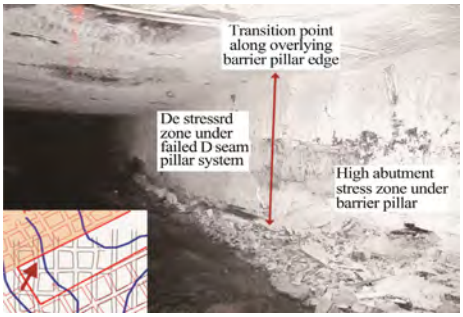

Fig. 11. Kellioka Seam mining having de-stressed conditions under the failed Owl Seam pillar system and also showing a definite location of the overlying edge of the Owl Seam barrier.

As noted in Fig. 13, depth of cover and underlying Harlan Seam workings (magenta) show Kellioka workings are surrounding mining at the time of 2001 event.

In the vicinity of the burst events, the Kellioka Seam is underlain by workings in the Harlan Seam with 50–53 m interburden [8]. Investigators at the time of the events inferred that the Harlan Seam barriers underlying the Kellioka Seam bursts were highly stressed. It appears that yield in the Harlan Seam pillar systems created a pseudo gob that transferred stress onto the adjacent barriers. When coupled with the depth of cover and Kellioka Seam burst prone geologic conditions, the events occurred when the Kellioka Seam development advanced over the underlying barriers.

An ARMPS version 6 evaluation of the Harlan Seam pillars involved in the 1999 and 2001 events found an SF that exceeded 2.0, which would normally suggest a stable pillar system. However,

Fig. 12. Coal pillar and immediate roof material filling entry after the 2001 Kellioka Seam burst event.

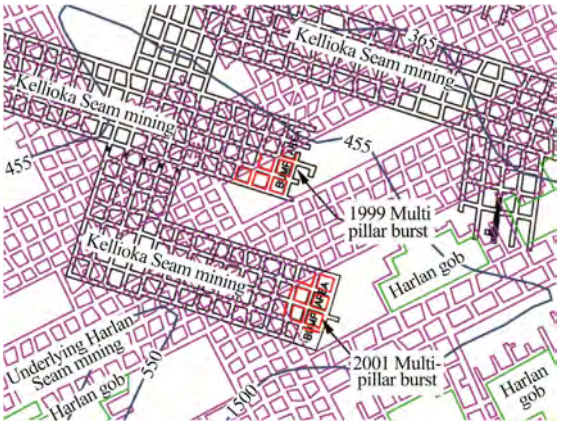

Fig. 13. Kellioka Seam burst events with affected pillars identified in MSHA–TS investigations outlined in red.

a reevaluation by Harris, applying LaModel multiple seam scenarios and strain softening coal properties for the Harlan Seam, determined sufficient yield could take place for stress transfer to the Harlan Seam barriers [8]. A thorough back analysis of the burst events using LaModel 3.0 for the multiple seams determined site specific pillar design criteria considered appropriate to allow pillar recovery in the presence of multiple seam mining structure. The study for site specific criteria included overlying Darby Seam and underlying Harlan Seam workings [8]. Pillar recovery was conducted, primarily at 300 m maximum depth, after evaluation of the mining plan for a specific limited area met the established LaModel criteria.

3.5. Pillar burst-West Virginia

The mining operation is located in Boone County, West Virginia in the Central Appalachian coal mining region in the Powellton Seam. In 2006 while advancing an eight entry main, the mine encountered a pillar burst on the right side of the section where the immediate roof consisted of sandstone. Degraded roof conditions were encountered on the left side of the section where the immediate roof consisted of shale (Fig. 14). Gauna and Phillipson concluded that yielding pillars in the overlying seam caused stress transfer to the adjoining larger pillars [9]. Also the example points out that mitigation for future mining can involve historical back analysis of successful and unsuccessful multiple seam mining configurations across the reserve area using empirical pillar design methods to minimize risk.

Fig. 14. Powellton Seam mains (black) showing burst pillar area (red hatch) with depth of cover and overlying No. 2 gas seam workings (orange); larger overlying remnant barriers identified by orange shading.

Fig. 15. Pillar burst material filling No. 8 entry.

Fig. 16. Failed shale roof under No. 2 gas seam remnant barrier where roof is being squeezed downward by pressure from Powellton Seam pillar and immediate roof dilation.

The Powellton Seam burst region (Fig. 15) and degraded shale roof (Fig. 16) were both situated approximately 18 m beneath large pillars, 73 m × 69 m and 58 m × 69 m, that had been left in the overlying No. 2 gas seam. The No. 2 gas seam large pillars are surrounded by much smaller pillars, measuring 12 m × 15 m. The apparent lack of loading observed on the Powellton Seam pillar ribs located beneath the overlying small pillars indicated that the small pillars were acting as pseudo gob, transferring load to the large pillars which acted as remnant barriers.

The No. 2 gas seam small pillars immediately surrounding the remnant barriers had ARMPS version 6 SF over 1.9. Away from the large pillars, where a wide development span exists, the ARMPS SF diminishes to 1.4. SF of these magnitudes normally suggests a relatively stable pillar system. However, it was interpreted that long-term flooding in the No. 2 gas seam in a region above the active mining had softened the overlying pillar system and degraded the load bearing capacity of the smaller pillars.

The pillars used in the Powellton Seam active mining also maintained an adequate pillar system SF exceeding 2.0. However, the burst apparently resulted from the multiple seam stress concentration combined with conditions including the transition to strong massive sandstone, the burst pillar's position in the bottom of a trough within the coal horizon, and the narrowing of the burst pillar to avoid the sand channel intrusion with the resultant decrease in load bearing capacity. Mitigation for future mining involved redirecting mining away from the sandstone channel region and increasing the pillar size to better cope with unexpected loading should multiple seam stress be encountered again. The determination of appropriate pillar size was conducted with historical back analysis of successful and unsuccessful multiple seam mining configurations across the reserve area. NIOSH ARMPS and pillar load bearing capacities were relied upon in the back analyses. At the time of the evaluation, AMSS had not yet been developed.

4. Summary

Mining operations including their management, planning staff, and mining personnel must recognize that multiple seam stress can be encountered even where no full extraction has been conducted in the overlying or underlying old workings. Mining crews and management may not realize they have encountered a pseudo gob problem until they encounter deteriorated conditions that can't be explained in terms of a change in geologic condition, increased depth of mining, or inadequate pillar size.

At the onset of unexpected and unexplained rib sloughing, roof scale out, coal seam rolls or dips indicative of subsidence, etc., mining crews and management should immediately consider that underlying or overlying pillars have yielded and are behaving as pseudo gob. Mining operations must exercise vigilance and immediately react when evidence of such stresses are encountered.

Examples of conditions that could lead to the formation of pseudo gob in overlying or underlying development pillars are low pillar stability factors or high coal recovery coupled with old age of the workings and water weakening the pillar foundation. The impact on the active mining will be more pronounced if the pseudo gob is an underlying feature. For mining to safely and successfully continue, a variety of methods have been applied to mitigate the stresses from pseudo gob situations. The hazard mitigation has required:

(1) At remnant or gob-solid multiple seam crossings, pillar design should be evaluated and adjusted if necessary to insure adequate global stability in the regions impacted by the elevated stresses.
(2) Roof and rib support will often need to be increased to maintain adequate ground control at the elevated stress regions in the active seam along the perimeter and over/under the remnant structure of the overlying or underlying seam.
(3) Acquiring roof support equipment to install appropriate roof rib support to cope with the stresses, and having the machine work stations designed for protection from both roof and rib fall hazards.

(4) Multiple seam stress interaction can be mitigated by redirecting advance elsewhere away from the high stress region. Applying techniques such as superimposing entries, avoiding mining under or over intact remnant barriers, and striving to establish mining into the destressed zones serve to mitigate the stress interaction when redirecting mining.
(5) Mitigation can involve no mining in a given region or at a given depth of cover to avoid the impact of multiple seam stress interaction.
(6) If a credible back analysis can be performed where criteria for safe multiple seam mining can be determined, site specific design has the potential to mitigate stress interaction. The design criteria must be stringent, and the evaluation must focus on relatively small regions to determine the elevated multiple seam stress levels that should be avoided.

References

[1] Mark C, Chase FE, Pappas DM. Analysis of multiple seam stability. In: Proceedings of the 26th international conference on ground control in mining. Morgantown, WV: West Virginia University; 2007. p. 5–18.
[2] MSHA. Fatal accident report, crandall canyon mine Available at <http://www.msha.gov/fatals/2007/CrandallCanyon/ CrandallCanyonreport.asp>; 2008.
[3] Gauna M, Tyrna P. MSHA Technical review of proposed mine designs for u.s. underground coal mines. In: Proceedings of the 30th international conference on ground control in mining. Morgantown, WV: West Virginia University; 2011. p. 277–85.
[4] Mark C, Gauna M. Evaluating the risk of coal bursts in underground coal mines. In: Proceedings of the 34th international conference on ground control in mining. Morgantown, WV: West Virginia University; 2015. p. 47–53.
[5] MSHA. Coal mine fatal accident report, fall of rib; February 1, 2006.
[6] Mark C. Pillar design for deep cover retreat mining: ARMPS version 6. In: proceedings of the third international workshop on coal pillar mechanics and design. Morgantown, WV; 2010. p. 106–21.
[7] Phillipson S, Muto E. 15AA28-evaluation of rib conditions. Mine safety and health administration-technical support agency memorandum; 2015. p. 13.
[8] Harris KW, Raffaldi MJ, Perry KA. A case study for multiple seam calibration of LaModel in bump prone ground. In: Proceedings of the 33rd international conference on ground control in mining. Morgantown, WV: West Virginia University; 2014. p. 165–9.
[9] Gauna M, Phillipson S. Evaluation of a multiple seam interaction coal pillar bump. In: Proceedings of the 27th international conference on ground control in mining. Morgantown, WV: West Virginia University; 2008. p. 51–9.

International Journal of Mining Science and Technology 27 (2017) 139–143

Contents lists available at ScienceDirect

International Journal of Mining Science and Technology

journal homepage: www.elsevier.com/locate/ijmst

A roof model and its application in solid backfilling mining

Ju Feng, Huang Peng *, Guo Shuai, Xiao Meng, Lan Lixin

State Key Laboratory for Geomechanics and Deep Underground Engineering, China University of Mining & Technology, Xuzhou 221116, China

ARTICLE INFO

Article history:
Received 18 May 2016
Received in revised form 5 August 2016
Accepted 25 October 2016
Available online 10 December 2016

Keywords:
Backfill mining
Backfilling material
Compaction characteristic
Thin plate model

ABSTRACT

Through changing the axial load on backfilling material compaction test to reflect different overlying strata pressure on backfilling material, the stress-strain relations in the compaction process of backfilling material under the geological condition can be obtained. Based on the characteristic of overlying strata movement in backfill mining, a model of roof thin plate is established. By introducing the stress-strain relation in compaction process into the model and using RIZT method to analyze the bending deformation of roof, the bending deflection and stress distribution can be obtained. The results show that the maximum roof subsidence and maximum tensile stress occurring at the center are 255 mm and 5 MPa, respectively. Tensile fracture of roof under the geological condition of Dongping Mine did not occur. The dynamic measurement results of roof in Dongping Mine verify the theoretical result from the aforementioned model, thereby suggesting the roof mechanical model is reliable. The roof thin plate model based on the compaction characteristic of backfilling material in this study is of importance to research on backfill mining theories and application of backfilling material characteristics.

1. Introduction

Solid backfilling mining (SBM) is a green mining technology in which the solid waste materials is placed into the gob to support the overlying strata and to control roof's subsidence and movement [1–3]. SBM has been successfully used in several mines to solve many problems, including coal extraction under buildings, water bodies and railways, surface subsidence, and environmental problems. Good results have been obtained in many mines [4]. The key in the application of SBM technology is to control strata movement. However, the critical factor influencing the controlling effect of strata movement is compaction characteristics of backfilling materials. Thus, a roof model of SBM is built based on the filling materials' compaction characteristics. A subsidence equation and the critical failure condition of roof was given and field verification was performed at panel 15061 of Dongping Mine.

To date, many studies have been conducted to investigate the roof movement in SBM and tremendous progress has been made. For example, Zhang analyzed the key layer deformation by building a beam model on an elastic foundation; Huang used a numerical model to access the effect of backfilling ratio on strata movement control and surface subsidence; Li analyzed the effect of elastic foundation coefficient of filling materials on roof's deformation and failure using a foundation plate theory. However, the aforementioned research which assumed filling materials as a constant foundation coefficient did not introduce filling materials' compaction characteristics to the mechanic model [5–9]. Therefore, the models built in their research cannot accurately reflect the characteristic behavior of filling materials. In this study, the constitutive relation of the filling materials during compaction will be first obtained in the laboratory, and then introduced in a model. Finally, a deformation equation and bending stress will be given.

2. Principle and deformation characteristics of the surrounding rock of SBM

2.1. Basic principles of SBM

In SBM, solid waste materials, such as gangue, fly ash and loess, are transported through a vertical pipe and then were delivered to the backfilling area with the belt conveyor. With the backfilling conveyor, backfilling hydraulic support and compactor, the filling materials are delivered to fill up the gob. The face layout of SBM is shown in Fig. 1. Comparing with the conventional face layout, a belt conveyor in the tailgate in a SBM face delivers the filling materials to a conveyor in the gob side of the face behind the shield supports. Therefore in SBM, the face layout allows simultaneous mining and backfilling operations.

* Corresponding author. Tel.: +86 18796280203.
E-mail address: cumt_hp@126.com (P. Huang).

http://dx.doi.org/10.1016/j.ijmst.2016.11.001
2095-2686/

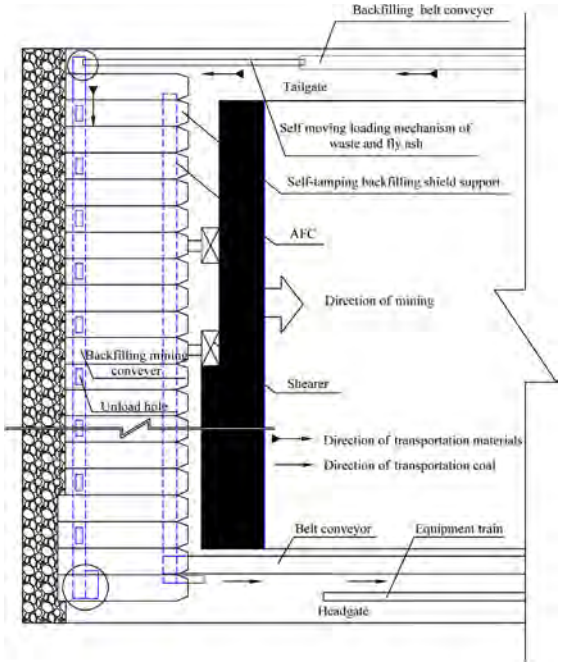

Fig. 1. A SBM face layout.

2.2. General characteristics of overlying strata movement in SBM

In SBM, the movement of overlying strata is divided into two zones, fractured and continuous bending zones, as compared to three zones in the conventional mining [10,11]. After the backfilling materials have filled up the gob, a new support system consisting of solid coal, shield support and backfill materials body forms, which is different from the traditional support system consisting of the solid coal, shield support and caved gob [12–14]. The immediate roof and main roof will not fail and only localized fractures will occur when the backfilling operation is properly implemented. There will be no caving zone in SBM. The rock strata above the fractured zone bend, subside and deform slightly, inducing little surface subsidence.

3. Compaction test of solid backfilling materials

3.1. Test equipment

The YAS-5000 electro-hydraulic servo-controlled rock mechanic test system, manufactured Changchun Kexin Test Instrument Company, was employed for the compaction tests. The circular cylinder for test sample was a Q235 seamless steel tube with a yield strength of 170 MPa. Using a safety factor of 1.5, a compaction cylinder chamber with an outer diameter of 274 mm, an inside diameter of 250 mm, a thickness of 24 mm and a height of 304 mm was made. The test machine and compaction cylinder are shown in Fig. 2.

3.2. Test materials and scheme

The test materials were waste rocks from Dongpin Mine. Given the mining depth was 120 m, a maximum uniaxial pressure of 3 MPa was chosen in the compacting test. The loading rate was 0.1 kN/s, resulting in a testing period for each group of 1500 s. The data were recorded every 3.0 s. The maximum radial pressure was 2.01 MPa when the confining pressure coefficient was 0.67.

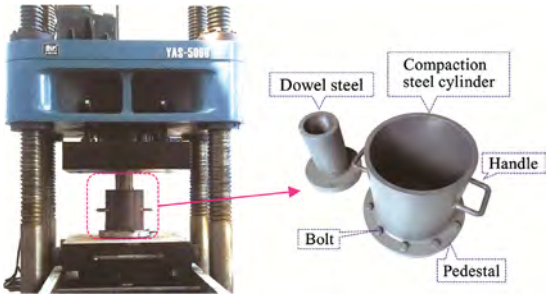

Fig. 2. Test equipment and compaction cylinder chamber.

3.3. Test results

Fig. 3 shows the stress and strain curve for axial stress from 0 to 3 MPa. The curve was regressed in the polynomial equation form (Eq. (1)) to obtain Eq. (2) as the regression equation. The maximum strain was 0.084 in the compaction test.

$$\sigma(\varepsilon) = d_1\varepsilon^3 + d_2\varepsilon^2 + d_3\varepsilon + d_4 \tag{1}$$

$$\sigma(\varepsilon) = 6778.19\varepsilon^3 - 306.43\varepsilon^2 + 12.01\varepsilon - 0.0045 \quad R^2 = 0.99 \tag{2}$$

4. Elastic foundation plate model and solution for SBM

4.1. Model assumptions

In theory of elasticity, a thin plate must satisfy the following conditions [9,15,16]:

$$\left(\frac{1}{100} \sim \frac{1}{80}\right) \leqslant \frac{h}{l} \leqslant \left(\frac{1}{8} \sim \frac{1}{5}\right) \tag{3}$$

where h is the height of plate, m; and l the short length of plate, m. The panel width is usually from 80 to 150 m and the roof is from 3 to 20 m in SBM. So the ratio of the thickness and width meet the condition of an elastic plate.

4.2. Roof model

The roof which carries the overburden load $q(x, y)$ and supports by elastic foundation $p(x, y)$ at the bottom in SBM can be treated as a quadrilateral rectangular plate. A backfilling roof model is established as shown in Fig. 4, in which the positive of x coordinate in the model is the face advancing direction, while y is the seam dip direction, being b wide. Z is the vertical direction.

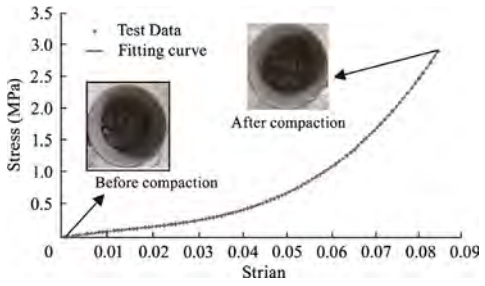

Fig. 3. Stress-strain curve for waste rock compaction test.

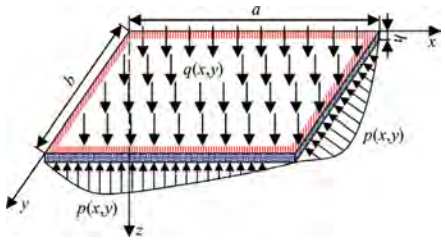

Fig. 4. Roof model in SBM.

4.3. Bending and deformation of elastic thin plate

The differential equation of bending surface for an elastic plate is assumed as follows:

$$D\left(\frac{\partial^4 w}{\partial x^4}+2\frac{\partial^4 w}{\partial x^2\partial y^2}+\frac{\partial^4 w}{\partial y^4}\right)=q(x,y)-p(x,y) \tag{4}$$

where the plate flexural rigidity is D, N·m; the plate elastic modulus is E, GPa; and the plate Poisson's ratio is u.

The boundary conditions of elastic plate model are

$$\begin{cases}(w)_{\substack{x=0\\x=a}}=0\\ \left(\frac{\partial w}{\partial x}\right)_{\substack{x=0\\x=a}}=0\\ (w)_{\substack{y=0\\y=b}}=0\\ \left(\frac{\partial w}{\partial y}\right)_{\substack{y=0\\y=b}}=0\end{cases} \tag{5}$$

The deflection function of elastic plate must satisfy the boundary conditions. The deflection function of elastic plate is assumed as a form of trigonometric series [17,18].

$$\begin{aligned}w&=\sum_{m=1}^{\infty}\sum_{n=1}^{\infty}C_{mn}w_u\\&=\sum_{m=1}^{\infty}\sum_{n=1}^{\infty}C_{mn}\left(1-\cos\left(\frac{2m\pi x}{a}\right)\right)\left(1-\cos\left(\frac{2n\pi y}{b}\right)\right)\end{aligned} \tag{6}$$

The potential deformation energy of the whole system of a fix-ended quadrilateral rectangular plate is as follows.

$$U=\frac{D}{2}\int\int\left(\nabla^2 w\right)^2 dxdy \tag{7}$$

To simplify the computation and eliminate the loss of accuracy, the infinitesimal terms are ignored. Substituting Eqs. (6)–(7), Eq. (8) is obtained

$$U=\sum_{m=1}^{\infty}\sum_{n=1}^{\infty}2D\pi^4C_{mn}^2\left(\frac{3bm^4}{a^3}+\frac{3an^4}{b^3}+\frac{2m^2n^2}{ab}\right) \tag{8}$$

The deformation potential energy of an inelastic foundation V is

$$V=\frac{1}{2}\int\int\sigma(x)\frac{w(x)}{h}dxdy \tag{9}$$

Substituting Eqs. (1) and (6) to (7), the foundation's deformation potential energy is

$$\begin{aligned}V=&\sum_{m=1}^{\infty}\sum_{n=1}^{\infty}\frac{15,625abC_{m,n}}{18h^4}\left(11,025C_{m,n}^3d_1+3600C_{m,n}^2hd_2\right.\\&\left.+1296C_{m,n}h^2d_3+576h^3d_4\right)\end{aligned} \tag{10}$$

The sum of deformation potential energy and the foundation deformation potential energy is

$$\prod=U+V \tag{11}$$

According to the principal of RIZT, the following equation is got [19]

$$\delta\left(\prod\right)=\int\int qw_u dxdy \tag{12}$$

The deflection equation can be obtained by first solving for C_{mn} and then substituting it into Eq. (6).

The portion of pressure in the first stratum attributed to stratum N in the overburden strata is [20,21].

$$q=\frac{E_1h_1^3\sum_{i=1}^{n}\gamma_i h_i}{\sum_{i=1}^{n}E_ih_i^3} \tag{13}$$

4.4. Bending stress of elastic thin plate

According to the plate theory, the bending moment is

$$\begin{cases}M_x=-D\left(\frac{\partial^2 w}{\partial x^2}+\mu\frac{\partial^2 w}{\partial y^2}\right)\\ M_y=-D\left(\frac{\partial^2 w}{\partial y^2}+\mu\frac{\partial^2 w}{\partial x^2}\right)\\ M_{xy}=-D(1-\mu)\frac{\partial^2 w}{\partial x\partial y}\end{cases} \tag{14}$$

Substituting Eqs. (6)–(14),

$$\begin{cases}M_x=-D\left[\frac{4C_{mn}\cos\left(\frac{2m\pi x}{a}\right)m^2\pi^2\left(1-\cos\left(\frac{2n\pi y}{b}\right)\right)}{a^2}+\frac{4uC_{mn}\cos\left(\frac{2n\pi y}{b}\right)n^2\pi^2\left(1-\cos\left(\frac{2m\pi x}{a}\right)\right)}{b^2}\right]\\ M_y=-D\left[\frac{4uC_{mn}\cos\left(\frac{2m\pi x}{a}\right)m^2\pi^2\left(1-\cos\left(\frac{2n\pi y}{b}\right)\right)}{a^2}+\frac{4C_{mn}\cos\left(\frac{2n\pi y}{b}\right)n^2\pi^2\left(1-\cos\left(\frac{2m\pi x}{a}\right)\right)}{b^2}\right]\\ M_{xy}=-D(1-\mu)\left(\frac{4C_{mn}\sin\left(\frac{2m\pi x}{a}\right)mn\pi^2\sin\left(\frac{2n\pi y}{b}\right)}{ab}\right)\end{cases} \tag{15}$$

The bending stress of thin plate is

$$\sigma_x=\frac{12M_xz}{h^3},\quad \sigma_y=\frac{12M_yz}{h^3} \tag{16}$$

Substituting Eqs. (15)–(16), the bending stresses are obtained.

Rock as a typical brittle material. The first strength theory can be used to determine whether or not it fails [21]

$$\sigma_{\max}\leqslant[\sigma] \tag{17}$$

where $\sigma_{\max}$ is the maximum tensile stress in the thin plate; and $[\sigma]$ the allowable stress.

5. A case study

5.1. Mining geological conditions

Dongping Coal Mine is located west of the Moutain Taihang with a typical rolling terrain. The first backfill panel was 15061. Its average length along the strike direction was 286 m and the average width along the dip direction was 84 m. It mined the #15 coal seam, 6.8 m on average, of the lower segment of Taiyuan group. The structure of the coal seam was relatively complex, mostly containing 1–3 layers of mudstone dirt bands. The roof was limestone, 9.7 m thick and included a mudstone false roof of around 0.5 m thick, while the coal seam bottom is sandy mudstone. The mining height 3.0 m was conducted in the lower part of the coal seam and the remaining 3.8 m served as the immediate roof and the backfill material is gangue. Fig. 5 shows the panel 15061 layout. Based on the rock mechanics properties tests, the

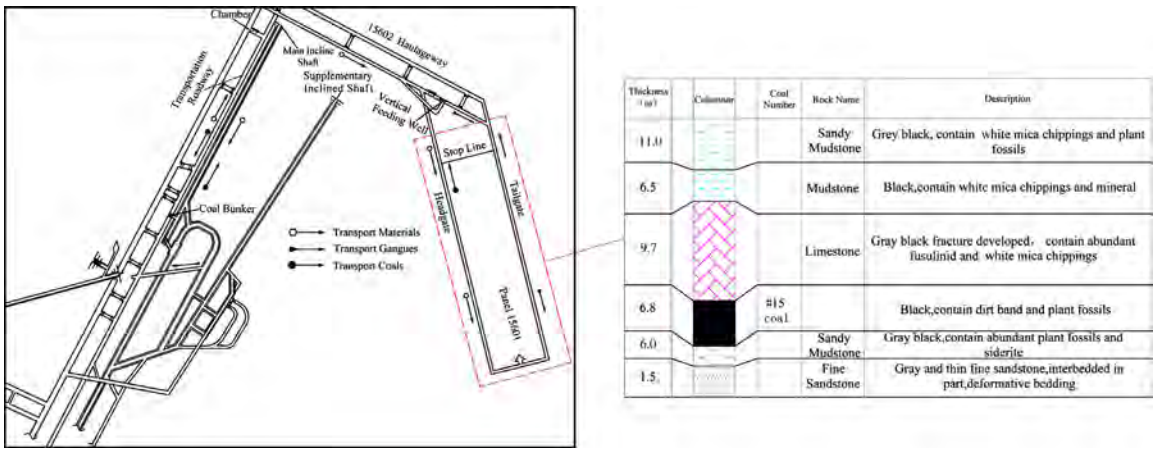

Fig. 5. Panel 15061 layout.

Table 1
Third order panel deflection functions.

C11	C12	C13	C21	C22	C23	C31	C32	C33
0.06589	0.01645	0.00252	0.00106	0.00086	0.00068	0.00051	0.00043	0.00004

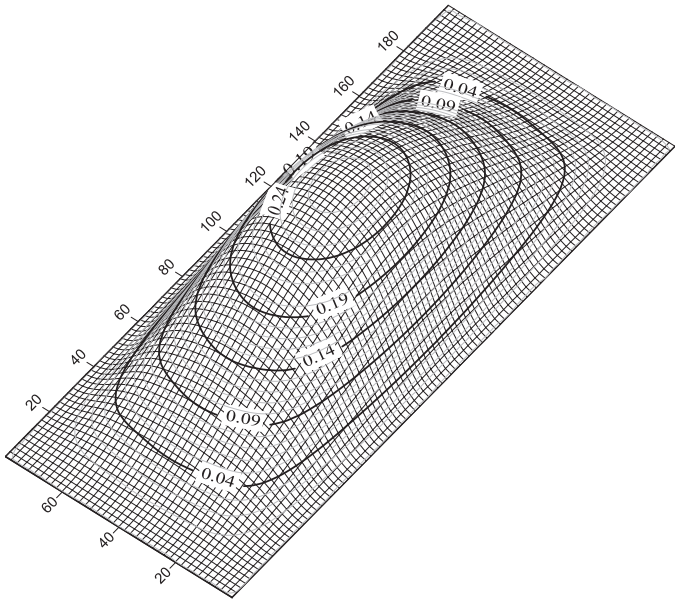

Fig. 6. Roof three-dimensional subsidence surface.

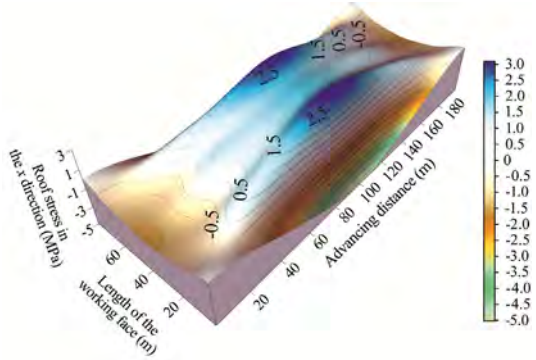

Fig. 7. Roof stress in the *x* direction.

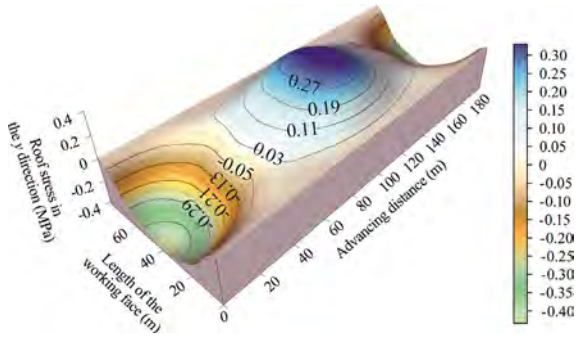

Fig. 8. Roof stress in the *y* direction.

elastic modulus of coal is 5.8 GPa; Poisson's ratio is 0.27 and the allowable tensile stress is 6.13 MPa. According to the key strata theory, the related geological parameters are substituted into Eq. (13). It is found that the sandy mudstone with a thickness of 11 m above the coal seam plays a key role in the overburden strata control. Thus, the roof load is imposed mainly by the two overlying strata, q = 400 kN.

5.2. Modelling a case study

The parameters mentioned in the previous sections were substituted into Eq. (12) to obtain the deflection function. In order to satisfy the computation accuracy, the third order deflection function of thin plate was used. The coefficients are listed in Table 1.

By substituting the coefficients into the function, the three-dimensional roof subsidence diagram is obtained as shown in Fig. 6.

It is clear from Fig. 6 that roof subsidence is mainly bending instead of failure. Roof subsidence changes gradually, no abrupt changes. The maximum subsidence and strain, 262 mm and 0.087, respectively, appear at the center of the mining area.

From Eq. (15), the maximum tensile stress in the thin plate occurs at the center part of the top and bottom surfaces. When substituting $z = -\frac{h}{2}$ into Eq. (15), the three-dimensional stress dis-

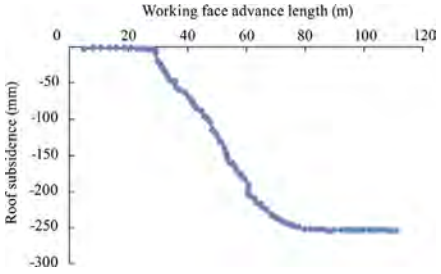

Fig. 9. Roof subsidence as the face advanced.

tribution cloud graph in the x and y directions of the thin plate is obtained as shown in Figs. 7 and 8, respectively.

It can be concluded from Figs. 7 and 8 that the maximum tensile stress occurs in the center of the bottom surface of the roof, and the top surface of the roof has the maximum tensile stress at the clamped edge.

When $z = -\frac{h}{2}$ is substituted into Eq. (15), the peak tensile stress in the x direction of the thin plate is 3.1 MPa; when $z = +\frac{h}{2}$ is substituted into Eq. (15), the peak tensile stress in the y direction of the thin plate is 5 MPa. Substituting the peak values into Eq. (17), it is shown that the roof will not fail due to the tensile tress.

5.3. Field validation of the model

During the retreat mining, roof subsidence in No. 2 measuring point, which was located at panel center 25 m from the set up room panel 15061 was monitored. The measured roof subsidence is shown in Fig. 9.

From Fig. 9, the following conclusions can be made:

(1) The roof subsidence curve is continuous without any sharp increase, indicating the roof moved as a unit throughout the mining process without failure.
(2) When the face has advanced 50–70 m, the roof movement is strong and the maximum subsidence velocity is 13 mm/d. This corresponds to the preliminary compression process of the backfill material.
(3) After the face has advanced 80 m, the roof is basically stable. In this process, the backfill material is compressed and the backfill body can provide effective support to the roof. The maximum subsidence is 255 mm.

The field test shows that the roof at the face is continuous bending as a unit rather than fail. The compression amount of backfilling material equals to the final subsidence of the roof. The maximum strain is 0.085, which coincides with the results from compression experiments and theoretical calculation.

6. Conclusions

(1) According to the geological conditions, a compression test for backfill material is designed. Based on the stress strain curve, a linear regression curve is obtained.
(2) With the relationship obtained from the tests, a roof model of backfill mining is established by using the elastic thin plate theory. Then the analytic solutions for roof stress and deflection functions are solved. Besides, the critical condition for roof failure is given.
(3) According to the geological conditions, the theoretical calculation for roof subsidence is close to the field measurement. The maximum tensile stress does not exceed the allowable tensile stress and this is in good agreement with the field results. All these verify the reliability of the model.
(4) This paper establishes an elastic foundation thin plate model based on the compaction characteristic of the backfill material.

Acknowledgment

The authors are grateful for financial assistance provided by the National Natural Science Foundation of China (No. 51304206) and China Postdoctoral Science Foundation funded project (No. 2015M580492).

References

[1] Miao XX. Progress of fully mechanized mining with solid backfilling technology. J China Coal Soc 2012;37(8):1247–55.
[2] Miao XX, Zhang J, Guo GL. Study on waste-filling method and technology in fully-mechanized coal mining. J China Coal Soc 2010;35(1):1–6.
[3] Miao XX, Ju F, Huang YL, Guo GL. New development and prospect of backfilling mining theory and technology. J China Univ Min Technol 2015;44(3):391–9. +429.
[4] Zhang JX, Miao XX, Guo GL. Development status of backfilling technology using raw waste in coal mining. J Min Saf Eng 2009;26(4):395–401.
[5] Zhang JX, Li J, An TL, Huang YL. Deformation characteristic of key stratum overburden by raw waste backfilling with fully-mechanized coal mining technology. J China Coal Soc 2010;35(3):357–62.
[6] Zhang JX, Zhang Q, Huang YL, Liu JW, Zhou N, Zan DF. Strata movement controlling effect of waste and fly ash backfillings in fully mechanized coal mining with backfilling face. Int J Min Sci Technol 2011;21(5):721–6.
[7] Huang YL, Zhang JX, Zhang Q, Nie SJ, An BF. Strata movement control due to bulk factor of backfilling body in fully mechanized backfilling mining face. J Min Saf Eng 2012;29(2):162–7.
[8] Li M, Zhang JX, Liu Z, Zhao X, Huang P. Mechanical analysis of roof stability under nonlinear compaction of solid backfill body. Int J Min Sci Technol 2016;26(5):863–8.
[9] Li M, Zhang JX, Jiang HQ, Huang YL, Zhang QA. Thin plate on elastic foundation model of overlying strata for dense solid backfill mining. J China Coal Soc 2014;39(12):2369–73.
[10] Zhang JX, Jiang HQ, Deng XJ, Ju F. Prediction of the height of the water-conducting zone above the mined panel in solid backfill mining. Mine Water Environ 2014;33(4):317–26.
[11] Huang YL. Ground control theory and application of solid dense backfill in coal mines. Xuzhou: China University of Mining and Technology; 2012.
[12] Zhang Q, Zhang JX, Ju F, Li M, Geng DK. Backfill body's compression ratio design and control theory research in solid backfill coal mining. J China Coal Soc 2014;39(1):64–71.
[13] Zhou YJ, Chen Y, Zhang JX, He Q. Control principle and technology of final compression ratio of backfilling materials. J Min Saf Eng 2012;29(3):3.
[14] Huang YL, Zhang JX, Du J. Time-dependence of backfilling body in fully mechanized backfilling mining face. J China Univ Min Technol 2012;41 (5):697–701.
[15] Wang LF. Theory of elasticity. Beijing: Science Press; 1984.
[16] He FB. Theory of plates and shells. Xi'an: Xi'an Jiaotong University Publishing House; 1993.
[17] Xue Y. Numerical analysis and scientific computing. Beijing: Science Press; 2011.
[18] Liu Z. Compaction properties of gangue and its application in backfilling coal mining. Xuzhou: China University of Mining and Technology; 2014.
[19] Xu ZL. Mechanics of elasticity. Beijing: Higher Education Press; 1990.
[20] Qian MG, Miao XX, Xu JL, Mao XB. Key strata theory of strata control. Xuzhou: China University of Mining and Technology Press; 2003.
[21] Liu HW. Mechanics of material. Beijing: Higher Education Press; 2004.

International Journal of Mining Science and Technology 27 (2017) 145–152

Contents lists available at ScienceDirect

International Journal of Mining Science and Technology

journal homepage: www.elsevier.com/locate/ijmst

Longwall mining under gateroads and gobs of abandoned small mine

Li Yang *, Zhu Enguang, Zhang Kangning, Li Minghao, Wang Jiaxing, Li Chengkun

School of Resources and Safety Engineering, China University of Mining & Technology, Beijing 100083, China

ARTICLE INFO

Article history:
Available online 23 December 2016

Keywords:
Disturbed zone
Recovery mining technology
Abandoned gateroads
Inclined face
Numerical simulation

ABSTRACT

Due to the use of outdated mining technology or room and pillar mining process in small coal mines, the coal recovery ratio is only 10–25%. In many regions of China, the damage area caused by the small coal mines amounted to nearly one hundred square kilometers. Therefore, special mining techniques must be taken to reclaim the wasted resource in disturbed coal areas. This paper focuses on the different mining methods by analyzing the longwall panel layout and abandoned gateroad (AG) distribution in the abandoned area of Cuijiazhai coal mine in northwestern China. On the basis of three-dimensional geological model, FLAC3D numerical simulation was employed. The abutment pressure distribution was simulated when the panel face passed through the disturbed areas. The proper angle of the inclined face was analyzed when the panel face passed through the abandoned gateroads. The results show that the head end of the face should be 13–20 m ahead of the tail end. The pillars on both sides of abandoned gateroads had not been damaged at the same time, and no large-area stress concentration occured above the main roof. Therefore, the coal reserves of disturbed areas can be successfully recovered by using underground longwall mining.

1. Introduction

During the 70–90s, there were a lot of small coal mines in China. Due to their disordered mining, most of the small coal mines left a great many abandoned gateroads (AG for short) and a large area of damage coal seam. In these type of coalfields, there exist many mining risk issues, including non-uniform stress in the overburden, flooding and hazardous gases accumulated in the gob. Therefore, how to lay out a longwall panel and successfully mining under this type of abandoned small mines is a big issue nowadays in China.

As mentioned above, longwall panel is being performed in the damaged coal seams in order to increase recovery of coal reserves [1]. However, the abandoned geteroads intersect to each other all around the area. Thus, a series of production issues arose while the panel face is passing through these AG. Jia and Gong analyzed the roof stability and abutment pressure distribution when the face was passing those AG that were parallel and inclined to the faceline [2]. Xie et al. proposed the ground control mechanism by passing the AG in top-coal caving longwall mining, and recommended to stop the face advance until the roof is over, using high strength bolts and cable bolts, and grouting consolidation [3]. This paper studies the different mining methods by analyzing the longwall panel layout and AG distribution in damage coal seams. Theoretical analysis and field observation were conducted to determine the overburden movement when the face was advancing under the AG. The pillar between face and parallel AG changes from elastic to plastic and eventually to the residual supporting status. All these three status was combined with the roof structure to establish the theoretical model to calculate the shield support capacity. Numerical modeling was employed to simulate the pillar stability and determine the abutment pressure distribution as the face inclined to the AG during longwall mining.

2. Background

There are two panels E13103 and E13105 located in Cuijiazhai Coal Mine in north-central China. Coal seam is 306–320 m deep. The average mining height is 4 m. The dip angle of coal seam is 5°. The panel length is 1086.5 m and panel width is 110 m in E13103. And in panel E13105, the panel length is 769 m and panel width is 115 m. Panel layout is shown in Fig. 1. The AG distribution is very irregular.

3. Methods of mining through AG

There are cross AG parallel and perpendicular to the faceline. The stress equilibrium conditions are destroyed due to the

* Corresponding author.
E-mail address: kobe8leon@163.com (Y. Li).

http://dx.doi.org/10.1016/j.ijmst.2016.11.004
2095-2686/

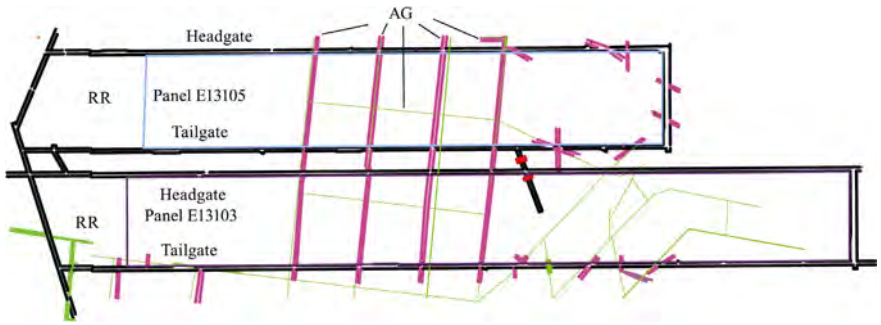

Fig. 1. Panel layout for E13103 and E13105.

presence of AG. Based on the different types of AG in panel E13105 and E13103, there are different methods to pass.

3.1. Mining through AG which is perpendicular to faceline

As for the AG perpendicular to the faceline, there are 3–4 shields located in the AG all the way to the panel stop line. During mining, those shields should be located 0.6–1.2 m, or two shearer's cuts, ahead of the remaining shields in the face. This mining method can efficiently control the roof fall in the AG. Besides, other auxiliary methods are also performed: the grouted resin bolt are installed in the face around the AG. Solid-wood planks (3000 mm × 220 mm × 180 mm) are inserted into the interface between shield canopy and roof to control the broken roof (Fig. 2).

3.2. Mining through AG which is parallel to faceline

The inclined faceline method is employed when mining through AGs that are parallel to the faceline. The angle to the faceline can reduce the exposure area of AG at any time. Meanwhile, according to the geological condition, the face advancing rate increases as much as possible so that the face can pass the AG as soon as possible.

This method is usually conducted by making the head end of the face ahead of the tail end. The procedure for inclined face mining is shown in Fig. 3. It consists of the following seven steps. In step 1 (Fig. 3a), the face starts to incline when the face is about 30 m to the parallel AG. The shearer cuts a full web head-to-tail. In step 2 (Fig. 3b), in the return trip, when the shearer cuts back to the head end, about 15 shields in the tail end are not advanced. In step 3 (Fig. 3c), cutting continues to the head end and shields keep pushing the conveyor forward. Cutting stops after the shearer travels to the spot where the conveyor is not pushed forward in previous cut. Repeat the step 2 and 3 until the head end is 13–15 m ahead of the tail end. As soon as the face becomes inclined, normal face cutting sequence resumes and the face advances until it has passed through the AG. Thereafter, the face is straightened back from the tail to the head and keeps advancing forward.

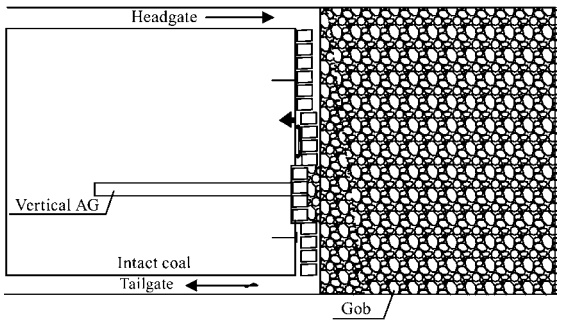

Fig. 2. Mining through Mining through a vertical AG.

4. Overburden movement

4.1. Theoretical analysis

Theoretical analysis is necessary to explain how the overlying strata move [4,5]. It is also the way to prove the accuracy of the results from measurement and numerical model.

There are two theories used to analyze the overburden strata movement: (1) loading capacity, and (2) failure interval.

4.1.1. Determination the hard-thick strata

When a longwall panel with sufficient width and length is excavated, the overburden roof strata are disturbed in order of severity from the immediate roof toward the surface [6,7]. The hard-thick strata in the overburden play an important role in controlling the movement. How to identify these hard-thick strata is the first priority to study overburden movement in longwall mining. Table 1 is the stratigraphic sequence for the panel area.

Based on composite beam theory, layer-1 is assumed as the first hard-thick strata. The strata between layer-1 and layer-m deform uniformly with layer-1. But layer-$m+1$ is not influenced by the movement of layer-1. Therefore, layer-$m+1$ is determined as the second hard-thick strata. Due to the coordinate deformation of the strata from layer-1 to layer-m, the curvature of each layer is the same, so these strata can be simplified as a composite beam. The vertical load on the first hard-thick strata can be expressed as:

$$q_1(x)|_m = \frac{E_1 h_1^3 \sum_{i=1}^{m} \gamma_i h_i}{\sum_{i=1}^{m} E_i h_i^3} \tag{1}$$

where $q_1(x)|_m$ = the loading capacity of the first hard-thick layer which is loaded by overlying strata; E the elastic Modulus; h_i the layer thickness; and γ the weight per unit volume of the layer.

Since layer-$(m+1)$ is the second hard-thick strata, and its deformation is less than that of the lower strata layer-1 to m. So the vertical load on layer r-$(m+1)$ cannot be transmitted to the lower strata, Thus:

$$q_1(x)|_{m+1} < q_1(x)|_m \tag{2}$$

Substituting Eqs. (1) into (2),

$$\gamma_{m+1} \sum_{i=1}^{m} E_i h_i^3 < E_{m+1} h_{m+1}^2 \sum_{i=1}^{m} h_i \gamma_i \tag{3}$$

Therefore, Eq. (3) is used to determine the location of hard-thick strata. In practice, the strata would be computed one by one from the first layer above the coal seam. While the Eq. (3) is satisfied, the computation stops and the hard-thick layer should be the $m+1$.

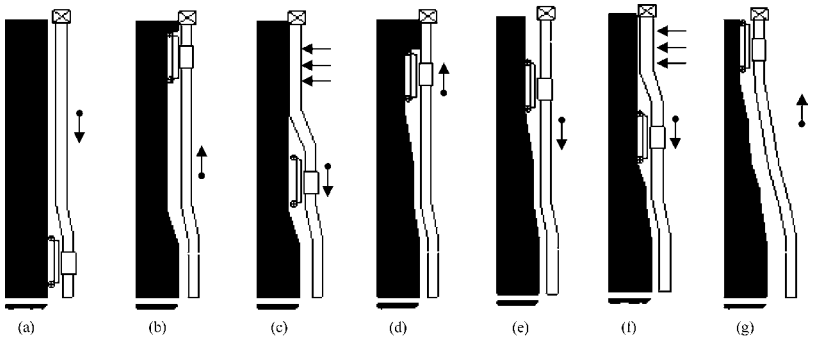

Fig. 3. Shearer's cutting steps when the inclined face is employed.

Table 1
Synthesis column map and strata mechanical parameters of panel E13105.

Serial number	Strata	Thickness (m)	Volume force (kN/m^3)	Tensile strength (MPa)	Elastic modulus (GPa)
Y31	Loess	44.00	13.8	0.10	0.010
Y30	Pebble	10.80	26.2	0.10	0.020
Y29	Fine sand	3.60	25.4	10.00	2.700
Y28	Egg gravel	8.30	26.1	0.10	0.020
Y27	Clay	21.60	17.3		0.008
Y26	Gravel bearing Sandstone	13.70	28.2	6.40	12.200
Y25	Claystone	42.89	24.1	2.10	10.900
Y24	Conglomerate	3.18	24.8	4.30	28.400
Y23	Silty claystone	7.84	25.7	3.20	4.600
Y22	Fine sand conglomerate	1.00	25.9	4.30	28.600
Y21	Claystone	9.34	24.1	2.10	10.900
Y20	Silty claystone	21.68	25.7	3.20	4.600
Y19	Siltstone	12.47	25.2	4.52	23.200
Y18	Silty claystone	6.94	25.7	3.20	4.600
Y17	Fine sandstone	4.50	27.5	8.64	35.900
Y16	Siltstone	1.34	25.2	4.52	23.200
Y15	Claystone	3.20	24.1	2.10	10.900
Y14	#6 coal seam	1.45	13.0	0.01	0.400
Y13	Siltstone	10.01	25.2	4.52	23.200
Y12	Fine sand conglomerate	19.44	25.9	8.20	28.600
Y11	#5 coal seam	5.68	13.0	0.01	0.400
Y10	Siltstone	6.79	25.2	4.52	23.200
Y9	Silty claystone	17.17	25.7	3.20	4.600
Y8	Fine sand conglomerate	8.62	25.9	4.30	28.600
Y7	Siltstone	12.94	25.2	4.52	23.200
Y6	Fine sandstone	6.95	27.5	8.64	35.900
Y5	Claystone	6.85	24.1	2.10	10.900
Y4	Fine sandstone	2.99	27.5	8.64	35.900
Y3	Siltstone	10.07	25.2	4.52	23.200
Y2	Fine sandstone	1.20	27.5	8.64	35.900
Y1	Siltstone	10.53	25.2	4.52	23.200
Y0	#1 coal seam	4.60	13.0	0.01	0.4000
Y-1	Claystone	1.90	24.1	2.10	10.900
Y-2	Oolitic clay rock	13.16	22.5	1.90	10.200

Next, the upper strata are computed one by one from the first layer above the layer $m+1$. So, all the hard-thick strata could be determined in the same way until the last hard-thick is identified.

4.1.2. Failure interval of the hard-thick strata

The failure of hard-thick strata can be treated as a plate failure in the theory of elasticity. To simplify the computation, the clamped beam theory is used to calculate the failure interval of hard-thick strata. The failure interval L_k of hard-thick strata layer-k could be expressed as:

$$L_k = h_k\sqrt{\frac{2\sigma_k}{q_k}} \tag{4}$$

where h_k is the thickness of layer-k; σ_k the tensile strength; and q_k the vertical load on layer-k.

4.1.3. Comparison with failure interval of hard-thick strata

According to the following principles, the failure intervals of hard-thick layer are compared with each other to determine the key strata.

(a) If layer-k is the key stratum, it should be one hard-thick layer and its failure interval should be smaller than the other hard-thick strata interval above it. The criterion is

$$L_k < L_{k+1} \tag{5}$$

(b) If the failure interval L_k is greater than that of hard-thick layer $(k+1)$, the vertical load on layer$(k+1)$ should be added to that of layer-k and the failure interval L_k needs to be calculated again with new vertical load.

Table 2
Key strata in overburden.

Serial number	Lithology	Thickness (m)	Broken interval (m)	Key strata	Distance from the coal seam (m)
Y12	Fine sand conglomerate	19.44	56.50	Key strata	79.26
Y6	Fine sandstone	6.95	62.93	Sub-key strata II	21.11
Y1	Sandstone	10.53	68.01	Sub-key strata I	0

(c) Repeating the steps 1 and 2, all hard-thick strata from bottom up are identified one by one.

Based on the criterion, the three key strata in the overburden are shown in Table 2. They are layer-1 silty sandstone, layer-6 fine sandstone and layer-12 fine sand conglomerate.

4.2. Fracture zone development

4.2.1. Gap height under the unbroken strata

When the coal seam is excavated, the roof breaks and falls as soon as it is undermined. As it falls, its volume increases. There will be a gap left between the waste rock and the sagged and uncaved stratum. Due to the expansion of broken strata, the gap continues to decrease as the caving propagates upward. Meanwhile, the broken rock would be compacted layer by layer, so the residual expansion ratio is employed to calculate the volume of broken stratum. Generally, the strata are considered to expand only in caving zone and fracture zone. Therefore, the gap height of each rock stratum could be expressed as:

$$\Delta_i = M - \sum_{j=1}^{i-1} h_j(k_j - 1) \tag{6}$$

where Δ_i is the gap height of layer-i; M the mining height; h_j the thickness of layer j; and k_j the residual expansion ratio of layer j.

4.2.2. Relations between gap height and strata failure

Strata can only fail when there is a gap below.

Generally, hard-thick strata (especially the key strata) hardly bend. Therefore, if there is gap below the hard-thick strata, the strata are broken into blocks by fractures and horizontal cracks. As for soft strata, due to the bending characteristic, they may only have a plastic deformation instead of break. Whether the soft strata is plastically deformed or is broken into blocks is determined by comparing the gap and maximum allowable sagging.

As the panel advances, the maximum allowable sagging of rock strata is

$$\omega_{\max} = \frac{5ql^4}{384EI} \tag{7}$$

If the maximum allowable sagging of soft strata is larger than the gap height (see Eq. (8)), the soft strata would keep the plastic state instead of failure. And the development of fracture zone stops here.

$$\omega_{i,\max} > M - \sum_{j=1}^{i-1} h_j(k_j - 1) \tag{8}$$

Conversely, the soft strata would break if its maximum allowable sagging is smaller than the gap height (see Eq. (9)).

$$\omega_{i,\max} < M - \sum_{j=1}^{i-1} h_j(k_j - 1) \tag{9}$$

Determination of the height of fracture zone follows the four criteria:

(a) For the key strata, the fracture zone would not develop if the free length between both ends is smaller than the failure interval.
(b) For the key strata, when the free length between two ends of stratum is larger than the failure interval, the fracture zone would not develop if there is no gap or separation below. Otherwise, the fracture zone would develop upward.
(c) For the soft strata, the fracture zone would not develop if the horizontal tensile strain of soft strata is smaller than its maximum allowable horizontal tensile strain.
(d) For the soft strata, when the horizontal tensile strain is larger than its maximum allowable horizontal tensile strain, the fracture zone would not develop if the maximum allowable sagging is larger than the gap height below, otherwise, the fracture zone would develop upward.

As shown in the failure interval determined previously (Table 2), the sub-key strata I broke when the face advance distance was 50.59 m. The overlying strata controlled by the sub-key strata I broke immediately afterward and the height of fracture zone increased to 31.64 m. The sub-key strata II broke when the face advance distance was 62.93 m and the key strata broke when the face advance distance was 68.01 m. When the fracture zone developed to layer 15 (clay), maximum allowable sagging of this stratum was larger than gap height below. The fracture zone stopped its development which means the fracture zone has reached 123.89 m above coal seam eventually (Fig. 4).

4.3. Periodic weighting pressure analysis

The mine pressure observation point was set up at shield 45 at the panel center and the corresponding theoretical analysis was performed. The relationship between support working resistance and panel advancing length is shown in Fig. 5.

Pressure measurement started when the face had advanced to 250 m. As shown in Fig 5, the face was in the state of weighting period and maximum support resistance was 4640 kN. When the face had advanced to 262 m, the face was in another weighting period. As the face advanced, the weighting showed up periodically and the support resistance changed between 3500 and 4600 kN.

The maximum support resistance occurred when AG was 5 and 15 m outby the face. But when the face was right in the AG, the support resistance was the minimum in the mining cycle. Periodic weighting interval is 8.54 m.

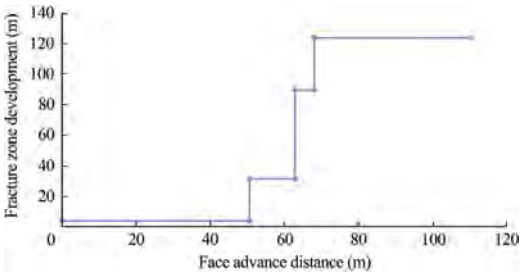

Fig. 4. Fracture zone development.

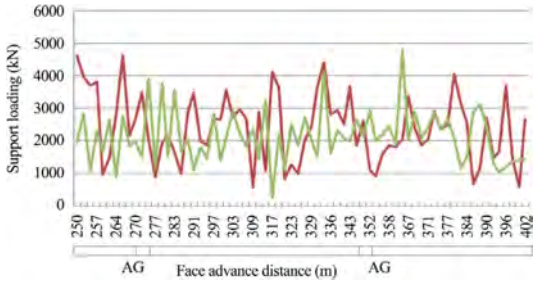

Fig. 5. Measured shield loading.

4.4. Main roof behavior and shields design

4.4.1. Main roof behavior when the face is passing through parallel AG

When passing through a parallel AG, the pillar between the face and AG becomes thinner and smaller as the face keeps moving forward. The main roof caves in different forms as the face advances [8]. According to the support loading measurement, the maximum support resistance occurred when AG was 5 and 15 m outby the face. But no weighting occurred when the face was right in the AG. Therefore, there are four types of roof structures in terms of roof caving sequence when the face is passing through the parallel AG.

(a) Phase 1: elastic pillar with multiple supports to the broken main roof model

Before the face approaches the AG, the condition is just like retreat mining of pillar. When the distance between the face and AG is long enough, the pillar is in elastic state and stable to support the roof. The roof weighting is the same as the normal weighting in longwall panel mining without AG. The main roof caves periodically right after the face advances. It is supported by shields, intact coal and the waste rock in gob. The main roof behavior at this phase is shown in Fig. 6a. According to the theoretical analysis of two force-transmitting blocks in main roof, the equation for supporting capacity in this phase is shown below.

$$P_T = F_T + G_T = \frac{G_B L_B \cos\alpha}{2L_1} + \frac{L_B \cos\alpha G_A f}{2L_1(f+\tan\alpha)} + \frac{L_B G_A \sin\alpha}{2L_1(f+\tan\alpha)} - \frac{h_m^2[\sigma_x]}{6L_1} - \frac{F_N L_2}{L_1} + \gamma_{im} h_{im} L_S \quad (10)$$

where P_T is the supporting capacity of the shield; F_T the supporting strength from shield to block B; G_T the weight of immediate roof; G_B the weight of block B; L_B the length of block B; α the angle between block A and the horizontal; h_{im} the thickness of immediate roof; γ_{im} the weight per unit volume of immediate roof; f the friction coefficient; L_S the average length of the immediate roof on the shield; L_1 the average overhanged length of the immediate roof; and L_2 the horizontal distance between the faceline and the point of main roof caving in the gob.

(b) Phase 2: point-supports of broken main roof model

When the face moves to the location where the main roof caves, the intact coal no longer supports the broken main roof. At that time the main roof is supported at two location: shield at the face and the waste rock in gob. Its behavior in this phase is shown in Fig. 6b. Eq. (11) for supporting capacity determination in this phase is shown below.

$$P_T = F_T + G_T = \frac{G_B L_B \cos\alpha}{2L_1} + \frac{L_B \cos\alpha G_A f}{2L_1(f+\tan\alpha)} + \frac{L_B G_A \sin\alpha}{2L_1(f+\tan\alpha)} + \gamma_{im} h_{im} L_S \quad (11)$$

where G_A is the weight of block A.

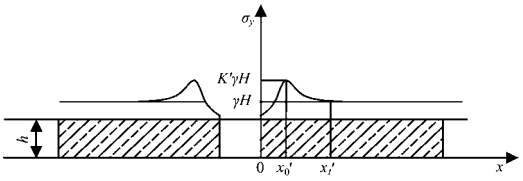

Fig. 7. Abutment pressure distribution aside the AG.

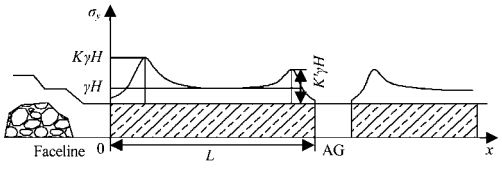

Fig. 8. Abutment pressure distribution for the distance is greater than 46.6 m between the face and AG.

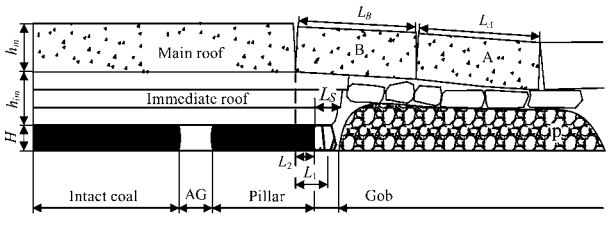

(a) Phase 1: elastic pillar with multiple supports to the broken main roof

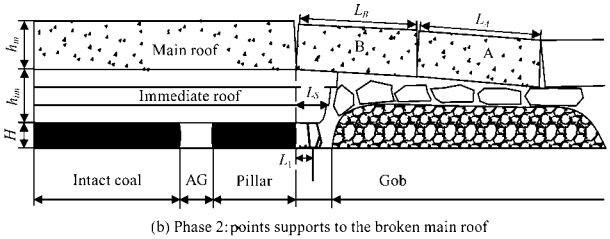

(b) Phase 2: points supports to the broken main roof

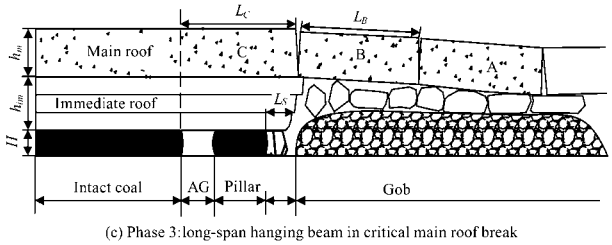

(c) Phase 3: long-span hanging beam in critical main roof break

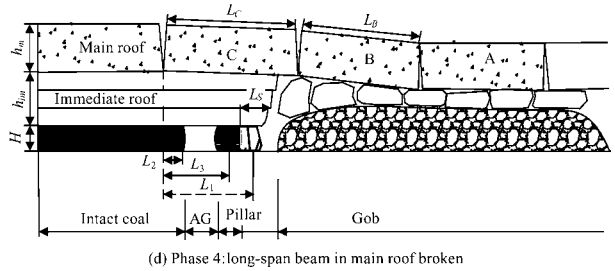

(d) Phase 4: long-span beam in main roof broken

Fig. 6. Main roof behavior of face passing the parallel AG.

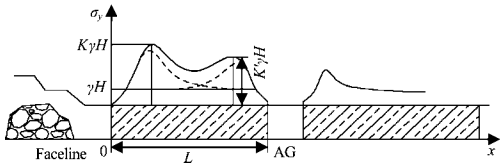

Fig. 9. Abutment pressure distribution for the distance is smaller than 46.6 m between the face and AG.

(c) Phase 3: long-span overhanging beam of pre-failure main roof model

As the face keeps advancing, the pillar between the face and AG becomes thinner and smaller. The vertical loading has exceeded the pillar strength and makes the pillar unstable. So the pillar loses its support to the roof. There is a long-span overhanging beam over the AG in the main roof. The rear end of the beam is located above the shield support and the immediate roof. The front end is in pre-failure state. Therefore it is so called long-span overhanging beam. Its behavior in this phase is shown in Fig. 6c. Eq. (12) for supporting capacity determination in this phase is shown below.

$$P_T = \frac{G_B f}{2(f + \tan\alpha)} + G_C - F_M - F_N + \gamma_{im} h_{im} L_S \tag{12}$$

(d) Phase 4: long-span multiple support main roof failure model

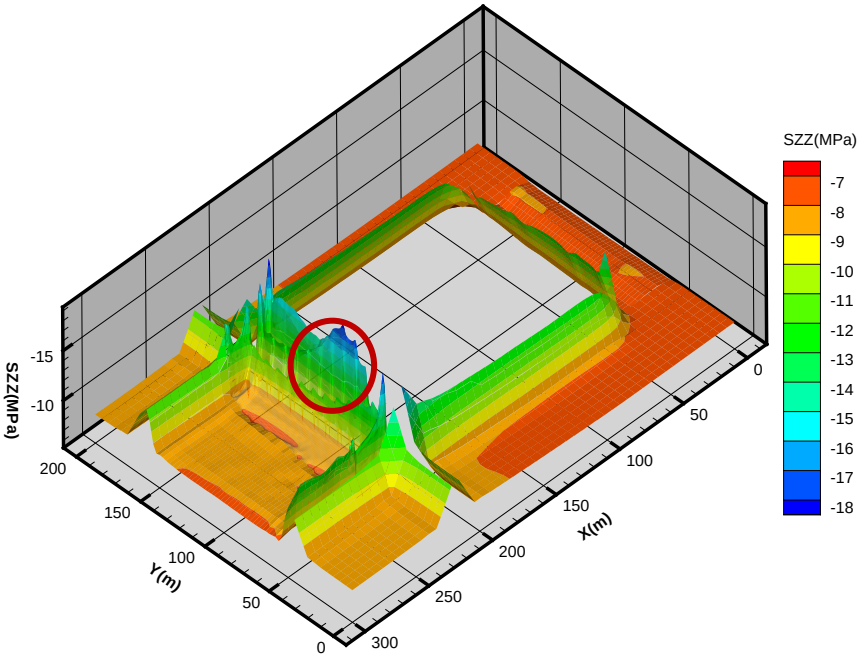

(a) Face starts to expose the AG

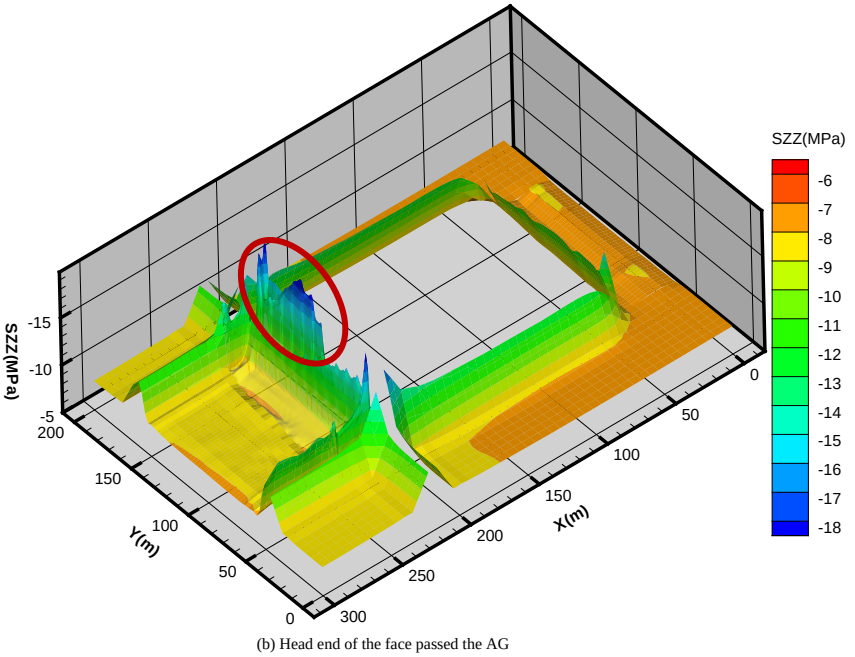

(b) Head end of the face passed the AG

Fig. 10. Abutment pressure distribution of face inclined.

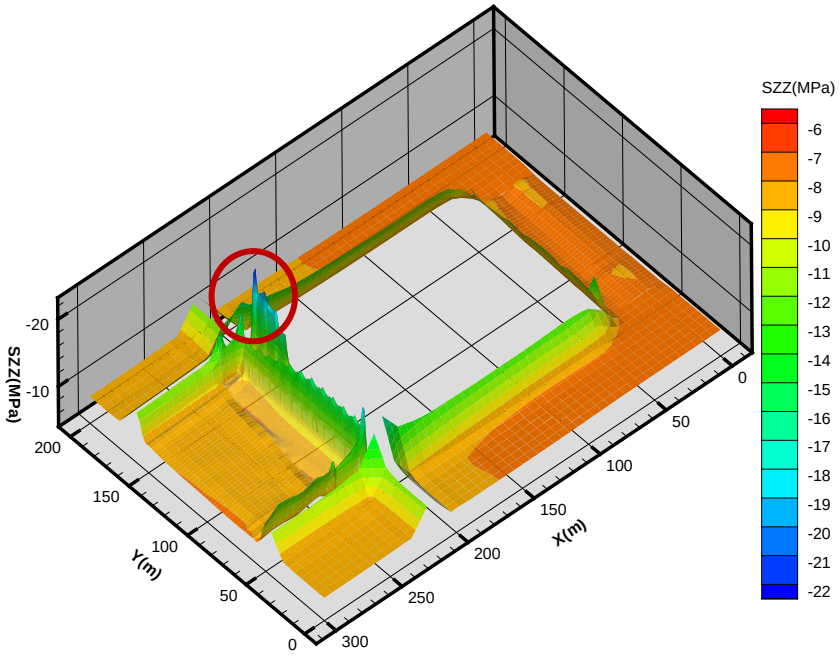

(c) Tail end of the face exposed the AG

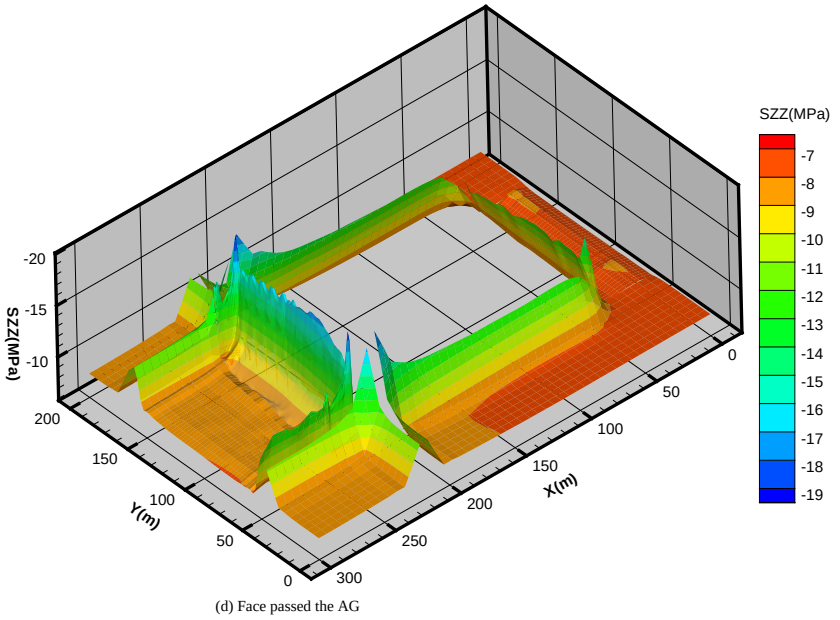

(d) Face passed the AG

Fig. 10 (*continued*)

The front end of long-span beam is broken in phase 4 as the face keeps advancing. The pillar is in unstable state and the main roof breaks into a long beam over both the AG and pillar. This long-span beam is supported by the shields, intact coal, pillar with residual strength and the waste rock in gob. Its behavior in this phase is shown in Fig. 6d. The equation for supporting capacity determination in this phase is shown below.

$$P_T = F_T + G_T$$
$$= \frac{G_B L_B \cos\alpha}{2L_1} + \frac{L_B \cos\alpha G_A f}{2L_1(f+\tan\alpha)} + \frac{L_B G_A \sin\alpha}{2L_1(f+\tan\alpha)} - \frac{h_m^2[\sigma_x]}{6L_1} - \frac{F_N L_2}{L_1} - \frac{F_M L_3}{L_1} + \gamma_{im} h_{im} L_S \quad (13)$$

4.4.2. Determination of support capacity and shield design

According to the measurement of support loading in two shields in panel E13105, the maximum support resistance occurred when AG was 5 and 15 m outby the face. Based on the analysis of main roof behavior, the roof was in phase 1 and phase 2 when AG was 15 m outby the face. And the main roof was in state of phase 3 and phase 4 when AG was 5 m outby the face.

In phase 1 and phase 2, the support resistances calculated by Eqs. (10) and (11) are 3000 and 5300 kN, respectively. The measured shield loads are between 4600 and 4800 kN when AG was 15 m outby the face. Therefore, this main roof weighting occurred in phase 2.

In phase 3 and phase 4, the support resistances calculated by Eqs. (12) and (13) are 1150 and 4120 kN, respectively. The mea-

sured shield loads are more than 4000 kN when AG was 5 m outby the face. Therefore, this main roof weighting occurred in phase 4.

4.5. Abutment pressure

4.5.1. Theoretical analysis

When there is no abandoned gateroad (AG) in front of the faceline, the front abutment pressure extended 38.5 m outby the face. The peak front abutment pressure is 5.6 m outby the face. So there is no abutment influence in the AG when the face is 38.5 m away. However, stress distribution is readjusted due to the presence of the AG. Since the AG was abandoned year ago, its support system has been reduced considerably. The abutment pressure is lowered as the influence zone of AG expands. Fig. 7 shows the abutment pressure distribution induced by AG.

Using the theoretical analysis and field test, $x_0' = 2.5$ m is the yield zone width, and $x_t' = 8.1$ m is the abutment influence distance.

Consequently, when AG is $L > x_t + x_t' = 46.6$ m outby the face, there is no abutment influence for both face and AG. Fig. 8 shows the abutment pressure distribution when the distance between the face and AG is >46.6 m.

When AG is $L < x_t + x_t' = 46.6$ m outby the face, the abutments induced by the face and AG intersect and superimpose on each other.

When AG is $L < x_0 + x_0' = 8.1$ m outby the face, the pillars between face and AG is all in the yield zone. So the pillars yield or fail. The abutment pressure generally transfers to the other side of the AG. The peak abutment pressure increases as the pillar size decreases. The influence range expands (Fig. 9).

4.5.2. Abutment pressure distribution of inclined face

Fig. 10a–d shows the vertical stress distribution from a three-dimensional model when the face is passing through the AG. During mining, the headgate T-Junction is moving 13 m more than that of tailgate T-Junction so that the faceline is inclined to the AG. It avoids the entire face moving simultaneously toward the AG such that the front abutment pressure is superimposed.

The inclined faceline makes the stress concentration occur earlier at the headgate T-Junction side of the pillar. Therefore, the front abutment pressure at the headgate side is larger than the tailgate side. The pillar at the headgate side yields and fails first (Fig. 10a). The pillar is in triangle shape in the inclined face. The stress concentration occurs all the pillar when the headgate intersect the AG first. As the inclined face keeps moving, the pillar becomes smaller. The front abutment pressure is divided into two parts. One is in the intact coal outby the face and the other one is in the triangular pillar. They both are subjected to the abutment pressure until the pillar is mined out (Fig. 10b). After passing AG, the stress concentration transfers to the intact coal outby the face as the front abutment pressure (Fig. 10c). The whole of passing is over and the faceline returns to be vertical to the gateroads (Fig. 10d).

5. Conclusions

(1) Different methods for passing through the AG. For vertical AG, 3–4 shields inside the AG are pulled forward for 0.6–1.2 m or two cuts ahead of all shields and advance through the whole length of the vertical AG. The inclined faceline method is employed for passing through parallel AG.
(2) There are three key strata controlling the overburden movement. The fracture zone development reached 123.89 m above coal seam eventually.
(3) When passing through an AG, the maximum support resistance occurred when AG was 5 and 15 m outby the face. The support resistance was minimum when the face was right in the AG.
(4) When passing through a parallel AG, the main roof caves in 4 phases. Main roof weighting occurs in phase 2 and phase 4.

Acknowledgments

The paper is supported by the National Natural Science Foundation of China (Nos. 51404275 and U1361209), and the Fundamental Research Funds for the Central Universities of China (2013QZ03).

References

[1] Wang JC. The theory and technique on the thick coal seam mining. Metallurgical Industry Press; 2009. p. 147–55.
[2] Jia G, Gong PL. Surround strata stability of face passing through the abandoned gateroads. ShanXin Coal 2015;04. p. 32–35+43.
[3] Xie SR, Li SJ, Wei Z, Sun YJ, Zhang GZ, Song BH, et al. Stability control of support-surrounding rock system during fully mechanized caving face crossing abandoned roadway period. J China Coal Soc 2015;40(3):502–8.
[4] Li Y. Overburden movement in solid waste rock cemented backfill mining methods. J China Coal Soc 2011;36(S1):370–4.
[5] Li Y. Groundwater system for the periods of pre- and post-longwall mining over thin overburden. Int J Min Reclam Environ 2016;30(4):295–311.
[6] Peng SS. Longwall mining, 2nd ed. Morgantown (WV); 2006. p. 46–55.
[7] Peng SS. Coal mine ground control, 3rd ed. Morgantown (WV); 2008. p. 319–30.
[8] Wang JC, Yang SL, Li Y, Wang ZH. A dynamic method to determine the supports capacity in longwall coal mine. Int J Min Reclam Environ 2015;29(4):277–88.

International Journal of Mining Science and Technology 27 (2017) 153–158

Contents lists available at ScienceDirect

International Journal of Mining Science and Technology

journal homepage: www.elsevier.com/locate/ijmst

Quantification of ventilation enhancement using the Eye CAN roof support

Shook Michael T. [a,*], Sindelar Mark F. [b], Jiang Hua [b], Luo Yi [b]

[a] Burrell Mining Products, Inc., New Kensington, PA 15068, USA
[b] Department of Mining Engineering, West Virginia University, Morgantown, WV 26506, USA

ARTICLE INFO

Article history:
Received 6 June 2016
Received in revised form 1 September 2016
Accepted 18 October 2016
Available online 7 December 2016

Keywords:
Standing roof support
CAN
Ventilation
Load-displacement
Eye CAN

ABSTRACT

Convergence of roof and floor in underground mine openings is a common occurrence. This convergence not only adversely affects the ability of workers, equipment and supplies to travel through the mine, it also reduces the effectiveness of the mine ventilation system, which is essential for the dilution of methane gas and airborne respirable dust. While installing secondary standing supports to control floor and roof convergence, such supports, by nature, partially obstruct a portion of the airway. These added obstructions inhibit the ability of the ventilation system to operate as efficiently as it could by increasing the resistance in and reducing the cross-sectional area of the airway. This study introduces and demonstrates the benefits of The Eye CAN™ standing roof support, which controls floor and roof convergence and is less obstructive to air flow than conventional wooden cribs. Laboratory findings show that the normal resistance of a supported lined airway is reduced by using this new product from Burrell Mining Products, Inc., while providing the same roof support characteristics of an established product—The CAN®. Load vs. displacement curves generated from laboratory tests demonstrated that this new product behaves with the same roof support characteristics as others in The CAN product family. Ventilation data gathered from a simulated mine entry was then used for computational fluid dynamics (CFD) modeling. The CFD analysis showed an improvement with The Eye CAN vs. other accepted forms of standing roof support. This proof-of-concept study suggests that, when using this new product made by Burrell Mining Products, Inc., not only will the convergence from the roof and floor be controlled, but airway resistance will also be reduced.

1. Introduction

One of the basic elements of underground mining is the necessity to support the mine roof. It is well-known that easier reserves have been mined so that today's underground mines present challenging conditions. Factors influencing roof support decisions include mine depth, mining method, overburden composition, and agency regulations. Mining engineers, therefore, have to balance three objectives: safety, engineering, and cost.

While safety is obviously paramount, and engineering often complements safety, the cost effectiveness of any product, method, or device warrants additional consideration in today's harsh business climate. Avenues for adaptation and improvement are found at the intersection of the three objectives.

Burrell Mining Products, Inc., developed The CAN® cribbing system of standing roof support two decades ago in the shadow of the Valley Camp Mine located in New Kensington, Pennsylvania. When Valley Camp opened in 1910, it relied on timbering for roof support. This historical reference to a room and pillar drift mine in a 1.82 m seam is important since it illustrates the early origins of the evolution in standing roof support and recognizes that one of the most basic forms, wooden cribs, is still in use after a century.

Mining engineers of the Valley Camp era could not visualize four-mile longwall panels with extensive bleeder entries, their associated ventilation plans and, therefore, their critical roof support requirements. Nor could they have anticipated the ever-expanding regulatory requirements that today include roof control and ventilation plans, as applied to longwall coal mining. To address ground control issues, a number of primary strategies are employed for standing roof support in longwall bleeder entries, including wooden cribs, pumpable cribs, and The CAN cribbing system.

Since its introduction, The CAN, manufactured exclusively by Burrell Mining Products, Inc., has been a popular choice for roof support, especially in challenging areas of underground coal mines

* Corresponding author. Tel.: +1 724 339 2511.
E-mail address: mshook@burrellinc.com (M.T. Shook).

http://dx.doi.org/10.1016/j.ijmst.2016.11.011
2095-2686/

where convergence is very pronounced, as in bleeder entries. Convergence, however, not only affects roof support but also restricts ventilation both by reducing the cross-sectional area of the entry and by introducing non-uniformities, such as rib sloughage, that change the air flow dynamics.

Recent directives from the Mine Safety and Health Administration (MSHA) amplify the necessity to maintain open access and sufficient air flow in bleeder entries. Since standing roof support intrinsically obstructs a portion of the cross-section of any entry where it is installed, reducing the impact on ventilation from the standing roof support furthers the objective of improving ventilation while maintaining support for the roof.

Burrell Mining Products, Inc., has added a new member to The CAN product family—The Eye CAN. This paper describes the motivation for developing The Eye CAN (patent pending), examines how this new product has been evaluated as a standing roof support, and introduces initial findings of the current study to evaluate its efficacy as a less-obstructive component to the ventilation system.

2. Background

The CAN is recognized as the most stable of the deformable concrete supports and "remains the dominant form of tailgate support," particularly in mines of the Western United States [1,2]. As such, it is a prime candidate for enhancements that would allow it to be more transparent to air flow while still maintaining the same roof support capabilities for which it has earned its reputation.

All products of The CAN family, including The Eye CAN, consist of a thin cylindrical steel shell filled with aerated concrete. As part of a standing roof support system, The CAN is placed axially in a mine entry, and the space between the top of The CAN and the mine roof is packed with wood timbers [3]. Fig. 1 depicts a typical installation.

Establishing full contact between the roof and the top of the support is necessary to obtain full benefit from the support system [4]. Barczak and Tadolini have shown the stiffness of the system with the following equation [2]:

$$K_{system} = \frac{K_{crib}K_{CAN}}{K_{crib} + K_{CAN}} \quad (1)$$

where K is the stiffness in kips/in. A study by Gearhart and Batchler investigated a number of relevant parameters that affect performance of The CAN, including the species of wood. With varying K_{crib}, the same researchers investigated multiple layers of cribbing, as well as the errant procedure of not completely filling the interface between The CAN and mine roof with cribbing [5]. They found decreased performance in terms of stiffness for both scenarios. Using a single layer of closely packed and appropriate timbers is one of the recommended installation guidelines [4].

Thus, when properly installed, The CAN has never failed as a standing roof support and over one million have been installed worldwide. Published reports of possible "drawbacks" for using The CAN list only simple errors that happen during improper installation [4–6]. The product itself has not been criticized. It is capable of withstanding in excess of 50.8 cm of vertical convergence while simultaneously accommodating 38.9 cm of displacement in the horizontal direction [5]. As The CAN takes load, it exhibits elastic behavior with a steep load-displacement curve dependent on the stiffness of Eq. (1). The support then yields longitudinally at a load amplitude that is a function of The CAN diameter. Larger diameters are positively correlated to more load-bearing capacity, as shown in the chart of Fig. 2. Conversely, while pumpable cribs may initially exhibit a high stiffness, significant load shedding occurs so that post-failure capacity is commensurate with that of wood cribs [1]. Wood cribs, then, become the baseline for comparison.

This elastic-plastic behavior and the characteristic curve define what constitutes The CAN roof support system. Since its introduction, over 130 tests have been performed by the NIOSH Mine Roof Simulator (MRS) in Pittsburgh, Pennsylvania [5]. The performance characteristics of The CAN are well established, and mines using The CAN for standing roof support rely on a standard of performance defined by this load-displacement curve so that any new The CAN product must meet these requirements. Note that tests were conducted by independent laboratories using imperial units to remain consistent with historical test data for The CAN product line, such as the curve shown in Fig. 2.

If The CAN provides excellent roof support, then why would anyone want to modify it? Consider next the motivation for an enhanced standing roof support. At the end of 2013, MSHA issued Program Policy Letter (PPL) No. P13-V-12, "to provide consistency in the application of the standards with regard to travel, examination, evaluation, and means for determining the effectiveness of bleeder systems" [7]. The guidance provided therein was in response not only to the noted explosion at the Upper Big Branch Mine in April, 2010, but also to increasing numbers of both ignitions/explosions and imminent danger orders resulting from conditions in longwall bleeder systems. A primary concern mentioned in the PPL was safe access to the bleeder entries for both inspection and evaluation. While the accumulation of water is a separate issue outside the scope of this paper, the occurrence of roof falls is germane. Roof falls and convergence both contribute to reductions in cross-sectional area, which negatively affects ventilation and can also create obstructions to travel for personnel.

Since the use of standing roof supports inevitably obstructs some of the cross-sectional area in the locations where the supports are placed, the objective would be to somehow allow more

Fig. 1. Installed The CAN® roof supports in mine entry, 0.46 m diameter.

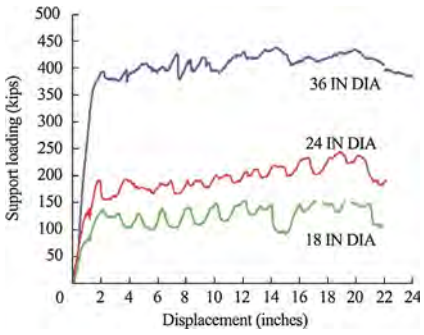

Fig. 2. Load-displacement curves for 45.72, 60.96, and 91.44 cm diameter The CANS® (Note: 1 kip = 0.453 metric ton; 1 in. = 2.54 cm).

of the ventilation air to flow around or through the support. This concept led to development of The Eye CAN.

3. The Eye CAN

The Eye CAN is manufactured with apertures located axially through the shell so that, when the centerline of the apertures is placed in alignment with an air flow, such as in a bleeder entry, the air can flow through the "eye," thereby reducing overall restriction in the entry. A 55.88 cm diameter Eye CAN is shown in Fig. 3, with appropriate top capping with wood cribs.

For example, in a 4.88 m wide entry with a 2.13 m mining height, the use of two The CAN supports measuring 55.88 cm in diameter would obstruct 22.92% of the cross-section, whereas two The Eye CAN supports with two 15.24 cm diameter apertures would only obstruct 22.57% of the cross-section, resulting in an improvement to cross-sectional area of 0.35%. Assuming 0.31 m of convergence, The Eye CAN then returns 0.41% of the cross sectional area. It should be noted that these cross-sectional area calculations are made at the full diameter of The Eye CAN. While each The CAN is set in compliance with the roof control plan of the mine, a double row on 238.76 cm centers is representative, whereas 198.12 cm centers would be required for wooden cribs so that the contribution of the "eye" is understated when considering solely cross-section.

The geometry of The CAN presents a number of advantages for ventilation. Considering the cross-sectional area of an entry at the location of the roof support, The CAN provides less obstruction than other types of roof support, such as four-point cribs. Furthermore, the round steel exterior provides a smooth surface that promotes air flow around The CAN, whereas four-point cribs are known for creating turbulence. Thus, to demonstrate effectiveness, The Eye CAN must demonstrate the same roof support capabilities and standards of previously developed supports of The CAN product family, and demonstrate a reduction in resistance to ventilation air flow better than can be obtained from only the cross-section calculations.

Burrell Mining Products, Inc., conducted some evaluations of the newly developed The Eye CAN, the classic roof support The CAN, and traditional four-point wood cribs.

4. Load-bearing evaluation

A unique feature of The CAN is how its strength increases as it bears load, while deforming along the axis of load. To confirm that The Eye CAN would perform similarly to The CAN, the load-displacement curve had to exhibit the same elastic-plastic characteristics. That is, for The CAN, as the support initially takes load, the response is elastic as it rapidly builds to yield, then becomes plastic as a strain-hardening phase occurs.

A total of 17 samples of The Eye CAN were tested: 12 at TÜV Rheinland Industrial Solutions, Inc., and 5 at the Mine Roof Simulator (MRS) at the NIOSH Pittsburgh Research Lab. Based on the results, the Research & Development (R&D) Department at Burrell Mining Products, Inc., made appropriate modifications to the design prior to each round of additional testing.

Vertical and biaxial loads were applied to a variety of The Eye CAN configurations during the research and development process. In all cases, each test employed The Eye CAN that maintained the recommended minimum aspect ratio of 5:1 [5]. A concentration of effort was placed on the popular 55.88 cm diameter, which the R & D department found to be more convenient for mines employing rail haulage than the 60.96 cm diameter.

Fig. 4 shows load-displacement curves for two different heights of the 55.88 cm diameter The Eye CAN, each with two 15.24 cm ports. This diameter, in addition to being popular, represents a conservative case for The Eye CAN support (see Fig. 2). Fig. 5 shows a comparison between The Eye CAN subjected to vertical loading and The CAN subjected to both vertical and shear loading at a ratio of 2:1.

In addition to the roof support capabilities, another important consideration in the design of The Eye CAN was the ability of the "eye" itself to remain intact (open) as long as possible as the support yields under load. Since the purpose of the eye is to allow for air flow, distortion of the eye, while maintaining as much cross-section as possible, was acceptable, as shown in Fig. 6. Obviously, as convergence of the entry would continue, in its limiting case, the eye would become closed. However, by this time, the bleeder entry would have been sealed, eliminating the need for travel by mine personnel and for ventilation.

The load-displacement curves for The Eye CAN are commensurate with that for The CAN.

5. Ventilation study

The load-bearing characteristics of The CAN versus four-point cribs are not one-to-one. Typical roof support plans per running 30.48 m of entry will use 30 four-point cribs, rated at 40 tons, versus 26 The CAN supports, rated at 80 tons. Therefore, even though the same number of four-point cribs and The CAN supports were compared for the ventilation study, this was a conservative approach since more wooden cribs would be required to achieve a similarly calculated amount of roof support. The goal of the ventilation study was to gather data about the performance of The Eye CAN, The CAN, and wood crib support systems for use in CFD. The CFD simulations have been shown to be effective in modeling ventilation phenomenon in mine entries when experimental data is used to validate the model [8].

Fig. 3. 55.88 cm diameter The Eye CAN® at NIOSH mine roof simulator (MRS).

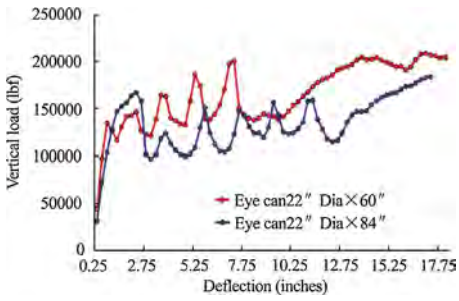

Fig. 4. Load-displacement curves for 55.88 cm The Eye CAN® support (Note: 60 in. = 152.4 cm; 84 in. = 213.36 cm; 1 lbf = 0.453 kg).

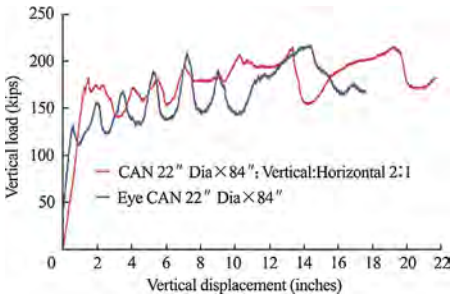

Fig. 5. Load-displacement curve comparing 22 in. (55.88 cm) diameter The CAN® and The Eye CAN (Note: 84 in. = 213.36 cm; 1 kip = 0.453 metric ton).

Fig. 6. The Eye CAN® with 45.72 cm vertical displacement (convergence), area of "eye" maintained.

A 21.34 m long simulated bleeder entry, characterized by low velocity air movement with some leakage and obstructions, was constructed at a warehouse. The sides and top of the simulated entry consisted of brattice cloth loosely fastened to wooden frames to simulate the imperfect ribs and top of a coal mine; the floor was the concrete floor of the warehouse. Fig. 7 shows the simulated entry which was 4.88 m wide and 2.13 m tall.

Exhaust ventilation was provided by a Master MAC-42-BDF shop fan. The differential pressures obtained were small and below the resolution of the manometer—an unsurprising result since obtaining these readings in working coal mines is often problematic.

Air leakage was controlled as best as could be expected given the nature of the setup. The largest concern was the seal at the fan, which had to be secured after each change in the type of roof support. Typical roof support configurations consisted of 14, 8, and 6 four-point crib sets; 14, 8, and 6 The CAN supports; and 8 and 6 The Eye CAN supports, all in parallel rows. Six configurations were arranged for the ventilation study; the remainder are for future work.

Air velocity readings were taken at three locations, 1.83, 9.14, and 18.29 m respectively, as measured from the intake end. At each location, 35 air readings were measured on a 7×5 grid, equally spaced along the width and height, respectively, with a CEM DT- 8880 hot wire anemometer. The velocity measurement range of the anemometer is from 0.10 to 25 m/s with a resolution of 0.01 m/s. Its ability to measure low air velocity is important for this study since air velocity in entries where the standing supports are used is normally low. All readings were taken by a certified mine foreman. Fig. 8 depicts The Eye CAN in the simulated entry with the measuring device used to assure consistency of location when taking readings with the hot wire anemometer. The geometries of the layouts are shown in Fig. 9.

Three pairs of data (six sets) generated for the standing roof support configurations, shown in Fig. 9, were used for CFD analysis. The first two pairs compared wood cribs to The CAN and the third pair compared The CAN to The Eye CAN.

CFD simulations were conducted with Cradle SC/Tetra 12.0 (Software Cradle Co., 2016). Three steady state simulation analysis cases were performed. Two were based on the simulated mine experiment readings. The third considered the use of The Eye CAN under the same conditions. A geometric model representing the three cases was built according to the design measurements of the full-scale simulated entry.

The geometry and associated boundary conditions are illustrated in Fig. 10. Air entering the simulation domain is depicted by an inlet with a natural inflow condition. An outlet with a negative static pressure was placed at the fan. All the other boundaries within were defined as walls. In order to model each case, eight supports were placed into the entry, seen in Fig. 10, with The Eye CAN depicted.

For the first two models, the average air velocities in the entry cross-section area were examined for the purpose of validation. After the validation process, the prediction case used the same simulation parameters to study the air flow distribution in the entry using The Eye CAN support.

Fig. 11 and Table 1 show the simulated and experimental entry cross-section velocity contours and average velocities. The CFD simulation cases agreed within ±5% of the experimental data. Therefore, a comparison between the results with the laboratory experiments indicates that the CFD model can accurately model and represent the simulated mine entry and reinforces the appropriateness of the boundary conditions.

Using the same number of The CAN supports instead of cribs, the air flow rate is higher. The effect is more pronounced when recognizing that eight The CAN supports are roughly equivalent in

Fig. 7. Simulated mine entry.

Fig. 8. The Eye CAN® (right) and "measuring stick" (left) (Note marks on floor).

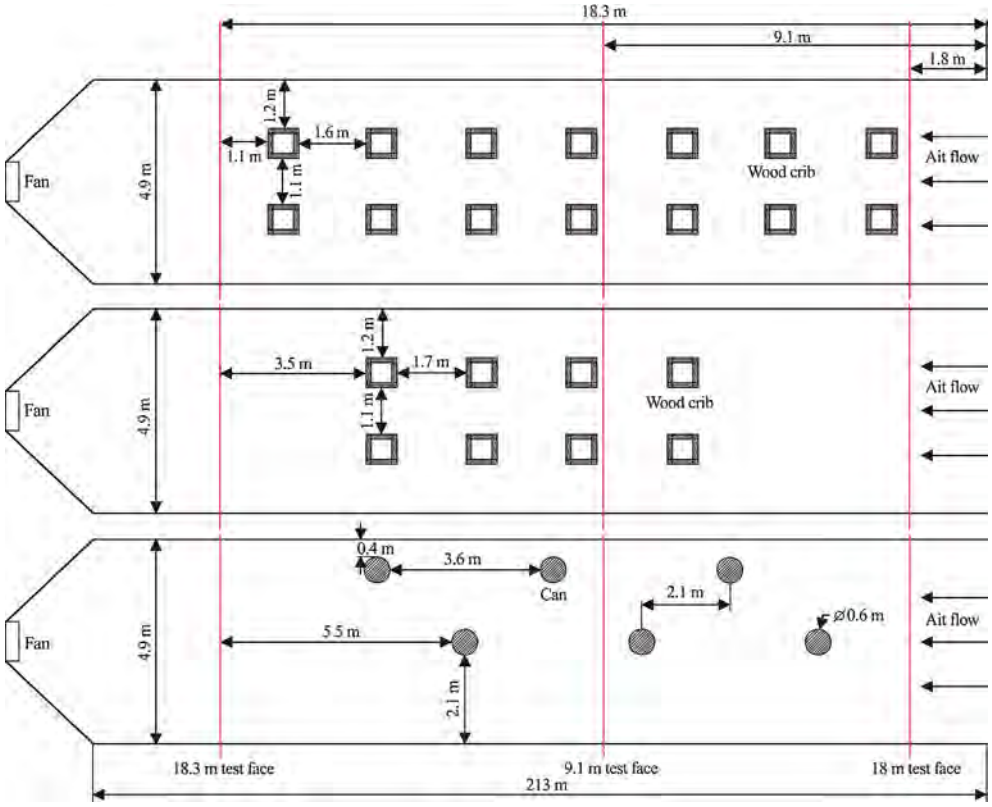

Fig. 9. Layouts for CFD modeling corresponded to the simulated mine entry experiment.

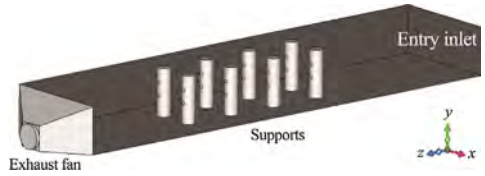

Fig. 10. Geometric and locations of boundary conditions for CFD model.

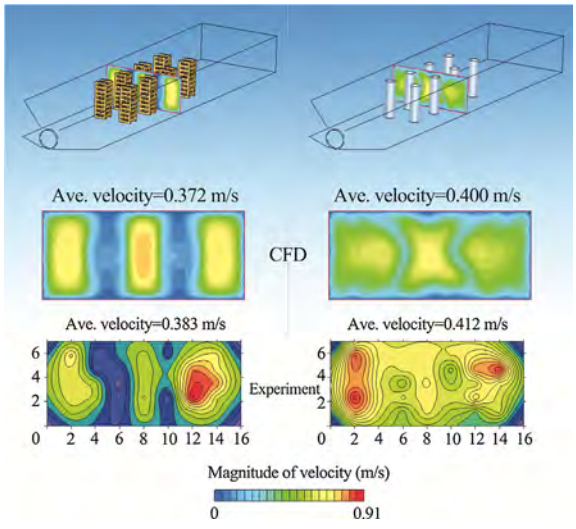

Fig. 11. Velocity contours of crib supports (left) and The CAN® supports (right) for CFD (up) and experiment (down) study.

roof support capacity to 14 four-point cribs. In this case, the flow rate has been increased by almost 30%. This is mainly due to the smoother surface and less contact surface area directly facing opposite the direction of air flow. As seen from the last pair of data, by using The Eye CAN supports in the entry, the air flow velocity is 0.22% higher than using traditional The CAN supports.

Table 1 shows the flow rates determined from the air velocity measurements at the three test locations for the cross-section (Fig. 9) for each of the experiments. Due to air leakage, some errors are believed to exist in the first data set of Experiment No. 1, so this data was omitted. Otherwise, the flow rates used in the analysis should be representative of the actual conditions of the scenario and comparable to those in standing entry between two mine longwall gobs. Comparing the flow rates, the ventilation impact of the different supporting structures is evident.

To obtain a quantitative assessment of ventilation performance for each of the supporting methods, CFD modeling technique is used where it is not practical to collect data by laboratory experiment. Airway resistance (R) and friction factor (K) are back-calculated from the pressure differences (H) obtained from the CFD simulations. The resulting R and K are used to assess the ease of mine ventilation through an airway and are defined by Eqs. (2) and (3) [9].

$$R = \frac{H_l}{Q^2} \tag{2}$$

$$H_l = \frac{KOLQ^2}{5.2A^3} \tag{3}$$

where R is the resistance, Pa s^2/m^8; H the head loss, Pa; Q the flow rate, m^3/s; K the friction factor, kg s^2/m^4; O the perimeter of the entry, m; L the length between two panels, m; and A the cross section area, m^2.

The head loss is obtained from the pressures measured at two airway cross-sections (P_1 and P_2 in Fig. 12) in the CFD model. The flow rate is determined from the average air velocity (V in Fig. 12).

Table 1
Flow rates and velocity data for the experiments and CFD simulations.

Exp. pair No.	Support method	Cross section distance from the air inlet point			Exp.	CFD
		1.83 m Flow rate (m/s)	9.14 m Flow rate (m/s)	18.29 m Flow rate (m/s)	Average flow velocity (m/s)	Average flow velocity (m/s)
1	14 cribs	35.02	19.41	36.86	0.3209	
	14 CAN	48.06	52.11	49.19	0.4446	
2	8 cribs	42.90	43.03	42.85	0.3832	0.3721
	8 CAN	45.96	48.98	43.38	0.4117	0.4004
3	6 CAN staggered	43.00	46.97	45.14	0.4021	
	6 Eye CAN staggered	47.35	45.73	50.88	0.4284	

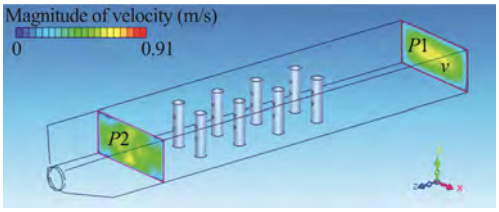

Fig. 12. CFD simulation results and parameter locations.

Table 2
Atkinson resistance and friction factor results for three cases.

Parameter	Support method		
	Crib	The CAN	Eye CAN
P_1 (Pa)	−1.1249E−02	−2.0922E−02	−2.2922E−02
P_2 (Pa)	−4.7459E−02	−4.2123E−02	−4.4031E−02
H_l (Pa)	3.6210E−02	2.1201E−02	2.1109E−02
v (m/s)	0.3718	0.3958	0.3967
Resistance (Pa s^2/m^8)	2.6047E−02	1.3455E−02	1.3337E−02
Friction factor ($\times 10^{10}$)	10841024.3	5600249.9	5543490.6

Table 2 shows that, by using either The CAN or The Eye CAN support, the resistance and friction factor is only 35% compared to wood crib supports. Smaller resistance makes it easier for ventilation air to pass through an entry. In a comparison between The CAN and The Eye CAN, the parameters are very close. The air velocity in The Eye CAN supported entry is 0.22% larger than The CAN supported entry. Although appearing numerically small, the experiment was performed with a limited number of standing roof supports in a 21.34 m long simulated entry with low velocities and known leakage. Since the resistance and friction factor indicate that the ventilation performance of The Eye CAN is an improvement versus The CAN, the cumulative effect is expected to be larger in environments such as a full-sized bleeder entry.

6. Conclusions

Initial laboratory tests of patent-pending The Eye CAN demonstrate that it has roof support characteristics commensurate with The CAN product family, and CFD modeling shows a reduction in resistance of 0.22% to air flow when using The Eye CAN versus The CAN. Additionally, the traditional The CAN shows a 35% improvement in ventilation when compared to using four-point wood cribs. Small modifications that provide cumulative benefits are often more cost effective than making large changes. This proof-of-concept study shows the efficacy of The Eye CAN. Future work includes an application to quantify the overall ventilation improvement in a bleeder entry.

Acknowledgments

The authors would like to thank the many individuals who assisted with this two-year project. Tim Batchler at the NIOSH Mine Roof Simulator provided technical support. Kris Lilly of Redbone Mining lent a truckload of cribbing for the experiment. Don Abel of Burrell Mining Products, Inc., supervised fabrications, coordinated movement of materials, and modified The Eye CAN designs as required. Jim Barbina, PA Operations Plant Manager, and his crew constructed the simulated mine entry and tirelessly reset roof supports for each of the thirteen test configurations.

References

[1] Software Cradle Co. SC/Tetra Software. Software Cradle Co., Ltd.; 2016 <http://www.cradle-cfd.com/products/sctetra/>.
[2] Barczak TM, Tadolini SC. Standing support alternatives in western longwalls. Min Eng 2006;58(2):10.
[3] Burrell Mining Products. The CAN®; 2012. <http://www. burrellinc.com/the-can/>.
[4] Barczak TM. Mistakes, misconceptions, and key points regarding secondary roof support systems. In: Proceedings of the 20th international conference for ground control in mining. Morgantown, WV: West Virginia University; 2001. p. 347–56.
[5] Gearhart DF, Batchler TJ. Aspect ratio and other parameters that affect the performance of Burrell CAN roof supports. In: Proceedings of the 31st international conference for ground control in mining. Morgantown, WV: West Virginia University; 2012. p. 9.
[6] Barczak TM, Tadolini SC. Pumpable roof supports: an evolution in longwall roof support technology. Trans Soc Min, Metall, Expl 2008;324:19–31.
[7] MSHA. Examination, evaluation, and effectiveness of bleeder systems. Program Policy Letter No. P13-V-12. Mine Safety and Health Administration; 2013. p. 7.
[8] Wala AM, Yingling JC, Zhang J, Ray R. Validation study of computational fluid dynamics as a tool for mine ventilation design. In: Proceedings of the 6th international mine ventilation congress. Pittsburgh, PA: SME; 1997. p. 519–25.
[9] Howard LH, Jan MM. Mine ventilation and air conditioning. 3rd ed. New York, NY: Wiley-Interscience; 1997.

International Journal of Mining Science and Technology 27 (2017) 159–163

Contents lists available at ScienceDirect

International Journal of Mining Science and Technology

journal homepage: www.elsevier.com/locate/ijmst

Comparison of L-band and X-band differential interferometric synthetic aperture radar for mine subsidence monitoring in central Utah

Jessica M. Wempen *, Michael K. McCarter

Department of Mining Engineering, University of Utah, Salt Lake City 84112, USA

ARTICLE INFO

Article history:
Received 9 July 2016
Received in revised form 18 August 2016
Accepted 20 September 2016
Available online 10 December 2016

Keywords:
Mine subsidence
DInSAR
TerraSAR-X
ALOS
Interferometry

ABSTRACT

Differential interferometric synthetic aperture radar (DInSAR), a satellite-based remote sensing technique, has potential application for measuring mine subsidence on a regional scale with high spatial and temporal resolutions. However, the characteristics of synthetic aperture radar (SAR) data and the effectiveness of DInSAR for subsidence monitoring depend on the radar band (wavelength). This study evaluates the effectiveness of DInSAR for monitoring subsidence due to longwall mining in central Utah using L-band (24 cm wavelength) SAR data from the advanced land observing satellite (ALOS) and X-band (3 cm wavelength) SAR data from the TerraSAR-X mission. In the Wasatch Plateau region of central Utah, which is characterized by steep terrain and variable ground cover conditions, areas affected by longwall mine subsidence are identifiable using both L-band and X-band DInSAR. Generally, using L-band data, subsidence magnitudes are measurable. Compared to X-band, L-band data are less affected by signal saturation due to large deformation gradients and by temporal decorrelation due to changes in the surface conditions over time. The L-band data tend to be stable over relatively long periods (months). Short wavelength X-band data are strongly affected by signal saturation and temporal decorrelation, but regions of subsidence are typically identifiable over short periods (days). Additionally, though subsidence magnitudes are difficult to precisely measure in the central Utah region using X-band data, they can often be reasonably estimated.

1. Introduction

Differential interferometric synthetic aperture radar (DInSAR) is a satellite-based remote sensing technique that can be used to measure surface displacement over large regions with high spatial resolution. Under good conditions, displacements can be measured with centimeter to subcentimeter accuracy [1,2]. DInSAR also has high temporal resolution, and imaging periods typically range from 10 to 50 days [3,4]. In the last two decades, the application of DInSAR for mine subsidence monitoring has been demonstrated in coal basins in Europe, Australia, China, and the United States. Overall, these studies have demonstrated good data resolution, strong relationships between mine development and subsidence, and reasonable agreement between displacements measured by DInSAR and displacements measured by conventional surveys [5–20].

In radar interferometry phase measurements from two nearly coincident radar images are used to precisely measure relative distances [21]. Surface deformation, topography, and changes in the satellite position contribute most significantly to changes in the radar path length. In general, changes in the path length due to changes in the satellite position and topography are known or can be estimated, and as a consequence, centimeter-level changes in the path length due to surface deformation can be measured.

Because phase measurements are used to quantify distance, the wavelength characteristics of the radar are important. Synthetic Aperture Radar (SAR) sensors most commonly use either L-band (24 cm wavelength), C-band (6 cm wavelength), or X-band (3 cm wavelength) radar, and the imaging characteristics of the radar bands are different. Radar waves tend to interact strongly with structures similar in size to the radar wavelength, and as a result, surfaces appear rougher in images acquired using shorter wavelengths. Longer wavelengths tend to have some penetration of vegetation, dry soils, and ice; phase measurements from longer wavelengths tend to be less sensitive to small changes in the surface conditions over time. Additionally, the maximum deformation gradients measurable by DInSAR depend significantly on the radar band and on the ground resolution (pixel size) of the image [22]. Longer wavelengths are less sensitive to deformation per pixel than shorter wavelengths, and larger deformation gradients are measurable in higher resolution data.

* Corresponding author. Tel.: +1 801 5853029.
E-mail address: jwempen@gmail.com (J.M. Wempen).

http://dx.doi.org/10.1016/j.ijmst.2016.11.012
2095-2686/

Though DInSAR has significant potential as a method for subsidence monitoring, SAR systems have variable characteristics. Using SAR data appropriate for the regional surface characteristics and deformation rates is important for subsidence monitoring. This study evaluates the effectiveness of L-band and X-band DInSAR for monitoring subsidence due to longwall mining in the Wasatch Plateau region of central Utah. L-band SAR data from the advanced land observing satellite (ALOS) and X-band SAR data from the TerraSAR-X mission are used.

2. Location and data

The Wasatch Plateau is characterized by rugged topography with flat topped mesas and steeply incised canyons. It is geologically complex and exists in a region of transition from the Colorado Plateau to the east and the Basin and Range province to the west [23]. Dominant structures include northward trending normal faults and grabens, vertical joints, and vertical strike-slip faults [24]. The subalpine region of the Wasatch Plateau is heavily vegetated; grasses, forbs, and low shrubs are dominant. Steep northern exposures at higher elevations are heavily forested, and at lower elevations, aspen, pine and tall shrubs are common [25]. Fig. 1 shows a TerraSAR-X image of a region of the Wasatch Plateau. In this image, topographic characteristics of the Wasatch Plateau region are discernable.

In the study area, coal has been mined from the upper and lower Hiawatha seams. These seams are present in the lower 75–110 m of the Blackhawk Formation (Mesaverde Group), which has a total thickness ranging from 190 to 245 m. Prominent near-seam geology includes the castlegate and the star point sandstones, both massive, medium- to course-grained sandstones. The castlegate sandstone overlays the Blackhawk Formation and has a thickness ranging from 45 to 150 m. The starpoint sandstone, lies beneath the Blackhawk Formation and has a thickness ranging from 25 to 300 m [26]. The mining heights range from to 3.8 m and the typical overburden thickness ranges from 305 to 550 m. Generally, the maximum vertical subsidence occurs near the center of the longwall panels, with maximum magnitudes from 1.5 to 1.8 m. The average reported angle of draw is 15° [27].

The L-band SAR data used in this study were imaged by the ALOS satellite. ALOS was operated by the Japanese Aerospace Exploration Agency from 2006 to 2011, and acquired data globally with a minimum recurrence cycle of 46 days. The data used in this study were imaged in fine-beam mode with both single and dual polarization; only the co-polarized images were used in interferometric processing. The images have swath widths of 70 km, azimuth resolutions of 10 m, and ground range resolutions of 10 and 20 m for single and dual polarizations, respectively [3]. Imaging dates and characteristics of the ALOS data are given in Table 1. The ALOS data were acquired from a repository of SAR data maintained by the Alaska Satellite Facility.

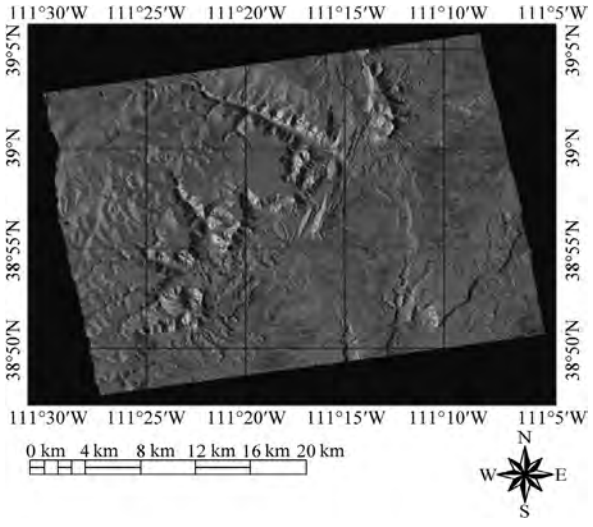

Fig. 1. TDX-1 intensity image of the Wasatch Plateau region (October 20, 2015).

The X-band SAR data used in this study were imaged by the TerraSAR-X mission satellites, TSX-1 which launched in 2007 and TDX-1 which launched in 2010. These satellites are operated by the German Aerospace Center, and acquire data with a minimum recurrence cycle of 11 days. The data used in this study were imaged in stripmap mode with single horizontal polarization. The images have 30 km swath widths and maximum ground resolutions of 3.3 m in azimuth and 1.7 m in range [28]. Imaging dates and characteristics of the TerraSAR-X data are given in Table 2. The TerraSAR-X data were acquired from the German Aerospace Center.

3. Processing

In this study, data processing was performed using SARscape® and ENVI® software. To generate a subsidence map using DInSAR, first the perpendicular and temporal baselines of paired SAR images are estimated. Next, the paired images are co-registered and a differential interferogram is formed. The interferogram is then filtered and the data coherence is estimated. Next, the interferogram is unwrapped and the absolute interferometric phases are determined. Finally, vertical deformation is calculated from the absolute phases [29].

Before interferometric processing, SAR images are often multi-looked, or spatially averaged. Significant amplitude and phase variation of the radar signal from pixel to pixel, caused by variation in the surface characteristics, make the images appear speckled [30]. Spatially averaging the data reduces speckle, but it also reduces the spatial resolution. Short wavelength X-band data are very sensitive to surface deformation, and deformation gradients on the order of 0.016 m/pixel are measurable. However, in areas with large deformation gradients, phases tend to saturate. In this study, the TerraSAR-X images were not multi-looked and were processed at full resolution to limit phase saturation. Longer wavelength L-band data are less sensitive to deformation, and deformation gradients on the order of 0.118 m/pixel are measurable. In this study, the ALOS images were multi-looked to produce images with 20 m by 20 m pixels.

4. Results

For the central Utah study region, three interferograms were generated using L-band data in intervals over the period from June 16 to December 17, 2010. The interferometric data parameters are summarized in Table 3. Phase fringes due to subsidence are identifiable in all of the interferograms, but all the interferograms have topographic artifacts and the data quality is variable. Coherence is a statistics that quantifies the sameness of the radar signals in two paired images and it ranges from zero, which represents complete decorrelation, to one which represents perfect correlation. In general, coherence reflects the quality of the phase measurements [30]. The average coherence of the ALOS data ranges from a low of 0.36 for the period from September 16 to December 17, 2010, to a high of 0.63 for the period from August 1 to September 16, 2010.

Vertical displacement maps derived from the interferograms for each period are shown in Fig 2, Fig. 3 shows accumulated displacement for the 184-day period from June 16 to December 17, 2010. In Figs. 2 and 3 subsidence is contoured every 10 cm starting from -10 cm of vertical displacement. Figs. 4 and 5 show the progression

Table 1
ALOS SAR data characteristics.

Orbit				Acquisition date	Polarization	Look angle (°)
Path	Frame	Number	Pass direction			
201	770	23,400	Ascending	06/16/10	Dual	34.3
201	770	24,071	Ascending	08/01/10	Dual	34.3
201	770	24,742	Ascending	09/16/10	Dual	34.3
201	770	26,084	Ascending	12/17/10	Single	34.3

Table 2
TerraSAR-X SAR data characteristics.

Satellite	Orbit			Beam	Acquisition date	Incidence angle (°)	
	Number	Cycle	Pass direction			Min.	Max.
TSX-1	30	266/44,285	Ascending	10R	06/10/15	36.1	38.5
TSX-1	30	267/44,452	Ascending	10R	06/21/15	36.1	38.5
TSX-1	30	270/44,953	Ascending	10R	07/24/15	36.1	38.5
TSX-1	30	271/45,120	Ascending	10R	08/04/15	36.1	38.5
TSX-1	30	272/45,287	Ascending	10R	08/15/15	36.1	38.5
TSX-1	30	273/45,454	Ascending	10R	08/26/15	36.1	38.5
TSX-1	30	274/45,621	Ascending	10R	09/06/15	36.1	38.5
TSX-1	30	275/45,788	Ascending	10R	09/17/15	36.1	38.5
TSX-1	30	276/45,955	Ascending	10R	09/28/15	36.1	38.5
TSX-1	30	277/46,122	Ascending	10R	10/09/15	36.1	38.5
TDX-1	30	278/29,559	Ascending	10R	10/20/15	36.1	38.5
TSX-1	30	279/46,459	Ascending	10R	10/31/15	36.1	38.5
TSX-1	30	280/46,623	Ascending	10R	11/11/15	36.1	38.5
TDX-1	30	281/30,060	Ascending	10R	11/22/15	35.9	38.6

Table 3
ALOS interferometric data parameters.

Acquisition date	Elapsed time (d)	Baseline (m)	Average coherence
06/16/2010–08/01/2010	46	299	0.59
08/01/2010–09/16/2010	46	−43	0.63
09/16/2010–12/17/2010	92	575	0.36

of subsidence over time along sections AA′ and BB′ (Fig. 3). Maximum measured subsidence during the June 16 to December 17, 2010 period is 1.5 m. Gaps in the data in all of these figures are due to pixels with low coherence.

As noted in Fig. 2, subsidence is contoured every 10 cm, starting from −10 cm of displacement.

As shown in Fig. 3, subsidence is contoured every 10 cm, starting from −10 cm of displacement.

Thirteen interferograms were generated using X-band SAR data from TerraSAR-X in intervals over the period from June 10 to November 22, 2015. The interferometric data parameters are summarized in Table 4. The average coherence of the X-band interferograms ranges from 0.54 to 0.66. Phase fringes due to

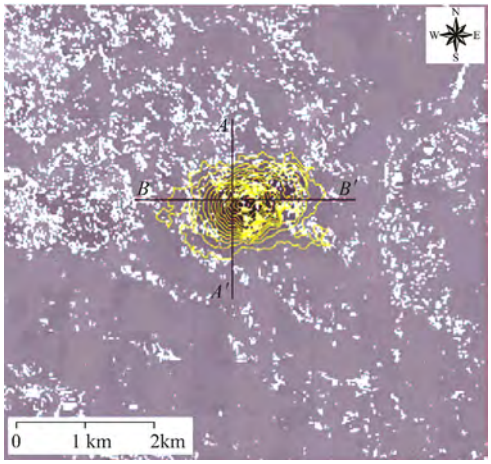

Fig. 3. L-band cumulative vertical displacement map for the period from June 16 to December 17, 2010 (184 days).

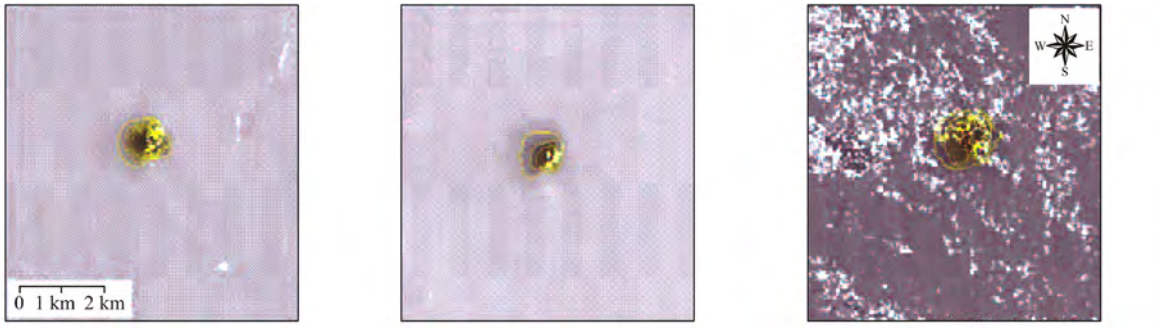

(a) June 16 to August 1, 2010 (46 days) (b) August 1 to September 16, 2010 (46 days) (c) September 16 to December 17, 2010 (92 days)

Fig. 2. L-band vertical displacement maps for the three periods.

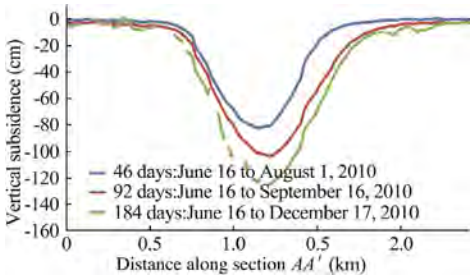

Fig. 4. Time series subsidence profiles of section AA' from Fig. 3.

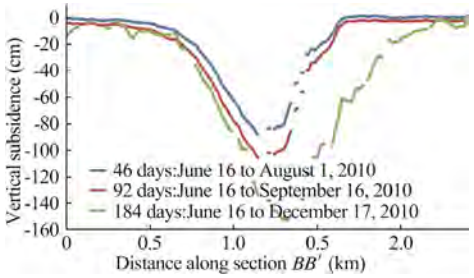

Fig. 5. Time series subsidence profiles of section BB' from Fig. 3.

Table 4
TerraSAR-X interferometric data parameters.

Acquisition date	Elapsed time (d)	Baseline (m)	Average coherence
06/10/2015–06/21/2015	11	−88	0.58
06/21/2015–07/24/2015	33	−37	0.54
07/24/2015–08/04/2015	11	14	0.58
08/04/2015–08/15/2015	11	−16	0.60
08/15/2015–08/26/2015	11	−44	0.66
08/26/2015–09/06/2015	11	−55	0.60
09/06/2015–09/17/2015	11	142	0.61
09/17/2015–09/28/2015	11	−25	0.61
09/28/2015–10/09/2015	11	−16	0.60
10/09/2015–10/20/2015	11	282	0.55
10/20/2015–10/31/2015	11	−360	0.54
10/31/2015–11/11/2015	11	82	0.60
11/11/2015–11/22/2015	11	90	0.56

surface displacement are identifiable in the majority of the interferograms, but in the areas with the largest magnitude subsidence, the fringes are difficult to interpret. Precise evaluation of the maximum subsidence magnitude is not attempted, but the subsidence magnitudes can be reasonably estimated in many of the interferograms. Fig. 6 shows an example of a filtered differential interferogram for the period from June 10 to June 21, 2015. Phase fringe due to subsidence are outlined in green. There are at least seven fringes indicating a maximum vertical displacement of more than 13 cm and a maximum subsidence rate of more than 1 cm per day.

5. Discussion

In the Wasatch Plateau, regions of subsidence can be identified by both L-band and X-band DInSAR, but the effectiveness of DInSAR for quantifying subsidence is dependent on the radar band. Generally, subsidence magnitudes are precisely measurable in the L-band data. The X-band data are more affected by signal saturation and by temporal decoration, and precisely measuring the subsidence magnitudes using X-band data is more difficult. Notably, though the data quality is variable, the L-band data and the X-band data have similar average coherence. However, in the X-band data, coherence is spatially dependent: coherence is generally high over the valley floor and low in the vegetated subalpine region. Variable surface conditions in the subalpine region contribute to both low coherence and significant phase noise in the X-band data, which make phases in the interferograms more difficult to interpret.

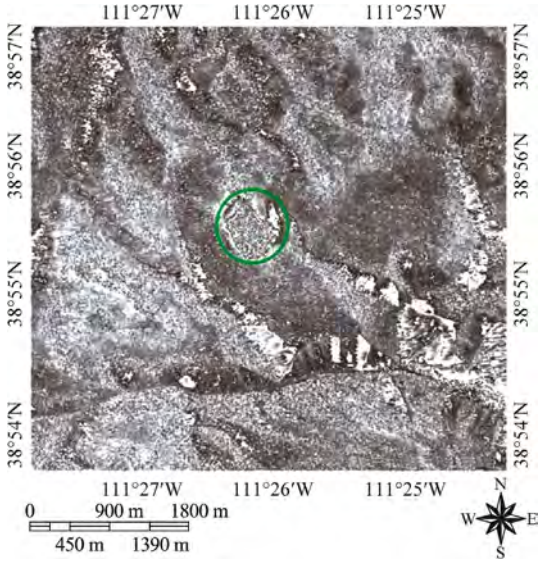

Fig. 6. X-band filtered differential interferogram: June 10 to June 21, 2015 (11 days).

Spatial variation in the coherence of the L-band data is less apparent. However, the L-band data are sensitive to significant changes in the surface conditions, and low coherence does affect the data quality. Variable surface characteristics, including snow cover, likely caused low coherence in the L-band interferogram from September 16 to December 17, 2010. As a result of low coherence, the quality of the displacement map for this period of Fig. 2c is lower than the quality of the displacement maps for periods when the surface condition were more stable and the coherence was higher in Fig. 2a and b. Additionally, in all of the L-band data, areas with very large deformation gradients are affected by low coherence due to phase saturation. Although it is likely that the imaging period from June to December did not capture the full development of subsidence, phase saturation has the potential to cause subsidence to be underestimated by tens of centimeters in the L-band data. The maximum cumulative subsidence reported for this area is on the order of 2 m [27].

In the X-band data, the interpretability of the phases is negatively affected by signal saturation as a result of large displacement rates and by temporal decorrelation, but the aerial extent of subsidence is clearly identifiable in most of the data. Additionally, though the maximum subsidence magnitudes are difficult to precisely measure, in most of the images the magnitudes of subsidence can be reasonably estimated. Because the X-band imaging periods are shorter than L-band imaging periods, the X-band data provide a more timely report of the subsidence extent. Consequently, short period X-band data has potential to accurately identify periods when subsidence has ceased or is minimal.

Acknowledgments

Funding for this research was provided by the National Institute for Occupational Health and Safety (NIOSH). The support of NIOSH

is thankfully acknowledged; however, the conclusions expressed in this paper are those of the authors and do not represent the opinions or policies of NIOSH. Data for this research was provided by the Alaska Satellite Facility, the Japan Aerospace Exploration Agency and the German Space Agency. The contributions of these organizations are gratefully acknowledged.

References

[1] Buckley SM. Radar interferometry measurement of land subsidence. Austin (TX): The University of Texas at Austin; 2000.
[2] Massonnet D, Feigl KL. Radar interferometry and its application to changes in the Earth's surface. Rev Geophys 1998;36(4):441–500.
[3] Rosenqvist A, Shimada M, Watanabe M. ALOS PALSAR: technical outline and mission concept. In: Proceedings of the 4th international symposium on retrieval of bio- and geophysical parameters from SAR data for land applications. Innsbruck (Austria); 2004.
[4] Roth A. TerraSAR-X science plan. TX-PGS-PL-4001, vol. 1; 2004. p. 2–19.
[5] Chen BQ, Deng KZ, Fan HD, Hao M. Large-scale deformation monitoring in mining area by D-InSAR and 3D laser scanning technology integration. Int J Min Sci Technol 2013;23(4):555–61.
[6] Carnec C, Delacourt C. Three years of mining subsidence monitored by SAR interferometry, near Gardanne, France. J Appl Geophys 2000;43(1):43–54.
[7] Yang CS, Zhang Q, Zhao CY, Ji LY, Zhu W. Monitoring mine collapse by D-InSAR. Min Sci Technol 2010;20:0696–700.
[8] Ge L, Chang HC, Rizos C. Mine subsidence monitoring using multi-source satellite SAR images. Photogram Eng Rem Sens 2007;73(3):259–66.
[9] Ge L, Chang HC, Ng A, Rizos C. Spaceborne radar interferometry for mine subsidence monitoring in Australia. In: Proceedings of first international future mining conference and exhibition 2008. Carlton South (Victoria, Australia); 2008.
[10] Fan HD, Deng KZ, Ju CY, Zhu CG, Xue JQ. Land subsidence monitoring by DInSAR technique. Min Sci Technol (China) 2011;21(6):869–72.
[11] Ismaya F, Donovan J. Applications of DInSAR for measuring mine-induced subsidence and constraining ground deformation model. In: Proceedings of the GeoCongress 2012: state of the art practice in geotechnical engineering. Reston (VA); 2012.
[12] Ng AHM, Ge L, Yan Y, Li X, Chang HC, Zhang K, et al. Mapping accumulated mine subsidence using small stack of SAR differential interferograms in the Southern coalfield of New South Wales, Australia. Eng Geol 2010;115(1–2):1–15.
[13] Perski Z. The interpretation of ERS-1 and ERS-2 InSAR data for the mining subsidence monitoring in Upper Silesian coal basin, Poland. Int Arch Photogram, Rem Sens Spat Inf Sci 2000;33:1137–41.
[14] Perski Z, Jura D. Identification and measurement of mining subsidence with SAR interferometry: potential and limitations. In: Proceedings of 11th FIG symposium on deformation measurements. Santorini (Greece); 2003. p. 25–8.
[15] Popiołek E, Krawczyk A. Post mining deformation monitoring based on satellite radar interferometry (InSAR). In: Proceedings of the 3rd IAG/12th FIG symposium. Baden (Austria); 2006. p. 22–4.
[16] Wegmuller U, Spreckels V, Werner C, Strozzi T, Wiesmann A. Monitoring of mining induced surface deformation using L-band SAR interferometry. In: Proceedings of geoscience and remote sensing symposium, 2005, IGARSS 05. Seoul (Korea); 2005.
[17] Wright P, Stow R. Detecting mining subsidence from space. Int J Remote Sens 1999;20(6):1183–8.
[18] Li XL, Liu DL, Song HJ, Chen RP, Li HY. Key technology of D-InSAR at X-Band for monitoring land subsidence in mining area and its application. J Electron 2014;31(5):441–52.
[19] Zhao C, Lu Z, Zhang Q, Yang C, Zhu W. Mining collapse monitoring with SAR imagery data: a case study of Datong mine, China. J Appl Rem Sens 2014;8(1):5946–57.
[20] Liu ZG, Bian ZF, Lü FX, Dong BQ. Monitoring on subsidence due to repeated excavation with DInSAR technology. Int J Min Sci Technol 2013;23(2):173–8.
[21] Rosen PA. UNAVCO short course: principles and theory of radar interferometry. In: Presented at InSAR: an introduction to processing and applications using ISCE and GIAnT. Boulder (CO), August 4–6; 2014.
[22] Baran I, Stewart M, Claessens S. A new functional model for determining minimum and maximum detectable deformation gradient resolved by satellite radar interferometry. IEEE Trans Geosci Remote Sens 2005;43(4):675–82.
[23] Arabasz WJ, Burlacu R, Pankow KL. An overview of historical and contemporary seismicity in central Utah. In: Central Utah—diverse geology of a dynamic landscape. Salt Lake City (UT): Utah Geological Association; 2007. p. 236–53.
[24] Pankow KL, McCarter MK, Arabasz WJ, Burlacu RL. Coal-mining-induced seismicity in Utah—improving spatial resolution using double-difference relocations. In: Proceedings of 27st international conference on ground control in mining. Morgantown (WV): West Virginia University; 2008.
[25] Ellison L. Subalpine vegetation of the Wasatch Plateau, Utah. Ecol Monogr 1954;24(2):89–184.
[26] Doelling HH. Central Utah coal fields: Sevier-Sanpete, Wasatch Plateau, Book Cliffs and Emery. Salt Lake City (UT): Utah Geological and Mineralogical Survey; 1972.
[27] Monroe JK. Subsidence report canyon fuel company, LLC SUFCO. Salt Lake City (UT): Utah Division of Oil, Gas, and Mining, Department of Natural Resources; 2014.
[28] DLR. TerraSAR-X ground segment basic product specification document. TX-GS-DE-3302. Wessling (Germany): DLR. 2013.
[29] SARscape®. User Guide. Purasca (Switzerland): Sarmap; 2014.
[30] Richards JA. Remote sensing with imaging radar. New York: Springer; 2009.

International Journal of Mining Science and Technology 27 (2017) 165–170

Contents lists available at ScienceDirect

International Journal of Mining Science and Technology

journal homepage: www.elsevier.com/locate/ijmst

Top coal caving mining technique in thick coal seam beneath the earth dam

Guo Wenbing [a,b], Tan Yi [a,*], Bai Erhu [a]

[a] School of Energy Science and Engineering, Henan Polytechnic University, Jiaozuo 454000, China
[b] Synergism Innovative Center of Coal Safety Production in Henan Province, Jiaozuo 454000, China

ARTICLE INFO

Article history:
Received 29 May 2016
Received in revised form 31 August 2016
Accepted 18 September 2016
Available online 2 December 2016

Keywords:
Earth dam
Thick coal seam
Top coal caving mining
Harmonic mining
Mining damages and protection

ABSTRACT

It is important to study the mining technology under structures for raising the coal resources recovery ratio. Based on the geological and mining conditions, the top coal caving harmonic mining technique in thick coal seam beneath the earth dam was put forward and studied. The 5 factors such as the panel mining direction, panel size, panel location, panel mining sequence and panel advance velocity were taken into account in this technique. The dam movement and deformation were predicted after the thick coal seam mining and the effects of mining on the dam were studied. By setting up the surveying stations on the dam, the movement and deformation of the dam were observed during mining. By taking some protective measures on the dam, the top coal caving mining technique in thick coal seam beneath the earth dam was carried out successfully. The study demonstrates that harmonic mining in thick coal seam is feasible under the dam. The safety of the earth dam after mining was ensured and the coal resources recovery ratio was improved.

1. Introduction

The surface movement and deformation caused by coal mining not only influence the ecology environment in the mining area, but damage the surface structures such as buildings, railroads, highways, water bodies and dams [1–3]. The movement of strata and surface caused by mining had disturbed various aspects of industrial and agriculture productions in the mining area [4]. The earth dam is a very important water retaining structures, so it must makes sure the safety of dam if mining under it. Therefore, to study the effect of mining on dam and control measures to ensure safety of mining under the dam are important factors for improving the mining recovery ratio, reliving the mining continuity, preventing or reducing damage to the dam [5–7].

By means of the harmonic mining technology, theoretical analysis and field observation, the mining method under an earth dam and the mining influences were studied and analyzed in this paper [8]. The mining of a thick coal seam under the dam was carried out safely and successfully.

2. Harmonic mining technique under an earth dam

Coal mining under the dam damages it and affects its normal usage. Once it becomes unstable and fails, it seriously threatens life and properties downstream. So it's essential to make sure the dam is safe [9–13]. Earth dam is one of the widely used types of dams. It is a water reservoir made of local soils, rocks or combined materials by roller compaction and filling. In order to reduce the damages to dam caused by undermining, based on the physical and mechanical properties of materials used to build the dam, the harmonic mining principle was confirmed as follows:

(1) Properly determination of the panel direction

To avoid or reduce the tensile cracks on the dam, the dam should not stretch over the panel. So the long axis of the dam should be parallel to the panel advance direction (Fig. 1). In this case, the dam is only influenced by dynamic deformation and the influence of mining on the dam is very small.

(2) Properly determination of the panel size

Based on the surface movement and deformation characteristics of subcritical or ultra subcritical mining condition, the width of panel is adjusted in order to reduce the effects of undermining

* Corresponding author. Tel.: +86 13453177787.
E-mail address: 517237667@qq.com (Y. Tan).

http://dx.doi.org/10.1016/j.ijmst.2016.11.005
2095-2686/

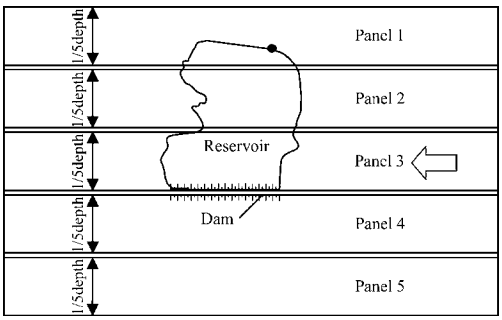

Fig. 1. Mining direction parallel to the long axis of the dam.

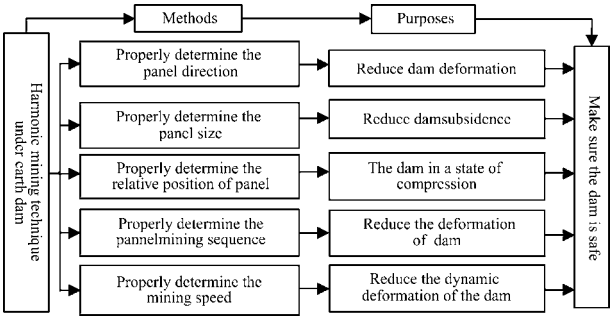

Fig. 3. Harmonic mining principle of the "5 factors" under earth dam.

the dam [14,15]. According to the design requirements of strip pillar mining, the surface movement and deformation are smooth and uniform when the panel width is 1/4–1/10 of mining depth. Based on the mining and geological conditions and mining efficiency, the panel width under the dam is less than 1/5 of mining depth.

(3) Properly determination of the relative position of panel

Based on the previous studies, the dam, made of loess and ashlars, will not be subjected to tensile deformation and cracks under compression [16]. And the permeability of dam will not be increased, thereby ensuring dam stability. Based on the location of the dam on the surface, the center position of panel is determined by the angle of maximum subsidence (Fig. 2). Under this condition, the subsidence of dam is larger, while the dam is in the horizontal compressive zone, which is good for the stability of the dam.

(4) Properly determination of the panel mining subsequence

By adjusting the panel mining sequence, the tensile and compressive deformation caused by adjacent panels mining could be offset to some extent, and the deformation on the dam can be minimized. Simultaneously, the mining effects on dam can be reduced by "skip-mining" because of subcritical mining of each small panel.

(5) Properly determination of the mining speed

A proper mining speed could minimize the dynamic deformation on the dam. Avoiding the face being advanced too slow or too fast; too slow speed will cause boundary effect in front of the face, while too fast speed will cause the deformation rate of dam to accelerate. Previous studies showed that the maximum subsidence velocity is related to the mining advance speed. So it's essential to determine a proper face advance speed and keep it uniform based on the geological and mining conditions.

Based on the previous studies, the maximum subsidence velocity increases linearly with the advancing speed of the mining face [17].

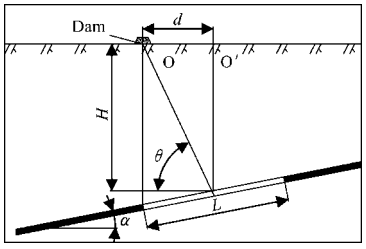

Fig. 2. Panel position determination.

$$V_{\mathrm{fm}} = K\frac{CW_{\mathrm{fm}}}{H_o}$$

where V_{fm} is the maximum subsidence velocity, m; K the subsidence velocity factor; C the advancing speed of working face, m/d; W_{fm} the maximum subsidence, mm; and H_o the mining depth, m.

In order to fulfill the safety of mining under the dam and ensure the stability of the dam, the above five factors should be considered all together in subsidence design. This is called "the harmonic mining method" (Fig. 3).

3. A case study

3.1. Geological and mining conditions

Micun Coal Mine, with 1.5 Mt/a production capacity, is located in Henan province, China. The longwall mining method was used and the whole seam thickness was mined by top coal caving method. The mining depth was 300–390 m. Coal mined in the area was No. 21 coal seam, 1.7–12.31 m thick. The average thickness was 4.65 m. The average dip angle was 10°. The recoverable reserves were 2190 thousand tons.

3.2. The earth dam conditions

The earth dam was located to the south of No. 26 enlarged area and was made of local soils and rocks. There was a paved road 8 m wide on the top. The dam surface was 3 m above the reservoir surface. The dam length was about 114 m, the angle of upstream slope was 40–50° and the slope length was 10–16 m. Fig. 4 shows the earth dam.

3.3. Determination of the harmonic mining scheme

Based on the principle of minimum mining damage to the dam, the panel width is 60–78 m, approximately 1/5 of mining depth. The panel advance direction should be parallel to the long axis of the dam and advancing speed should be uniform. Panels advance speed should be kept at 2.5–3.0 m/d.

Based on the results predicted of the surface movement and deformation, the panel 260061 was mined first and the deformation on the dam was compressive. The width of first panel was less than the 1/5 of its depth, and this is called subcritical mining. Because of the compressive deformation, fissures did not appear on the dam. And the dam was influenced by the dynamic deformation only.

To reduce the adverse influence on the dam, the skip-mining method was used. The second panel mined was panel 26071. This layout was similar to the wide strip skip-mining, and the movement and deformation was largely reduced [19]. Simultaneously, the compressive deformation on the dam caused by the first panel

(a) Slope of earth dam (b) Top of earth dam

Fig. 4. The earth dam before coal mining.

mining was partly offset by the tensile deformation caused by the second panel (Table 1). The third panel mined was the panel 260051 which was far from the dam and had minor effects on the dam. The width of the fourth panel 26081 was relatively small and its distance to the dam was greater. Meantime, the surface subsidence activity induced by mining the 2nd panel 26071 had basically stopped with much smaller influence on the dam. The last panel mined was panel 260071. Due to the fact that panel width of panel 260071 was small and the surface subsidence induced by mining of panels on both sides had stabilized, though dam subsidence increased after panel 260071 mining, its influence on the dam was small because it was a subcritical mining.

Based on the above analysis, the panels mining sequence was as follows: 260061, 26071, 260051, 26081, and 260071. At the same time, due to changes in the coal seam, resulting in the actual working face layout is shown in Fig. 5.

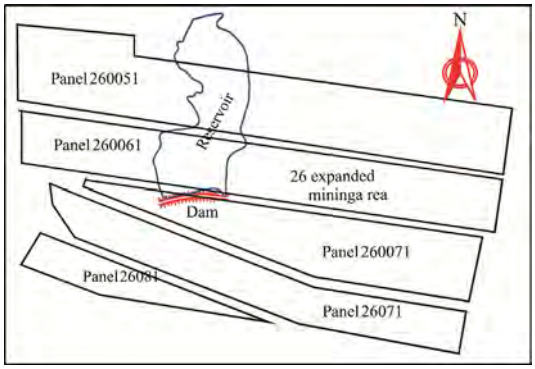

Fig. 5. Location of the earth dam and the panels.

3.4. Mining conditions

By properly adjusting the panel mining sequence and arranging the mining boundary, the harmonic mining technique was carried out and the mining influence on the dam was reduced during mining. This method ensured the safety and stability of the dam. There were 5 panels in the 26 enlarged mining area and the top coal caving mining method was used in all of the panels. In this area, 213.2 million tons of coal was mined and great economic and social benefits were achieved.

4. Prediction of mining influence on the dam

4.1. Surface movement and deformation on the dam

To determine the surface movement and deformation caused by each mined panel and analyze the thick seam-top caving harmonic mining influence on the dam, the probability integral method was adopted for the determination of dam movement and deformation [18–22].

The prediction parameters were determined by the mining geological conditions and the empirical method. The subsidence factor q was 0.80; horizontal movement coefficient b was 0.24; the offset of inflection point s was $0.01H$ (H is mining depth); the tangent of major influence angle β was 2.16; and the propagation angle of extraction θ was 84°.

The subsidence and deformation of the dam were predicted with the probability integral method. The results demonstrate that the dam subsidence and deformation are the smallest according to the panels mining sequence: 260061, 26071, 260051, 26081 and 260071 (Fig. 6). The maximum surface movement and deformation on the dam location is shown in Table 1.

4.2. Analysis of effects of surface movement and deformation on the dam

The subsidence, slope and horizontal strain have influences on the dam after mining. Subsidence of the dam will lower the water impoundment level. The horizontal strain, especially the tensile strain, will cause cracks on the dam and induce landslide on the dam slope.

As shown in Fig. 6, the dam was almost in compressive condition after each panel was mined by the top coal caving harmonic mining method, and the tensile strain was only found in partial areas after mining of panels 260051 and 26081. There were no

Table 1
Maximum subsidence and deformation on the dam after each panel mining.

Panel	Maximum subsidence (mm)	Maximum slope (mm/m)	Maximum horizontal displacement (mm)	Maximum horizontal strain (mm/m)		Maximum curvature (mm/m^2)
260061	1820	11.9	710		−13	⩽0.3
26071	2025	3.2	330		−10	⩽0.2
260051	2350	9.0	630	+2.5	−2.2	⩽0.2
26081	2380	8.8	650	+3.3	−2.1	⩽0.2
260071	2910	2.0	350	+0.6	−1.4	⩽0.2

Note: + means tensile strain, and − indicates compressive strain.

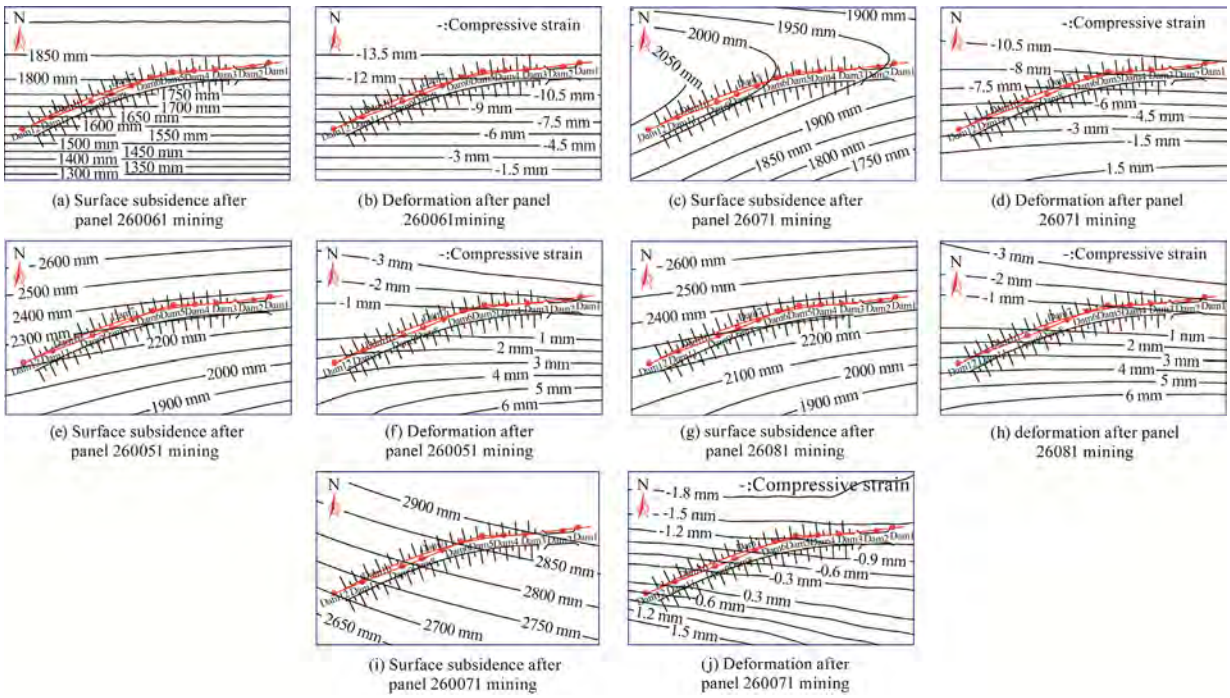

Fig. 6. Predicted surface subsidence and deformation after mining.

tensile cracks on the dam, especially the transverse cracks. Consequently it protected the dam from mining damage and made sure the dam was safe during and after mining.

From Table 1, after the panel 260071 was mined, the whole dam was almost in compressive condition. The maximum compressive strain was 1.4 mm/m. But, the surface movement and deformation due to mining are a dynamic process. The dynamic tensile strain was 3.3 mm/m. Based on the Chinese regulations, the allowable tensile deformation is 6 mm/m if the dam has an overflow chute. So, as shown in the Table 1, the maximal tensile strain on the dam is less than the permissible value. All the panels can be mined and the dam is safe during and after mining.

Based on the analysis above, mining under the dam is feasible by predicting the results of movement and deformation. However, the tensile strain would appear after panel 26081 mining. Maintenance and reinforcement measures on the dam should be adopted for protecting the dam.

4.3. Protective measures for the earth dam

In order to eliminate the mining influences on the dam and improve the impoundment level, some measures had been taken as follows during and after mining:

(1) Drain water from the reservoir to lowering the water level during undermining especially during the flood period. This measure can reduce the lateral pressure of the water on the dam and subsequently lower the risk of dam break caused by mining.
(2) Based on the dam subsidence, heightening and widening measures were adopted for increasing the impoundment level. Simultaneously, grouting was implemented to improve the dam strength in the tensile strain area if cracks appeared.
(3) In order to increase the dam stability and impermeability, the upstream slope of the dam was reinforced with stone plates, as shown in Fig. 7.

Fig. 7. Dam body after reinforcement.

5. Observation and analysis of the dam subsidence

5.1. Layout and observation of surveying station

In order to know the dam subsidence and damages in time during and after mining, the surface movement observation stations were set up on the dam before mining. 12 observation stations were established on the dam and the distance between each two observation station was 10 m. The arrangement of observation stations is shown in Fig. 6.

During and after mining, 8 observation surveys were carried out and the results are shown in Table 2.

To reflect the harmonic subsidence of each surveying station and compare the predicted with the actual observed results, the radar map at different mining periods was plotted based on the actual measurements in Table 2 (see also Fig. 8). In Fig. 8, the numerical numbers around the outer circle represent the 12 survey stations, and the radius of each survey station at each circle represents the amount of subsidence obtained at each survey. Therefore, the more circular the circle is, the more uniform the dam subsidence is across the 12 survey stations. Fig. 9 is the comparison of measured and predicted subsidence at each survey station.

Table 2
Observation results of the earth dam subsidence (mm).

Observation control station	1 Subsidence	2 Cumulated subsidence	3 Cumulated subsidence	4 Cumulated subsidence	5 Cumulated subsidence	6 Cumulated subsidence	7 Cumulated subsidence	8 Cumulated subsidence
12	138	201	328	1971	1976	2048	2084	2144
11	174	229	356	1943	2041	2104	2157	2200
10	276	334	424	2308	2422	2471	2516	2564
9	316	366	445	2392	2500	2550	2591	2634
8	348	395	463	2478	2580	2621	2661	2703
7	366	412	470	2557	2623	2668	Lose	2815
6	342	384	434	2606	2678	2721	2772	2803
5	365	407	458	2672	2746	2781	2839	2868
4	343	381	423	2699	2764	2803	2846	2875
3	324	358	386	2709	2807	2838	2881	2909
2	299	350	366	Destroyed	Destroyed	Destroyed	Destroyed	Destroyed
1	276	298	326	2726	2773	2799	2835	2848

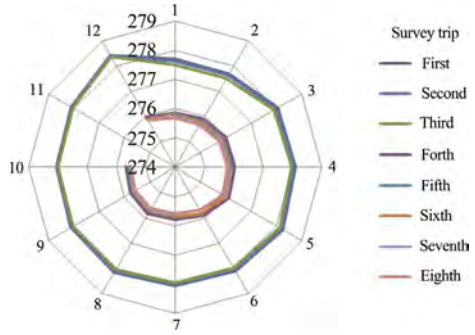

Fig. 8. Radar map of elevation of dam observation stations at different times.

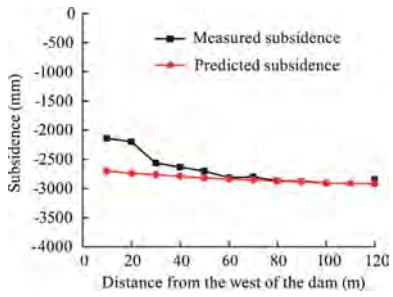

Fig. 9. Predicted and measured subsidence of the dam.

5.2. Analysis of the observation results

From Table 2, the observed subsidence of the first three times was very small. The main reason is the subsidence was caused only by panel 260061 mining at that time. The mining depth of panel 260061 was 370 m with small panel width, so it is subcritical mining. Therefore, the results showed that narrowing the panel width is a very effective way to decrease the subsidence and protect the dam.

Through the analysis above, the movement and deformation caused by one subcritical panel are so small that skip-mining method and a proper mining sequence of panels could be used to reduce the influences effectively on the dam. Owing to the mining influence of panel 260071 and 26081, the measured subsidence from the fourth survey trip changed rapidly.

From Fig. 8, it can be seen that the accumulated subsidence after each survey trip form a concentric circle in the radar map, which shows the subsidence of the earth dam was basically synchronic and thus reduces the adverse influences on the dam during mining. As shown in Fig. 9, the subsidence from observation station 12 to 1 (from west to east) gradually increases. The predicted subsidence was larger than the measured ones and the average error of subsidence was 166 mm. The main reason was that surface subsidence was not completely stable when the last observation was perforated.

6. Conclusions

(1) Based on the characteristics of earth dam and the surface movement and deformation prediction, the "five-factor" harmonic mining method under the dam was put forward. The five factors are: properly determining the panel mining directions, panel size, panel location, mining sequence of the panels and face advance speed. The top coal caving mining in thick coal seam under the earth dam was carried out successfully.

(2) Based on the field observation, surface movement and deformation prediction and theoretical analysis, the mining influence on the earth dam was studied during and after mining. Based on the mining adverse effects on the dam, the protective measures for the dam were put forward and carried out after undermining.

(3) The "five-factor" harmonic top coal caving mining technique in thick seam had been successfully applied in Micun Coal Mine. It ensured the safety and stability of the earth dam after all the panels were mined. The recovery ratio was raised to the fullest extent and the service life of the coal mine was extended. The preferable economic and social benefits are obtained. The precious experience of undermining the earth dam was accumulated for the similar conditions.

Acknowledgments

This project was sponsored by the National Natural Science Foundation of China (No. 51374092).

References

[1] Miao XX, Qian MG. Research on green mining of coal re-sources in China current status and future prospects. J Min Saf Eng 2009;26(1):1–14.
[2] Qian MG, Miao XX, Xu JL. Green mining of coal resources harmonizing with environment. J China Coal Soc 2007;32(1):1–7.
[3] Guo WB. Damage and protection of coal mining. Beijing: China Coal Industry Publishing House; 2013.
[4] Behnia D, Ahangari K, Goshtasbi K, Moeinossadat SR, Behnia M. Settlement modeling in central core rockfill dams by new approaches. Int J Min Sci Technol 2016;26(4):703–10.
[5] Peng SS. Coal mine ground control. New York: Wiley; 2008.

[6] Yuan L, Wu K. Theoretical research and technical practice of coal mining under the embankment of Huaihe. Xuzhou: China University of Mining and Technology Press; 2003.
[7] Guo WB, Yang ZG, Zhan M. Subsidence rule of "Three Soft" coal seam and its application. Beijing: Science Press; 2013.
[8] Guo WB, Xu FY. Numerical simulation of overburden and surface movements for Wongawilli strip pillar mining. Int J Min Sci Technol 2016;26(1):71–6.
[9] Kendorski FS. Effect of full-extraction underground mining on ground and surface waters-a 25-year retrospective. In: Proceedings of 25th international conference on ground control in mining. Morgantown; 2006. p. 425–30.
[10] Xu ZM, Sun YJ. Height prediction of the water conducted zone for mining under reservoir. China Min Magaz 2008;17(3):96–9.
[11] Kendorski FS. Effect of full-extraction mining on ground and surface waters. In: Proceedings of 12th international conference on ground control in mining. Morgantown; 1993. p. 412–25.
[12] Palchik V. Formation of fractured zones in overburden due to longwall mining. Environ Geol 2003;44(1):28–38.
[13] Guo WB, Shao Q, Shi XY. Coordinated top coal caving mining technology of thick seam under reservoir dam. Coal Sci Technol 2013;40(9):133–7.
[14] Guo ZZ, Wang JZ, Dai HY. Prediction method of surface movement and deformation in the extremely insufficient mining. Mine Survey 2000;3:35–7.
[15] Tian JZ, Xu FK, Wang ZC. Mining subsidence rule of extremely insufficient mining deep coal-seam in Xingcun Colliery. Coal Min Technol 2012;17(1):96–9.
[16] Guo WB, Shao Q, Yin SX, Shao HF. Analysis of the security of mining under a reservoir. J Min Saf Eng 2006;23(3):324–8.
[17] State Bureau of Coal Industry. Regulations of buildings, water, railway and main well lane leaving coal pillar and press coal mining. Beijing: China Coal Industry Publishing House; 2000. p. 225–33.
[18] Guo WB, Deng KZ, Zou YF. Research on surface movement parameters of strip-partial mining. J China Coal Soc 2005;30(3):596–600.
[19] Guo WB. Surface movement predicting problems of deep strip pillar mining. J China Coal Soc 2008;33(4):369–72.
[20] Tan ZX, Deng KZ. Comprehensive analysis and application study on ground deformation prediction parameters of fully-mechanized mining with sublevel caving. Chin J Rock Mech Eng 2007;26(5):1041–7.
[21] Dai HY, Liao MG, Meng XY, Bai ZH, Ren LY, Li DT, et al. Analysis of the security of mining under the reservoir in Jiulong coal Mine of Fengfeng mining area. J China Coal Soc 2014;39(S2):95–300.
[22] Song JJ, Han CJ, Li P, Zhang JW, Liu DY, Jiang MD, et al. Quantitative prediction of mining subsidence and its impact on the environment. Int J Min Sci Technol 2012;22(1):69–73.

International Journal of Mining Science and Technology 27 (2017) 171–177

Contents lists available at ScienceDirect

International Journal of Mining Science and Technology

journal homepage: www.elsevier.com/locate/ijmst

Whole-mine subsidence over tabular deposits and related seismicity

Pariseau William G. *, McCarterr Michael K.

Department of Mining Engineering, University of Utah, Salt Lake City, UT, USA

ARTICLE INFO

Article history:
Received 28 June 2016
Received in revised form 8 October 2016
Available online 10 December 2016

Keywords:
Whole mine subsidence
Multi-scale
Finite element analysis
Mine induced seismicity

ABSTRACT

The challenge of estimating mine-wide subsidence and linkages to seismicity over tabular deposits is addressed by a special finite element technique (dual node–dual mesh). Subsidence and mine-induced seismicity begins near the face when caving occurs and propagates to the surface as extraction reaches a critical extent. Thus, the challenge is to obtain details at the face at the meter scale and also at the surface over the whole mine at the kilometer scale. Interactions between old and new sections of a mine are automatically taken into account with this technique. The finite element method is well established technology based on fundamentals of physical laws, kinematics and material laws. With this technique, no empirical "scaling" or fitting computer output by input data "adjustment" to mine measurements is necessary. Capability is demonstrated for doing practical whole-mine subsidence analysis from first principles. Mine-induced seismicity is shown to correlate well with face advance and element failure.

1. Introduction

Seismicity associated with coal mining has been under study for several years by a team at the University of Utah. Team members include mining faculty, research geophysicists and students from the Departments of Mining Engineering and Geology & Geophysics. Mines in central Utah that have been studied include the Trail Mountain Mine the Beehive Mine, also known as the Des-Bee-Dove, and the Crandall Canyon Mine [1–3]. These mines were developed from outcrops in the Wasatch Plateau coal field west of Price, Utah, where the topography is characterized by steeply incised canyon drainages and high plateaus with relief of a thousand meters or so.

Seismicity associated with coal mining in central Utah has been of interest for many years and includes studies in the Book Cliffs to the east of Price, Utah, where mining is still active and to the northwest [4–11]. Results of many micro-seismic studies are summarized perhaps best by Iannacchione et al. in stating, "Deviations from normal strata response can provide useful stability information" [12].

This study concerns a fourth underground coal mine in the southern portion of the Wasatch Plateau coalfield, hereafter referred to as the MINE. Focus is on mining from 2004 to 2008 with the objective of examining mining in relation to seismicity.

2. Problem statement

The problem is to relate strata mechanics to seismicity associated with mining. Seismic events observed as mining proceeds are associated with mining but may not be caused by mining. However, events in close proximity to an active longwall face may be reasonably assumed to be mining induced. Close proximity means within a zone of influence of the face, a distance equal to the face length for a single, isolated panel or to the cumulative face lengths in case of adjacent panels. Four panels, each with a face length of 300 m, would have a zone of influence of 1.2 km. This observation indicates interactions between panels, certainly, and between sections of a large underground coal mine should be expected. Subsidence should be maximum, although depth of overburden, strata properties and chain pillars need to be taken into account when estimating surface subsidence. Thus, the problem is to do a whole mine analysis, past and present, following the mining sequence and the evolution of stress, strain and displacement changes induced by mining.

3. Problem approach

Whole mine analysis of strata-bound tabular deposits (e.g., coal, salt, trona) is a challenge of scale, regardless of the numerical method. When stratigraphy is taken into account, the popular finite element method is the most practical. The reason is to account for all the different rock types present. However, the extent of a finite element model is limited by an element aspect

* Corresponding author. Tel.: +1 801 5815164.
E-mail address: W.Pariseau@Utah.edu (W.G. Pariseau).

http://dx.doi.org/10.1016/j.ijmst.2016.11.013
2095-2686/

ratio required for numerical reliability. In a coal seam with a mining height of 3 m, the lateral dimensions of elements should be no more than 9 m. At a mine scale of kilometers, the number of elements required is an impossibly large number, in the hundreds of millions. A graded mesh would reduce the number of elements required but not nearly enough for practical computation.

A dual node–dual mesh technique meets the challenge of scale where a large mesh at the kilometer scale allows for interactions amongst sections of a mine and a dual mesh allows for details at the meter scale of a working face. The program is a special version of UTAH3 that has been in use for many years. Dual nodes and dual meshes have been used in past studies, but were linked for the first time in our mine-induced seismicity studies [13,14]. Fig. 1 illustrates the relationship between meshes. Both meshes are finite element meshes for conventional continuous Galerkin finite element computations. The mining seam is replaced by node pairs in the big mesh. In the dual mesh, the mining seam is explicitly represented by elements. Boundary nodes of the dual mesh have prescribed displacements obtained from the large mesh through interpolation when necessary. Although the volume of the big mesh is much greater than the dual mesh, the number of elements and nodes in each is often nearly the same (12–16 million).

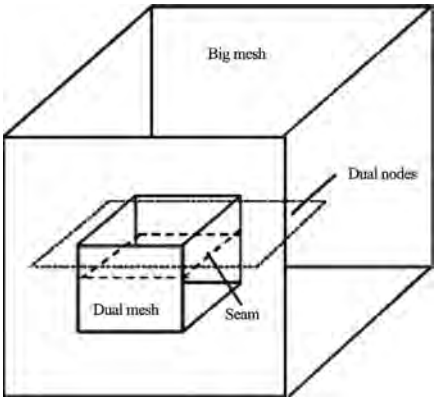

Fig. 1. Schematic of the dual node-dual mesh technique [1].

4. Whole-mine finite element analysis

As with all finite element models, preprocessing input data (mainly mesh generation) and post-processing output data (mainly presentation of results) are major components of model effort. Mesh generation must be consistent with topography, stratigraphy, jointing and strata properties. An equilibrium and consistent premining stress field is essential. Results include surface subsidence, extent of yielding indicated in element safety factor distributions, and correlations with observed seismicity. Computational effort is nearly automatic once input data are prepared.

4.1. Mesh generation

Mesh generation begins with a download of the surface topography from the Shuttle Radar Topography Mission. The file used in our work has a point spacing of 10 m. Coordinates are state plane coordinates.

Fig. 2 shows the topography in color at the MINE from the download; redlines define mined areas. Of some interest is the depth of cover over much of the mined area near the figure center. As the color scale indicates much of the surface is "table top" and indicates a depth of cover of about 300 m. In this regard, seam elevation is taken to be 2300 m and the MINE is developed from outcrop. Overburden elevation above the panels of interest is about 2621 m, as the elevation scale indicates near the figure center. Topographic relief indicated in Fig. 2 is over 1219 m. Portal eleveation is 2304 m.

As shown in Fig. 2, map width is about 21.6 km, and north is in the *y* direction.

Mesh construction begins with the topographic map and is extended above and below the surface terrain according to the geologic column for the MINE. Fig. 3 is a plot of topography and mined areas of interest during the period between 2004 and 2008 and is a plan view of a finite element mesh for this study. There are more than 124,000 elements in Fig. 3. Individual elements are 70 m × 70 m in lateral extent and are not discernable because of the scale and the use of the same color for element boundaries as for the elements proper. Fig. 3 is approximately 21.64 km wide (east-west) and 23.46 km in the north-south direction.

Mesh generation includes representation of mining geometry and stratigraphy. In this regard, the seven longwall panels mined

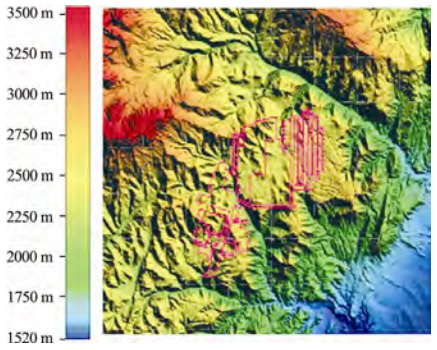

Fig. 2. Elevation map of the MINE.

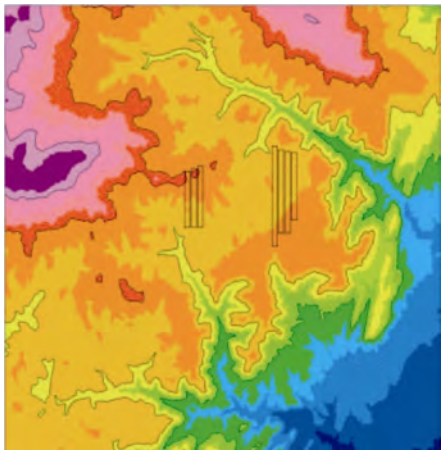

Fig. 3. Mined areas at the MINE.

between 2004 and 2008 are outlined in Fig. 3. Seismicity associated with mining these panels may be correlated with production, as is generally the case and demonstrated in the case of mining P13 at the Trail Mountain mine. Anomalous seismicity was observed during barrier pillar mining at the Crandall Canyon mine, but also associated with production. Panels on the right hand side of Fig. 3 were mined first; panels on the left hand side were mined later.

Panel face width is approximately 280 m; length varies, as shown in Fig. 3. A three-entry system was used to develop the panels. Entries were assumed to be 6.1 m wide; pillars were assumed to be 18.3 m wide and 24.4 m long.

As shown in Fig. 3, colors correspond to surface elevations in Fig. 2, and North is in the *y* direction.

4.2. Stratigraphy, jointing and properties

Stratigraphy refers to the major geologic formations present. Formations include a variety of rock types, but nevertheless show differences in properties. Jointing makes strata more compliant and weaker than intact rock, of course; properties of most importance are elastic moduli and strengths. The MINE was considered dry, so hydraulic conductivities were not needed.

4.2.1. Stratigraphy

Geology of coal fields in Utah is described by Doelling [15]. The geologic column used for the study is shown in Fig. 4. Strata thicknesses are relative, but not to scale in Fig. 4; coal is between the Blackhawk and Starpoint formations. Material properties for the several formations present in a stratigraphic column for the MINE were adapted from laboratory test data [16,17].

4.2.2. Jointing

Three joints sets were taken into consideration [18]. Two sets contained vertical joints at right angles; a third set consisted of bedding plane joints. Spacings were 6 and 8 m for the vertical joints, and 9 m for the bedding plane joints. All joints were considered to be 30 cm thick. Sampling of a jointed cube with ever larger edge dimension leads to equivalent jointed rock mass moduli, shown graphically in Fig. 5, as fractions of intact rock moduli [1]. Vertical joints are at a small angle to north. Details of the equivalent properties computation can be found in the work of Pariseau [19].

Because the mesh is too large (over 16 million elements) to accommodate explicit joint representation, joint strengths were reduced in the same proportion as the moduli. This procedure keeps the uniaxial strain to failure (strength divided by modulus) the same at the field scale as measured in the laboratory. As the data in Fig. 5 show little change in equivalent properties occurs for sample cubes much larger than the maximum joint spacing. The underlying reason for this result is the fact that the sample cube becomes a representative volume element, a periodic structure much like a brick wall structure as illustrated in Fig. 6 [1]. Incorporating the effects of joints into the finite element model is an important step toward greater model realism.

4.2.3. Elastic moduli and strengths

Tables 1 and 2 are the results of equivalent properties computations for elastic and strength properties, respectively. Joints induce directional properties in all strata, as seen in Tables 1 and 2; for this reason, an anisotropic elastic model is required. In fact, an orthotropic model with three orthogonal material axes is used. This model requires nine independent elastic constants, though only six are shown in Table 1. The other three are Poisson's ratios computed from symmetry requirements. Strengths are also specified in consideration of anisotropy (orthotropic model). Nine strength properties are also required for strengths; three unconfined compressive and tensile strengths (Cs and Ts) and three shear strengths (Rs) are shown in Table 2. When joints are skewed relative to mine coordinates, rotation of material properties matrices is necessary. The rotation angles are specified input data.

Nonlinear yield conditions limit the range of purely elastic deformation in each stratum. Yield criteria used in the study have anisotropic forms and are *N*-types, [20]. Thus,

$$J_2^{N/2} + I_1 = 1 \tag{1}$$

All strength constants are computed from uniaxial strength data. Rules of flow are associated; the yield criterion and plastic potential are the same. This type of criterion takes into account the intermediate principal stress and reduces to the well-known Drucker-Prager criterion in case of isotropy and an exponent $N = 1$ that is determined from test data. Because the $N = 1$ case increases strength more rapidly with confining pressure than usually observed in test data, $N = 2$ is often used. Fractional values are possible and may be used when data are fitted using a test *N*.

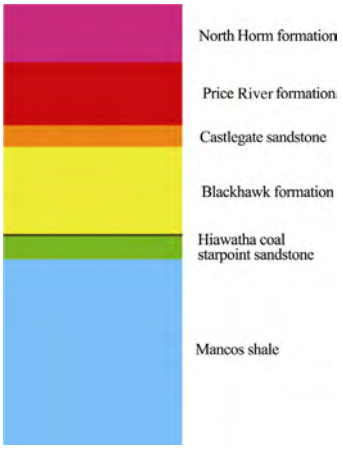

Fig. 4. Geologic column, major formations.

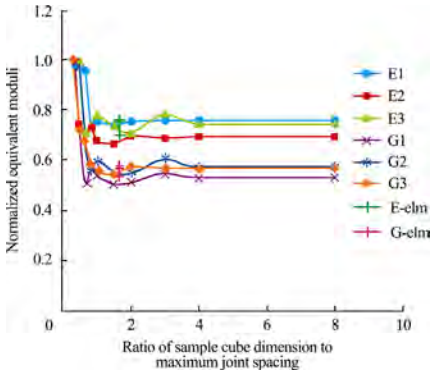

Fig. 5. Equivalent moduli of a rock mass containing joints from three joint sets.

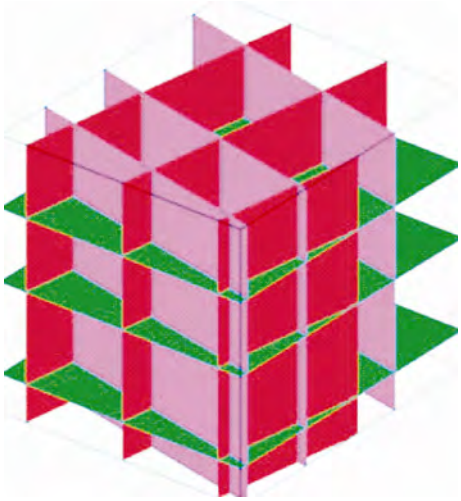

Fig. 6. A sample of joints in three joint sets.

Table 1
Formation elastic moduli (GPa).

Formation	E1	E2	E3	G12	G23	G31	PR12	PR23	PR31
North Horn	14.0	12.5	13.5	3.7	4.1	3.8	0.21	0.18	0.20
Price River	16.4	14.3	15.7	4.1	4.6	4.3	0.20	0.17	0.19
Castlegate	15.7	13.7	15.0	4.0	4.5	4.2	0.17	0.15	0.16
Blackhawk	19.4	16.5	18.3	4.5	5.2	4.7	0.18	0.16	0.17
Coal	2.97	2.97	2.97	1.32	1.32	1.32	0.12	0.12	0.12
Starpoint	14.0	12.5	13.5	3.8	4.2	3.9	0.17	0.16	0.17
Mancos	12.3	11.1	11.8	3.3	3.6	3.4	0.29	0.26	0.28

Note: E1, G1, PR12, etc., are Young's moduli, shear moduli and Poisson's ratios, respectively.

Table 2
Formation strengths (MPa).

Formation	C1	C2	C3	T1	T2	T3	R1	R2	R3
North Horn	63.6	56.6	61.1	3.8	3.4	3.6	8.9	8.0	8.6
Price River	51.3	44.7	44.9	2.0	1.7	1.9	5.8	5.1	5.5
Castlegate	46.9	41.2	44.8	2.1	1.8	2.0	5.7	5.0	5.5
Blackhawk	76.0	64.8	71.8	3.5	3.0	3.3	9.4	8.0	8.9
Coal	28.5	28.5	28.5	1.9	1.9	1.9	4.3	4.3	4.3
Starpoint	51.9	46.1	49.8	1.9	1.8	1.9	5.8	5.2	5.6
Mancos	57.4	51.8	55.4	0.3	0.3	0.3	2.5	2.3	2.4

Note: C1, T1, R1, etc., are unconfined compressive, tensile and shear strengths, respectively.

A local (element) safety factor (fs) is a ratio of "strength" to "stress". Thus,

$$fs = \frac{J_2^{1/2}(strength)}{J_2^{1/2}(stress)} \tag{2}$$

where the numerator is computed from the yield criterion and the denominator is obtained from an analysis of stress (element stress). If $fs > 1$, the element is in the elastic domain; if $fs = 1$, the element is at the elastic limit and may subsequently yield or remain elastic depending on the subsequent loading. An $fs < 1$ is numerically possible, but should be near 1 in a computation.

4.3. Variability, uncertainty

All strata property sets are considered variable in nature. Variability makes properties uncertain in a test specimen before testing and in the MINE at any particular location. For this reason, statistical distribution of properties in Tables 1 and 2 are adopted, specifically, a normal distribution with clipped tails that avoid physically unrealistic strengths, negative and very large, is used. Other distributions such as log normal and Weibull functions could also be used as could a simple histogram of test data. Indeed, a histogram of unconfined compressive strength data is shown in Fig. 7. There are 118 samples in the data; mean strength is 175 MPa and the standard deviation is 69 MPa, giving a coefficient of variation (CV) of 39%, typical of such data. These data were obtained from a run of about 77 m from immediate roof strata through the seam and into floor strata. Similar histograms of coal UCS and Young's modulus from 318 tests have been plotted [3,1].

In Fig. 7, the sample size is 118.

Statistical distribution of laboratory test specimens may be mapped back to the source location of samples, usually drill core, in the field as with these data. This mapping then allows one to observe spatial variability in situ. Incorporating spatial variability into the finite element model is then a step toward greater realism in analyses of strata mechanics. Fig. 8 shows the results of mapping sample values back to the drill source locations above and below the mining horizon. The regression line indicates little association of strength with depth.

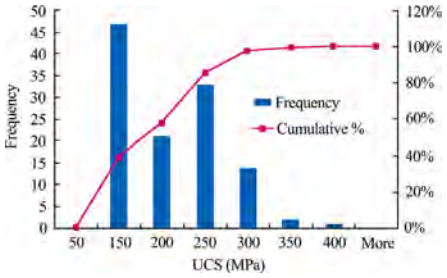

Fig. 7. A histogram of unconfined compressive strength data (UCS) showing statistical variability in test data.

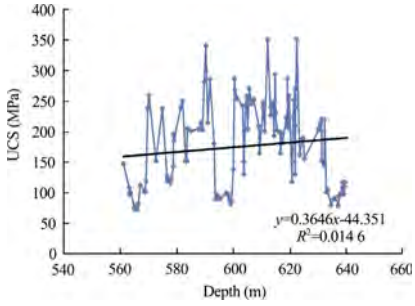

Fig. 8. Unconfined compressive strength as a function of depth showing spatial variability of the same test data.

4.4. Premining stress field

Gravity forces were first applied to the large mesh that contained over 16 million three-dimensional cuboid elements. Fig. 9 shows the distribution of vertical (SV) and horizontal (SH) stress as functions of depth in this mesh. The effect of properties variability is clearly evident in the 10-element strings at each sampled depth. A deterministic gravity field would show jumps in horizontal stress across strata interfaces, but variability obscures this phenomenon.

Excavation to current topography followed. Results of the topographic cut are illustrated in Fig. 10. Colors in Fig. 10 distinguish

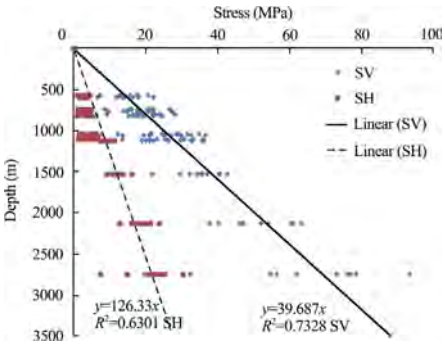

Fig. 9. Vertical and horizontal stress versus depth after application of gravity forces to the big mesh with variable rock properties.

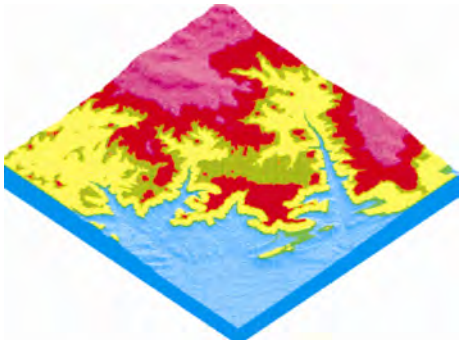

Fig. 10. Finite element mesh in perspective showing ground surface after excavating to current topography.

strata, as seen in Fig. 3. Lateral dimensions are the same as in Fig. 2 (21.6 km × 23.5 km). Original mesh thickness was 2743 m. Maximum thickness in Fig. 10 is nearly the same in the upper left, northwest corner of the mesh. The topographic cut produces a premining stress field that is consistent with topography, stratigraphy, strata properties and properties variability. In fact, the stress field is an equilibrium field and the associated strain field is a compatible field.

5. Results

Computer output is voluminous, especially in the case of 10–15 million element meshes. Some selectivity is necessary to reduce post-processing efforts. Output that lends credibility to an analysis is essential. In case of whole mine analysis, comparisons of mine observations of surface subsidence with model output demonstrates model reliability and serves the purpose. Although distributions of stress, strain and displacement induced by mining are of general interest, the extent of yielding ground is of first importance as an indicator of potential roof falls, pillar spalls and floor heaves. Distributions of element safety factors serves the purpose of identifying extent of yielding ground and also shows regions of near yielding about panels of interest. Relationship of observed seismicity to production is also of importance. Seam closure about panels of interest may also be of some interest. Although mining progresses day by day through time and so do related surface subsidence and seismicity, only a year by year time scale is used in studying the seven panels considered in the years 2004–2008.

Yearly subsidence progress is certainly of interest, although not shown. However, yearly face advance and seismicity are presented. An important reason for this selectivity, in addition to computer output, is the mine study data show only yearly progress.

5.1. Surface subsidence

A sequence of longwall panel mining was then done, beginning with the premining stress field provided by the topographic cut. Displacements from the large mesh were applied at the boundary of the smaller but more refined dual mesh to take into account the effects of the rock mass outside the dual mesh.

Fig. 11 shows contours of a whole-mine computation of subsidence after mining all past, present and some future areas of the mine. The colors indicate subsidence as a percentage of mining height 3 m assumed in the model. Maximum subsidence is about 2 m, and is somewhat less than the maximum observed subsidence, although there are "hot spots" of greater subsidence, up to 2.7 m and more over the panels where mining height is greater. As a percent of mining height, maximum subsidence is approximately 78%. Chain pillar details were omitted in this whole mine

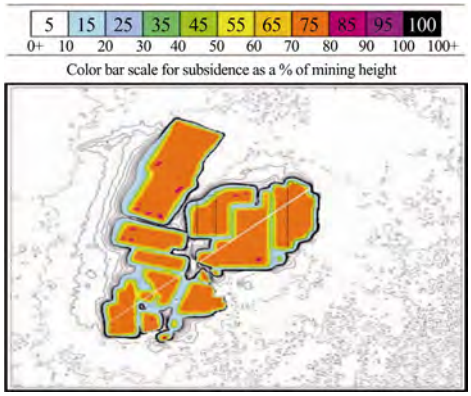

Fig. 11. Computed surface subsidence over the MINE. North is in the *y*-direction.

estimate. The white streak in Fig. 11 is an artifact of the plot routine.

Fig. 11 is about 21.6 km wide.

There are several possible reasons for the underestimation, although based on first principles. One reason is simply numerical–that is, mesh point spacing that is too great to allow for accurate estimation. For example, if a surface subsidence trough varies by several meters over a distance, say, of 10 m, then point spacing of much more than 10 m will not produce an accurate trough profile.

The actual surface subsidence profile is "bumpy" in that subsidence is about 0.3 m or so, less over the chain pillars than over the panel centers. This feature also suggests a mesh that is too coarse. However, a number of numerical experiments with much smaller elements also show smooth surface subsidence profiles.

Another reason for the discrepancy is physical. If the mechanics of subsidence are associated with vertical joints and graben formation accompanied with vertical shearing and plug-like or chimney subsidence as suggested by Maleki, then a complex material model with explicit accounting of joint effects is needed rather than a simple elastic model limited by strengths [10]. Unfortunately, a caving model with explicit jointing requires even more computer capacity than that needed for 15 million element meshes [3].

An alternative to a complex caving model is to require complete seam level closure. This specification is done by specifying a 100 percent relative displacement between roof and floor. Complete closure seems likely over panels 280 m wide (and much longer). Fig. 12 shows the surface subsidence results associated with this model. Panels are about 280 m wide and are separated by 61 m of chain pillars and entries in a three-entry system. Contours follow the color scale above Fig. 11. Maximum subsidence in this case is approximately 65 percent of mining height, about 2 m. Interestingly, the

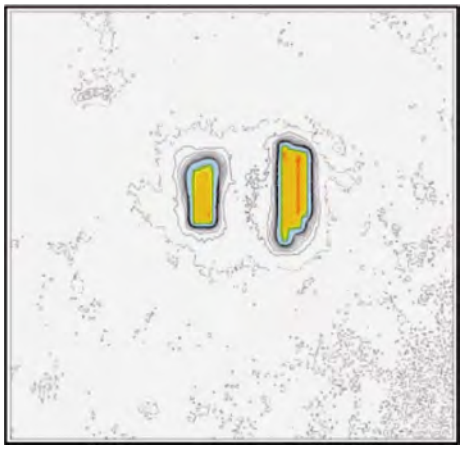

Fig. 12. Surface subsidence over seven mined panels when seam closure is complete.

chain pillars have an effect as shown in the color contrast. Better agreement with observed maximum subsidence could be obtained with different proportions of roof sag and floor heave to obtain complete closure; however, fitting model output to mine measurements is contrary to the goal of obtaining results based on first principles.

Fig. 13 shows a subsidence profile through the mined panel center and the widths of the seven panels. Interestingly, the profile is bumpy across the mined areas, and the "bumps" align with chain pillars between panels. The highest bump is less than 0.2 m. However, observed rises in the profile over the chain pillars is greater, perhaps, 0. 3 m.

5.2. Extent of yielding ground

The extent of yielding ground in the big mesh is shown in Fig. 14 in a cross-section through the panel centers that follows the surface subsidence profile. Only the first four panels on the right are shown. The width of Fig. 14 is 5.5 km; yielding elements are in black. These elements have safety factors of one. The color scale indicates element safety factors elsewhere in Fig. 14. Red elements are near failure while blue elements are far from failure. The extent of failure is almost to the surface directly above each of the seven panels. Failure is much less above the chain pillars between panels, as evident in Fig. 14. The speckled appearance is caused by strata variability. Seam depth is approximately 300 m. Some floor yielding is also evident in the figure. Shapes of the yielding zones suggest a plug-like subsidence mechanism.

5.3. Mining and seismicity

Observed seismicity during the 2004–2008 period is shown in Fig. 15. Mining during this period included four panels on the right hand side in the rectangle and, later, three panels on the left hand side (also in a rectangle). The colored plot points are according to year; the size indicates magnitude, although not readily discerned because of the plot size. The maximum and minimum magnitudes during this time period were 3.3 and 1.1, respectively. The mean magnitude of 317 events was 1.8. The location of events with respect to the panels mined suggests a systematic error in epicenter event locations. Background seismicity is always present and an important but unresolved question is how to distinguish between mine-induced events and other events, not caused by mining. Event depth would seem to be a likely criterion but hypocenter location with a wide area network is highly uncertain and thus not a candidate criterion. Events do correlate well with mining

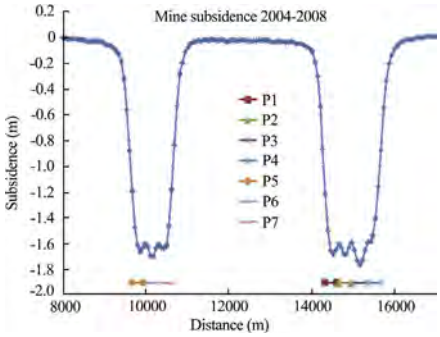

Fig. 13. East-west profile across panel mid-length.

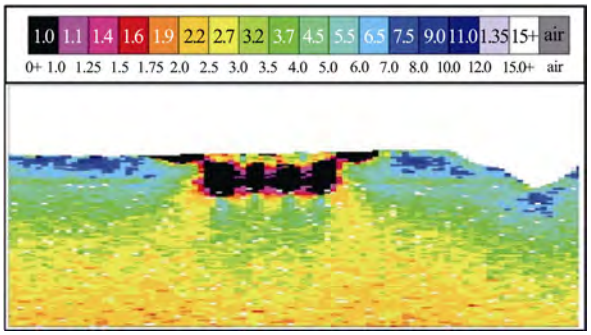

Fig. 14. Extent of yielding and element safety factor distribution after mining seven panels.

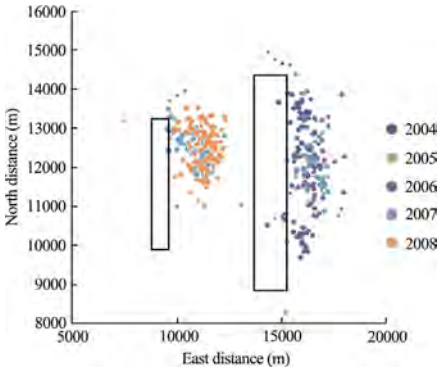

Fig. 15. Seismicity at the MINE 2004–2008.

progress as shown in the year by year data that suggests minimal background seismicity in comparison.

Not too surprisingly, the number of events correlates well with face advance, a proxy for production, as shown in Fig. 16. Mine-induced seismicity in this case appears steady rather episodic as in the classification of Iannacchione et al. [12].

For general interest, Fig. 17 shows the detail one can obtain in the dual mesh where failures about panel entries, chain pillars and crosscuts, as well as a panel face, are of concern. Gray elements are the entries and crosscuts that are excavated according to the mining sequence.

One would also expect the number of failed elements in the finite element model to correlate with cumulative face advance. That is indeed the case, as shown in the Fig. 18, for mining in the seven panels of interest from 2004 to 2008, where cumulative failed elements in the dual mesh of the dual node–dual mesh model correlate quite well with face advance. Also shown in Fig. 17 is an accumulation of magnitudes, a proxy for seismic

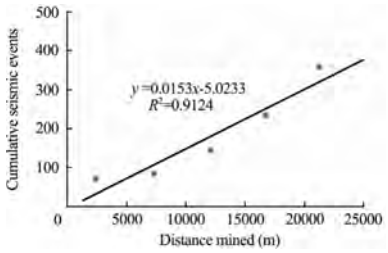

Fig. 16. Cumulative seismic events as a function of cumulative panel face advance from 2004 to 2008.

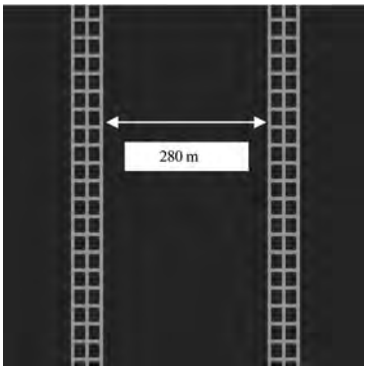

Fig. 17. Example of development detail in a dual mesh.

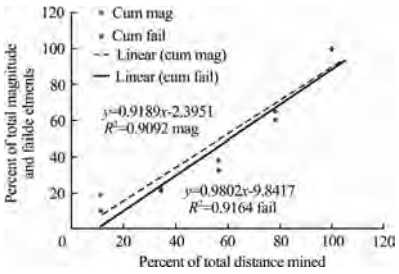

Fig. 18. Cumulative magnitude and element failure versus face advance during the 2004–2008 period.

energy, with face advance. Data in the figure are normalized to percentages of totals accumulated during the study period. The high correlations obviously relate mine-induced seismicity parameters to face advance, that is, production. Physically, element failures are directly related to face advance as the zone of failure about the face travels with the face during panel mining.

6. Conclusions

Application of a new dual-node–dual mesh finite element technique to strata mechanics was made to several underground coal mines in central Utah. Mines include longwall, room and pillar and barrier pillar mining methods. Topography, stratigraphy, jointing and variability in elastic moduli and strengths were taken into account in a new study of the MINE in Utah. Comparisons of MINE observations of surface subsidence with computed subsidence are in reasonable agreement. Key findings based on first principles rather than "scaling" demonstrate a capability for doing whole-mine analyses, thus allowing for interactions between all sections of a mine while taking into account topography, stratigraphy, strata properties variability and mining sequences. High correlations ($R^2 > 0.9$) between face advance, extent of yielding or failure of model elements and parameters of mine-induced seismicity were obtained.

Acknowledgments

Financial support for "Analysis of Mine Seismicity and Geotechnical Modeling for Improved Safety in Underground Coal Mines" by NIOSH/CDC is gratefully acknowledged. Helpful topographic file conversion by Jessica Wempen, Ph.D. student, is much appreciated as is assistance in laboratory testing by Jack Petersen and seismicity data provided by Jared Stein, M.S. graduate, and his advisor Dr. K.L. Pankow. The views expressed here are those of the authors and do not necessarily reflect official policy of NIOSH/CDC or of the University of Utah.

References

[1] Pariseau WG. An advance in multi-scale analysis of tabular deposits. In: Proceedings of 13th international congress of rock mechanics. ISRM Congress. Montreal, Canada; 2015. p. 807.
[2] Pariseau WG, McCarter MK. Rock mechanics of tabular deposits–a computational challenge. In: Proc 37th international symposium: application of computers and operations research in the mineral industry. Englewood, Colorado; 2015. p. 369–400.
[3] Pariseau WG. A multi-scale approach to mining tabular deposits. In: Labuz JF et al., editors. Proceedings of 48th U.S. symposium on rock mechanics. Minneapolis, Minnesota, USA: American Rock Mechanics Association (ARMA); 2014.
[4] Smith RG, Winkler PL, Anderson JG, Scholz CH. Source mechanisms of micro-earthquakes associated with underground mines in Eastern Utah. Bull, Seismol Soc Am 1974;64(4):1295–317.
[5] Agapito JFT, Goodrich RR, Moon M. Dealing with coal bursts at deer creek. Min Eng 1997;49(7):31–7.
[6] Arabasz WJ, Perchmann JC, McCarter MK, McKenzie JD. Seismic characterization of coal-mining seismicity in Utah for CTBT monitoring. Final report, Lawrence Livermore National Laboratory, Research Agreement. No. B344836, 124; 2001.
[7] Arabaszb WJ, Nava SJ, McCarter MK, Pankow KL, Pechmann JC, Jensen ME, et al. Ground-motion recording and analysis of mining-induced seismicity in the trail mountain Area, Emery County, Utah Final report. State of Utah, Salt Lake City, Utah: School and Institutional Trust Lands Administration (SITLA); 2002.
[8] Flectcher JB, McGarr A. Moment tensor inversion of ground motion from mining-induced earthquakes, Trail Mountain, Utah. Bull Seismol Soc Am 2005;95(1):48–57.
[9] McGarr A, Fletcher JB. Development of ground-motion prediction equations relevant to shallow mining- induced seismicity in the Trail Mountain Area, Emery County, Utah. Bull, Seismol Soc Am 2005;95(1):331–477.
[10] Maleki H. Control of mining-induced seismicity through mine design application of U.S. experience and numeric modeling to the Cottonwood Tract. Final report, School and Institutional Trust Lands Administration (SITLA). State of Utah, Salt Lake City, Utah; 2005.
[11] Ellenberger JL, Heasley KA, Swanson PL, Mercier J. Three-dimensional micro-seismic monitoring of a Utah Longwall. In: Proceedings 38th U.S. symposium on rock mechanics. Balkema, Lise; 2001. p. 1321–1326.
[12] Iannacchione AT, Esterhuizen GS, Bajpayee TS, Swanson PL, Chapman MC. Characteristics of mining-induced seismicity associated with roof falls and roof caving events. In: Proceedings of 40th U.S. symposium on rock mechanics. Anchorage, Alaska; 2005.
[13] Pariseau WG, Eitani IM. Comparisons between finite element calculations and field measurements of room closure and pillar stress during retreat mining. Int J Rock Mech Min Sci Geomech Abstr 1981;18(4):305–19.
[14] Pariseau WG, Johnson JC, McDonald MM. Poad ME. (In three parts) geomechanical monitoring and modeling using UTAH3. U.S. Bureau of Mines Report of Investigations 9618. 29; 1996.
[15] Doelling HH. Central Utah coal fields: Seveier-Sanpete, Wasatch Plateau, Book Cliffs and Emery. Monograph Series No. 3. Utah Geological and Mineralogical Survey. University of Utah, Salt Lake City; 1972.
[16] Pariseau WG, Hustrulid WA, Swanson SR, Van Sambeek LL. Coal pillar strength study. U.S. Bureau of Mines. Final report. Contract HO2422059, 417; 1977.
[17] Jones RE, Pariseau WG, Payne V, Takenaka G. Sandstone escarpment stability in the vicinity of Longwall mining operations. In: Proceedings of 31st U.S. symposium on rock mechanics. Rotterdam, Balkema; 1990. p. 555–62.
[18] Hucka B. Analysis and implication of cleat and joint systems in selected coal seams, carbon, Emery, Sanpete. Utah Geological Survey Special Study 74, 47, Utah; 1991.
[19] Pariseau WG. An equivalent plasticity theory for jointed rock masses. Int J Rock Mech Min Sci 1999;36(7):907–18.
[20] Pariseau WG. Plasticity theory for anisotropic rocks and soils. In: Proceedings of 10th U.S. symposium on rock mechanics. New York: SME/AIME; 1972. p. 267–95.

International Journal of Mining Science and Technology 27 (2017) 179–184

Contents lists available at ScienceDirect

International Journal of Mining Science and Technology

journal homepage: www.elsevier.com/locate/ijmst

Monitoring strata behavior due to multi-slicing top coal caving longwall mining in steeply dipping extra thick coal seam

Yun Dongfeng [a,b,*], Liu Zhu [a], Cheng Wendong [c], Fan Zhendong [d], Wang Dongfang [e], Zhang Yuanhao [a]

[a] College of Energy, Xi'an University of Science and Technology, Xi'an 710054, China
[b] Ministry of Education Key Laboratory of Western Mine Exploitation and Hazard Prevention, Xi'an University of Science and Technology, Xi'an 710054, China
[c] College of Architecture and Civil Engineering, Xi'an University of Science and Technology, Xi'an 710054, China
[d] Huating Coal Group Co., Ltd., Huating 744100, China
[e] Dongxia Coal Mine, Huating Coal Group Co., Ltd., Huating 744100, China

ARTICLE INFO

Article history:
Received 18 June 2016
Received in revised form 19 August 2016
Accepted 8 October 2016
Available online 10 December 2016

Keywords:
Monitoring
Steeply dipping seam
Slicing
Longwall along the strike
Fully mechanized top-caving face
Strata behavior

ABSTRACT

For studying the strata behavior due to multi-slicing top coal caving longwall mining along-the-strike direction in steeply dipping extra thick coal seams, the shield support pressures of the upper and lower slices of panel 37220 in Dongxia Coal Mine were monitored using the KJ513 dynamic monitoring system. The set up rooms adopted the "horizontal line-arc segment-inclined line" form and used different types of shield supports. The results show that the strata pressure of upper slice panel 37220-1 changed slightly along the strike direction, while along the dip direction it exhibited strong to weak pressure from bottom to top. The first weighting interval of lower slice panel 37220-2 was about 60.8 m, and the average periodic weighting interval were about 22.6 m. The strata behavior of panel 37220-2 exhibited a spatio-temporal characteristic in that periodic weighting occurred first in the middle-upper part, followed by the middle and upper parts, arc segment, and finally the lower part. During the periodic weighting, the weighting interval and intensity also exhibited strong space characteristics. The average dynamic load coefficient was 1.48 and the maximum lateral load of the side shield was 20–25 MPa.

1. Introduction

The steeply dipping coal seams account for about 20% of proven reserves and 10% of output in China [1]. About 50% of coal mines in the western China have steeply dipping seams, and are mainly distributed in Sichuan, Gansu, and Chongqing. When the steeply dipping seam, employing longwall mining along the strike direction is used, the waste rocks fill the gob non-homogeneously along the dip direction, the deformation and caving of surrounding rocks exhibit obvious asymmetry and spatio-temporal characteristics with particular and complex strata behavior [2–6]. In recent years, many research studies on strata behavior due to multi-slicing top coal caving longwall mining along-the-strike direction in steeply dipping extra thick coal seams have been performed with significant results [7–12]. However, there has been a complete lack of research on monitoring the strata behavior due to multi-slicing top coal caving longwall mining in steeply dipping extra thick coal seam. Therefore the strata behavior of multi-slicing panels 37220-1 and 37220-2 was systematically investigated in this research.

The coal seam of the panel 37220 in Dongxia Coal Mine was steep with extra thick and complicated structure. In spite of less technical difficulties (without support toppling or sliding problems), the horizontal slicing mining method has the shortcomings of multiple sections, short face width and high development rate. Although the conventional top coal caving of whole seam requires low development rate, the top coal recovery rate is low, and special measures to control shield support stability have to be taken. While the development rate in multi-slicing method is twice more than the whole seam mining with support toppling and sliding problems, it has a higher top coal recovery rate. All factors being considered, the multi-slicing top coal caving longwall mining along-the-strike direction in steeply dipping extra thick coal seams was adopted for panel 37220 [13]. Based on the thickness of coal seam, the coal seam is divided into two slices in the inclined plane. Panel 37220 was divided two slices of panel 37220-1 and 37220-2 with combined mining height covering the whole seam thickness of 19.6 m.

* Corresponding author. Tel.: +86 13002953881.
E-mail address: 752651395@qq.com (D. Yun).

http://dx.doi.org/10.1016/j.ijmst.2016.11.002
2095-2686/

The purpose of strata behavior monitoring was to understand the characteristics of overburden movement, thereby predict roof weighting.

2. Geological conditions and mining technique

2.1. Geological conditions

The main coal seam of panel 37220 is 6–2 seam with a dipping angle of 55–74°. Its Protodyakonov coefficient is $f = 2.0–3.0$. The mining depth is 603–616 m. The carbonaceous mudstone parting in the middle of 6–2 seam is 0.97 m thick and used as the base for slicing boundary. The lithology of roof and floor is as shown in Table 1.

2.2. Mining technique

In order to reduce the risk of investment for shield supports, lower the difficulty in support operation and management, and increase top coal recovery, the width of panel 37220-1 (upper slice) was 60 m and coal thickness was 9.9 m. The set up room adopted the "horizontal line-arc segment-inclined line" shape. The shield supports consisted of three ZFG5200/20/30 transition supports, thirty-five ZF5000/17/28 face supports and one ZTF11520/23/32 gate-end support. The mining height was 2.6 m and caving height was 7.3 m, so the caving ratio was 1:2.8. Coal production employed two cuts and one coal drawing with drawing interval = 1.2 m.

The width of panel 37220-2 (lower slice) was 102 m and coal thickness was 9.7 m. The development around the set up room was similar to that of panel 37220-1. The shield supports consisted of three ZFG5200/20/30 transition support (#1–#3), sixteen ZF6200/17/30 arc segment supports (#4–#19), thirty-five ZF5000/17/28 face supports (#20–#63) and two ZTF11520/23/32 gate-end supports. The mining height was 2.6 m and caving height was 7.1 m, thereby the caving ratio was 1:2.8. Similarly, coal production employed two cuts and one coal drawing with drawing interval = 1.2 m.

Table 1
Roof and floor lithology.

Category	Lithology	Thickness (m)
Main roof	Gray sandstone	More than 10
Immediate roof	Silty mudstone and grey mudstone	1.0–2.3
False roof	Carbonaceous mudstone	0.16–0.86
Immediate floor	Oil shale and carbonaceous mudstone	1.0–2.3
Main floor	Sandstone	More than 10

3. Strata behavior monitoring scheme

3.1. Layout of monitoring area

Based on the width of panel 37220-2, five survey areas along the dip direction were selected: #1 shield for the lower part, #13 shield for the arc segment, #25 shield for the middle part, #42 for the middle-upper part, and #60 shield for the upper part, as shown in Fig. 1. Each of the five survey areas has two monitoring lines, using the KJ513 dynamic monitoring system to monitor in real time the shield leg pressures, and hydraulic jack loads of side shield and base adjusting mechanism.

3.2. Monitoring system

The monitoring system is mainly composed of two parts: surface and underground. The surface components include a server, UPS and serial port server; the underground components contain communication substation and pressure sensors, etc. The underground monitoring data are automatically stored and transmitted in real time to the computer on the surface, realizing automatic online monitoring.

4. Analysis of strata behavior

4.1. Strata behavior of panel 37220-1

Based on the width of panel 37220-1, four monitoring areas along the dip direction were selected; #2 shield for the lower part, #3 shield for the arc segment, #11 for the middle-upper part, and #31 shield for the upper part, as shown in Fig. 2.

Based on Fig. 2, the strata behavior for panel 37220-1 can be summarized as follows:

(1) The average periodic weighting interval was about 19.5 m. Strata pressure changed slightly along the strike direction, while along the dip direction it varied from strong to weak in the face from bottom to top. The yield pressures of shield supports were different in different parts of the face in the following descending order of intensity, arc segment > lower part > middle-upper part > upper part.
(2) Along the dip direction, the main roof fails to form a masonry structure in the upper part, while in the lower part, the arch abutment is located above the head entry. The waste rocks could not fill up the lower part of the gob void, leading to high pressure at the head entry, and causing the gate-end shield to be crushed. Panel 37220-1 adopted

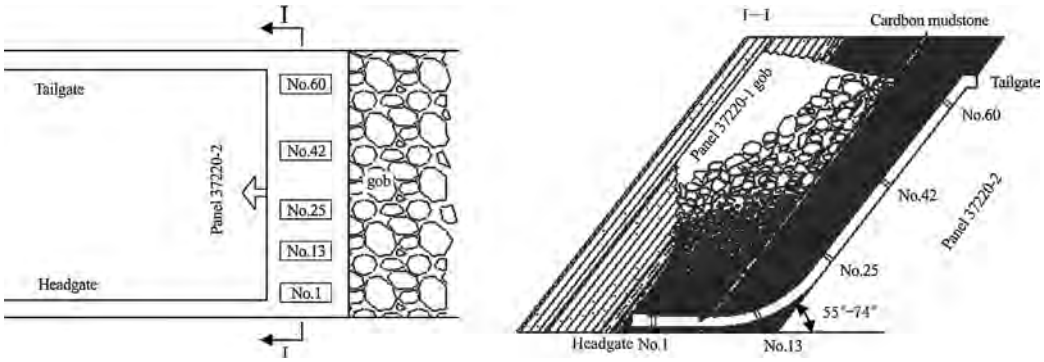

Fig. 1. Plan of panel 37220-2 survey area.

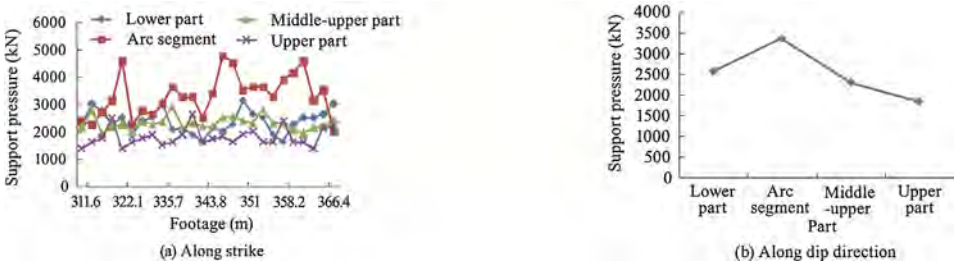

Fig. 2. Support pressure of shield supports.

artificial roof caving by means of explosives, whereby the roof pressure was released, allowing the gate-end shield to be advanced.

(3) Due to its short panel width, the caved roof and top coal could not fill up the gob void, causing high shield support pressures in the arc segment and lower part. Since the seam is steep, the normal (vertical) overburden pressure on the shield is not high, so support pressures in the middle-upper and upper part are low.

4.2. Strata behavior of panel 37220-2

After mining panel 37220-1, panel 37220-2 was mined. The weighting interval and intensity of panel 37220-2 is shown in Table 2.

Along the dip direction the weighting intensity and support pressure varied with area of the face, as shown in Fig. 3.

Based on Fig. 3, the strata behavior for panel 37220-2 can be summarized as follows:

(1) The first weighting lasted for 4–5 d with an interval of about 60.8 m. Shield support load during the first weighting was about 4578 kN. However during the non-weighting period, the shield load was 3012 kN. So the average dynamic load coefficient was 1.52. The average periodic weighting lasted for 2–3 d with an interval of about 22.6 m. The support load during weighting was about 4437 kN. However during the non-weighting period, shield load was 3050 kN. So, the average dynamic load coefficient was 1.46.

(2) Since the width of panel 37220-2 was larger than that of panel 37220-1, the gob backfill condition by the waste rocks varied along the dip direction of the face with the lower part fully filled up while the upper part was empty. The sequence of occurrence of periodic weighting is in order of descending order of the upper, middle and higher, arc segment, and lower part. The support pressure and weighting intensity also varied with segment of the face.

4.3. Shield support pressure

By analyzing the monitoring data, the support yield pressure distribution histogram (Fig. 4) and yield pressure statistics (Table 3) can be obtained.

The characteristics of shield support pressure are as follows:

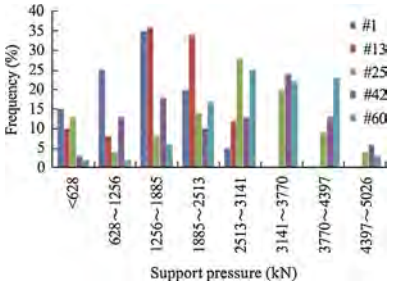

Fig. 4. Support pressure distribution histogram.

Table 2
Weighting interval and intensity for panel 37220-2.

Weight sequence	Weighting interval (m)	Pressure during weighting (kN)	Pressure during non-weighting (kN)	Dynamic load coefficient
First weighting	60.8	4578	3012	1.52
First period weighting	23.5	4393	3009	1.46
Second period weighting	21.7	4481	3090	1.45

Fig. 3. Strata behavior of panel 37220-2.

Table 3
Support pressure statistics.

Number	Average setting pressure (kN)	Average yield pressure (kN)	Average pressure of cycle end (kN)	Maximum pressure (kN)	Minimum pressure (kN)
#1	2359	2879	3390	3767	1765
#13	2516	3268	3641	4018	1882
#25	2613	3768	4267	5020	2070
#42	2598	4045	4646	5152	2149
#60	2452	3593	4395	5089	1983

(1) The average setting load of transition support and arc segment support (#1 and #13) was 2438 kN, which was about 50% of the rated setting load 4960 kN. The average setting load of face shield support was 2554 kN, which was about 63.8% of the rated setting load 4000 kN. Since the measured setting load was low, the rated emulsion pump pressure of 31.5 MPa should be maintained. Fluid supply to the hydraulic legs can only be stopped after the shield canopy is in full contact with the roof. Moreover, hydraulic fluid should be supplied as soon as the hydraulic leg pressure is relieved.
(2) During periodic weighting, the maximum shield load for shield #1 and #13 was 3893 kN with mean square error of 203 kN. The average measured shield load was 4096 kN which was 66.1% of the rated yield load 6200 kN. So the shield load utilization rate was low. The maximum shield load for shields #25, #42, and #60 was 4763 kN with mean square error of 109 kN. The measured shield load was 4872 kN, which was 97.4% of the rated yield load of 5000 kN. So the shield load utilization rate was very high.
(3) The shield supports in the arc segment were of special type with narrow canopy and wide base for better roof control, solving the practical problems for adjacent canopies that squeezed each other. It lowered the floor pressure and enhanced the support stability.
(4) The shield support pressure distribution is more reasonable and could meet the requirement of the roof control.

5. Shield loading characteristics for panel 37220-2

5.1. Loading of side shield

Compared with the horizontal and gently inclined coal seams, the shield supports in steeply dipping coal seams topple and slide more easily. The lateral load should be monitored due to the downward trend of shield supports. Fig. 5 shows the measured lateral side shield load. The higher load of the side shield corresponds to the first weighting (April 7) and first periodic weighting (April 19) of panel 37220-2. The canopy and caving shield are equipped with two side plates, and each has a double acting large diameter (Ø100 mm) cylinder [14]. In order to adapt to the large lateral load, the side plate is made of high strength steel and internal stiffeners. Moreover, the cylinder can be replaced underground.

A comprehensive analysis of the side shield load shows that:

(1) The lateral load was usually small. When shields toppled or skidded, especially during periodic weighting shield toppling was serious, the lateral pressure was up to 20–25 MPa indicating the top coal and roof slided dramatically along the strata contact planes.
(2) The maximum lateral load occurred in the middle part. At the same time due to restraint and buffer of the arc segment the shield stability was better and the lateral load at the lower part was the minimum. The magnitude of lateral load depends on the support stability with a larger lateral load during shield toppling or skidding and vice versa.
(3) The side shield of shield supports in the steeply dipping seams is used not only to prevent leakage of waste rocks between adjacent shield supports, but more importantly to push and guide the shield supports laterally, anti-toppling, adjust unstable shields, and maintain transverse stability. This is the identifying difference from those of longwall mining for the flat seams. During actual operation, the operator should make good use of the side shield's capacity for anti-toppling, anti-skidding to right the unstable shield supports.
(4) Comprehensive analysis of data obtained during practical application and monitoring data of side shield showed that except deformation occurred at the edges of side shields, the side shields can successfully adjust the unstable shield due to its high strength. The side shield with a large diameter (Ø100 mm) cylinder is able to adjust the unstable shield supports. Therefore, the side shield should be called the "side adjusting plate", with the function of adjusting unstable shield supports and preventing waste rocks from entering.

5.2. Load on base adjusting mechanism

The base adjusting mechanism of the steeply dipping shield support is an important mechanism for maintaining the correct attitude of the shield support. This is the device identifying its difference from those of longwall mining for the flat seams [15]. It consists of base adjusting jack, guide bar, and base adjusting beam. It could stretch in non-parallel directions in order to enhance the applicability of the base adjusting mechanism. Its measured data are shown in Fig. 6.

A comprehensive analysis of the base adjusting mechanism load data shows that:

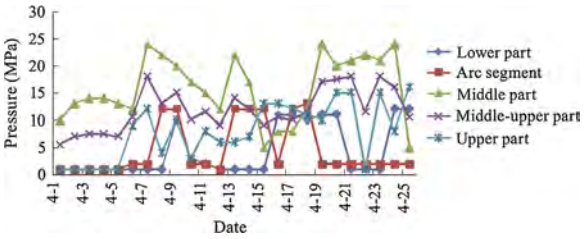

Fig. 5. Measured side shield loads.

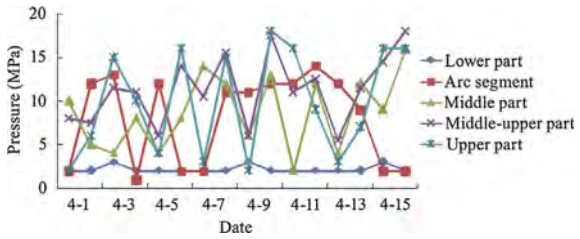

Fig. 6. Load of the base adjusting mechanism.

(1) The maximum load occurred in the upper part, while the minimum in the lower part, indicating that the shield's roof contact area in the upper part was small, therefore the shield supports could topple or skid easily. Shields in the arc segment are located in the vertical curved surface where the base distance between adjacent shield supports increases, so the base skids easily, causing shield support instability. By implementing the dynamic tracking program of shield supports in which the deviation and inclination of shield supports are monitored in real time, the abnormal shields can be adjusted timely [16].
(2) The non-parallel stretch function enhances the applicability of adjusting unstable shield supports. When adjusting the unstable shield supports, the base adjusting mechanism and side plate coordinate each other, solving the adjusting problem effectively and enhancing the shield supports applicability in steeply dipping coal seams.
(3) Although the overall strength of base adjusting beam is higher and its failure rate is reduced, the base adjusting jack cannot be replaced underground and needs to be solved by design.

5.3. Analysis of front and rear leg loads

The #42 shield support located in the middle-upper part was a four-leg choke-shield type. Its measured front and rear leg loads are shown in Fig. 7.

A comprehensive analysis of the front and rear leg loads shows that:

(1) Generally speaking, the front legs load is higher than that of the rear leg. During periodic weighting, the front leg load could reach yield load, while the rear leg could not (as shown in Fig. 7). In the steeply dipping coal seams, the front leg load is most often larger than that of the rear leg and the rear leg is often pulled up in fully mechanized top-caving face longwall mining along the strike direction. The main reason is that due to the large dip angle, the top coal above the canopy under repeated shield support loading and unloading is crushed and slides easily, creating gaps between adjacent shield supports. During setting of the front legs, since the front end of the canopy is constrained by the top coal and the roof, the rear legs tend to jack up. This situation has been proved by ground control research and field practice in longwall mining worldwide. The four-leg choke-shield has long been abandoned in the U.S., and the two-leg shields are the industry standard in longwall mining [17]. According to the monitoring data of panel 37220-1, when mining the panel 37220-2, the additional shields required were the two-leg shields, resulting in better roof control.
(2) With the increase of dipping angle of coal seam, the unbalanced characteristics of support load in steeply dipping full mechanized top caving face is more apparent. The load is asymmetric with large variation in the front and rear legs, especially in the upper and middle-upper parts. Sudden dynamic caving of roof occurs easily along the dip direction, indicating the complex relations of support-surrounding rock system.
(3) The stability of shield supports during advancing is the worst in steeply dipping coal seams and the procedure for support advance is particularly crucial. During shield advance, the legs must be lowered first. When the valve for leg lowering is opened to the predetermined position, the cylinder is connected to the return pipe and the hydraulic leg pressure vanishes instantaneously (as shown in Fig. 7). It is recommended "lower slightly but quickly pull the support forward" as adopted by Dongxia Coal Mine be used. The best practice is to turn on the leg lowering valve first to the shield advance position and then carefully lower the legs as little as possible to prevent support from toppling. Thus, skilled labors are required in operating the shield supports in steeply dipping seams by advancing and adjusting the support simultaneously.

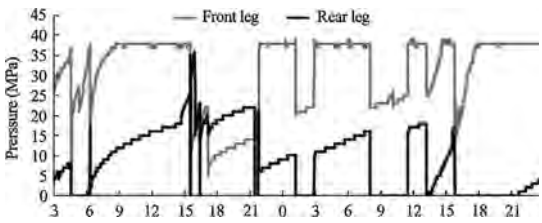

Fig. 7. Front and rear legs load of the #42 shield support.

6. Conclusions

(1) The strata pressure of panel 37220-1 changes slightly along the strike direction, while along the dip direction it varies from strong to weak for areas from bottom to top. The first weighting interval of panel 37220-2 is about 60.8 m, and the average periodic weighting interval is about 22.6 m. The panel 37220-2 strata behavior exhibits a spatio-temporal characteristic. The sequence of occurrence of periodic weighting is first in the middle-upper, followed by the middle and higher, arc segment, and finally the lower part.
(2) The setting pressure and yield pressure are reasonable and could meet the requirement of roof control. The two-leg shied is superior to four-leg choke-shield.
(3) The "sliding advance of supports" should be revised to the "lower slightly but quickly pull the support forward" to ensure the most stable condition of shield supports during the operation.
(4) The "horizontal line–arc segment–inclined line" is adopted for the set up room in steeply dipping coal seams, eliminating toppling and skidding, improving the stress state, and enhancing the stability of support system.

Acknowledgement

Thanks to funds supported by the Key Program of National Natural Science Foundation of China (No. 51634007).

References

[1] Wu YP, Liu KZ, Yun DF, Xie PS, Wang HW. Research progress on the safe and efficient mining technology of steeply dipping seam. J China Coal Soc 2014;39(8):1611–8.
[2] Shi PW. The complexity of movement of broken overlying strata in steep coal seam mining. Ground Press Strata Control 1999;16(3):26–8.
[3] Cao SG, Liu YC, Peng Y, Li Y, Liu HL. Roof control of long-wall full-mechanized mining along strike of steep coal seam. J Min Safety Eng 2009;26(4):441–4.
[4] Zhang YD, Cheng JY, Wang XX, Feng ZJ, Ji M. Thin plate model analysis on roof break of up-dip or down-dip mining stope. J Min Safety Eng 2010;27(4):487–93.
[5] Xie SR, Zhang GC, Zhang SB, He FL, Xiao DC, Tian CY. Stability control of support-surrounding rock in the large inclination fully mechanized island face. J Min Safety Eng 2013;30(3):343–7.
[6] Ma LQ, Qiu XX, Dong T, Zhang JX, Huang YL. Huge thick conglomerate movement induced by full thick longwall mining huge thick coal seam. Int J Min Sci Technol 2012;22(3):399–404.
[7] Zhao YF, Zhang XY, Tu M. Roof caving characteristic and strata behavior in exploiting steep coal seams. J Min Safety Eng 2007;24(2):231–4.

[8] Wang SR, Wang JA, Dai Y. Numerical analysis on movement and failure of coal and stress condition of support structures in mechanized top-coal caving in steep thick seam. Chinese J Rock Mech Eng 2004;23(S1):4531–4.
[9] Yin GZ, Li XS, Guo WB. Photo-elastic experimental and field measurement study of ground pressure of surrounding rock of large dip angle working coalface. Chinese J Rock Mech Eng 2010;29(S1):3336–43.
[10] Wu YP, Xie PS, Ren SG. Analysis of asymmetric structure around coal face of steeply dipping seam mining. J China Coal Soc 2010;35(2):182–4.
[11] Wu YP, Xie PS, Wang HW, Ren SG. Incline masonry structure around the coal face of steeply dipping seam mining. J China Coal Soc 2010;35(8):1252–6.
[12] Ji YL, Reng T, Peter W, Wang ZJ, Ma ZY, Wang ZD. A comparative study of dust control practices in Chinese and Australian longwall coal mines. Int J Min Sci Technol 2016;26(2):199–208.
[13] Yun DF, Liu Z, Cheng WD, Fan ZD, Su PZ, Wang DF. Longwall fully-mechanized mining technology on the strike of inclined slicing in high inclined and ultra thick spontaneous combustion tendency coal seam. Coal Sci Technol 2015;43(10):7–11.
[14] Yun DF, Liu Z Cheng WD, Fan ZD, Su PZ, Wang DF. Fully-mechanized top coal caving inclined slicing along the strike mining technique in steeply dipping extra thick spontaneous combustible coal seam. In: Proceedings of the 34th international conference on ground control in mining (China 2015). Jiaozuo, Henan: Henan Polytechnic University; 2015. p. 128–130.
[15] Yun DF, Liu Z, Cheng WD, Wang DF, Su PZ, Meng XJ, et al. Analysis of application effect of steeply dipping powered support base adjust mechanism. Coal Technol 2015;34(5):230–3.
[16] Yun DF, Zhang YH, Cheng WD, Wang DF, Su PZ, Meng XJ, et al. Support state analysis and control of fully mechanized longwall caving layered face with large inclined. Safety Coal Mines 2015;46(5):213–6.
[17] Peng SS. Longwall Mining. 2nd ed. New York, USA: Wiley; 2006.